A Study of Defects in Single Crystal CVD Diamond

Claire Glover

A thesis submitted for the degree of Doctor of Philosophy.

University of Warwick, Department of Physics.

September 2003

Contents

Acknowledgements

Many people have provided invaluable help throughout my PhD. I'd like to start by thanking my supervisor, Dr Mark Newton, for giving me excellent supervision, all the guidance and support needed to complete my PhD, and ensuring the move to Warwick went as smoothly as possible. I would also like to thank Dr Daniel Twitchen from Element Six Ltd and Dr Philip Martineau from the DTC Research Centre, who have provided me with the samples needed to make this work possible, and also for many useful discussions. I also want to thank Dan for being a good friend by giving me encouragement throughout my PhD and for proof reading this manuscript.

I would like to thank Element Six Ltd for providing me with financial support and giving me the opportunity to do this PhD.

I also want to thank Samantha Quinn, Andy Taylor, Chris Kelly and many others from the DTC Research centre in Maidenhead, who have characterised many of the samples used for the work presented in this thesis.

From the University of Warwick I would like to thank Prof. Malcolm Cooper for providing me with the facilities to carry out the experiments, Keith Briggs who helped to get the lab up and running quickly, and all of the staff in the workshop for making pieces of equipment to such a high standard. I would also like to thank all my friends from the department of Physics who have helped to make my time at Warwick highly enjoyable.

From King's College London I would like to thank Prof. Alan Collins and Prof. Gordon Davies for allowing me to use the facilities, and Bill Luckhurst for all his help in the labs. I would also like to thank Hannah Smith and Alex Connor for being great friends throughout my entire university career.

I would like to thank Prof. J. M. Baker for providing great knowledge and expertise when it has been needed most.

Finally, I would like to thank my family and in particular my parents for giving my their total support through my seemingly endless university career, and last but not least Rob Heathcote for being in my life and giving me lots of love and happiness.

Declaration

I declare that the work presented in this thesis is my own except where stated otherwise, and was carried out entirely at the University of Warwick, King's College London and the DTC Research Centre, Maidenhead, during the period between October 2000 and September 2003, under the supervision of Dr M. E. Newton. The research reported here has not been submitted, either wholly or in part, in this or any other academic institution for admission to a higher degree.

Some parts of the work reported in this thesis have been published, as listed below:

1. Claire Glover, M. E. Newton, P. Martineau, D. J. Twitchen and J. M. Baker, *Hydrogen Incorporation in Diamond: The Nitrogen-Vacancy-Hydrogen Complex*, Physical Review Letters **90**, 185507 (2003)
2. Claire Glover, M. E. Newton, P. Martineau, S. Quinn and D. J. Twitchen, *Hydrogen Incorporation in Diamond: The Vacancy-Hydrogen Complex*, Submitted to Physical Review Letters (2003)

Parts of this work, and other work not reported in this thesis, have also been presented at several national and international conferences between 2001 and 2003:

1. Claire Glover and M. E. Newton, *EPR studies in single crystal CVD diamond*, The 52nd Diamond Conference, Bristol (2001). Poster.
2. Claire Glover, M. E. Newton, J. M. Baker, P. Martineau and D. J. Twitchen, *EPR studies of defects incorporating hydrogen in CVD diamond*, The 53rd Diamond Conference, Oxford (2002). Talk.
3. Claire Glover, M. E. Newton, P. Martineau and D. J. Twitchen, *Defect related optical absorption of CVD diamond in the mid infrared*, The 53rd Diamond Conference, Oxford (2002). Poster.

4. Claire Glover, M. E. Newton, A. M. Connor, A. T. Collins and T. R. Anthony, *EPR and optical studies of HTP GE-POL treated type II diamonds*, The 53rd Diamond Conference, Oxford (2002). Poster.
5. Claire Glover, M. E. Newton, A. M. Connor, A. T. Collins and T. R. Anthony, *What can EPR tell us about the annealing of brown type IIa and type IIb natural diamond?*, International Conference on New Diamond Science and Technology 8 (ICNDST-8), Melbourne (2002). Talk.
6. Claire Glover, M. E. Newton, P. Martineau, D. J. Twitchen and J. M. Baker, *The incorporation and properties of hydrogen in CVD diamond*, The Physics of Group IV Semiconductors, University of Exeter (2003). Poster.
7. Claire Glover, M. E. Newton, P. Martineau, Samantha Quinn and D. J. Twitchen, *The vacancy-hydrogen centre*, The 54th Diamond Conference, Cambridge (2003). Talk.
8. Claire Glover, M. E. Newton, P. Martineau, Samantha Quinn and D. J. Twitchen, *Mid and near infrared optical absorption measurements in nitrogen doped single crystal CVD diamond*, The 54th Diamond Conference, Cambridge (2003). Poster.
9. Claire Glover, M. E. Newton, P. Martineau and D. J. Twitchen, The nitrogen vacancy centre in diamond: *EPR and optical properties in Isotopically enriched CVD diamond*, The 54th Diamond Conference, Cambridge (2003). Poster.
10. Claire Glover, M. E. Newton, P. Martineau, D. J. Twitchen and J. M. Baker, *The incorporation and properties of hydrogen in CVD diamond*, Diamond 2003, Salzburg (2003). Talk given by P. Martineau.

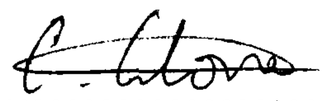

.....

Claire Glover

September 2003

Abstract

Electron paramagnetic resonance (EPR) and Fourier transform infrared spectroscopy (FTIR) have been used to study defects in single crystal diamond grown by chemical vapour deposition (CVD).

EPR measurements have been carried out on a range of differently doped samples, and amongst the many systems observed, two previously unreported defects have been identified. They both incorporate hydrogen and are the first defects to be positively identified to contain hydrogen in the diamond lattice. The two defects have been identified as the negatively charged nitrogen-vacancy-hydrogen centre (NVH^-), and the negatively charged vacancy-hydrogen centre (VH^-).

The NVH^- centre has been identified as having trigonal (C_{3v}) symmetry and an overall electron spin of $S = ½$. The spin Hamiltonian parameters have been determined and explained in terms of the proposed model of the defect. The hydrogen atom of the defect is located in the vacancy of the nearest-neighbour nitrogen-vacancy defect and appears to be bonded to the nitrogen atom, thus maintaining the observed C_{3v} symmetry.

The VH^- centre has also been identified as having C_{3v} symmetry, but has an overall electron spin of $S = 1$. The hydrogen atom is bonded to one of the four carbon atoms surrounding the vacancy and produces a very small hyperfine interaction. This is explained with the aid of the model and by performing an extended dipole calculation between the hydrogen atom and the unpaired electron probability density localised on the three equivalent carbon neighbours. No reasonable predictions on this defect could be made from studying the same defect found in silicon.

The well-documented NV^- defect has also been studied and modified spin Hamiltonian parameters have been determined. They vary significantly from the previously accepted ones and for the first time can explain the accepted model of the defect.

Optical absorption measurements have been performed on a series of CVD diamond samples and specific absorption bands studied in great detail. Correlations have been made between certain peaks and energy level diagrams proposed to describe the systems being studied. It has been determined that many peaks originate from the same system.

List of figures

List of tables

Glossary

$\underline{\mathbf{A}}$	Electron nuclear hyperfine matrix
$A_{\parallel}$	Hyperfine coupling parallel to the symmetry axis
$A_{\perp}$	Hyperfine coupling perpendicular to the symmetry axis
a	Isotropic component of the hyperfine interaction (also given as A_{iso} or A_s), which can be defined as $^1/_3(A_{\parallel} + 2A_{\perp})$
α	Optical absorption coefficient
AFC	Automatic Frequency Controller
B	Magnitude of magnetic flux density
b	Anisotropic component of the hyperfine interaction (also given as A_{aniso} or A_p), which can be defined as $^1/_3(A_{\parallel} - A_{\perp})$
^{12}C	Carbon-12 isotope
^{13}C	Carbon-13 isotope
CVD	Chemical Vapour Deposition
$\underline{\mathbf{D}}$	Electronic zero field splitting matrix
DTGS	Deuterated tri-glycine sulphate
ENDOR	Electron Nuclear Double Resonance
EPR	Electron Paramagnetic Resonance
FTIR	Fourier transform infrared
$\underline{\mathbf{g}}$	Anisotropic electronic Zeeman splitting factor such that the anisotropic Zeeman interaction is $\mu_B\mathbf{B}.\underline{\mathbf{g}}.\mathbf{S}$
g_e	Free electron g-value
g_N	Isotropic nuclear Zeeman splitting factor such that the nuclear Zeeman interaction is $-\mu_N g_N \mathbf{B}.\mathbf{I}$
h	Planck constant
HPHT	High pressure high temperature
I	Nuclear spin quantum number
$\underline{\mathbf{I}}$	Nuclear spin
I_0	Incident intensity of radiation
I_t	Transmitted intensity of radiation

ITC-3	Intelligent temperature controller
k_B	Boltzmann constant
L	Orbital angular momentum quantum number
MPCVD	Microwave plasma CVD
N_S^+	Positively charged single substitutional nitrogen centre
N_S^0	Neutral single substitutional nitrogen centre
^{14}N	Nitrogen-14 isotope
^{15}N	Nitrogen-15 isotope
NV^-	Negatively charged nitrogen-vacancy centre
NV^0	Neutral nitrogen-vacancy centre
NVH^0	Neutral nitrogen-vacancy-hydrogen centre
NVH^-	Negatively charged nitrogen-vacancy-hydrogen centre
$\underline{\mathbf{P}}$	Nuclear quadrupole interaction
ppm	Parts per million carbon atoms
Q	Nuclear quadrupole moment
q	Electric field gradient at the nucleus for which the quadrupole interaction is determined
R	Pearson's product moment correlation coefficient
r	In the point dipole approximation, r is the magnitude of the vector that joins the unpaired electron to the nucleus responsible for the observed hyperfine interaction
S	Effective electron spin quantum number
$\underline{S}$	Effective electron spin
T	Temperature
t	Optical path distance used in absorption measurements
μ_B	Bohr magneton
μ_N	Nuclear magneton
μ_0	Vacuum permeability = $4\pi \times 10^{-7}$ $Js^2C^{-2}m^{-1}$
VH^-	Negatively charged vacancy-hydrogen centre
VH^0	Neutral vacancy-hydrogen centre
ZPL	Zero phonon line

Chapter 1

Introduction

1.1 The History of Natural Diamond

Diamonds were first discovered in the alluvial river deposits in India around 800 BC and this remained the only place they were found until 1725 when they were discovered in Brazil. Again this was as an alluvial deposit and it wasn't until the end of 1869 that the first diamond was found in South Africa in a gravel deposit on the southern bank of the Orange River [1.1, 1.2].

In 1869 they were finally discovered away from river deposits in gravelly soil and weathered rock. Miners dug down and were able to find diamond in the harder, darker rock underground. The soft rock had a yellow colour and was known as "yellow ground", and as the miners dug further underground they came across harder rock with a bluish tint. This was referred to as "blue ground". This type of rock is all known now as kimberlite [1.1].

In the 19^{th} and 20^{th} centuries, diamonds were discovered in other parts of Africa, including Botswana and Namibia. Botswana is now one of the biggest diamond producers worldwide, and is the richest diamond deposit in terms of value. Other places where natural diamonds are found include Russia, Australia and Canada. The total annual worldwide diamond production in 1999 was 110.5 million carats [1.3].

It is the structure of diamond that gives it its unique properties. Its lattice is made up of a uniform framework of carbon atoms each of which is covalently bonded to the surrounding ones. The strong bonds combined with the light carbon atoms give rise to the extreme properties observed which include hardness and a thermal conductivity five times that of copper at room temperature [1.1].

1.2 Applications of Diamond

Diamond has been used for many years for industrial applications such as grinding, sawing and drilling, but the advances in diamond synthesis and corresponding increase in economic viability, has widened the range of available applications. For example:

- Optical windows [1.4, 1.5]: diamond is ideal as a radiation window for applications involving high power levels and mechanical, thermal or chemical loads. This is due to its large band gap (~5.5 eV) and the lack of infrared active fundamental vibrational modes. This results in it being optically transparent over a large wavelength range, even at high temperatures. Figure 1.1 shows an example of a polycrystalline CVD diamond window, grown by Element Six Ltd.

Figure 1.1: CVD diamond window (taken from Element Six website [1.5])

- Thermal management [1.6]: at room temperature, high purity (type IIa) natural diamond has a thermal conductivity five times that of copper (~2000 rather than ~400 $Wm^{-1}K^{-1}$ [1.6]). This makes diamond ideal for 'heat spreading' applications.
- Hard or protective coatings: diamond grown using CVD techniques can be deposited on a range of substrates with almost any shape, which provides the ability to produce a protective coating [1.7].
- Radiation detectors [1.8, 1.9]: diamond is radiation hard which makes it ideal as a radiation detector. Research has shown that CVD diamond detectors would operate with little degradation for ten years in the high radiation zones of the Large Hadron Collider at CERN. At the radiation dose used (2×10^{14} 1 MeV neutrons cm^{-2} per year [1.8]), silicon detectors would cease to function within a few months.

1.3 Diamond Classification and Defect Names

The classification of diamond is based mainly on the defect-induced one-phonon optical absorption [1.10] and was originally introduced by Robertson et al in 1934 [1.11]. Type I diamonds contain nitrogen in considerable concentrations (type Ia ~ 100 – 1000 ppm, and type Ib ~ 50 – 300 ppm). Type II diamonds are divided into two; those which are semiconducting through the presence of boron, (type IIb), and those which are not, (type IIa). Type IIa diamonds may contain nitrogen at a concentration of <0.1 ppm. Figure 1.2 summarises the classification of diamond.

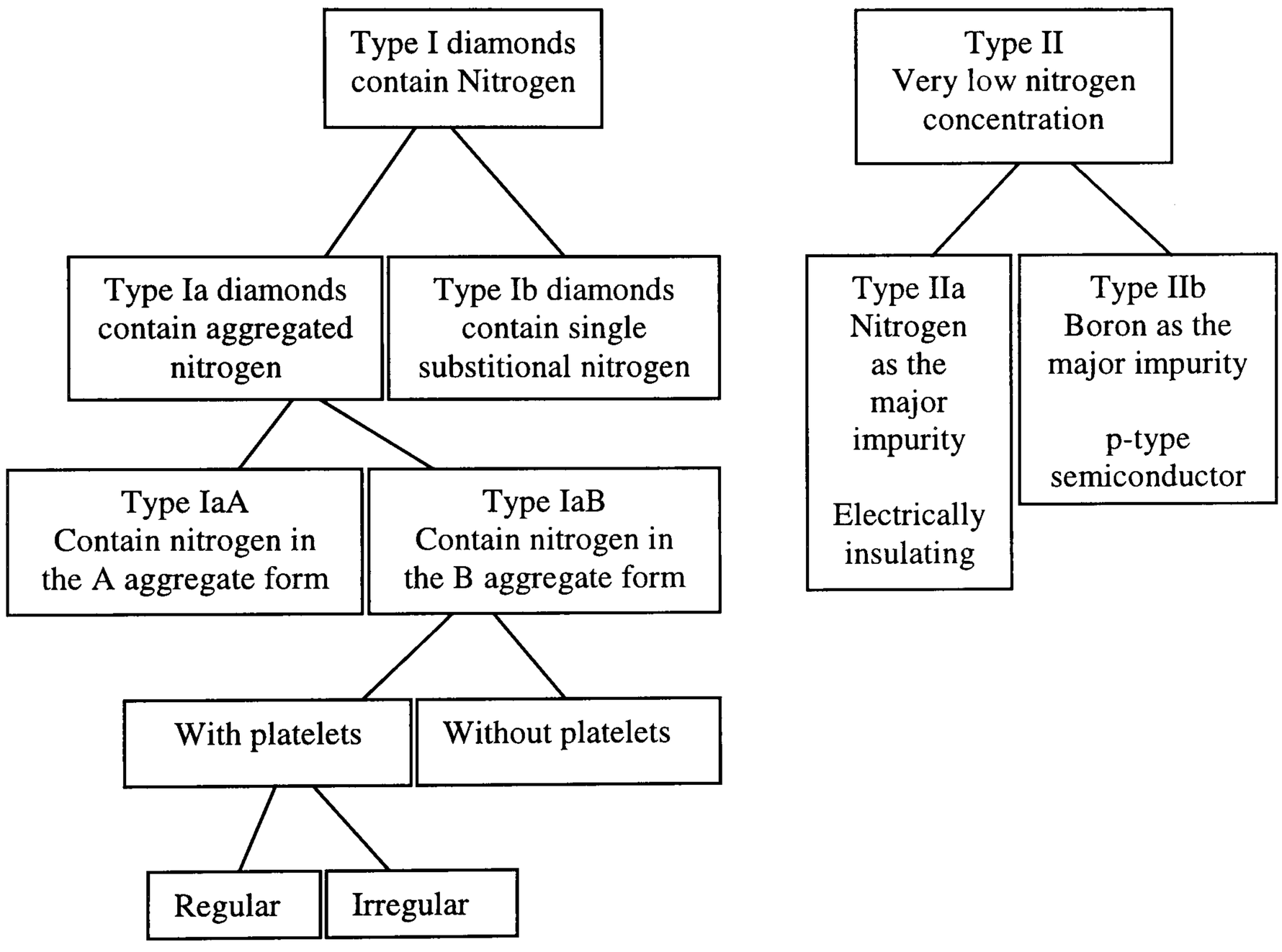

Figure 1.2: The diamond classification scheme [1.10].

Defects can greatly affect the properties of diamond, and many have been identified since diamond research began, and for this reason consistency is needed when they are named. Defects identified using EPR use the first letter of the institution at which it was first identified, followed by a number. The number represents the number of the defects previously identified at the institution. For example, R1 denotes the first defect to be identified at the University of Reading while O3 refers to the third defect identified at the University of Oxford. A comprehensive list of EPR defects discovered prior to 2001 is given by Ammerlaan [1.12].

Defects identified by optical systems use two labelling systems: the first corresponding to the energy or wavelength of the zero-phonon line, and the second according to the production method, for example GR1 is the general radiation damage defect number one. A comprehensive list of optical defects discovered before 1998 is presented by Zaitsev [1.13].

1.4 Why Study Diamond?

Some of the applications of diamond have already been discussed, and it is the potential of many more exciting applications to emerge in the future, which is the driving force for this research. The motivation stems from the exceptional material properties of diamond, such as growth methods that can be used to engineer the desired properties of materials via the control of doping, crystallinity and morphology, and the relative intellectual and computational simplicity of a single element material with a low number of electrons [1.14]. The properties of diamond are limited by the impurities and defects that it contains.

Diamond can be intentionally or unintentionally doped with impurities such as boron, nitrogen, phosphorous, sulphur, silicon and hydrogen, and crystallinity can vary from ultrananocrystalline to nanocrystalline, and polycrystalline to single crystal. Today, doping can be engineered to varying degrees and it is this that enables the design and fabrication of structures that exploit many of the desirable properties of diamond in a controllable manner [1.14].

Recent developments in the techniques of growing single crystal CVD diamond mean that diamond has a potential use as a host material in quantum computing, and the N-V defect has been exploited recently for single photon quantum cryptography [1.15].

Electron and hole mobilities more than twice the previously accepted values for diamond have recently been reported from measurements taken on very high purity, single crystal CVD diamond [1.16]. The improvement of electronic properties of single crystal diamond and the reproducibility of these properties are encouraging for the research and development of high performance diamond electronics [1.17]. For reference, table 1.1 compares the electronic properties of diamond with those of the common semiconductors, silicon (Si), gallium nitride (GaN) and silicon carbide (SiC).

	Silicon	**GaN**	**SiC**	**Diamond**
Band gap (eV)	1.12	3.0	3.2	5.5
Electron mobility ($cm^2V^{-1}s^{-1}$)	1500	2000	900	4500
Hole mobility ($cm^2V^{-1}s^{-1}$)	450	200	120	3800

Table 1.1: The latest RT mobilities of diamond in comparison to other semiconductors [1.17].

1.5 Thesis Outline

This thesis contains four background chapters and four experimental chapters, which cover the following work:

Chapter 1 is the introduction, which provides an overview into the study of diamonds and introduces the rules that are used to classify and name them. It also discusses the reasons why diamond is such an interesting topic to study.

Chapter 2 provides a literature review on the important aspects of the work relevant to what is presented in this thesis. There will be a review on the process of chemical vapour deposition (CVD) and the various different ways of growing CVD diamond, with slightly more emphasis on microwave plasma CVD (MPCVD). It will then review some of the past work on hydrogen and nitrogen in diamond.

Chapter 3 provides a brief theoretical background to the experimental technique of electron paramagnetic resonance (EPR), concentrating on the relevant details that have been used for the analysis of the experiments presented in this thesis.

Chapter 4 is the last background chapter, which discusses the most important aspects of the experimental techniques used throughout. It also provides details on how data was analysed.

The last four chapters present the experimental results. Chapter 5 discusses the previously unreported NVH^- defect, which is observed using EPR. Chapter 6 reports the modified spin Hamiltonian parameters for the NV^- defect and explains for the first time how they agree with the accepted model of the defect. Chapter 7 presents another previously unreported EPR defect, which has been labelled KCL1. The spin Hamiltonian parameters will be discussed and explained in terms of the proposed model. Finally, chapter 8 presents some optical absorption measurements recorded in the near infrared region of the spectrum.

References

[1.1] S. Tolansky, The History and Use of Diamond, Methuen & Co Ltd, London (1962)

[1.2] E. Brunton, Diamonds, N. A. G. Press, London (1970)

[1.3] The Gemmological Association and Gem Testing Laboratory of Great Britain, Gem Diamond Diploma Course notes (2000).

[1.4] C. Wild and P. Koidl, C1.1, Optical Properties of diamond and applications as radiation windows, in M. H. Nazare and A. J. Neves, Properties, Growth and Applications of Diamond, INSPEC: IEE, London (2001)

[1.5] Element Six Website. www.e6.com

[1.6] R. Berman, Thermal Conductivity of Vapour Deposited and Isotopically Enriched Diamond, in J. E. Field, The Properties of Natural and Synthetic Diamond, Academic Press Ltd. (1997)

[1.7] P. Ball, New Scientist **2067**, 22 (1997)

[1.8] L. Allers, A. S. Howard, J. F. Hassard and A. Mainwood, Diam. Rel. Mater. **6**, 353 (1997)

[1.9] A. Mainwood, L. Allers, A. T. Collins, J. F. Hassard, A. S. Howard, A. R. Mahon, H. L. Parsons, T. Sumner, J. L. Collins, G. A. Scarsbrook, R. S. Sussmann and A. J. Whitehead, J. Phys. D **28**, 1279 (1995)

[1.10] A. T. Collins, Physica B **185**, 284 (1993)

[1.11] R. Robertson, J. J. Fox and A. E. Martin, Phil. Trans. Roy. Soc. A **232**, 463 (1934)

[1.12] C. A. J. Ammerlaan, Paramagnetic Centres in Diamond, Springer (2001)

[1.13] A. M. Zaitsev, Optical Data on Superhard Semiconductors, Part 1, Diamond, Istok (1998)

[1.14] J. E. Butler, The Electrochem. Soc. Int. **12**, 22 (2003)

[1.15] A. Beveratos, R. Brouri, A. Villing, J. P. Poizat and P. Grainger, Phys. Rev. Lett. **89**, 187901 (2002)

[1.16] J. Isberg, J. Hammersberg, E. Johansson, T. Wikstrom, D. J. Twitchen, A. J. Whitehead, S. E. Coe and G. A. Scarsbrook, Science **297**, 1670 (2002)

[1.17] G. A. J. Amaratunga, Science **297**, 1657 (2002)

Chapter 2

Literature Review

2.1 Introduction

Interest in diamond has grown enormously in recent years, and as a result the literature available has increased dramatically. However, because of the speed at which the research is advancing, much of the work published will soon be out of date. There are different grades of diamond available, for example, polycrystalline and single crystal. Most of the work presented in this thesis has been carried out on single crystal CVD diamond.

Each experimental chapter contains a separate literature review that covers the work relevant for the contents of that chapter. This chapter begins by discussing diamond grown by chemical vapour deposition and the various techniques available. Finally, there will be a short discussion on some of the common defects in diamond and how they are incorporated within the diamond lattice.

2.2 Diamonds and Diamond Physics

The field of diamond physics has been extensively reviewed by Field [2.1] and by Wilks and Wilks [2.2]. In addition to this, the IEE have produced data reviews which collate many of the important ideas and results in diamond physics [2.3, 2.4]. The Properties and Growth of Diamond [2.3], devotes a lot of time to defects and impurities in diamond, and in particular nitrogen related and radiation damage defects. There is also a large, but now mostly out-of-date, section on the growth of diamond and CVD [2.3].

The Properties, Growth and Applications of Diamond [2.4], is a similar style book and covers some more recent work than [2.3]. It contains a large, relevant section on nitrogen and hydrogen in diamond. It also presents information on some of the applications of diamond, several of which have been discussed in Chapter 1. Each review contains a useful list of references relevant to the work being described [2.3, 2.4].

2.3 Chemical Vapour Deposition (CVD)

Many papers and books have been written about CVD diamond growth and Talbot-Ponsonby [2.5] gives a good review of the work carried out up to 1997. Scientists' attempts to synthesize diamond go as far back as the early 1800's [2.8]. The first attempts were to recreate the conditions needed to grow diamond naturally i.e. high temperatures and high pressures. It took many years and many failed attempts, and finally, in 1955, the first diamond was grown using high temperature and pressure (HPHT) in the presence of a transition metal catalyst [2.6].

The idea of being able to grow a diamond from the vapour phase however, was not a new one and experiments were performed as early as the early 1950's. Eventually in 1958 the first report of diamond growth from a vapour source was reported by Eversole [2.7, 2.8], who introduced methane at 0.15 Torr (1 Torr = 133 Pa [2.28]) over fine diamond powders at a temperature of 1300 K. In the early days of Eversole, the growth rate of CVD diamond was, at best, a mere tenth of a micron per hour (10^{-7} m/hr). This was too slow to become commercially viable when the process of HPHT could produce them at a much higher rate. The result of this was that very few people showed interest in the technique. However, a small group of scientists remained interested with the possibilities of CVD diamond. These efforts primarily came from the Institute of Physical Sciences in Moscow and the Case Western Reserve University in Cleveland, Ohio. They worked on the problem independently and both achieved success in the late 1960's. They discovered that using hydrogen at temperatures higher than 1000 °C greatly enhanced diamond growth [2.9, 2.10].

Later, in 1982 it was discovered that it was possible to grow diamond on surfaces other than diamond [2.22]. The principle was essentially based on the addition of atomic hydrogen to methane. The atomic hydrogen could be generated from the dissociation of molecular hydrogen using a hot filament or electric discharge in the methane. The effect this has on the growing diamond is that it is free from other types of carbon, for example, graphite and amorphous hydrogenated carbon. Further details of the role hydrogen plays in a CVD reactor will be discussed in section 2.5, Hydrogen in Diamond.

The mechanism behind the growth of diamond using CVD won't be discussed in this chapter, but is described in great detail by Goodwin and Butler [2.12]. A schematic demonstrating the process is summarised in figure 2.1.

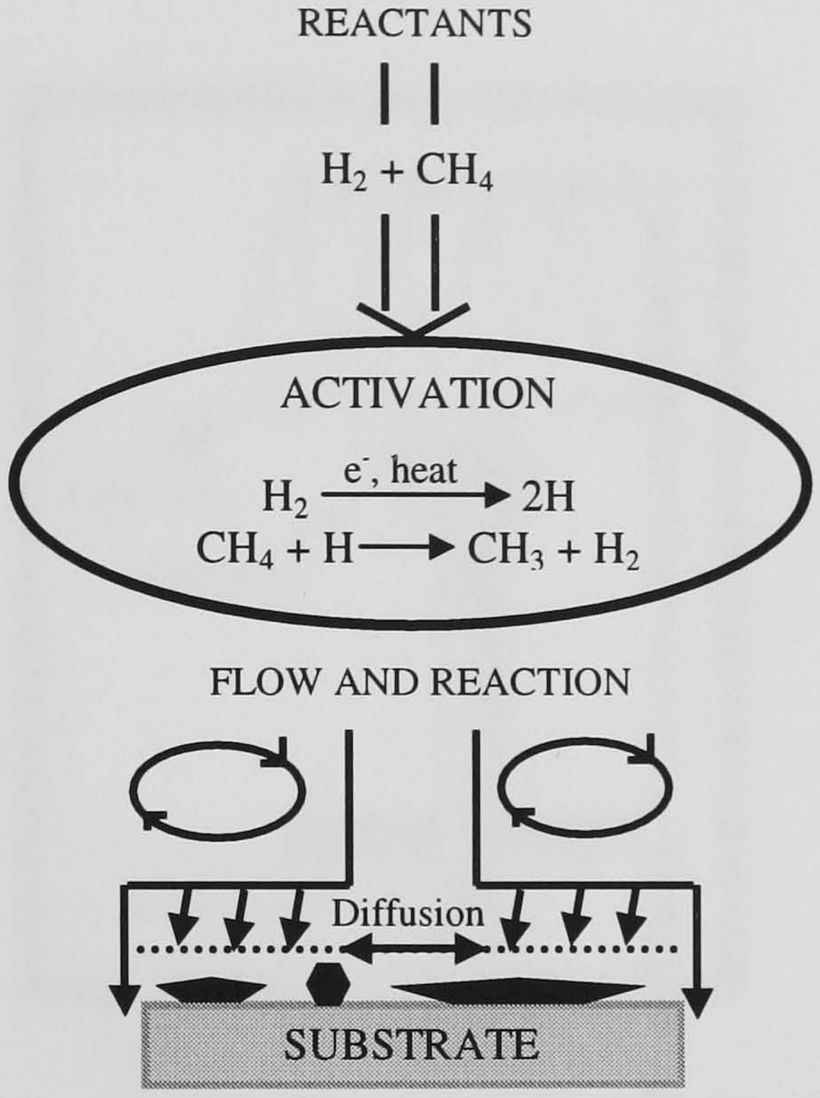

Figure 2.1: Schematic of processes occurring during diamond CVD diamond growth [2.11, 2.12]

Techniques were developed further, with methane still being used as the source of carbon, but with the concentration of hydrogen being increased. Eventually the number of techniques used for growing CVD diamond multiplied fast with the main difference in each being the way the energy is fed into the reactor to dissociate the gas.

2.3.1 CVD Diamond Reactors

The most common gas phase activation methods for CVD diamond growth are detailed below:

2.3.1a Hot Filament CVD Reactors

This was one of the earliest methods for low-pressure synthesis of diamond on non-diamond substrates. Further information can be found in the following references, [2.13, 2.14, 2.15], and the main principles are outlined in figure 2.2.

The main advantages of hot filament methods are:

- Relatively inexpensive equipment

- Large areas of homogeneous deposition are possible when multi filament arrangements are used
- Variable gas activation parameters allow the deposition conditions to be controlled.

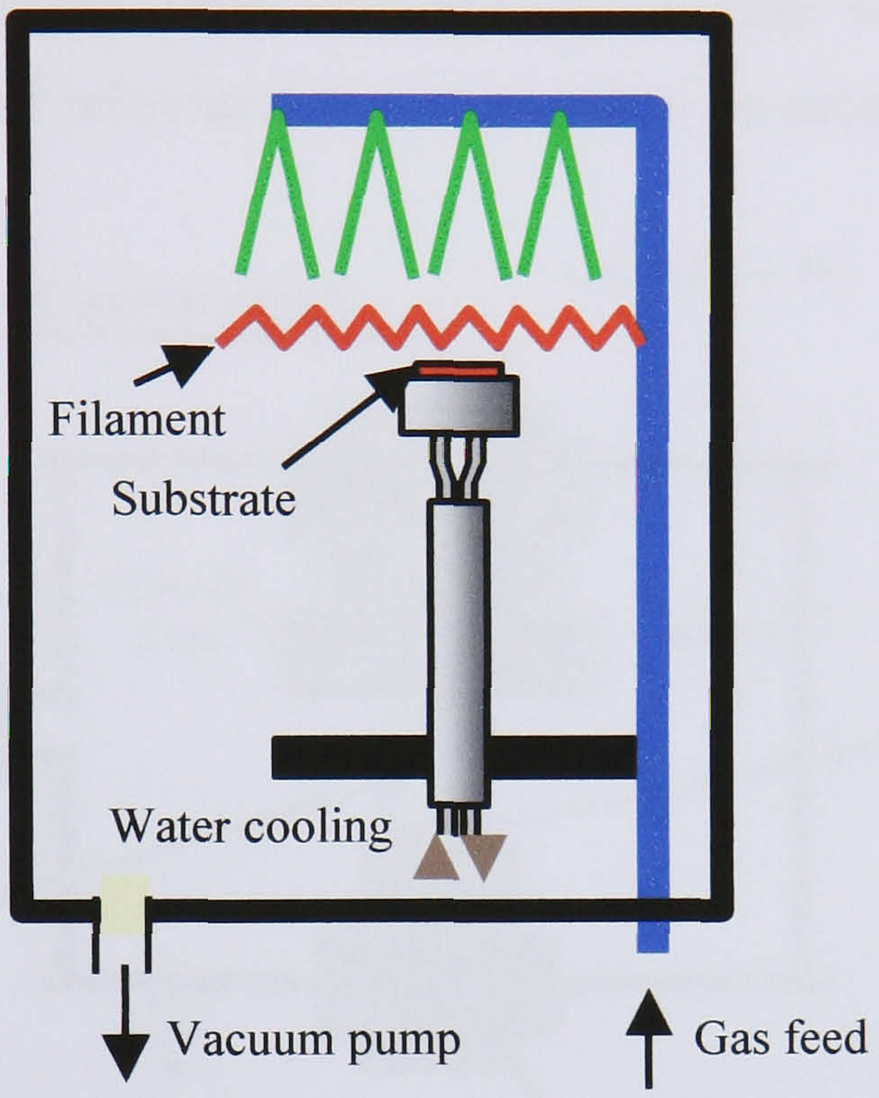

Figure 2.2: Schematic showing the basic principle of a hot filament CVD reactor. The source gases interact with a hot surface, usually a thin wire, and decompose to form atomic hydrogen and hydrocarbon free radicals. These active species then diffuse to the substrate where diamond is then formed.

The main disadvantages are:

- The lifetime of the filament materials is limited
- The diamonds deposited can contain traces of the filament material
- The reproducibility can be lower than other methods
- There is an upper limit on the temperature that the filament can reach (~2600 °C), which results in the production of less atomic hydrogen and therefore lower growth rates (the role of hydrogen will be discussed in more detail in section 2.5).

The conditions used for this method are [2.15]:

- Pressure between a few and several hundred Torr
- Substrate temperature between 600 – 1200 °C
- Filament temperature of between 2000 – 2600 °C
- Filament materials of tungsten, tantalum or rhenium

Growth rates between 0.5 – several μm per hour.

2.3.1b DC Plasma

This method uses an electrical discharge to radicalize the hydrogen and decompose the carbon carrier to form CVD diamond [2.16]. A DC plasma is the simplest way to form an electrical discharge at low pressures, figure 2.3. At low powers and pressures the temperature of the gas remains fairly low and heat transfer from the discharge is not sufficient to reach the desired substrate temperature and so the substrate needs to be heated.

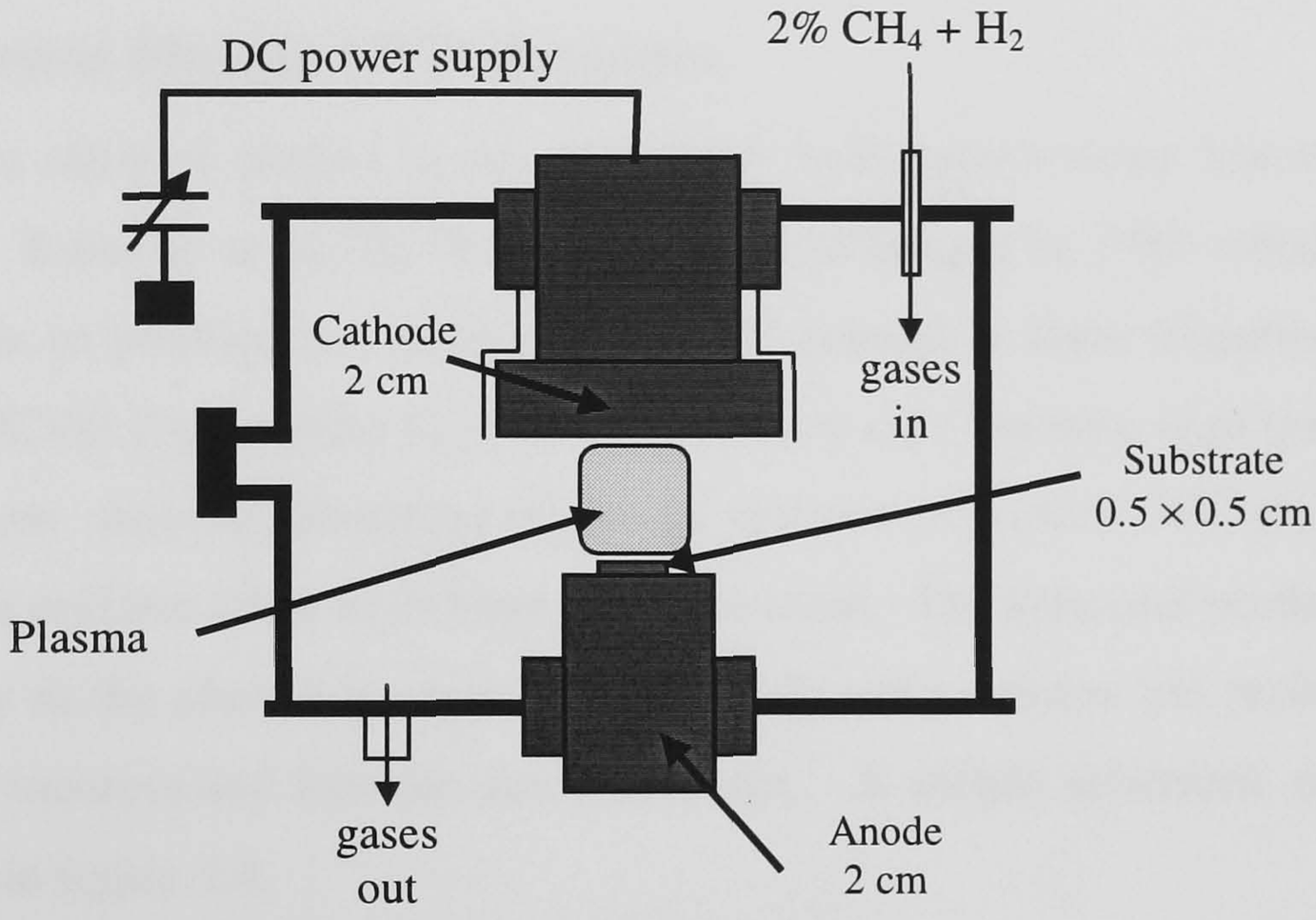

Figure 2.3: DC plasma CVD reactor for diamond deposition at different plasma power levels [2.17, 2.18].

Advantages of the DC Plasma method include

- Large area at low pressure/power
- High linear growth rates at high pressure/power
- Simple set-up

Disadvantages of the method include

- Bad quality at low pressures/powers
- Low growth rates at low pressure/power
- Small deposition area at high pressure/power.

The conditions used for this method are:

- Temperature of the hot zone between 1400 °C at low pressure/power up to >6000 °C for high pressure/power
- Substrate temperature of between 600 – 1100 °C
- Growth rates vary from <0.1 μm per hour at low pressure/power to 20-250 μm per hour at 200 mbar and 0.5-10 Acm^{-2}.

2.3.1c DC Arcs and DC Jets

The use of a direct-current plasma jet was successfully demonstrated for the first time for the synthesis of diamond, in 1988 by Kurihara *et al* [2.19]. By increasing the pressure of a DC plasma system a plasma jet can be generated. The substrate is cooled between 800–1100 °C while the gas is maintained at a temperature of ~3500 °C. The growth rate varies between 20 and 1000 μm per hour [2.20, 2.21].

2.3.1d Microwave Plasma CVD Reactors

All of the samples studied in this work have been grown using Microwave Plasma CVD, MPCVD. Kamo et al [2.22] first reported the technique in 1983 where they used a 2.45 GHz plasma to produce the hydrogen radicals needed to form diamond. The main advantage of MPCVD is the ability to produce extremely reproducible, high quality diamond at a reasonable cost. Another advantage of plasma systems over other CVD techniques is the ability to produce uniform films over large substrate areas. The diamond produced can be of very high quality as the plasma is clean, which significantly reduces the probability of any impurities being incorporated into the diamond lattice. A simple schematic of an MPCVD reactor is shown in figure 2.4.

The main disadvantage of MPCVD was the low growth rate (<15 μm/h) when compared with other CVD reactors, for example, arcjet torches which can grow at a rate of ~100 μm/h [2.23, 2.24]. The low growth rate is a result of the low pressure of the plasma.

Nitrogen can be added to the reactive gas during growth because it has shown to have the beneficial effect of creating more growth sites, therefore enhancing the growth rate of the diamond by up to three times [2.25, 2.26]. The addition of nitrogen in the reactive gas also has the effect of creating single substitutional nitrogen centres within the diamond lattice, N_s^0 (P1 EPR centre) [2.27]. Nitrogen in diamond will be discussed in more detail in section 2.6.

Until 2002, only low growth rates, up to about 15 μm/h, had been reported using MPCVD [2.28]. In 2002, Yan *et al* [2.28] reported growth rates of single crystal CVD diamond between 50-150 μm/h, depending on stage design, methane concentration and addition of nitrogen. The conditions used by Yan *et al* to produce the reported high growth rates, are given below:

- Reactor pressure of 160 Torr
- 3% N_2/CH_4
- 12% CH_4/H_2

- Substrate temperature of 1220 °C
- Microwave power of 1.6 kW
- Growth rate of 58 μm/h
- Unpolished crystal size of $4.2 \times 4.2 \times 2.3$ mm^3.

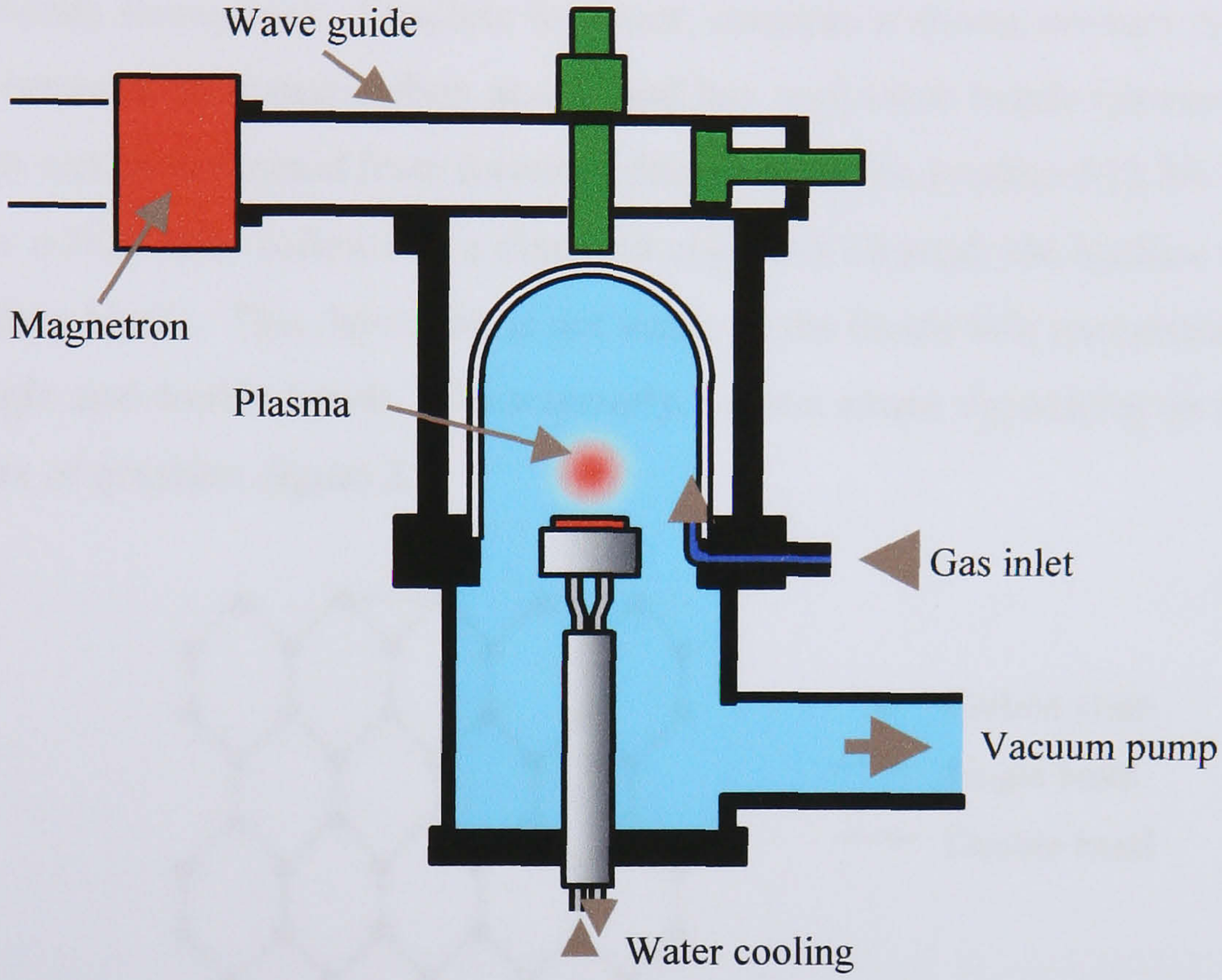

Figure 2.4: Schematic of an MPCVD diamond reactor.

Information on the growth of thick, CVD diamond crystals can be found in the following patents [2.29, 2.30, 2.31]. Patents [2.29] and [2.30] produced by Element Six Ltd. have shown the method of growing very high purity single crystal CVD diamond without the addition of nitrogen. However, there is no mention of growth rates.

It has also been shown that the addition of oxygen to the reactive gas can remove nitrogen-related defects and reduces the number of silicon and hydrogen impurities [2.32]. Hydrogen is incorporated into CVD diamond during growth because of its dominating presence in the growth process. Silicon can also be incorporated due to the etching of the quartz reactor walls and substrate holder [2.33].

2.5 Hydrogen in CVD Diamond

Hydrogen plays an essential role in the growth of CVD diamond and as a result hydrogen related defects are formed. Hydrogen is important in diamond because of its ability to affect the optical and electrical properties. It was mentioned back in section 2.3 that atomic hydrogen in the growth process prevents the formation of graphite. The differences between graphite and diamond are that diamond has a 3D structure with very strong single bonds throughout. Graphite however, contains a strong mixture of single and double bonds between its planar carbon atoms, and has very weak bonds between its layers. If double bonds can be prevented from forming, diamond will be produced [2.34, 2.35].

This is achieved as follows: if a diamond crystal is cleaved, the surface will consist of single dangling bonds. This, however, is not stable so the bonds will reconstruct to form a mixture of single and double bonds. Consequently, carbon atoms depositing on this surface will form layers of graphite, figure 2.5.

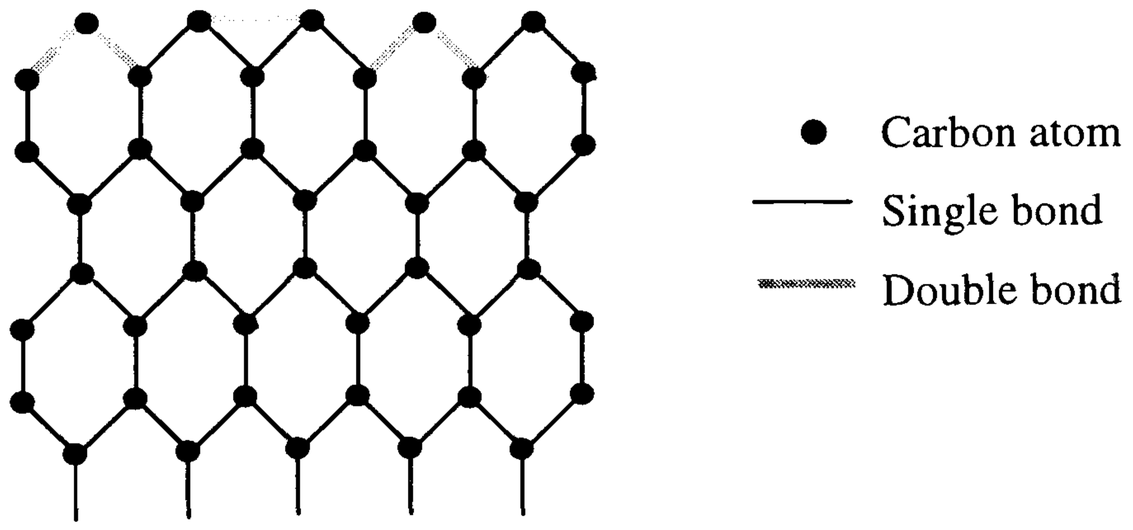

Figure 2.5: Reconstruction of the diamond surface (taken from [2.34])

This reconstruction can be prevented, however, by exposing the surface to atomic hydrogen. The atoms will react with the carbon to form single bonds, which then stabilizes the diamond surface [2.36], figure 2.6. However, the hydrogen-carbon bond (E = 413 KJ mol^{-1}) is stronger than the carbon-carbon bond (E = 348 $KJmol^{-1}$) [2.37], which means that no further diamond can grow on this surface.

However, the atomic hydrogen can then collide with the diamond surface, which produces a hydrogen molecule and a vacant site. In CVD diamond growth there is approximately fifty times more atomic hydrogen in the gas mixture than there is carbon, so it is likely that the next process to happen will be the collision of another hydrogen atom. This process repeats until eventually a carbon atom collides with the vacant site, thereby generating diamond growth.

Hydrogen defects will be formed in the diamond lattice when hydrogen atoms are not removed and replaced with a carbon atom, and therefore overgrown with diamond. Diamonds are often highly contaminated with hydrogen in the non-crystalline regions, for example grain boundaries and dislocations. These impurities can be detected using infrared absorption spectroscopy [2.38].

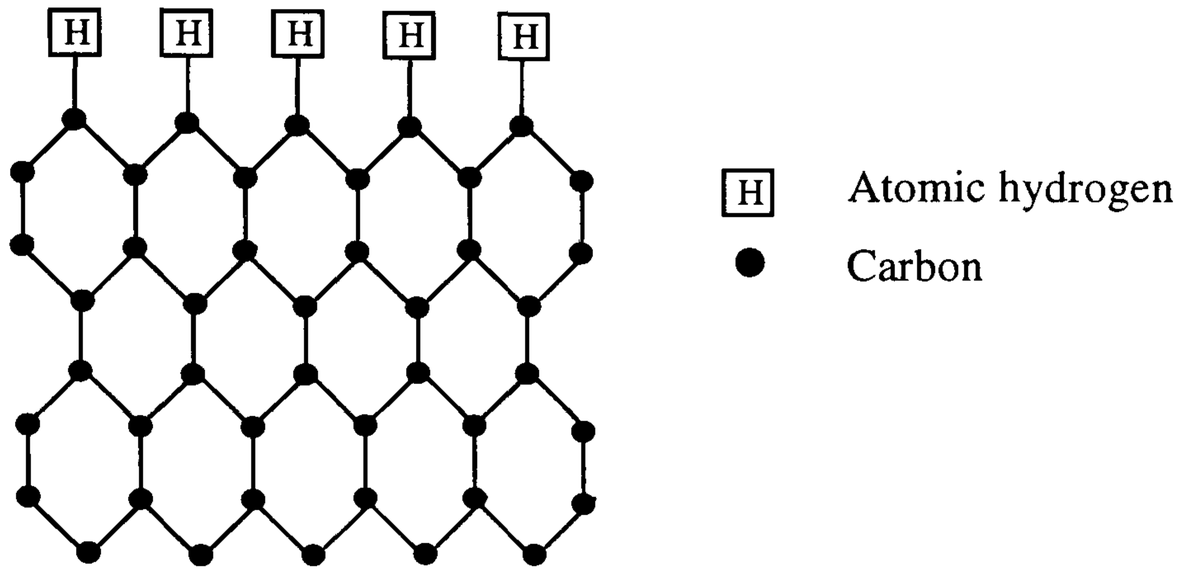

Figure 2.6: Diamond surface stabilized by atomic hydrogen (taken from [2.34])

Hydrogen in silicon has been extensively studied (see literature review in Chapter 7), and there is a long way to go before the same detail is known about hydrogen in diamond. However, the properties of muonium can be used as a comparison to study the expected behaviour of hydrogen found in diamond [2.39], since muonium is considered to be a light isotope of hydrogen and so should have similar properties.

A muon is an elementary particle with a mass 209 times that of an electron and an overall negative charge. Binding an electron and a positive muon forms Muonium [2.40]:

$$\mu^+ e^- = Mu$$

Since the mass of the muon is much larger than that of the electron, muonium is considered to be a light isotope of hydrogen. The two particles have very similar properties in a vacuum, see table 1 in [2.40], and for this reason it is expected that these two atoms will have similar electronic structures when implanted in a solid.

Muons have been identified in diamond through muon-spin-rotation experiments (μSR). In these experiments, a muon decays into a positron that is emitted and detected. There are two different muonium states that have been shown to exist in diamond: anomalous muonium (Mu*) and normal muonium (Mu). Mu* has ⟨111⟩ axial symmetry,

and Mu is isotropic (T_d symmetry). The two muonium states have also been detected in silicon [2.41, 2.42] and germanium [2.43].

Temperature variation experiments have shown that, in diamond, Mu* is the more stable of the two forms. In Mu*, the muon is located at a bond-centred position compared with in a tetrahedral site in Mu [2.44]. There is an energy barrier of about 2 eV between the two, and the stability of the bond-centred muon is the result of an unusually large lattice relaxation. For this reason, it can be postulated that hydrogen in the bond centred position will also be the most stable form, which is in agreement with theoretical predictions for hydrogen incorporation [2.50]. Very light nuclei such as a muon will have very high zero-point energy, which may result in difficulties localising it. This means that if the muon can be stabilised, the heavier hydrogen atom would also be expected to be stable there. As yet, however, there is no positive experimental evidence for bond centred hydrogen.

Hydrogen was not widely identified in diamond using electron paramagnetic resonance (EPR) prior to the work presented in this thesis, and no defects incorporating hydrogen had been identified in single crystal diamond. However, many hydrogen related absorption peaks have been observed in diamond using infrared absorption spectroscopy. The literature review in Chapter 8 will discuss this.

Prior to this work, two defects involving hydrogen had been identified in diamond using EPR. These defects are labelled H1 and H2 and were first discovered in 1996 by X. Zhou *et al* [2.45, 2.46]. H1 and H2 differ from the hydrogen related defects presented in this thesis because the hydrogen atom is not incorporated in the actual diamond lattice. Instead it is located in grain boundaries or other non-crystalline regions. Zhou *et al* proposed that H2 was only present when H1 wasn't, but further work carried out by Talbot-Ponsonby *et al* [2.47] proposed that H2 always accompanied H1.

H1 and H2 are commonly observed in polycrystalline diamond. Zhou *et al* identified H1 as having a spin of ½ and observed it using microwave frequencies of 9.8, 14, 20 and 35 GHz. They also concluded that the defect contained a single hydrogen atom which was located ~1.9 Å away from the unpaired electron. This separation was calculated from the anisotropic component of the hyperfine interaction (see section 3.2.3). The H1 defect is believed to be electrically active [2.45], with a level around 1 eV above the valence band [2.48].

The H2 defect was also reported by Zhou *et al*, but was only observed using microwave frequencies of 14 and 20 GHz. It was concluded that the hydrogen atom in the defect was located ~2.3 Å away from the unpaired electron. In each case it was believed that the hydrogen atom was located in a stretched bond at a grain boundary or other misfit

regions, which allowed the carbon atoms to relax backward, one bonding to the hydrogen and the other with an unpaired electron in its dangling bond. The EPR system belonging to H1 always contained a weak pair of partially resolved satellites that were believed to arise from forbidden nuclear spin flip transitions of a hydrogen atom weakly coupled to the unpaired electron spin [2.49]. This was the proof needed to identify the involvement of hydrogen.

Much theoretical work has been conducted on the incorporation of hydrogen in diamond and an excellent review is given by Goss [2.50]. The details of the review will not be presented here, but the important points will be summarised. The interaction of hydrogen with other defects in diamond, such as boron, phosphorous and sulphur, often results on electrically active centres. The bond centred hydrogen defect, which is suggested to be the lowest energy site for hydrogen in the perfect diamond lattice [2.51], possesses both donor and acceptor levels deep in the band gap, and migrates in diamond with an activation barrier around 1.6 and 2.0 eV. Hydrogen is relatively strongly bound to almost all defects in diamond, with energies of the order of several eV.

2.6 Nitrogen in Diamond

Nitrogen is the most common impurity in diamond and single substitutional nitrogen, N_s^0, was the first impurity to be identified using EPR in 1959 [2.52]. N_s^0 was first identified in CVD diamond in 1988 by Watanabe and Sugata [2.53]. The structure of the single substitutional nitrogen atom consists of the nitrogen atom bonding with its four carbon neighbours, with the extra electron localised in an antibonding orbital between the nitrogen and one of the carbon atoms. This unique carbon-nitrogen bond is approximately 20-30% longer than a normal C-C bond [2.54, 2.55, 2.56], and forms the principal axis of the defect, which has C_{3v} symmetry. N_s^0 can form a deep-lying donor state about 2 eV below the conduction band and often donates an electron to other defects in its vicinity [2.57].

Cox provides an extensive review on the EPR and ENDOR measurements made on the single substitutional nitrogen centre (P1) [2.58]. The P1 EPR spectrum consists of three equally spaced, equal intensity lines. This is characteristic of a spin 1 nucleus, of which ^{14}N is one of only a few occurring at a significant natural abundance, ~99.6%. When the P1 defect consists of a ^{15}N nucleus instead of a ^{14}N nucleus, a spectrum consisting of only two lines is observed. This is the characteristic pattern of a nucleus with a spin of ½. The single substitutional nitrogen in diamond has a g value of 2.0024(1) [2.53] and hyperfine and quadrupole values as given in table 2.1.

^{14}N	^{15}N
$A_{\parallel}$ = 114.032(3) MHz ⟨111⟩	$A_{\parallel}$ = 159.730(7) MHz ⟨111⟩
$A_{\perp}$ = 81.318(2) MHz	$A_{\perp}$ = 113.838(6) MHz
$P_{\parallel}$ = -3.973 (1) MHz	

Table 2.1: ^{14}N and ^{15}N hyperfine and quadrupole parameters for the N_s^0 centre determined by Cox et al [2.59].

Not only is single substitutional nitrogen readily observed by EPR, it is also observed using optical absorption spectroscopy. In the mid-infrared, there is an absorption maximum at 1130 cm^{-1} and a sharp peak at 1344 cm^{-1} [2.60]. Replacing ^{14}N with ^{15}N during growth causes the peak at 1130 cm^{-1} to shift to a lower energy by about 15 cm^{-1} [2.61], proving the involvement of nitrogen. A change in nitrogen isotope has no effect on the peak at 1344 cm^{-1}. The peak at 1344 cm^{-1} shifts to 1292 cm^{-1} in diamonds doped with ^{13}C [2.61]. The 1344 cm^{-1} peak correlates with the 1130 cm^{-1} peak, which indicates that the 1344 cm^{-1} peak is related to nitrogen. However, because there is no effect on the 1344 cm^{-1} peak when ^{14}N is replaced with ^{15}N, it can be concluded that nitrogen is not moving in this vibration. The change in peak position with $^{12}C/^{13}C$ indicates that the peak is a carbon vibration, which is associated with N_S^0.

Nitrogen can act as a donor, and when this happens an N_s^+ centre is formed. This centre is diamagnetic and so cannot be observed using EPR, but it has a well-known infrared absorption peak [2.62, 2.63]. The mid-infrared region of the spectrum will be discussed in more detail in appendix 3, when all of the peaks associated with nitrogen in diamond will be identified.

Other nitrogen related defects observed in CVD diamond include the neutral and the negatively charged nitrogen-vacancy centre. The NV^- centre has been observed using optical absorption, EPR and photoluminescence [2.64, 2.65, 2.66]. The NV^0 centre has been observed using optical absorption and cathodoluminescence [2.67]. The nitrogen-vacancy centres will be discussed in more detail in the literature review in Chapter 6.

References

[2.1] J. E. Field, editor, The Properties of Natural and Synthetic Diamonds, Academic Press, London (1992)

[2.2] E. Wilks and J. Wilks, Properties and Applications of Diamond, Butterworth-Heineman, Oxford (1991)

[2.3] G. Davies, editor, Properties and Growth of Diamond, INSPEC: IEE, London (1994)

[2.4] M. H. Nazare and A. J. Neves, editors, Properties, Growth and Applications of Diamond, INSPEC: IEE, London (2001)

[2.5] D. Talbot-Ponsonby, D.Phil Thesis, University of Oxford (1997)

[2.6] F. P. Bundy et al, Nature **176**, 51 (1955)

[2.7] W. Eversole, U.S. Patents 3030187, 3030188 (1962)

[2.8] R. M. Hazen, The Diamond Makers, Cambridge University Press (1999)

[2.9] J. C. Angus, H. A. Will, and W. S. Stanko. J. Appl. Phys. **39**, 2915 (1968)

[2.10] B. V. Derjaguin, D. V. Fedoseev, and V. M. Lukyanovich. J. Cryst. Growth **2**, 380 (1968)

[2.11] J. E. Butler and R. L. Woodin, Philos. Trans. R. Soc. London **342**, 209 (1993)

[2.12] D. G. Goodwin and J. E. Butler, Theory of Chemical Vapour Deposition. In M. A. Prelas, G. Popovici and L. K. Bigelow, Handbook of Industrial Diamonds and Diamond Films, Dekker, New York, p527 (1998)

[2.13] R. Gat and J. C. Angus. Principles of Hot-filament assisted deposition of diamond. In G. Davies, editor, Properties and Growth of Diamond, chapter 11.1, INSPEC (1994)

[2.14] R. Haubner and B. Lux. Techniques of Hot-filament assisted deposition of diamond. In G. Davies, editor, Properties and Growth of Diamond, chapter 11.2. INSPEC (1994)

[2.15] A. Argoitia, C. S. Kovach and J. C. Angus, Hot-Filament CVD Methods, in M. A. Prelas, G. Popovici and L. K. Bigelow, Handbook of Industrial Diamonds and Diamond Films, Dekker, New York, p797 (1998)

[2.16] P. K. Bachmann. Plasma CVD synthesis of diamond. In G. Davies, editor, Properties and Growth of Diamond, chapter 11.4. INSPEC (1994)

[2.17] K. Suzuki, A. Sawabe, H. Yasuda and T. Inuzuka, Appl. Phys. Lett. **50**, 728 (1987)

[2.18] K. Suzuki, A. Sawabe, H. Yasuda and T. Inuzuka, Jpn. J. Appl. Phys. **29**, 153 (1990)

[2.19] K. Kurihara, K. Sasaki, M. Kawarada and N. Koshino, Appl. Phys. Lett. **52**, 437 (1988)

[2.20] M. A. Cappelli, Arcjet Synthesis of Diamond, in M. A. Prelas, G. Popovici and L. K. Bigelow, Handbook of Industrial Diamonds and Diamond Films, Dekker, New York, p865 (1998)

[2.21] Yu. A. Mankelevich, N. U. S. Suetin, M. N. R Ashfold, W. E. Boxford, A. J. Orr-Ewing, J. A. Smith and J. B. Wills, Diam. Rel. Mat. **12**, 383 (2003)

[2.22] M. Kamo, Y. Sato, S. Matsumoto, and N. Setaka. J Cryst. Growth, **62**, 642, (1983)

[2.23] B. V. Spitsyn, L. L. Bouilov and B. V. Derajahuin, Jnl. Cryst. Growth **52**, 219 (1981)

[2.24] P. K. Bachmann, Microwave Plasma Chemical Vapour Deposition of Diamond, in M. A. Prelas, G. Popovici and L. K. Bigelow, Handbook of Industrial Diamonds and Diamond Films, Dekker, New York, p821 (1998)

[2.25] W. Muller-Sebert, E. Worner, F. Fuchs, C. Wild and P. Koidl, Appl. Phys. Lett. **68**, 759 (1996)

[2.26] A. Afzal, C. A. Rego, W. Ahmed and R. I. Cherry, Diam. Rel. Mat. **7**, 1033 (1998)

[2.27] C. Yan and Y. K. Vohra, Diam. Rel. Mar. **8**, 2022 (1999)

[2.28] C. Yan, Y. K. Vohra, H. Mao and R. J. Hemley, Appl. Phys. Sci. **99**, 12523 (2002)

[2.29] Single crystal diamond prepared by CVD, De Beers Industrial Diamonds Ltd, Patent no: WO 01/96633 A1 (2001)

[2.30] Thick single crystal diamond layer, De Beers Industrial Diamonds Ltd, Patent no: WO 01/96634 A1 (2001)

[2.31] System and method for producing synthetic diamond, Apollo Diamond Inc., Patent no: WO 03/014427 A1 (2003)

[2.32] I. Sakaguchi, M. Nishitani-Gamo, K. P. Loh, S. Hishita, H. Haneda and T. Ando, Appl. Phys. Lett. **73**, 2675 (1998)

[2.33] I. Sakaguchi, M. Nishitani-Gamo, K. P. Loh, S. Hishita, H. Haneda and T. Ando, Appl. Phys. Lett. **71**, 629 (1997)

[2.34] T. R. Anthony, Vacuum **41**, 1356 (1990)

[2.35] W. Piekarczyk, Cryst. Res. Technol. **34**, 553 (1999)

[2.36] B. B. Pate, Surface Sci. **165**, 83 (1986)

[2.37] Handbook of Chemistry and Physics, 57th Ed., CRC Press, (1997)

[2.38] B. Dischler, C. Wild, W. Muller-Sebert and P. Koidl, Physica B **185**, 217 (1993)

[2.39] G. Davies, Hydrogen in Diamond. In G. Davies, editor, Properties and Growth of Diamond, chapter 4.3. INSPEC (1994)

[2.40] E. Holzschuh, W. Kundig, P. F. Meier, B. D. Patterson, J. P. F. Sellschop, M. C. Stemmet and H. Appel, Phys. Rev. A **25**, 1272 (1982)

[2.41] J. H. Brewer, K. M. Crowe, F. N. Gygax, R. F. Johnson, B. D. Patterson, D. G. Fleming and A. Schenck, Phys. Rev. Lett. **31**, 143 (1973)

[2.42] B. D. Patterson, A. Hintermann, W. Kundig, P. F. Meier, F. Waldner, H. Graf, E. Recknagel, A. Weidinger and T. Wichert, Phys. Rev. Lett. **40**, 1347 (1978)

[2.43] E. Holzschuh, H. Graf, E. Recknagel, A. Weidinger, T. Wichert and P. F. Meier, Phys. Rev. B **20**, 1347 (1978)

[2.44] T. L. Estle, S. Estreicher and D. S. Marynick, Phys. Rev. Lett. **58**, 1547 (1987)

[2.45] X. Zhou, G. D. Watkins, K. M. McNamara Rutledge, R. P. Messmer and S. Chawla, Phys. Rev. B **54**, 7881 (1996)

[2.46] D. F. Talbot-Ponsonby, M. E. Newton, J. M. Baker, G. A. Scarsbrook, R. S. Sussman and A. J. Whitehead, Phys. Rev. B **57**, 2302 (1998)

[2.47] D. F. Talbot-Ponsonby, M. E. Newton, J. M. Baker, G. A. Scarsbrook, R. S. Sussman, A. J. Whitehead and S. Pfenninger, Phys. Rev. B **57**, 2264 (1998)

[2.48] J. Rosa, J. Pangrac, M. Vorlicek, M. Nesladek, K. Meykens, C. Quaeyhaegens and L. M. Stals, Diam. Rel. Mat. **7**, 1048 (1998)

[2.49] S. L. Holder, L. G. Rowan, J. J. Krebbs, Appl. Phys. Lett. **64**, 1091 (1994)

[2.50] J. P. Goss, J. Phys. Condens. Matter **15** , R551 (2003)

[2.51] J. P. Goss, M. I. Heggie, C. P. Ewels, P. R. Briddon and S. Oberg, Phys. Rev. B **65**, 115207 (2002)

[2.52] W. V. Smith, P.P. Sorokin, I. L. Gelles and G. J. Lasher, Phys. Rev. **115**, 1546 (1959)

[2.53] I. Watanabe and K. Sugata, Jap. Jnl. Appl. Phys. **27**, 1808 (1988)

[2.54] M. H. Nazare, Isolated substitutional nitrogen in diamond, 3.2, in M. H. Nazare and A. J. Neves, Properties, Growth and Applications of Diamond, INSPEC: IEE (2001)

[2.55] P. R. Briddon and R. Jones, Physica B **185**, 179 (1993)

[2.56] S. A. Kajihara, A. Antonelli and J. Bernholc, Phys. Rev. Lett. **66**, 2010 (1991)

[2.57] J. Mort, M. A. Machonkin and K. Okumura, Appl. Phys. Lett. **59**, 3148 (1991)

[2.58] A Cox, D Phil Thesis, University of Oxford (1993)

[2.59] A. Cox, M. E. Newton and J. M. Baker, J. Phys. Condens. Matter **6**, 551 (1994)

[2.60] R. M. Shrenko, H. M. Strong,and R. E. Tuft, Philos. Mag. B **11**, 313 (1965)

[2.61] A. T. Collins and G. S. Woods, Philos. Mag. **46**, 77 (1982)

[2.62] S. C Lawson, D. Fischer, D. C. Hunt and M. E. Newton, J. Phys., Condens. Matter **10**, 6171 (1998)

[2.63] M. E. Newton, Neutral and ionised single substitutional nitrogen in diamond, 5.4, in M. H. Nazare and A. J. Neves, Properties, Growth and Applications of Diamond, INSPEC: IEE (2001)

[2.64] G. Davies and M. F. Hamer, Proc. R. Soc A **348**, 285 (1976)

[2.65] J. H. N. Loubser and J. A. Van Wyk, Diam. Res., Suppl. to Int. Diamond Rev. (UK) **11**, 11 (1977)

[2.66] L. Bergman, M. T. McClure, J. T. Glass and R. J. Nemanich, J. Appl. Phys. **76**, 3020 (1994)

[2.67] A. T. Collins and S. C. Lawson, J. Phys. Condens. Matter **1**, 6929 (1989)

Chapter 3

Theory of EPR

3.1 Introduction

Many books have been written about EPR and the reader is referred to Abragham and Bleaney [3.1] and Wertz and Bolton [3.2] for a good introduction to the theory, and Poole [3.3] for a comprehensive introduction to the experimental technique.

A spectrum obtained using EPR can be rather complex, with lines arising from different electronic transitions, which may split by interactions with any number of nuclear moments. The field at which these transitions occur depends on the frequency of the microwave radiation and, if anisotropy is present, will also depend on the orientation of the magnetic field with respect to the crystal axes.

To get the maximum amount of information out of an EPR experiment, spectra need to be recorded under varying conditions of frequency, power, temperature and orientation; these points will be discussed in more detail in Chapter 4. Running spectra under all the necessary conditions results in a mass of data, which needs to be interpreted consistently in order to identify the defect(s) responsible. An EPR spectrum can frequently identify the lattice site and symmetry of a defect, particularly if a single crystal is used, and the link between theory and experiment is known as the spin Hamiltonian (equation 3.1). The spin Hamiltonian will be discussed in the next section.

This chapter briefly describes the theory of EPR. It begins by discussing the spin Hamiltonian and electron spin, and then presents some of the most important aspects of the theory, concentrating on what is most relevant to the work presented in this thesis.

3.2 The Spin Hamiltonian

The spin Hamiltonian describes the properties of a group of n states $|1\rangle$, $|2\rangle$....$|n\rangle$, which lie within a few wavenumbers of the ground state of the defect. The behaviour of this group can be represented by defining an effective spin, S, such that the total number of levels, n, in the group is 2S + 1. The behaviour of this group of levels can be described by a spin Hamiltonian using an effective spin, and when hyperfine interactions are present, nuclear spin. It is important to note that the effective spin is a fictitious spin determined entirely by the number of levels involved, and may not have a simple relationship with the real spin of the defect.

There is no unique way of constructing a spin Hamiltonian. However, there are three main criteria used: simplicity, symmetry and correspondence to free atoms. The effective spin Hamiltonian is usually written as:

$$H = \mu_B \boldsymbol{B}.\underline{\boldsymbol{g}}.\boldsymbol{S} + \boldsymbol{S}.\underline{\boldsymbol{D}}.\boldsymbol{S} + \sum_i \boldsymbol{S}.\underline{\boldsymbol{A}}_i.\boldsymbol{I}_i + \sum_i \boldsymbol{I}_i.\underline{\boldsymbol{P}}_i.\boldsymbol{I}_i - \sum_i g_N \mu_N \boldsymbol{B}.\boldsymbol{I}_I + \textit{higher order terms} \quad (3.1)$$

where S is the effective electron spin and I_i is the nuclear spin of the ith nucleus. The terms of the Hamiltonian are the electronic Zeeman interaction, the zero field splitting term ($\underline{\boldsymbol{D}}$), the hyperfine interaction ($\underline{\boldsymbol{A}}$), the quadrupole interaction ($\underline{\boldsymbol{P}}$), and the nuclear Zeeman interaction respectively.

In practice, spin resonance is performed at a fixed frequency. To be able to find the condition in which the energy levels are split by hν and to find the relative intensities of the transitions subject to the selection rules $\Delta M_S = \pm 1$ and $\Delta M_I = 0$, the eigenvalues and eigenfunctions of the spin Hamiltonian need to be calculated, the transition probabilities will be discussed in more detail in section 3.3. Abragham and Bleaney give a full treatment of this [3.1], and the next sections of this chapter concentrate on the important points of the process. Other texts have also proved to be extremely useful in writing the following sections [3.4, 3.5, 3.6, 3.7, 3.8, 3.9].

3.2.1 The Zeeman Effect (g)

This term describes the interaction of the magnetic dipole of the electron with the magnetic field. It is represented by the term

$$H_{ze} = \mu_B \boldsymbol{B}.\underline{\boldsymbol{g}}.\boldsymbol{S} \quad (3.2)$$

where μ_B is the Bohr magneton ($e\hbar/2m$) where m is the mass of the electron, and g is the spectroscopic splitting factor that measures the energy splitting under a magnetic field. In all cases it has been assumed that the g-value is positive.

When describing the coupling between states, Russell-Saunders coupling, also known as *LS* coupling, can be assumed. This assumes that the electron-electron interaction has already been considered, and therefore the spin-orbit coupling can be treated as a perturbation. The spin-orbit interaction only has a very small range and so is only significant close to the nucleus.

If an electron is located on an atom, it can possess an orbital angular momentum *L*. If the defect is then placed in a crystal, the motion of the electron is affected by the interactions with the other atoms close by. This can be interpreted in terms of the introduction of an electrostatic potential in the region occupied by the orbit of the electron. This field has the effect of lifting the degeneracy associated with it.

Using the *LS*-coupling scheme, the Hamiltonian can be written as:

$$H_Z = \mu_B \underline{B} \cdot (\underline{L} + 2\underline{S}) + \sum_i \xi_i(r_i)\underline{L}_i \cdot \underline{S} + \left\{ \frac{e}{2c} \sum_i \xi_i(r_i)(\underline{S} \cdot \underline{r}_i) \cdot (\underline{B} \cdot \underline{r}_i) \right\} \qquad (3.3)$$

The last term in the equation is the second order term, which can often be ignored because it is too small to have an effect.

In the absence of spin-orbit coupling, the orbital angular momentum can be 'quenched'. This means that the expectation value of its component along the Zeeman field is zero and the Zeeman interaction is represented by equation (3.2). Spin-orbit coupling can remove the quenching which results in the off diagonal elements of *L* being finite, therefore giving *L* a finite expectation value.

Spin-orbit coupling can mix excited states $|e\rangle$ into the original state $|0\rangle$:

$$|0\rangle = |0\rangle_o - \sum_e \frac{|e\rangle\langle e|\xi \underline{L}.\underline{S}|0\rangle}{E_e - E_0} \qquad (3.4)$$

The cross terms in $\langle 0|L|0\rangle$ are then finite and linear in the spin orbit coupling. If second order perturbation theory is applied to equation (3.4), the g-value can be obtained [3.10], and three field dependant components are obtained:

$$H = 2\xi\mu_B B.\underline{\Delta}.S + \xi^2 S.\underline{\Delta}.S + \mu_B^2 B.\underline{\Delta}.B \qquad (3.5)$$

Which has been simplified by the introduction of the tensor:

$$\Delta_{ij} = -\sum_{n} \frac{\langle 0 | L_1 | n \rangle \langle n | L_j | 0 \rangle}{E_n - E_o} \tag{3.6}$$

In equation (3.5), the first term is the linear Zeeman effect, the second term is the zero-field splitting term, which will be discussed in the next section, and the last term is the interaction of the magnetic field with the moment it induces, which in practice, is negligible at the fields used.

Re-writing equation (3.5) and putting it in its usual form gives:

$$H = \mu_B \boldsymbol{B}.\underline{\boldsymbol{g}}.\boldsymbol{S} + \boldsymbol{S}.\underline{\boldsymbol{D}}.\boldsymbol{S} \tag{3.7}$$

$$\text{Where } \underline{\mathbf{g}} = g_e\underline{\mathbf{1}} + 2\xi\Delta, \text{ and } \underline{\mathbf{D}} = \xi^2\Delta \tag{3.8}$$

As verified experimentally, defects in diamond typically exhibit very small deviations of g from g_e (the free electron value). This is the result of both ξ (the spin orbit coupling), and Δ (3.6), being particularly small in diamond. Δ proves to be small as it varies inversely to the energy gap separation, which in diamond is large, 5.5 eV.

3.2.2 The Zero Field Splitting ($\underline{D}$)

This term describes the interactions that cause splittings in the energy levels in the absence of a magnetic field, and can be grouped into a traceless matrix $\underline{D}$, which is described by the term

$$H_{zfs} = \boldsymbol{S}.\underline{\boldsymbol{D}}.\boldsymbol{S} \tag{3.9}$$

The term arises from electron – electron interactions and so can only be present when $S \geq 1$. There are three main contributions to this term:

1. Spin-orbit interaction, as described in the previous section,
2. Exchange between neighbouring magnetic ions, described in Abragham and Bleaney, Chapter 9 [3.1],
3. Dipole-dipole interactions between the unpaired electrons.

This interaction only causes splittings for S ≥ 1 and so the defect must contain at least two electrons. The magnetic dipolar Hamiltonian for two electrons, S = 1, is expressed as:

$$H_{dip} = \left(\frac{\mu_0}{4\pi}\right) g^2 \mu_B{}^2 \left[\frac{\underline{s}_1 \cdot \underline{s}_2}{r^3} - \frac{3(\underline{s}_1 \cdot \underline{r})(\underline{s}_2 \cdot \underline{r})}{r^5}\right] \tag{3.10}$$

where s_1 and s_2 are the spins of the two electrons and r is the separation between them. The Hamiltonian in (3.9) is often described in terms of components of a Cartesian system of axes, where the z direction is the principal direction:

$$H_{dip} = D\left\{S_z{}^2 - \frac{1}{3}S(S+1)\right\} + E(S_x{}^2 - S_y{}^2) \tag{3.11}$$

where D and E are expressed as:

$$D = \left(\frac{\mu_0}{4\pi}\right)\frac{3}{4} g^2 \mu_B{}^2 \left\langle \frac{r^2 - 3z^2}{r^5} \right\rangle \tag{3.12}$$

$$E = \left(\frac{\mu_0}{4\pi}\right)\frac{3}{4} g^2 \mu_B{}^2 \left\langle \frac{y^2 - 3x^2}{r^5} \right\rangle \tag{3.13}$$

Both D and E depend on the distance between two electrons with parallel spins, and the angular brackets imply an average over the electronic wavefunction. Equations (3.12) and (3.13) yield two pieces of information about the defect:

1. Its symmetry: E will vanish if it has axial symmetry (equivalent x- and y-axes), and D will vanish if the defect has cubic symmetry.
2. The magnitude of the zero-field splitting gives a measure of the dimensions of the defect if the dipole-dipole interaction dominates in $\underline{\mathbf{D}}$.

3.2.3 The Hyperfine Interaction ($\underline{\mathbf{A}}$)

This is the coupling between an unpaired electron (S) and a magnetic nucleus (I), and it gives a measure of the unpaired electron distribution. It is represented by the term:

$$H_{zfs} = \sum_{j} \; \boldsymbol{S} \,.\underline{\boldsymbol{A}}_j \,.\boldsymbol{I}_j \tag{3.14}$$

The hyperfine interaction can either be anisotropic (orientation-dependant), or isotropic (orientation-independent), and as a result can be separated into the two terms. The isotropic term arises from the *s*-electrons, as it depends on the density of unpaired electrons at the nucleus. It is given by:

$$H_{iso} = \frac{2\mu_0}{3} g_e \mu_B g_N \mu_N \, |\Phi(0)|^2 \; \underline{S}.\underline{I} \tag{3.15}$$

where μ_N is the nuclear magneton ($e\hbar/2M$), M is the mass of the nucleus, g_N is the g-factor of the nucleus, and $\Phi(0)$ is the wavefunction of the electron at the nucleus.

Each of the *p*, *d*, *f* etc shells have nodes at the nucleus and so have a zero probability of an electron ending up there. This forms the anisotropic term and is given by:

$$H_{aniso} = \left(\frac{\mu_0}{4\pi}\right) - g_e \mu_B g_N \mu_N \left[\frac{\underline{S}.\underline{I}}{r^3} - \frac{3(\underline{S}.\underline{r})(\underline{I}.\underline{r})}{r^5}\right] \tag{3.16}$$

which is analogous to equation (3.10). There are other terms that can contribute to the hyperfine interaction and these include polarization, correlation and relativistic effects [3.2].

When the hyperfine interaction is symmetric, it can be written as a diagonal matrix consisting of a parallel term and two perpendicular terms. From these the isotropic, *a*, and anisotropic parts, *b*, can be calculated:

$$A_{iso} = a = \frac{1}{3}(A_{\parallel} + 2A_{\perp}) \tag{3.17}$$

$$A_{aniso} = b = \frac{1}{3}(A_{\parallel} - A_{\perp}) \tag{3.18}$$

3.2.4 The Quadrupole Interaction (P)

This is the interaction of the asymmetric charge distribution of a nucleus with the electric field gradient due to the surrounding electronic charge. It is a measure of the

anisotropy of its charge distribution, and is expressed in terms of the matrix $\underline{\boldsymbol{P}}$. The interaction is represented by:

$$H_{quad} = \boldsymbol{I}.\underline{\boldsymbol{P}}.\boldsymbol{I} \tag{3.19}$$

The quadrupole moment, Q, is characteristic of the particular nucleus and is a measure of the departure of the nuclear charge distribution from a spherical shape – an elongated nucleus has a positive Q, and a flattened nucleus has a negative Q. The quadrupole moment is zero for nuclei with spin I<1. The general form of the equation is given by:

$$H_{quad} = P_{\parallel}[\{I_z^2 - \frac{1}{3}I(I+1)\} + \frac{1}{3}\eta(I_x^2 - I_y^2)] \tag{3.20}$$

where $P_{\parallel} = 3P_z/2$ and $\eta = (P_x - P_y)/P_z$. If axial symmetry is present $\eta = 0$. $P_{\parallel}$ can be written as:

$$P_{\parallel} = \frac{3eQq}{4I(2I+1)} \tag{3.21}$$

where q is the electric field gradient at the nucleus ($\partial^2V/\partial z^2$).

3.2.5 The Nuclear Zeeman Interaction ($\underline{\mathbf{g}}_N$)

This represents the interaction of the magnetic moment of the nucleus with the applied magnetic field. It is analogous to the electronic Zeeman interaction and is represented by the term:

$$H = -g_n \mu_n \boldsymbol{I}.\boldsymbol{B} \tag{3.22}$$

The nuclear Zeeman interaction is smaller than the electronic Zeeman effect by a factor of (m_e/M). It is not possible to determine the value of g_N from an EPR spectrum as the strong allowed transitions obey the selection rules $\Delta M_S = \pm 1$ and $\Delta M_I = 0$ and are therefore independent of the interaction.

3.3 Transitions Probabilities

By operating the spin Hamiltonian, H, on the spin states, $|M_S, M_I\rangle$, it is possible to calculate the matrix elements, $\langle M_S', M_I'|H|M_S, M_I\rangle$, and hence determine the energy matrix of the system. The eigenvalues of the energy matrix give the energy levels of the system between which the transitions may occur. The eigenstates of the system are linear combinations of the spin states $|M_S, M_I\rangle$.

There are two cases that need to be considered depending on the relative sizes of the diagonal, and off diagonal elements, $\langle M_S, M_I|H|M_S, M_I\rangle$ and $\langle M_S', M_I'|H|M_S, M_I\rangle$ respectively.

i) If the off diagonal matrix elements are small compared to those on the diagonal, then the energy levels can be estimated from the diagonal elements and the eigenfunctions are simply the spin states, $|M_S, M_I\rangle$. EPR transitions will occur between these states in accordance with the selection rules; $\Delta M_S = \pm 1$ and $\Delta M_I = 0$. These transitions are referred to as the 'allowed' transitions.

ii) If the off diagonal matrix elements cannot be neglected as in i), they have two effects; they shift the energy levels, and they mix spin states such that the eigenfunctions can no longer be described by individual spin states. The latter results in a relaxation of the selection rules such that transitions where $\Delta M_S \neq \pm 1$ and $\Delta M_I \neq 0$, may occur. These are known as the 'forbidden' transitions and generally have a significantly smaller intensity than the allowed transitions.

3.4 Symmetry

It has been mentioned previously in this chapter that the aim, when studying EPR data, is to identify the defect responsible. Determining the symmetry is fundamental to success in identifying defects. There are many texts on symmetry in physics [3.11, 3.12]. The symmetry of a defect is specified by the point group, which contains all of the operators under which the defect is invariant.

The symmetry of the matrices within the spin Hamiltonian depends on the symmetry of the defect; the **g** and $\underline{\mathbf{D}}$-matrices describe the overall symmetry of the defect's surroundings, whilst the $\underline{\mathbf{A}}$-matrix describes the symmetry of the unpaired electron distribution.

For a general site of low symmetry in diamond, the operations from the T_d symmetry would generate 24 different sites, but this number reduces as the symmetry of the defect increases. The number of different sites that can be recognised on an EPR spectrum gives

information about the site symmetry of the defect, a list of which can be found in table 3.1. There are two symmetry notations used in table 3.1, the Schoenflies Symbols and the Full International Symbols for the crystal point groups. An explanation of the Schoenflies symbols can be found in table 3.2, and the corresponding international symbols in table 3.3.

A roadmap is often a useful way of determining the symmetry of a defect. It follows the angular dependence of the EPR transitions as the sample is rotated in the magnetic field in a plane. The neutrally charged single substitutional nitrogen centre, N_S^0, is a well documented defect that will be used as an example. The N_S^0 defect has C_{3v} symmetry. It is axially symmetric about the C–N bond, i.e. the ⟨111⟩ symmetry axis. A ^{14}N N_S^0 defect has an electron spin of ½ and a nuclear spin of 1. This results in a characteristic three-line EPR spectrum, figure 3.1.

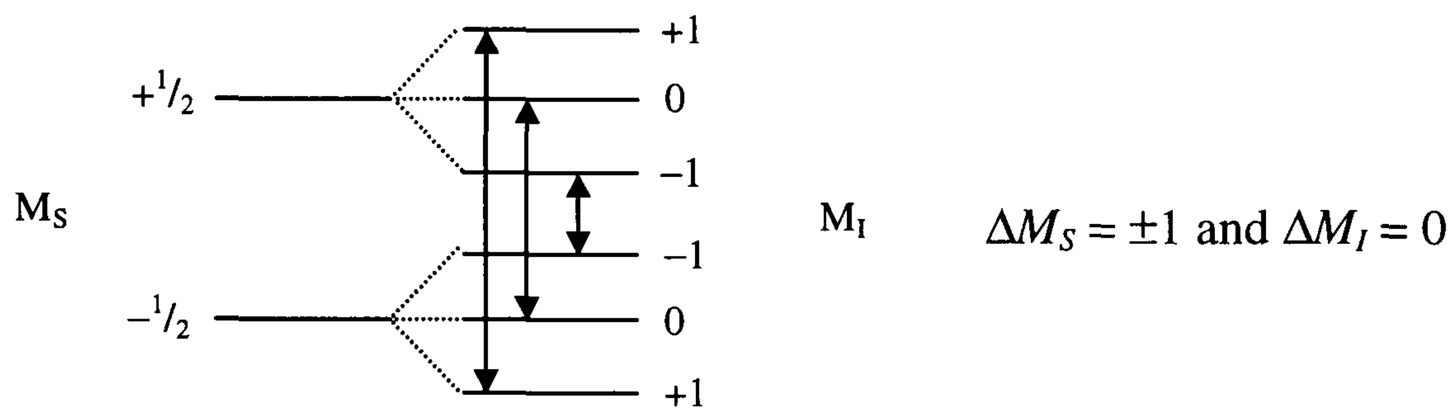

Figure 3.1: Schematic showing the allowed transitions of the P1 defect.

As shown in table 3.1, a defect with C_{3v} symmetry will have four sites associated with it. The number of sites is the maximum number of lines that each transition can split into, depending on the plane in which the measurements are being recorded, and for this example can be explained in the following way. If the N_S^0 defect were isotropic, i.e. orientation independent, the characteristic, spin 1, three line EPR spectrum would be observed regardless of the direction of the magnetic field, figure 3.2.

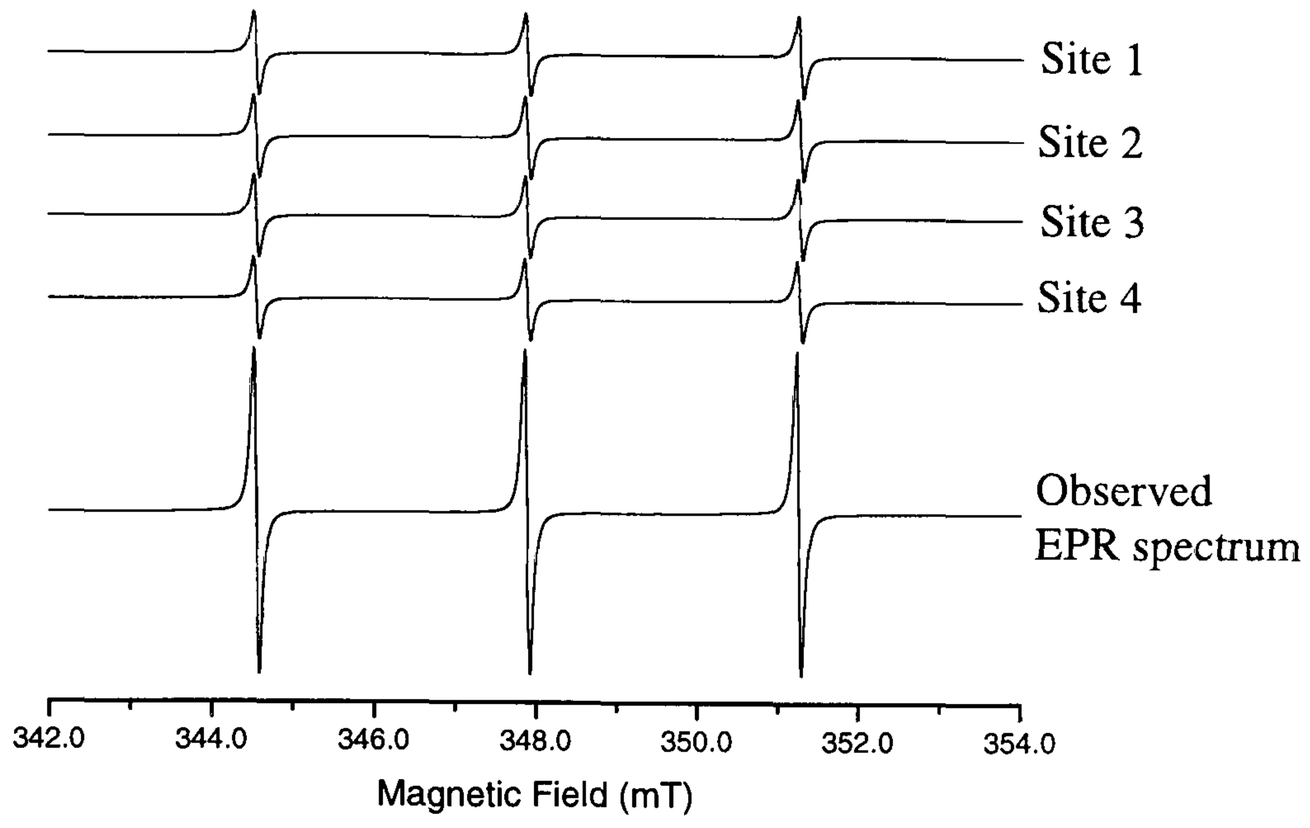

Figure 3.2: Simulation showing how the EPR spectrum is obtained when B || [001], created using a microwave frequency of 9.75 GHz.

However, N_S^0 is not isotropic and so this spectrum is only observed when B || [001], and the four sites are equivalent as a result of the field making the same angle with each. As the sample is rotated in the (110) plane through to B || [111], there will be two lines with relative intensities 1:3, arising from the magnetic field being parallel to one of the sites and making equivalent angles with the other three, figure 3.3(a). When B || [110], there will still be two lines, but this time with relative intensities 2:2, i.e. equal. This is because there are two pairs of equivalent angles, figure 3.3(b).

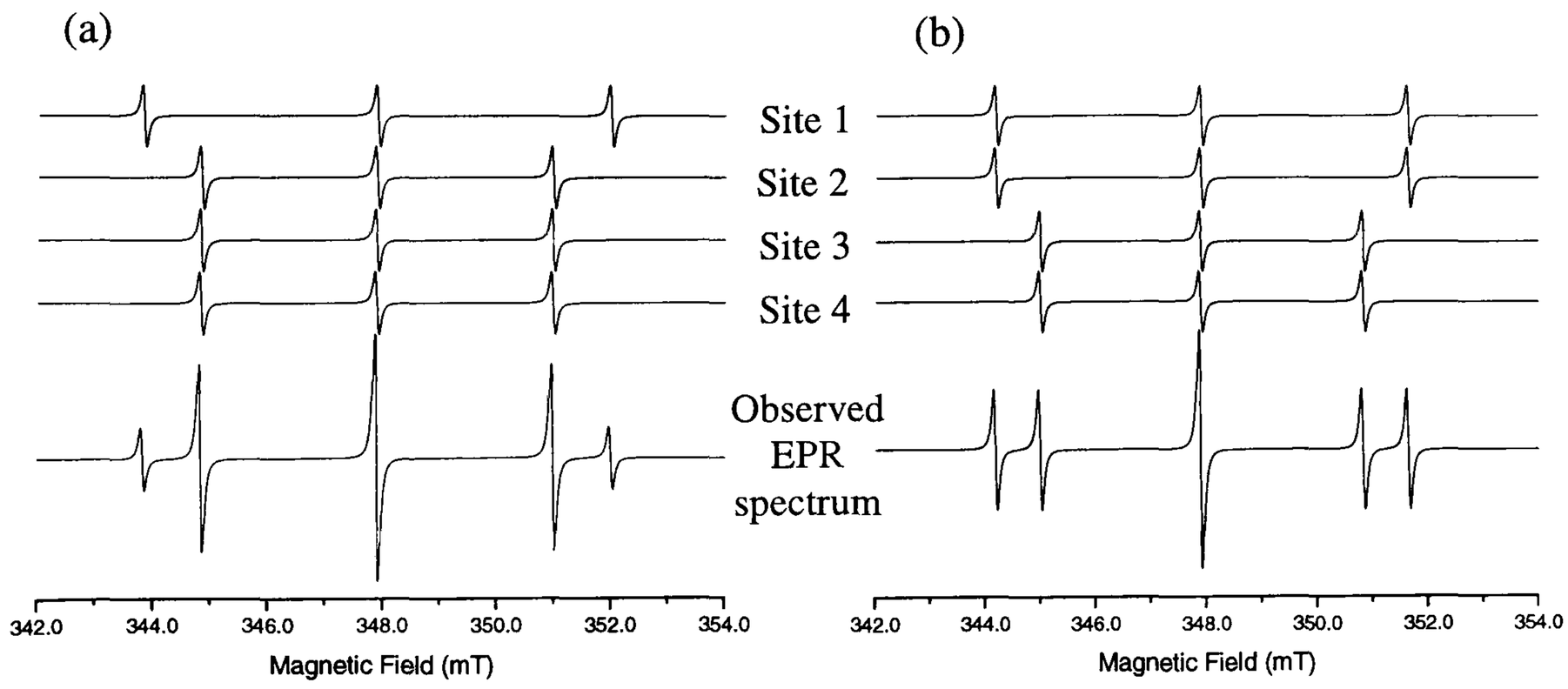

Figure 3.3(a)-(b): (a) shows the simulation of the four sites when B || [111], and (b) shows the simulation when B || [110]. Each simulation has used a microwave frequency of 9.75 GHz.

The behaviour of a defect such as this one can be plotted in the form of a roadmap by recording spectra at regular intervals between [001] and [110]. Figure 3.4 shows a roadmap for the N_S^0 EPR defect. The roadmap can be used to assist in the identification of the defect. All of the defects presented in this thesis have a corresponding roadmap.

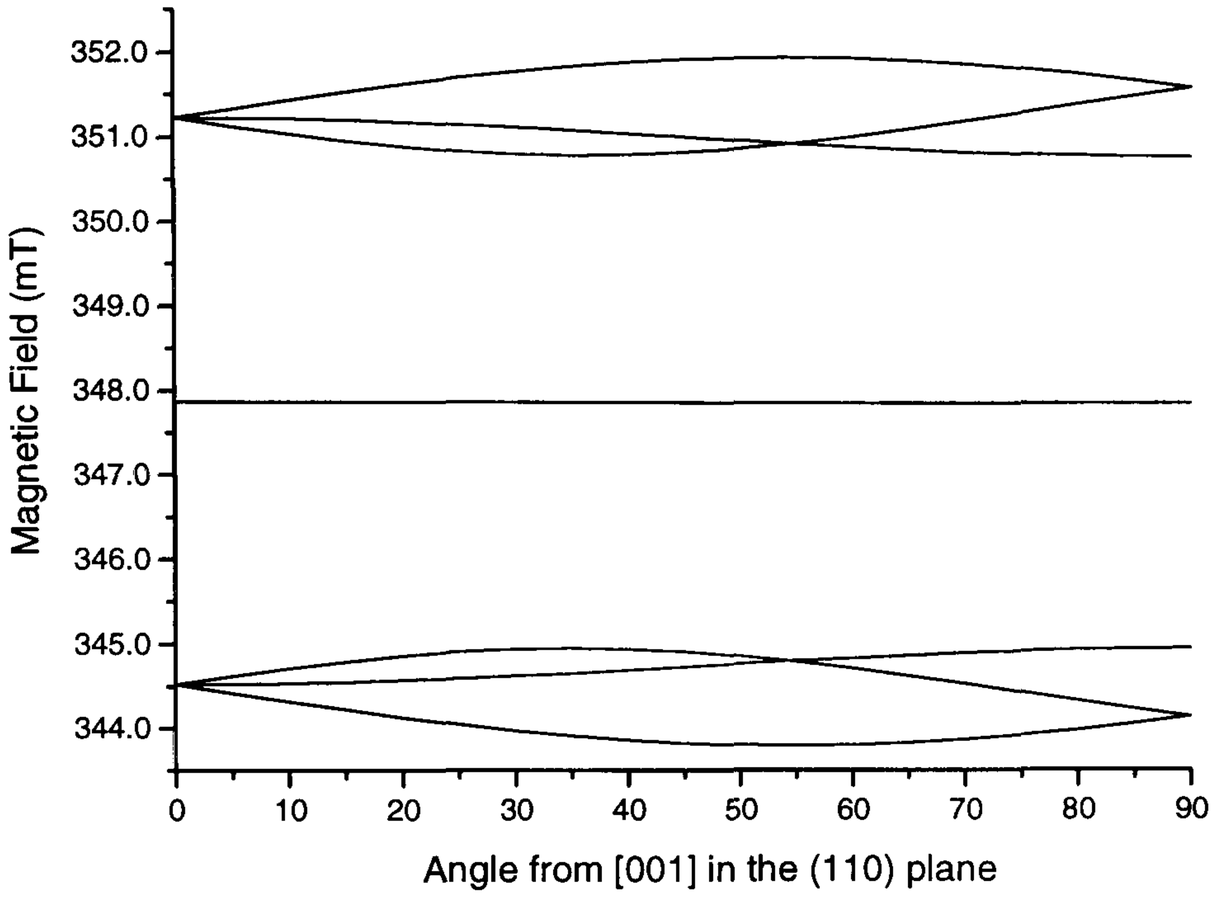

Figure 3.4: Simulated roadmap for the N_S^0 centre in single crystal diamond. The simulation was created using a microwave frequency of 9.75 GHz.

	<100>			<111>		<011>	
	No of Sites	No of Lines	Relative Intensities	No of Lines	Relative Intensities	No of Lines	Relative Intensities
T_d 43m No distortion	1	1	1	1	1	1	1
S_4 4 [100] axial distortion	3	2	2,1	1	1	2	2,1
C_{2v} mm2 [100] and [010] distortions	6	3	1,1,1	1	1	3	1,1,1
C_2 2 [100] and general non-axial distortion	12	3	1,1,1	2	1,1	4	2,2,1,1
C_{3v} 3m [111] axial distortion	4	1	1	2	1,3	2	2,2
D_{3d} [111] axial distortion with inversion	12	2	2,1	3	6,3,3	4	2,2,4,4
C_{1h} m [111] non-axial distortion one axis along [011] axis	12	2	2,1	3	2,1,1	4	2,1,2,1
C_1 1 [111] non-axial distortion not along [011]	24	3	1,1,1	4	1,1,1,1	6	1,1,1, 1,1,1
C_{2v} mm2 (rotation about [001]) [110] axial distortion	6	2	1,2	2	2,2	3	1,1,4
C_{2v} mm2 (rotation about [001]) [110 non-axial, one axis along [001]	6	2	1,2	2	2,2	3	1,1,4
C_{1h} m [110] non-axial not along [001]	12	2	1,2	3	2,1,1	4	2,1,2,1
C_1 1 Axial distortion, but not along axes	24	3	1,1,1	4	1,1,1,1	6	1,1,1, 1,1,1
C_1 1 Non-axial distortion, but not along crystal axes	24	3	1,1,1	4	1,1,1,1	6	1,1,1, 1,1,1

Table 3.1: Site symmetries; possible symmetries for distorted tetrahedral point sites (updated from A. Cox, DPhil Thesis [3.13]).

Symbol	Symmetry Element	Symmetry Operation
E	——	No change
C_n	n-fold axis of rotation (the principal axis of symmetry is that of largest n)	Rotation about an axis of symmetry by $360^0 / n$
σ_h	Plane of symmetry perpendicular to the principal axis of symmetry	Reflection in the plane of symmetry
σ_v	Plane of symmetry contains the principal axis of symmetry	Reflection in the plane of symmetry
σ_d	Plane of symmetry contains the principal axis of symmetry and bisects the angle between two a-fold axes of symmetry which are perpendicular	Reflection in the plane of symmetry
S_n	$C_n + \sigma_h$	Rotation about an axis by $360^0 / n$ followed by a reflection in a plane perpendicular to the axis of rotation
i	Centre of symmetry	Inversion in a centre of symmetry

Table 3.2: Symmetry symbols

$C_i : \bar{1}$	$C_s : m$			
$C_1 : 1$	$C_2 : 2$	$C_3 : 3$	$C_4 : 4$	$C_6 : 6$
	$C_{2v} : 2mm$	$C_{3v} : 3m$	$C_{4v} : 4mm$	$C_{6v} : 6mm$
	$C_{2h} : 2/m$	$C_{3h} : \bar{6}$	$C_{4h} : 4/m$	$C_{6h} : 6/m$
	$D_2 : 222$	$D_3 : 32$	$D_4 : 422$	$D_6 : 622$
	$D_{2h} : mmm$	$D_{3h} : \bar{6}2m$	$D_{4h} : 4/mmm$	$D_{6h} : 6/mmm$
	$D_{2d} : \bar{4}2m$	$D_{3d} : \bar{3}m$	$S_4 : \bar{4}$	$S_6 : \bar{3}$
$T : 23$	$T_d : \bar{4}3m$	$T_h : m3$	$O : 432$	$O_h : m3m$

Table 3.3: Schoenflies and International notation for point groups

3.5 Interpretation of Physical Parameters

Once the numerical parameters have been calculated from the spin Hamiltonian, the aim is then to determine a model for the defect under investigation, such that the model can explain the experimental parameters. By determining the spin of the nucleus involved it is often possible to identify the nucleus involved in the defect.

The hyperfine parameters are where much of the information is obtained. The hyperfine data are treated by assuming the unpaired electron wavefunction, Ψ, can be constructed as a linear combination of atomic orbitals (LCAO) centred on the atoms in and around the defect.

$$\Psi = \sum_j \eta_j \psi_j \tag{3.23}$$

where ψ_j is the atomic orbital on the jth site, and η_j is the fraction of unpaired electron localised in the ψ_j atomic orbital. In the case of the defects studied in this thesis, only s and p orbitals need to be considered because all other oribitals are either too high or too low in energy, which results in little or no mixing of interest. The electronic wavefunction can be written as an sp hybrid:

$$\psi_j = \alpha_j (\psi_s)_j + \beta_j (\psi_p)_j \tag{3.24}$$

Normalisation requires that:

$$\alpha_j^2 + \beta_j^2 = 1 \quad \text{and} \quad \sum_j \eta_j^2 = 1 \tag{3.25}$$

Any s electron present will produce an isotropic coupling, whereas p orbitals will contribute to the anisotropic coupling. The isotropic component, also known as the contact term, is non-zero when the electron has a finite probability of being localised at the nucleus. It can be defined as [3.2]:

$$A_s \approx \frac{2\mu_0}{3} g\mu_B g_N \mu_N \alpha_j^2 \eta_j^2 |\psi_s|^2 = A_s^* \alpha_j^2 \eta_j^2 \tag{3.26}$$

The anisotropic component, or the dipolar interaction, is zero for a spherically symmetric electron cloud and, hence, reflects the *p* character of the wavefunction. It can be described as:

$$A_p \approx \frac{\mu_0}{10} g\mu_B g_N \mu_N \beta_j^2 \eta_j^2 |\psi_p|^2 = A_p^* \beta_j^2 \eta_j^2 \tag{3.27}$$

A_s and A_p are defined in equations (3.17) and (3.18) as A_{iso} and A_{aniso} respectively. A^*_s and A^*_p are the values A_s and A_p would have if 100% of the unpaired electron were localised in the *s* and *p* orbitals respectively. Values for A^*_s and A^*_p have been calculated theoretically [3.14, 3.15], and are listed in Table C in Wertz and Bolton [3.2]. For the defects of interest to this thesis, the values for A^*_{2s} and A^*_{2p} are 1540/–2160 MHz and 47.8/–67.1 MHz respectively for $^{14}N/^{15}N$ and for carbon they are 3777 MHz and 107.4 MHz. The value of A^*_{1s} for hydrogen is 1420 MHz. The values of η_j, α_j and β_j can be determined from [3.16].

$$\eta_j^2 = \frac{A_s A_p^* + A_p A_s^*}{A_s^* A_p^*} \qquad \alpha_j^2 = \frac{A_s A_p^*}{A_s A_p^* + A_p A_s^*} \qquad \beta_j^2 = \frac{A_p A_s^*}{A_s A_p^* + A_p A_s^*} \tag{3.28}$$

The hybridisation ratio can also be determined because $\lambda = (\beta/\alpha)^2$. This approach gives information on the orbitals the unpaired electron occupies and may give information on bond angles and bond lengths of the atoms in the defect.

The anisotropic component of the hyperfine interaction can determine two things; i) the fraction of the unpaired electron localised on the nucleus involved in the defect, as just described, and ii) the fraction of unpaired electron localised away from the nucleus. This is done by assuming a dipole-dipole interaction between the unpaired electron and the nucleus. By using equation (3.29), and the value of *b* obtained from the experiment, the distance between the nucleus and the unpaired electron can be calculated (r).

$$b = \left(\frac{\mu_0}{4\pi}\right) \frac{g_e \mu_B g_N \mu_N}{r^3} \tag{3.29}$$

It should be noted however, that this only works by assuming the unpaired electron is localised at the same point. A more sophisticated approach is required if this is not the case, and will be dealt with in more detail in Chapters 6 and 7.

References

[3.1] A. Abragham and B. Bleaney, Electron Paramagnetic Resonance of Transition Ions, Dover Publications Inc. New York (1986)

[3.2] J. E. Wertz and J. R. Bolton, Electron Spin Resonance, Chapman and Hall (1986)

[3.3] C. P. Poole, Electron Spin Resonance: A Comprehensive Treatise on Experimental Techniques, John Wiley, New York (1983)

[3.4] D. J. Twitchen, DPhil Thesis, University of Oxford (1997)

[3.5] D. Hunt, DPhil Thesis, University of Oxford (1999)

[3.6] D. Talbot-Ponsonby, DPhil Thesis, University of Oxford (1997)

[3.7] R. Berman, Physical Properties of Diamond, Chapter 10, Clarendon Press, Oxford (1965)

[3.8] J. Bourgoin and M. Lannoo, Point Defects in Semiconductors II, Experimental Aspects, Springer-Verlag (1983)

[3.9] J. M. Spaeth, J. R. Niklas and R. H. Bartram, Structural Analysis of Point Defects in Solids, An Introduction to Multiple Magnetic Resonance Spectroscopy, Springer-Verlag (1992)

[3.10] A. M. Stoneham, Theory of Defects in Solids, chapter 13, Clarendon Press, Oxford (1975)

[3.11] P. W. Atkins and R. S. Friedman, Molecular Quantum Mechanics, 3rd Edition, Oxford University Press (2001)

[3.12] P. W. Atkins, Molecular Quantum Mechanics, An Introduction to Quantum Chemistry, Parts I and II, Oxford University Press (1970)

[3.13] A. Cox, DPhil Thesis, University of Oxford (1993)

[3.14] F. Herman and S. Skillman, Atomic Structure Calculations, Prentice-Hall, Englewood Cliffs, N.J. (1963)

[3.15] J. R. Morton and K. F. Preston, J. Magn. Res. **30**, 577 (1978)

[3.16] M. E. Newton, DPhil Thesis, University of Oxford (1989)

Chapter 4

Experimental Details

4.1 Introduction

The main spectroscopic techniques used for the work in this thesis are electron paramagnetic resonance (EPR) and Fourier transform infrared optical absorption (FTIR). Both EPR and FTIR are well documented, so this chapter will only give a brief overview of each of the instruments used. The majority of the chapter will concentrate on additions and changes made to the equipment in order to conduct the experiments in this thesis.

The chapter will begin with an introduction to the experimental aspects of EPR and a basic overview of the technique. It will then outline all of the changes made to the equipment and discuss how an EPR spectrum can be used to directly calculate the concentration of a defect within a sample. Finally it will discuss FTIR and the two spectrometers used for the measurements, concentrating on the actual methods used to perform the experiments.

4.2 Electron Paramagnetic Resonance (EPR)

4.2.1 Introduction

EPR was first discovered in 1944 by E. Zavoisky, in what was then known as the USSR. It is a spectroscopic technique used to detect unpaired electrons within a chemical species, in this thesis, paramagnetic defects in diamond. An external magnetic field is applied to the sample, which causes the individual magnetic moments arising from the unpaired electrons to be oriented either parallel or anti-parallel to the applied field. This separates the degenerate energy levels for the unpaired electrons, making it possible for absorption of microwaves to occur between these levels. Resonance occurs when the energy of the microwaves equals the energy difference, ΔE, of the energy levels involved. However, the allowed transitions must obey the selection rules:

$$\Delta M_S = \pm 1, \qquad \Delta M_I = 0$$

where M_S is the electron spin quantum number, and M_I is the nuclear spin quantum number. The reader is referred to [4.1, 4.2, 4.3] for further background.

4.2.2 The Bruker EMX X-Band Spectrometer

A Bruker ER200D spectrometer was used for the early experiments in this thesis. This spectrometer has been described in great detail in references [4.4, 4.5, 4.6, 4.7, 4.10]. A schematic of the microwave bridge used in this spectrometer is given in figure 4.2. For most of the experiments, a Bruker TE_{104} rectangular cavity was used, which, in conjunction with an Oxford Instruments ESR900 continuous flow system, meant that temperatures as low as 4 K were possible.

Mid way through the work, the spectrometer was upgraded to a Bruker EMX X-band spectrometer. This operates at a frequency of about 9.5 GHz and utilises the same microwave bridge shown in figure 4.2. There were some changes made to the experimental set-up of the new spectrometer and these will be discussed in section 4.2.2c.

4.2.2a The Magnetic Field

EPR differs from other forms of spectroscopy, for example FTIR, in that the magnetic field is varied and not the frequency. For this reason an accurate measurement of the magnetic field is required. This is achieved by placing a Hall probe as close to the poles of the magnet as possible. There is a correction term that needs to be applied to the

measured field to obtain the actual magnetic field. This has been determined using simulations for N_S^0 at the desired frequency, and found to be approximately 0.8 mT (8 G).

A significant difference between the ER200D and EMX spectrometers is the field modulation. The purpose of the field modulation, combined with the phase sensitive detection and time constant, is to reduce noise levels from sources such as electrical interference, and to obtain a strong EPR signal. Field modulation and phase sensitive detection can increase sensitivity by several orders of magnitude, but in order to do this, the modulation amplitude must be chosen accordingly, as if not, the signal can be greatly distorted, figure 4.1. A good compromise between signal intensity and signal distortion occurs when the amplitude of the field modulation is equal to the width of the EPR line. If the modulation amplitude is greater than the splitting between two EPR signals, the signals cannot be resolved. As an example, when running the reference sample, a 20 mT (200 G) scan would be collected, with 4096 points. This means that a point will be plotted every 0.005 mT (0.05 G). Any transition with a linewidth greater than or equal to this value will be resolved.

The EMX spectrometer gives an accurate measure of the modulation being used. For example, if the modulation is set to 0.5 G, then that is the modulation being used. The ER200D did not give as reproducible a measure of the modulation; hence quantitative EPR studies were less reliable.

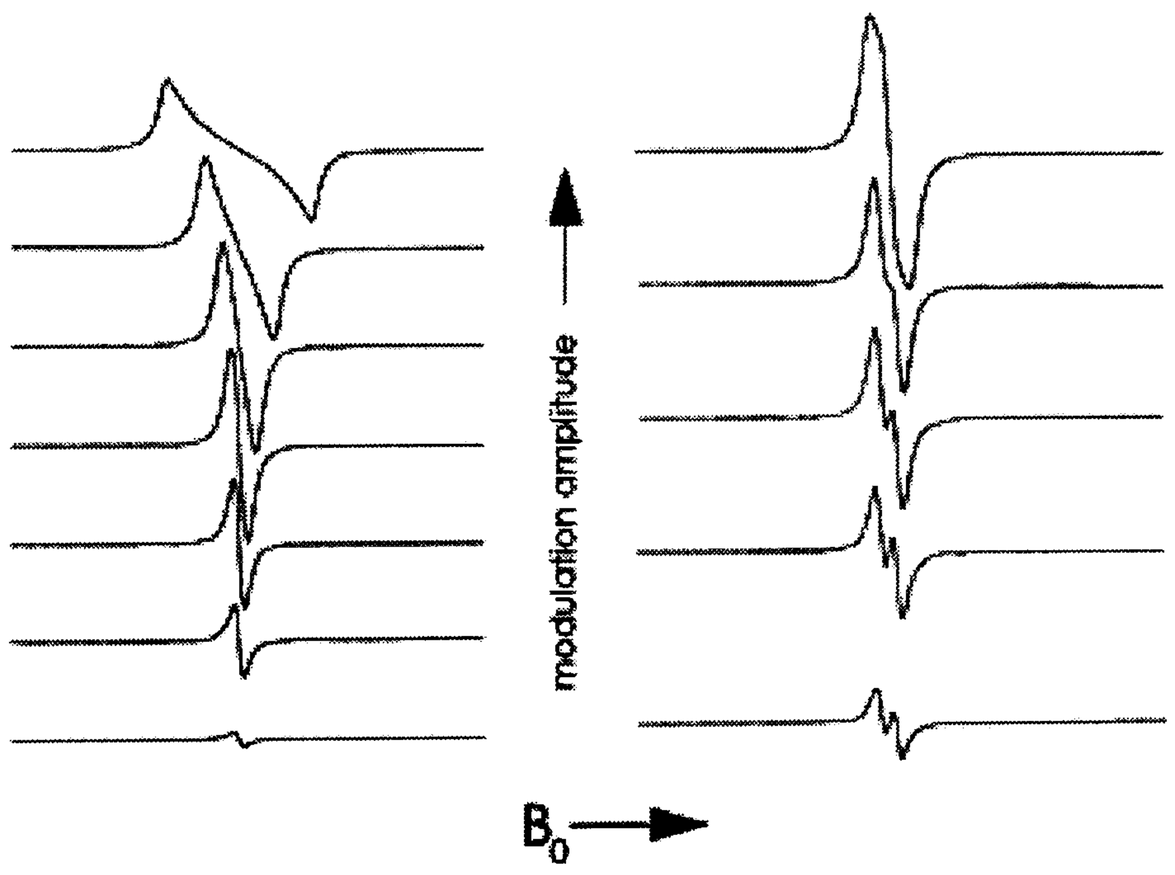

Figure 4.1: The effect of excessive field modulation on an EPR signal (taken from [4.8]).

An EPR spectrum is presented in the form of a first derivative line shape. This is a result of the interaction between the field modulation and the phase sensitive detection, as just discussed, and shown in figure 4.2.

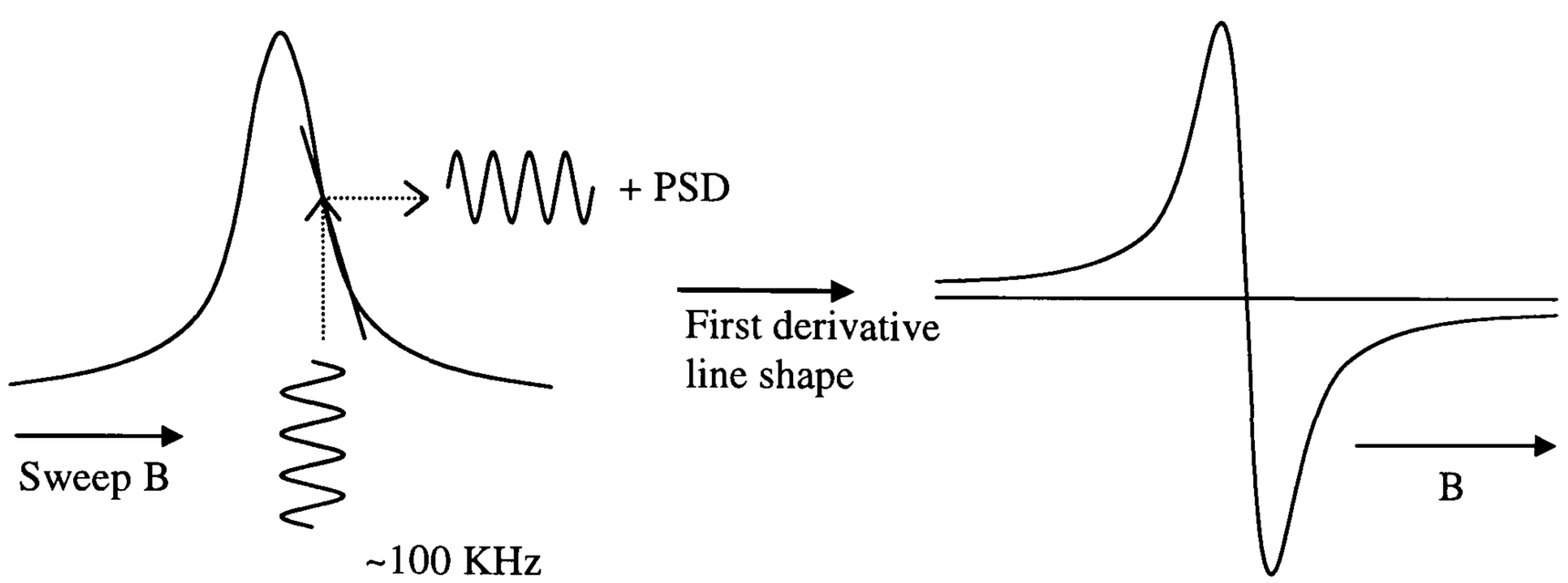

Figure 4.2: The effect the modulation field and the phase sensitive detection have on the final line shape appearing on the EPR spectrum.

4.2.2b The Microwave Bridge

A schematic of the microwave bridge is given in figure 4.3, [4.8]. The components are described in great detail by Poole [4.3], and a brief summary of how the bridge operates is given in this section.

The microwaves are produced by the Gunn Diode, and the attenuator controls the power that passes through the spectrometer. The attenuation and the power are linked by equation 4.1:

$$Attenuation = 10\log_{10}\left(\frac{P_1}{P_2}\right) \tag{4.1}$$

where P_1 is the incident power, and P_2 is the microwave power after passing through the attenuator.

The circulator allows only radiation reflected from the cavity to reach the detector as the microwave radiation can only travel round the circulator in one direction. The diode detects the reflected microwaves from the cavity and converts the microwave power to electrical current. Finally, the reference arm controls the power level by biasing the detector for optimum performance. The optimum results are obtained with a detector current of 200

μA. The microwaves from the cavity and the reference arm are combined at the detector diode and so the phase shifter ensures that the two signals are in phase with each other.

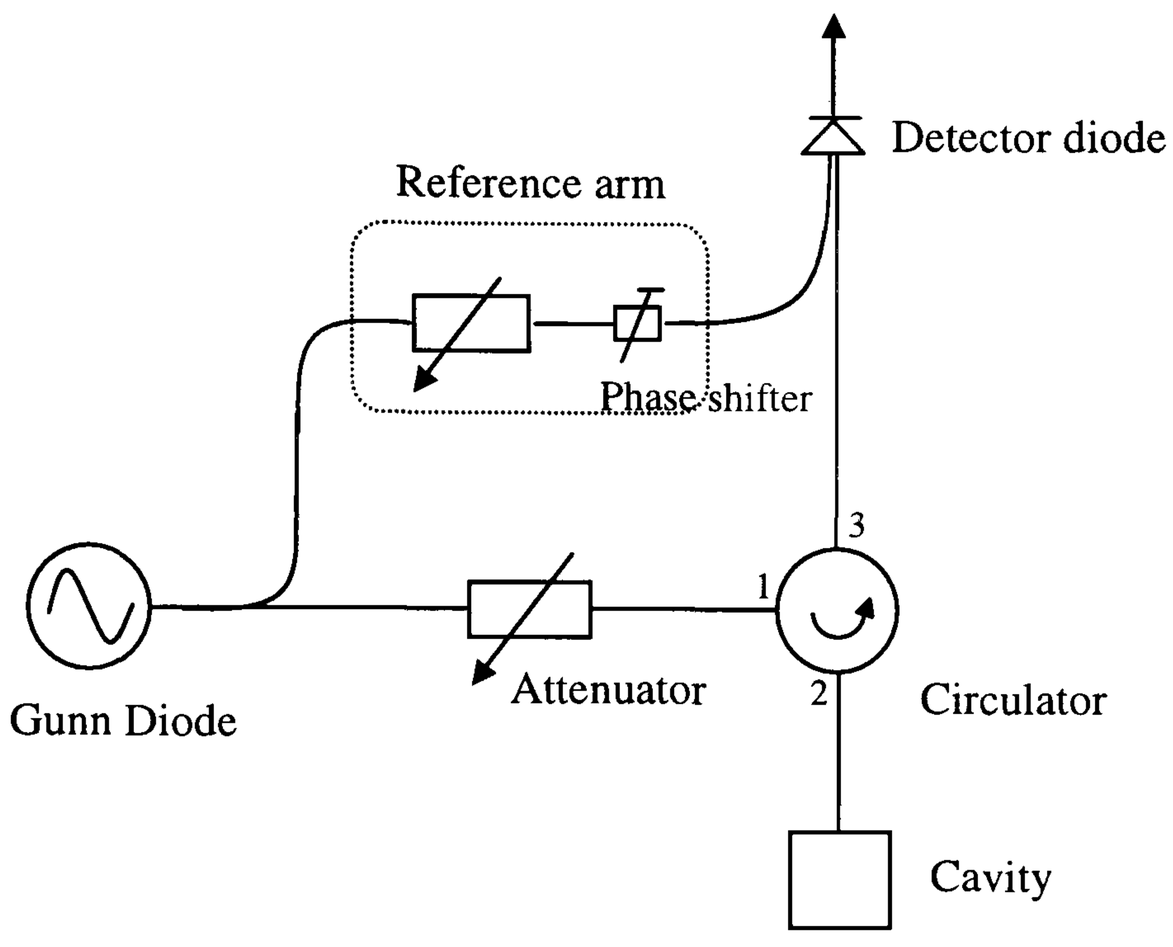

Figure 4.3: Schematic of the microwave bridge

An advantage of the EMX spectrometer over the ER200D is the ability to perform an automated power variation. This means that at the end of every scan, the bridge will automatically change the power at which the spectrum is being recorded and start all over again. This feature proves very useful, especially when investigating the saturation behaviour of certain centres, for example NV^-.

The Automatic Frequency Controller (AFC) controls the frequency of the microwaves. When a spectrum is obtained quickly, i.e. with only a few scans, the frequency varies by only about ± 1 KHz. When the experiment is left for many scans, for example, over a weekend, the frequency can vary by about ± 100 KHz. A change in frequency of 100 KHz can be interpreted by consideration of the following equations:

$$h\nu = g\mu_B B \qquad \text{and} \qquad h\Delta\nu = g\mu_B \Delta B \tag{4.2}$$

to get $$\frac{\Delta\nu}{\nu} = \frac{\Delta B}{B} \quad \Rightarrow \quad \Delta B \sim 0.0035 \text{ mT } (0.035 \text{ G})$$

This is only a very small change in the position of the transitions on the EPR spectrum and so can be considered negligible. However, a more significant change in frequency will have a much larger effect and so it is necessary to control the frequency to maintain stability. The AFC controls this by adjusting the frequency at the beginning of every scan and ensuring the cavity remains critically coupled.

4.2.2c The Experimental Set-up

The practical side of the experiment changed when the old spectrometer was upgraded. The first difference came about with the new cavity. The purpose of the cavity is to amplify weak signals from the sample. Each cavity has a Q-value associated with it, and this is a measure of how efficiently the cavity stores the microwave energy, equation (4.3).

$$Q = \frac{2\pi(energy\ stored)}{Energy\ dissipated\ per\ cycle} \tag{4.3}$$

The new cavity used is the Bruker ER4122SHQ (super high Q) cavity. It combines a super high Q with a large filling factor[1] and large modulation coils to provide excellent sensitivity [4.9]. In an unloaded cavity, the Q-value is about 15000. When a sample is placed inside, this reduces to about 8000.

A few practical aspects of the set-up needed to be changed in order to record accurate EPR spectra. The old goniometer (as described by Hunt [4.10]) was redesigned so that any conducting material was as far from the cavity as possible; this resulted in the rod of the new goniometer being made entirely of rexalite. The goniometer had approximately an extra 2 cm of length added to it in order for it to sit in the right part of the cavity, figure 4.4(a).

Because of the size of the tube leading to the cavity, it is possible to use larger wheels to accommodate the samples, figure 4.4(b). This enables a full angular movement of a much wider range of samples. The new wheels range between 2–3.5 mm in diameter. While the goniometers were being re-designed, it was found that looping the cotton around the wheel twice, instead of just once, helped with the turning and strength of the mount.

The EMX spectrometer has an automated goniometer. This means that the computer controlling the spectrometer can carry direct a full angular variation of an EPR spectrum. This has the advantage of over-night running, therefore maximising data collection time.

---

[1] The filling factor is the ratio of the integral of the microwave field over the sample volume relative to the integral of the total microwave field in the cavity.

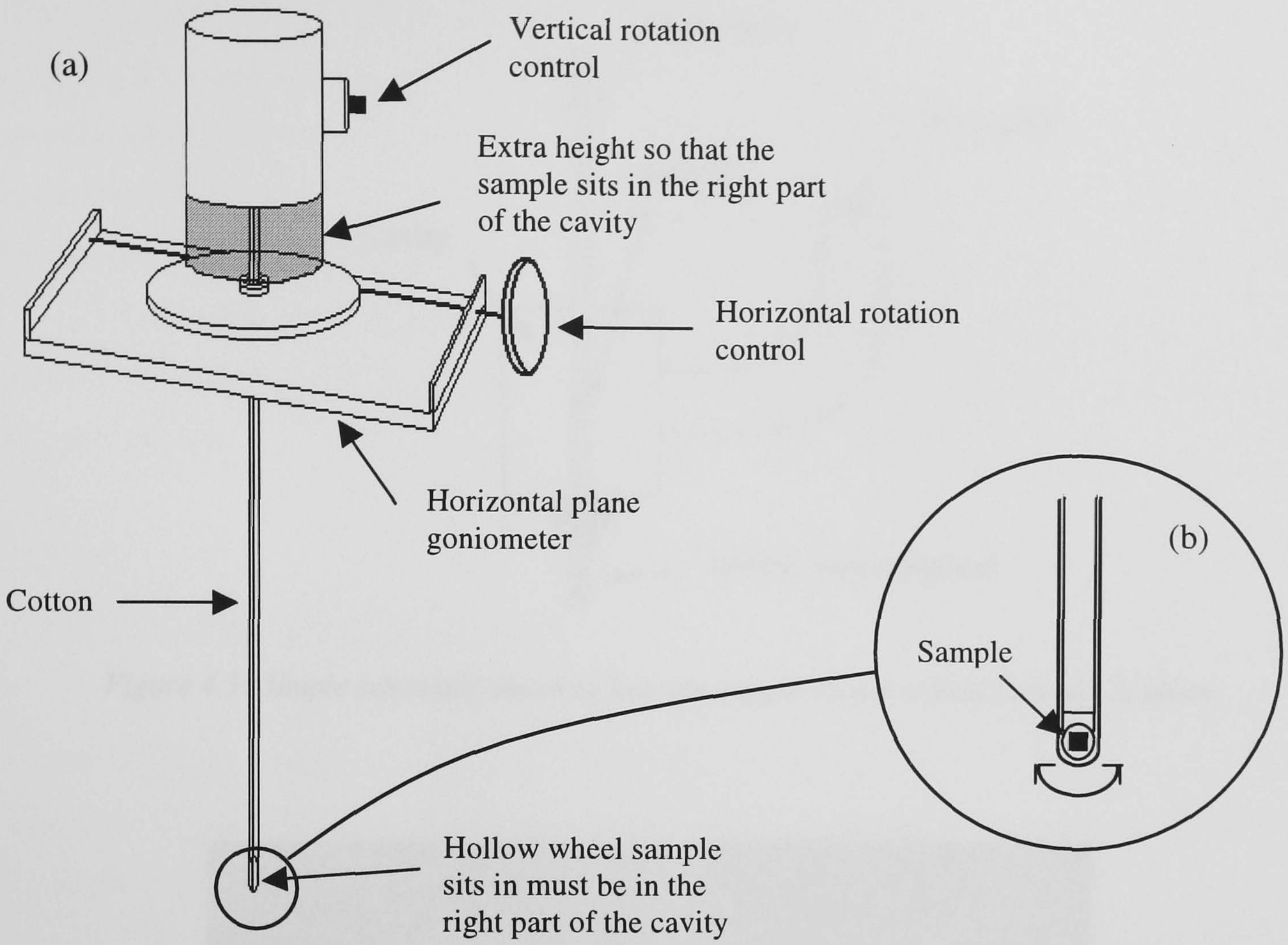

Figure 4.4: Schematic of the twin axis goniometer [4.10].

Because of the high Q-value, the new cavity is more sensitive to vibrations. The vibrations cause a change in the Q-value, which in turn causes a change in the reflected power and hence adds significantly to the overall noise level. The higher the Q, the more pronounced the effect. To overcome this problem, the sample mount is supported using a piece of teflon that is inserted into the cavity through a hole in the bottom, figure 4.5.

The cavity itself also needs to be secured in place because the slightest movement of the sample in respect to the magnetic field can have a large effect on the position of the EPR lines on a highly anisotropic defect, for example the NV^- defect. The cavity is secured by a pair of stabilisers that are placed on opposite sides between the cavity and the magnet, figure 4.6.

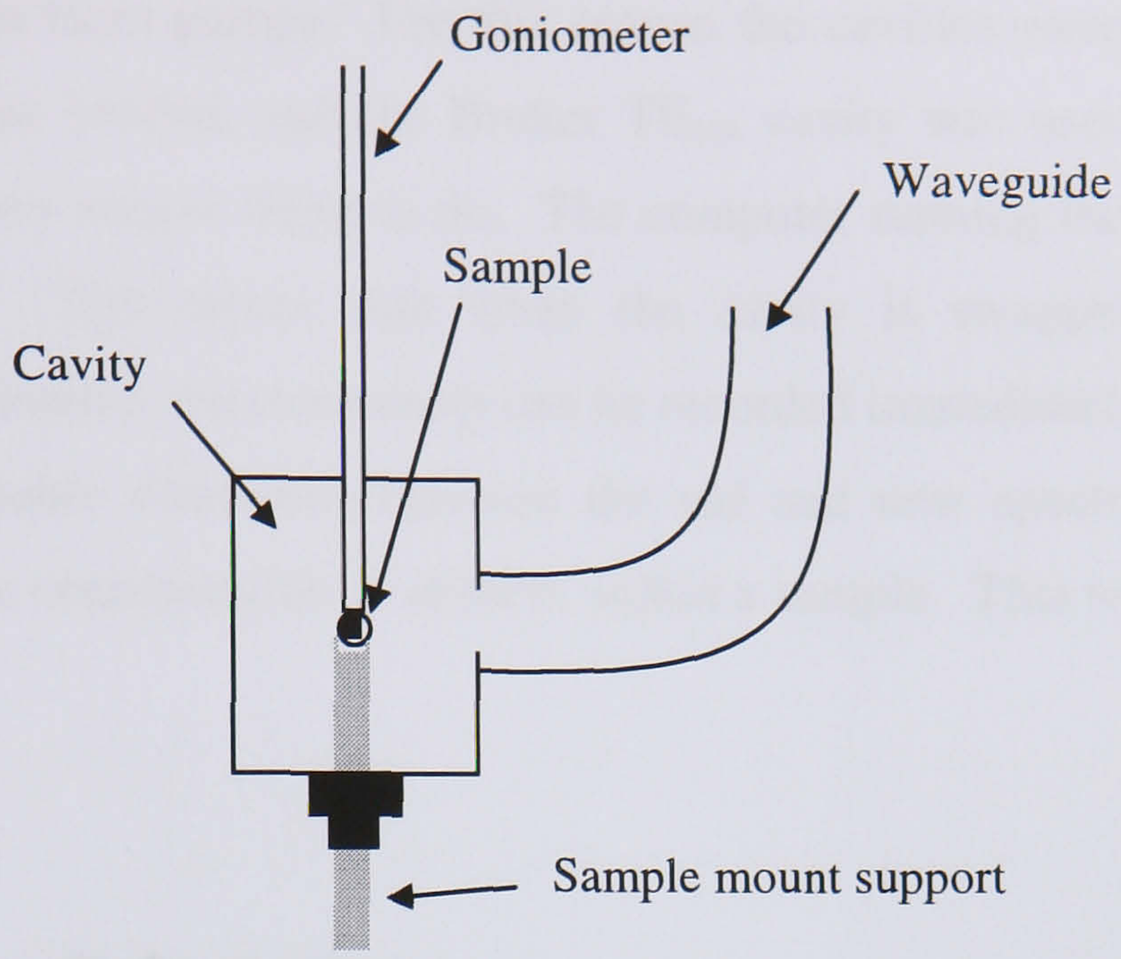

Figure 4.5: Simple schematic showing how the sample mount is held securely in place.

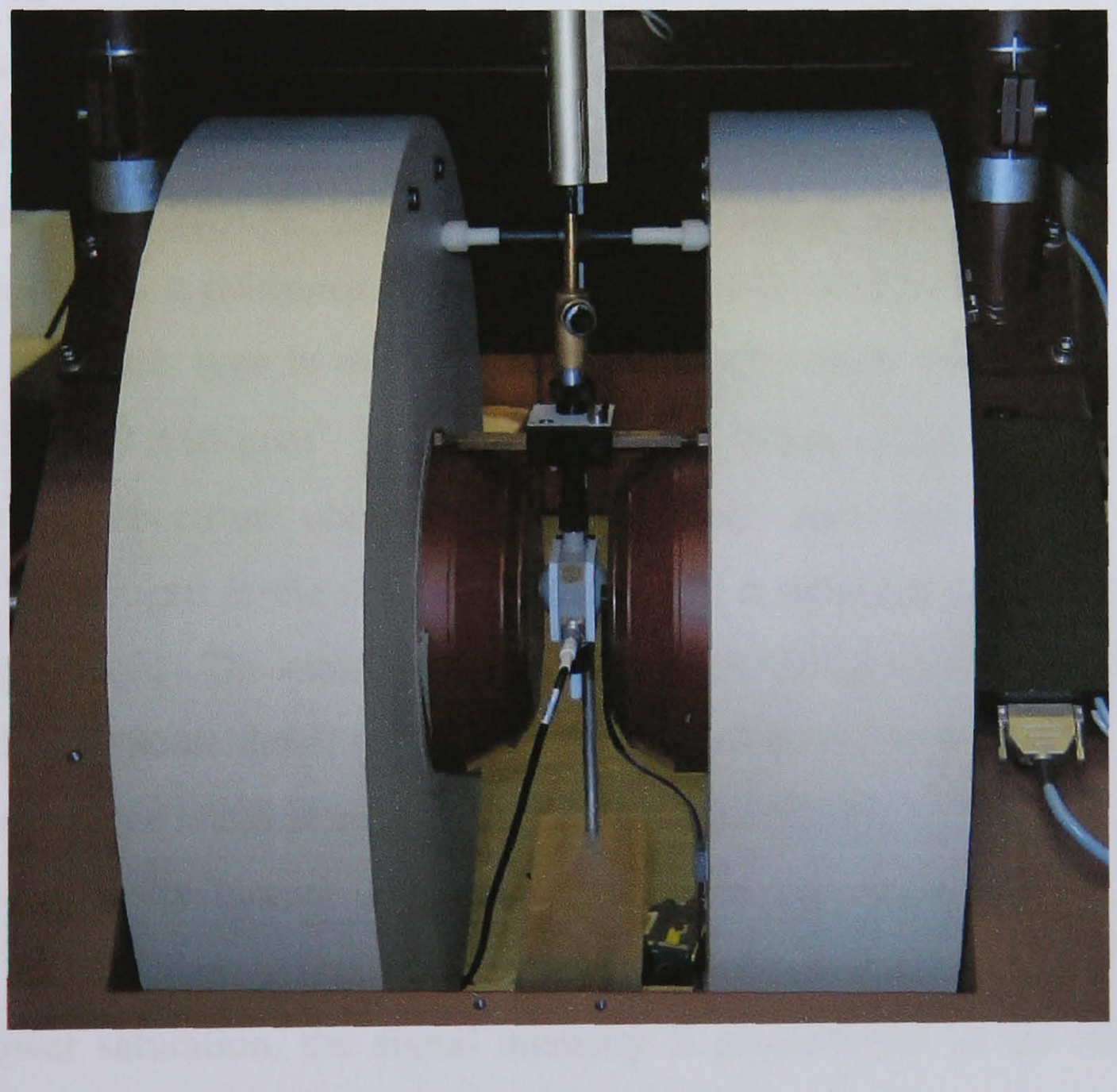

Figure 4.6: Photo showing the experimental set up of the EPR cavity. Note the stabilisers securing the cavity in place, and the small white teflon rod at the bottom of the cavity that is used for securing the sample rod in place.

The new cavity was not used to perform low temperature measurements. This is because, as mentioned before, the high Q of the cavity makes it very susceptible to

microphonics, which would result from the smallest things, such as a small change in helium flow and extra vibrations from pumps. For this reason the cavities were swapped when a temperature variation was needed, and the Bruker TE_{104} cavity was used. Unlike the old spectrometer, this is a very simple thing to do. The computer running the spectrometer has calibration files saved. This means that when the cavity is swapped over, once the calibration file has been loaded, measurements can be recorded immediately.

The most noticeable difference between the old and new spectrometers is in the process of calculating the concentration of defects within a sample. This will be discussed in the next section.

4.3 Concentration Calculations

The concentration of a defect within a sample is directly proportional to the intensity of the EPR spectrum arising from that defect. However, the concentration of defects determined is an average over the whole sample and hence does not provide any information about the homogeneity of the sample.

An absolute concentration measurement is possible using the spectrometer and sample parameters [4.2, 4.3], but it is far more practical and accurate to compare an unknown sample with a reference. The reference sample used for these measurements is a single sector, synthetic, type Ib diamond containing only single substitutional nitrogen at a concentration of 270 ±10 ppm[1] (4.75×10^{19} cm^{-3}). When using a reference sample it is essential that the spectrum obtained is reproducible each time it is required. The concentration of nitrogen in the reference sample was determined using infrared absorption [4.11] (see appendix 3). The saturation behaviour of the nitrogen in the reference sample has also been studied in some detail, and for optimum results and to ensure the nitrogen is not saturated, the reference is run at an attenuation of at least 50 dB.

There are many factors that need to be taken into account when calculating the concentration of a defect. The first being the microwave power. In the absence of microwave power saturation, the signal intensity is proportional to the microwave power (saturation will be covered in more detail in section 6.6). For this reason, when calculating the concentration of a defect, it is essential that either the sample and the reference are run at the same power, or one of the signals must be scaled accordingly.

---

[1] ppm = parts per million carbon atoms

Equation 4.4 describes the remainder of the factors that need to be considered to be able to accurately calculate the concentration of a defect in a sample in the absence of microwave power saturation [4.2].

$$[X]=\frac{[STD]I_X}{I_{STD}}\frac{[10^{-Attn/20}]_{STD}}{[10^{-Attn/20}]_X}\frac{Mass_{STD}}{Mass_X}\frac{Mod_{STD}}{Mod_X}\frac{g_{STD}^2[S(S+1)]_{STD}}{g_X^2[S(S+1)]_X}\frac{Gain_{STD}}{Gain_X}\frac{AqTime_{STD}}{AqTime_X}\frac{N_{STD}}{N_X} \quad (4.4)$$

Where: [*X*] is the concentration of species X, [STD] is the concentration of the reference sample, $I_{X/STD}$ is the double integrated intensity of the spectrum arising from the defect in the sample of interest, X, and of the reference sample, STD, which have been corrected to the same power using the factor $[(10^{-Attn/20})_{STD}/(10^{-Attn/20})_X]$. $Mod_{X/STD}$ is the modulation used for the acquisition of each spectrum, $Gain_{X/STD}$ is the gain at which the spectra were run, $AqTime_{X/STD}$ is the number of averages taken while sitting at a specific magnetic field, and *N* is the number of scans recorded for each spectrum. The *g* value is the g-value for the defect of interest and *S* is the overall electron spin of the defect. All of these parameters need to be considered when analysing spectra recorded using the Bruker EMX spectrometer. However, the ER200D spectrometer scaled many of the parameters to unity, which meant that the last three terms of equation 4.4 could be ignored.

Another important factor affecting the intensity of the EPR transition is the temperature. It is important that only spectra recorded at the same temperature be directly compared. In absence of microwave power saturation, the signal amplitude is inversely proportional to the absolute temperature, Curie Law, and it would get very complicated to try to compensate for a change in temperature. In most systems, the temperature also has an effect on the linewidth.

The intensity of a spectrum is determined by a baseline correction, followed by a double integration[1]. The double integration is needed because the spectra are recorded as a first derivative line shape, as discussed in section 4.2.2a. The integration process needs much care and attention as a baseline can contribute significantly to the overall error in the defect concentration. It is important to fit the baseline over a suitable width in order to ensure an adequate baseline is being accounted for.

Looking at equation 4.4, the main factors that could contribute an error to the concentration of a defect are the mass and the integrated intensity. Contributions to the error

---

[1] Integrations performed using Microcal Origin 7.0

in the integrated intensity arise from the signal to noise levels, having to perform a double baseline and overlapping spectra. When integrating a reference sample, the errors involved are very small as the spectrum contains only N_S^0. However, having checked the errors involved in a double integration in an unknown sample, a typical error would be of the order of a few percent. The largest potential problem comes from saturation, which will be discussed in detail in section 6.6.

To keep the concentration calculations simple, a spreadsheet was written in which the parameters could be entered and the concentration of a defect immediately calculated. This spreadsheet is given in Appendix 2.

Often there are problems with EPR spectra from different defects overlapping. To overcome this, a simulation[1] can be fitted to the experimental data, which deconvolves the separate components. The simulation is then integrated and this proves to be a more accurate method for integrating the spectrum as only the spectrum of interest is being considered. Care must be taken when fitting the simulation to ensure that the linewidth and shape fits as accurately as possible to the experimental data. If the width of the line increases by a factor of n, the integrated intensity of the line will increase by a factor of n^2.

4.4 Fourier Transform Infrared Spectroscopy (FTIR)

Infrared spectroscopy can be used to study impurity atoms in the diamond structure via infrared active induced vibrations. There are different spectrometers used for this, but all of the optical absorption work presented in this thesis has been carried out using FTIR. This section of the chapter will not describe how a basic spectrometer works because it is a technique on which many books have been written [4.12, 4.13, 4.14, 4.15, 4.16]. Instead it will cover the main advantages of a Fourier transform spectrometer over the, also common, dispersive spectrometer. The basic set up of an FTIR spectrometer consists of a Michelson Interferometer, the basic principles of which are shown in figure 4.7.

---

[1] All simulations in this thesis are produced using the code EPR.NMR, supplied by D. G. Gavin, M. J. Mombourquette and J. A. Weil. Written at the department of Saskatchewan, Saskatoon, Saskatchewan, Canada, S7N 0W0. Any correspondence should be addressed to Prof. J. A. Weil.

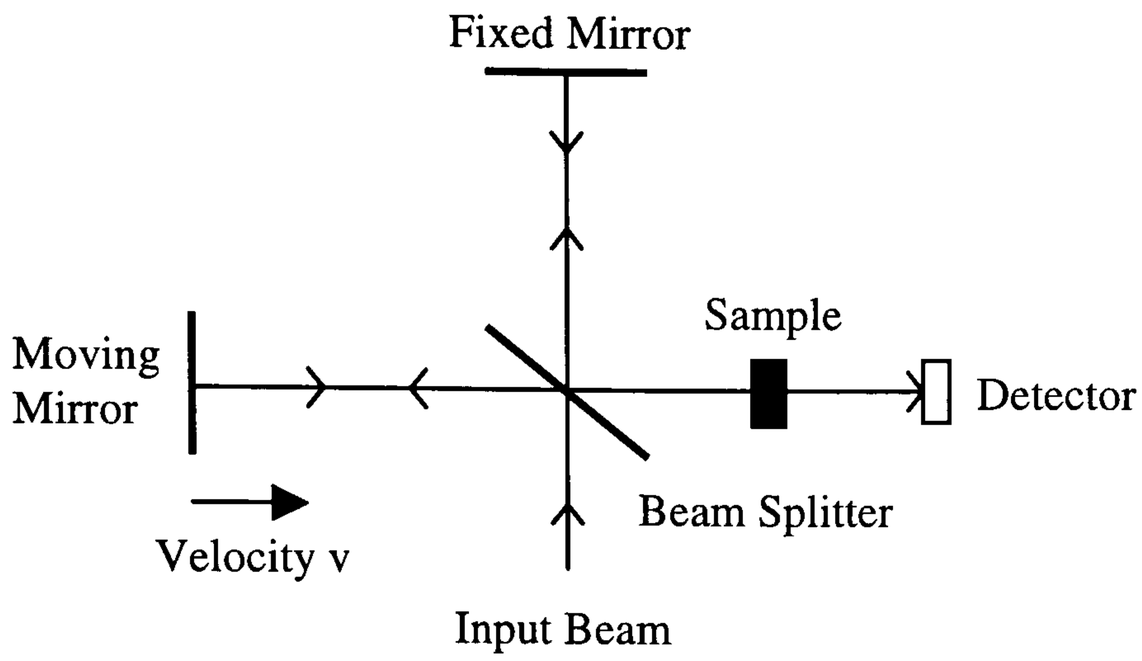

Figure 4.7: The basic principles of a Michelson interferometer (the basis of a Fourier transform spectrometer).

The detector in an FTIR spectrometer detects the intensity versus time of all wavelengths passing through the instrument. The computer then digitises this output signal and performs a Fourier transform, which converts the time scale to a frequency. A spectrum can then be produced which plots absorption coefficient (α) against frequency. The absorption coefficient is determined using equation (4.5)

$$\alpha = \frac{1}{t}\ln\left(\frac{I_0}{I_t}\right) \tag{4.5}$$

where t is the thickness of the sample, I_0 is the incident intensity and I_t is the transmitted intensity, figure 4.8.

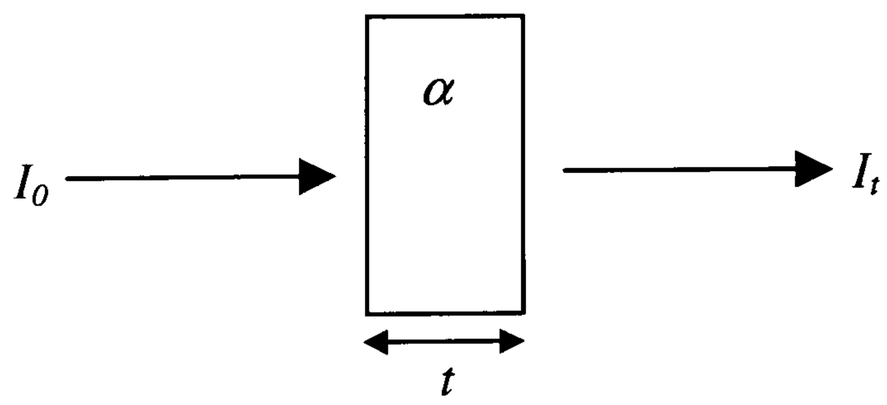

Figure 4.8: Transmission of light through a parallel slab of thickness t and absorption coefficient α.

The main advantage of FTIR over conventional spectroscopy is the speed at which data can be collected. The time spent obtaining a spectrum can be reduced from hours or minutes to seconds or even fractions of a second, and as a result, the number of samples that can be measured is greatly increased. There is also a throughput advantage with Fourier

transform spectroscopy. Parallel beams are used throughout, which means there is no need to focus the radiation through a slit, as is necessary in dispersive spectroscopy. This results in all the source energy passing through the instrument.

When performing optical absorption measurements it is important to ensure that the samples are completely free from any grease or dirt. Failure to do this could result in some unwanted absorption lines in the regions of interest appearing on the spectrum. Samples are cleaned by being immersed in a mixture of concentrated sulphuric acid and potassium nitrate, and heating to about 250 °C for approximately 30 minutes. The samples are then rinsed in deionised water. When carrying out optical absorption measurements, it is preferable for the sample to have two polished parallel faces in order to minimise any scattering of the light.

One of the disadvantages of a Fourier transform spectrometer is the single beam makes it very sensitive to changes in background absorption, for example water and carbon dioxide. For this reason a spectrum would be recorded with no sample in place, which could then be subtracted from the final experimental spectrum.

Finally, each spectrum needs to be scaled in order to be able to directly compare the absorption coefficient of any absorption bands observed. The path length of the light plays an important role in the intensity of a peak. To make sure each peak can be directly compared, each spectrum is scaled so that the absorption at 2000 cm^{-1} corresponds to a known absorption coefficient of 12.3 cm^{-1} [4.17, 4.18]. This is only true if there is no impurity absorption at 2000 cm^{-1}.

The intensity of an absorption band is proportional to the concentration of defects responsible for the peak. However, to calculate the concentration, the calibration factor must be known. This factor can be determined by a comparison with the corresponding EPR transition arising from that defect. Unlike EPR however, the concentration does not give a value over the whole sample. The concentration is calculated by using the intensity of the absorption peak through which the beam is passing. The result of this is that inhomogeneous samples are likely to produce different absorption spectra if run through different sections of the sample.

When the temperature variation measurements were carried out, it was ensured that the sample was left mounted for the duration of the study. This ensured that the light was always passing through the same part of the sample.

Two Fourier transform infrared spectrometers were used for the work presented in this thesis; a Bruker IFS66 FTIR spectrometer, and a Perkin Elmer Spectrum-GX

spectrometer. The changes made to the equipment for the purpose of these experiments will be presented in the next sections.

4.4.1 The Bruker IFS66 FTIR Spectrometer

Modifications were made to the basic spectrometer in order to facilitate experiments. A continuous flow cold finger dewar operated with either liquid helium or liquid nitrogen is used in order to carry out measurements between 5 and 300 K. The windows are made of calcium fluoride (CaF_2), as it has a low refractive index and is transparent over the wavelength range of interest. Figure 4.9 shows the deconstructed dewar so that each component can be seen. A heater is attached to the closest point to the sample in order to regulate the temperature as accurately as possible.

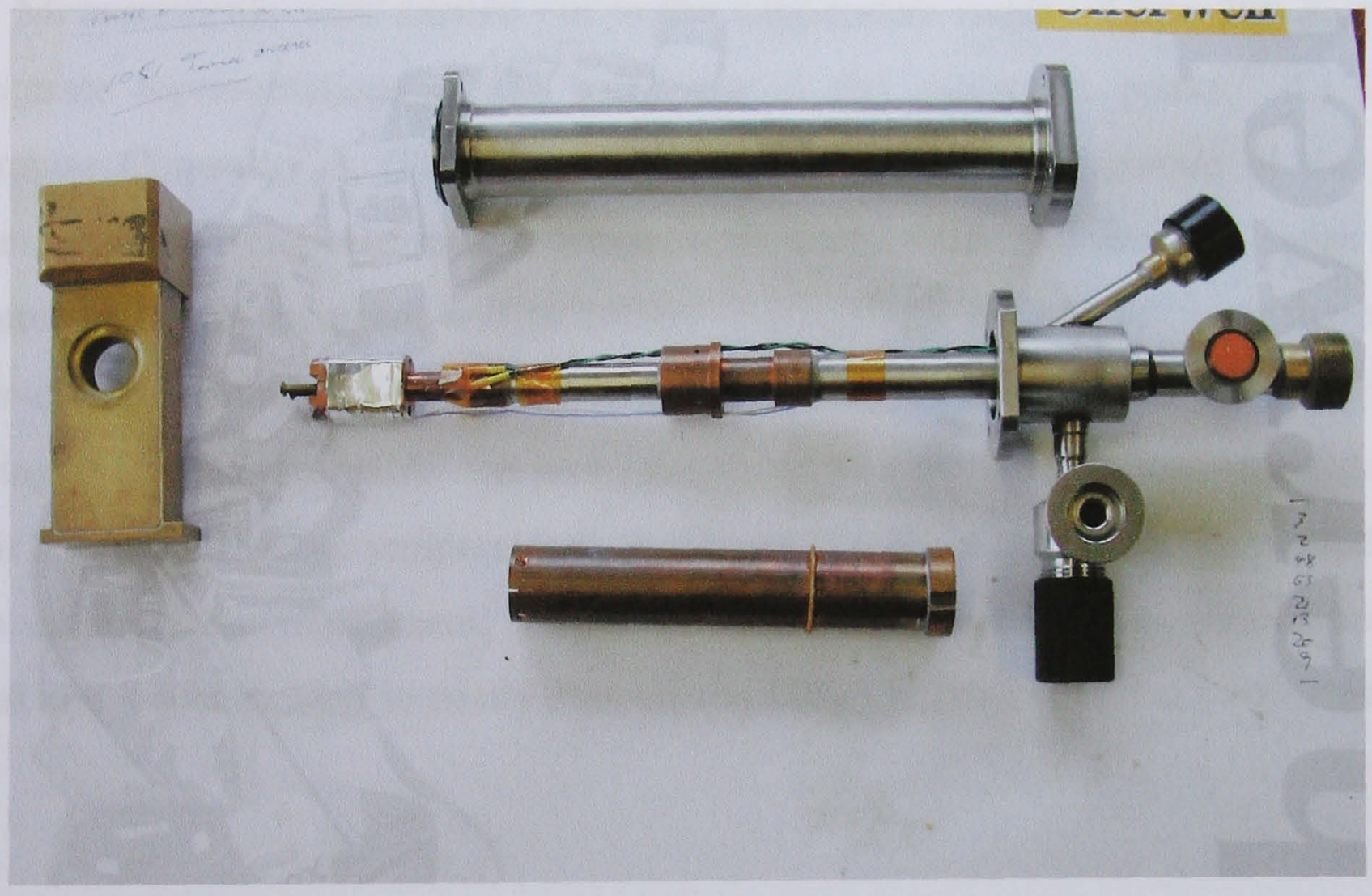

Figure 4.9: Photograph of the dewar used with the Bruker FT-IR spectrometer (constructed by Mark Whitney in the Clarendon Laboratory workshop, at the University of Oxford).

With the beamsplitters and detectors available, the Bruker IFS66 spectrometer covers the infrared and the visible range of the spectrum. A different beamsplitter and detector are used for the two regions of interest, table 4.1.

Available range	Detector	Beamsplitter
Infrared (1500 – 15000 cm^{-1})	DTGS [1]	Si on CaF_2
Visible (8500 – 25000 cm^{-1})	Si diode	Quartz

Table 4.1: The beamsplitters and detectors used with the Bruker IFS66 spectrometer.

The input beam shown on figure 4.7 is a tungsten lamp for this spectrometer. Unless otherwise stated, the measurements have been recorded using a resolution of $1cm^{-1}$.

The samples are mounted in copper sample mount and held in place with indium. It is important to ensure that there are no gaps around the sample through which light can pass. Only light that has passed through the sample should reach the detector.

4.4.1a Temperature Calibration

Measurements were carried out in the temperature range ~4.2 to 300 K in order to plot accurate representations of the behaviour of the absorption peaks. An Intelligent Temperature Controller 3, (ITC-3), was used to record the temperature of the readings. However, at many temperatures the temperature reading was not accurate since the diode therometer had been changed, and so another method was used to calibrate the controller. This involved attaching a voltmeter to measure the voltage across the silicon diode[2] measuring the temperature. When built, the diode is calibrated by measuring the voltage across it at three reference temperatures, 4, 77 and 273 K. A graph is then plotted which is used to calibrate the experiment, figure 4.10. From here the actual temperature can be recorded and a plot created to easily convert the ITC-3 reading to a real temperature, figure 4.11.

---

[1] Deuterated TriGlycine Sulphate
[2] Oxford Instruments Silicon Diode detector.

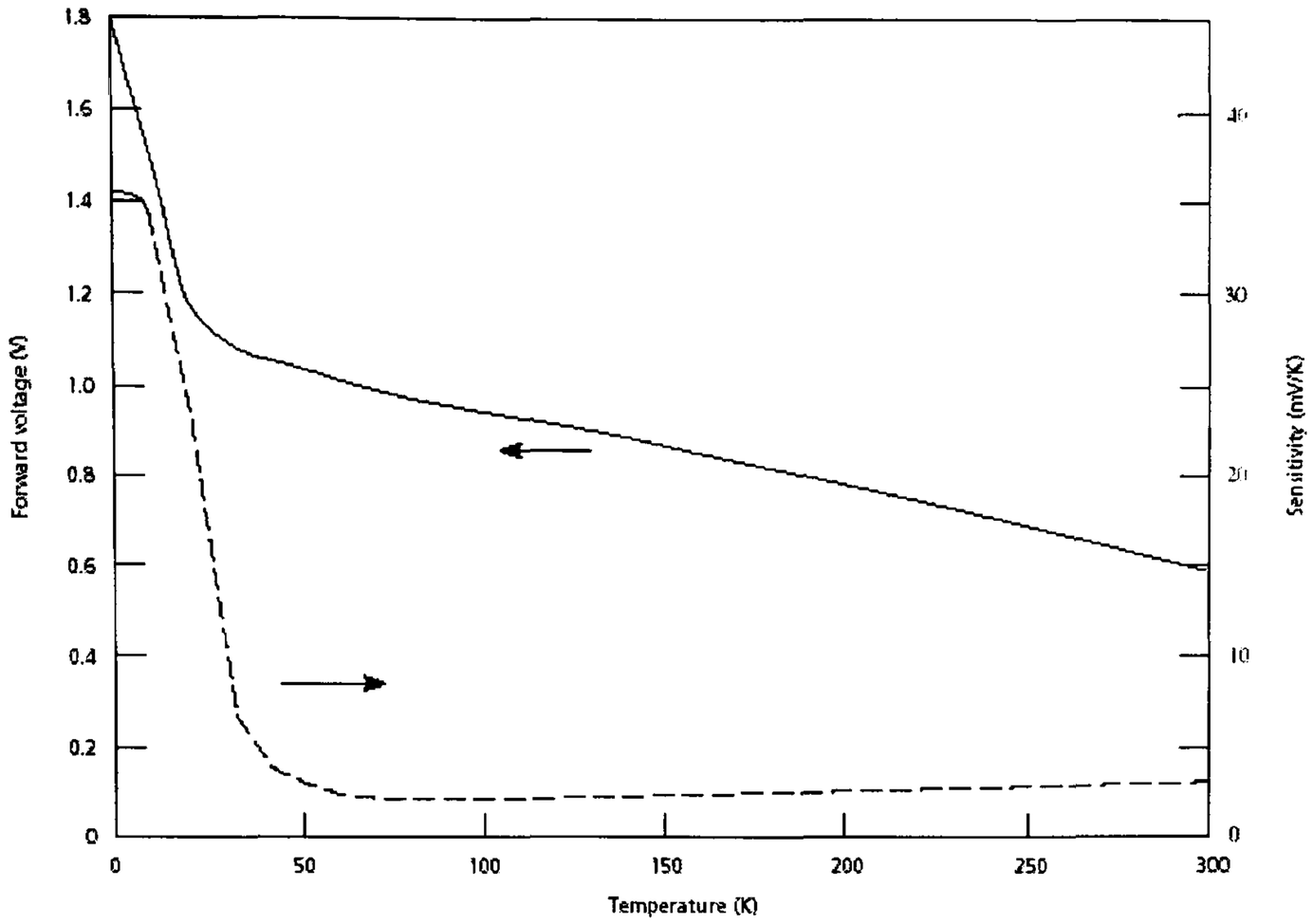

Figure 4.10: Typical curves of the silicon diode voltage (straight line) and sensitivity (dashed line) as a function of temperature (Taken from Oxford Instruments web site [4.19])

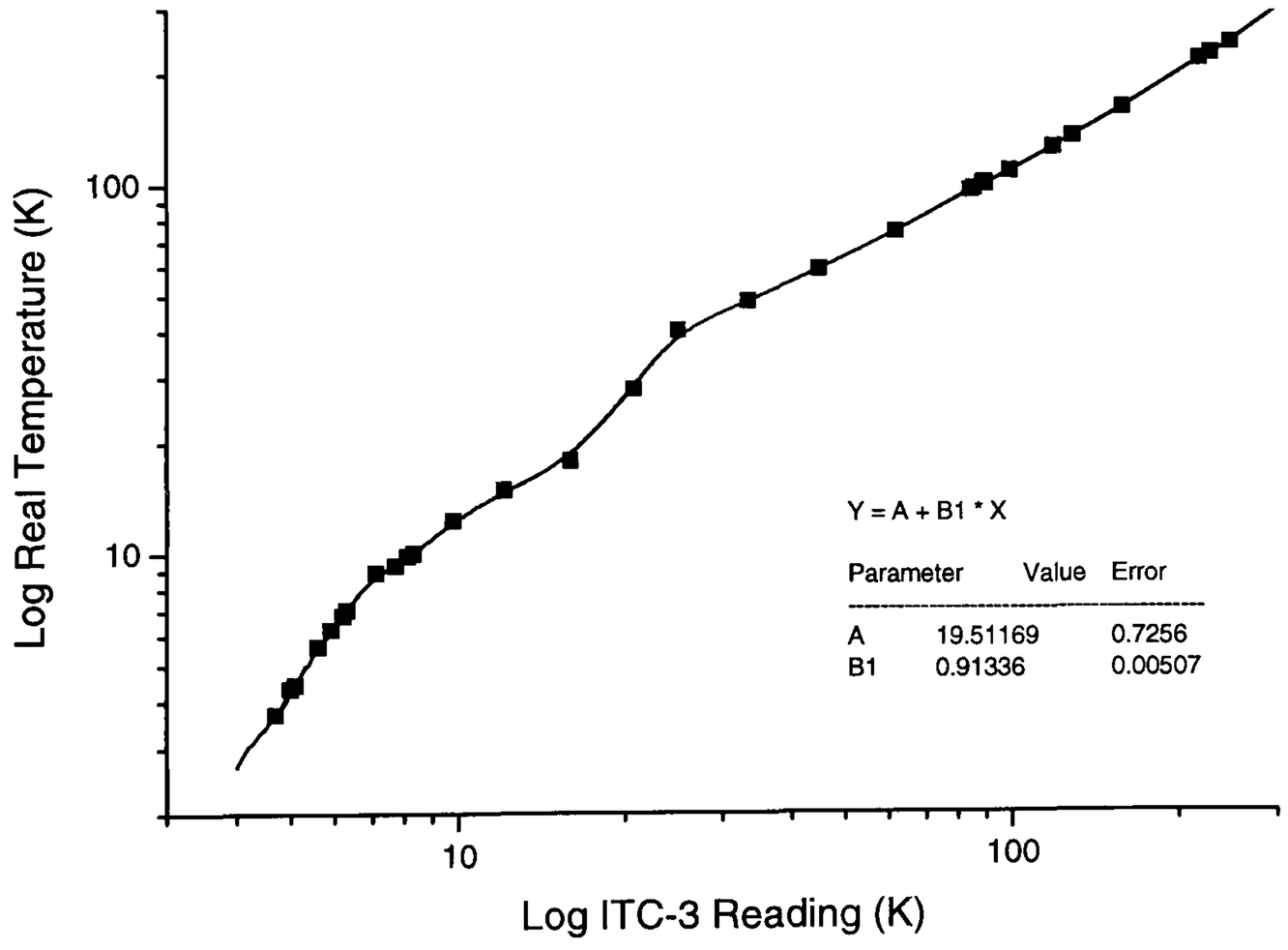

Figure 4.11: Calibration of the ITC-3 temperature controller used with the Bruker IFS66 spectrometer.

4.4.2 The Perkin Elmer Spectrum-GX Spectrometer

The complete operable range of the Perkin Elmer Spectrum-GX spectrometer is between 30–15000 cm^{-1} (0.0037–1.86 eV), but beamsplitters and detectors available for this work cover the near and mid-infrared regions, 370–15000 cm^{-1}, table 4.2.

Available range	Detector	Beamsplitter	Source
Near Infrared (2700 – 15000 cm^{-1})	DTGS	Quartz	Tungsten halogen lamp
Mid Infrared (370 – 7800 cm^{-1})	DTGS	Optimised KBr	Globar

Table 4.2: The beamsplitters and detectors used with the Perkin Elmer Spectrum-GX spectrometer.

Figure 4.12 compares two spectra taken through the same part of the same sample in the mid infrared region of the spectrum. It can be seen that the two spectra are different in the region between 0.05 – 0.2 eV. This feature occurs when the background recorded to subtract from the spectrum is not run through the correct size aperture. It is important to ensure that both the background and the sample are run through the same size aperture in order to reduce multiple reflections caused by stray light. Every optical component can contribute to stray reflections, for example the source and the detector. These multiple reflections passing through the interferometer produce double modulation of the IR beam, which results in false energy being folded back into the spectrum. The effect this has is to produce absorption in the regions of the spectrum being blocked by the filter being measured [4.20]. Consequently, the true characteristics of the filter are prevented from being recorded. By ensuring that both the background and the sample are recorded through the same size aperture minimises any reflected light that can contribute to the spectrum. The region of the spectrum that is affected by this is used to calculate the concentration of different forms of nitrogen within the sample so it is essential that it is as accurate as possible, (see appendix 3 for more details on this process).

The samples were mounted on a piece of aluminium each time, with the size of the aperture dependant on the size of the sample. The sample mounts were sprayed black to prevent any of the light being reflected back.

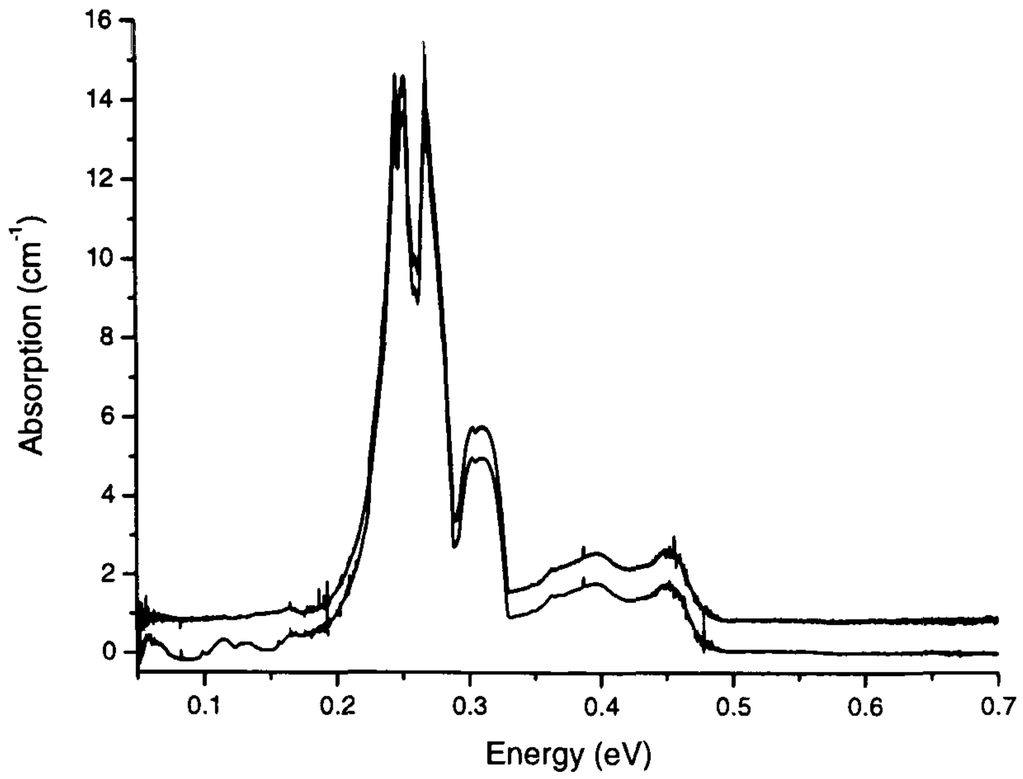

Figure 4.12: A comparison of spectra when different size apertures are used. The measurements were recorded at room temperature [4.21]. The top spectrum is obtained using the correct size aperture, and has been offset by 1 cm^{-1} for clarity.

References

[4.1] Abragam and Bleaney, Electron Paramagnetic Resonance of transition ions, Dover Publications inc., New York (1986)

[4.2] J.R. Bolton, J.A. Weil and J. E. Wertz. Electron Spin Resonance: Elementary theory and practical applications. Wiley, New York (1994)

[4.3] C.P. Poole, JR. Electron Spin Resonance: A complete treatise on experimental techniques. Dover Publications inc. (1996)

[4.4] A. Cox, D. Phil. Thesis, University of Oxford (1993)

[4.5] O. D. Tucker, D. Phil. Thesis, University of Oxford (1995)

[4.6] D. Twitchen, D. Phil. Thesis, University of Oxford (1997)

[4.7] D. Talbot-Ponsonby, D. Phil. Thesis, University of Oxford (1997)

[4.8] R. T. Weber, J. J. Jiang and D. P. Barr, EMX User's Manual, Manual Version 2.0, Software Version 2.3, Bruker Instruments (1998)

[4.9] Pathways to Experimental Freedom in EPR, E500 Series, available from Bruker UK Ltd, Banner Lane, Coventry, CV4 9GH

[4.10] D. Hunt, D. Phil. Thesis, University of Oxford (1999)

[4.11] Infrared Absorption measurements taken by Samantha Quinn at the DTC Research Centre

[4.12] C. N. Banwell and E. M. McCash, Fundamentals of Molecular spectroscopy, McGraw-Hill book company, 4th Ed. (1994)

[4.13] Perkin Elmer Spectrum-GX spectrometer, user's guide. To obtain a copy contact: PerkinElmer Ltd, Chalfont Road, Seer Green, Beaconsfield, BUCKS, HP9 2FX, UK

[4.14] B. C. Smith, Fundamentals of Fourier Transform Infrared Spectroscopy, CRC Press (1996)

[4.15] P. R. Griffiths and J. A. de Haseth, Fourier Transform Infrared spectroscopy, Wiley (1986)

[4.16] M. J. Hollas, Modern Spectroscopy, 3rd Edition, John Wiley & Sons (1997)

[4.17] A. M. Zaitsev, Optical Data on Superhard Semiconductors: Diamond, ISTOK (1998)

[4.18] Handbook of Optical Constants, ed. E. D. Palik, Academic, Orlando, New York (1985)

[4.19] http://www.oxford-instruments.com/cryospares/thermometry.shtml#silicon_diode

[4.20] Spectrum GX Optica notes, available from Perkin Elmer Instruments, 710 Bridgeport Avenue, Shelton, CT 06484-4794 USA

[4.21] Measurements taken by Donna Carroll at the University of Warwick.

Chapter 5

The negative nitrogen-vacancy-hydrogen centre (NVH^-)

5.1 Introduction

As discussed in Chapter 2, nitrogen is readily incorporated into single crystal CVD diamond unless special efforts are made to exclude it from the growth environment. In addition to the commonly found defects such as N_S^0 and NV centres, a new system of lines has been observed by EPR in nitrogen doped, single crystal CVD diamond. It will be shown that the new complex is the negatively charged, nitrogen-vacancy-hydrogen centre (NVH^-).

This chapter presents and discusses the results obtained using EPR and describes how the new centre was identified.

5.2 Literature Review

The first report of the EPR centre now identified as NVH^- was given by Damian Hunt in 1999 [5.1]. He was unable to identify the defect even though he carried out many experiments on its angular variation and temperature dependence. His experiments were carried out on a nitrogen doped, highly orientated, polycrystalline CVD diamond.

5.3 Samples and Experiments

Most of the nitrogen doped samples grown by CVD showed a group of EPR lines around g = 2.0024. In order to identify the defect or defects responsible for the new system of lines, detailed EPR studies were performed on two samples; one grown with natural abundance source gases, i.e. 99.9 % ^{14}N, and one doped with ^{15}N. The samples chosen were the ones that contained the most intense system of unidentified lines, and were all grown using microwave plasma CVD. Experiments showed that only samples that contained nitrogen, e.g. N_S^0 and N^+, showed the new system of lines. At the time this was positive identification that the new defect contained nitrogen. The list of samples in Appendix 1 shows how all the samples that contain this new series of lines also contain nitrogen.

Sample 8 is a ^{15}N-doped sample that showed the highest intensity transitions from the unidentified defect(s). A sample doped with ^{15}N was chosen as the main source for identifying the new system of lines, because of the simplicity of the spectra obtained from such samples (e.g. figure 5.1(a)). For example, the hyperfine interaction would be simplified and there would be no quadrupole interaction, as this only applies to a nucleus with a spin either equal to or larger than 1 (^{15}N has I = $^1/_2$). The overall spectrum obtained from a sample doped with ^{15}N is also much simpler than that obtained from a ^{14}N doped sample, in that the main N_S^0 spectrum consists of only two lines compared to the three line pattern arising from the spin 1 ^{14}N nucleus, figure 5.1(b).

The angular variation EPR experiments were carried out using the Bruker ER200D X-band spectrometer, which runs at a frequency of approximately 9.5 GHz at room temperature. The cavity used for the measurements was the Bruker TE_{104} cavity.

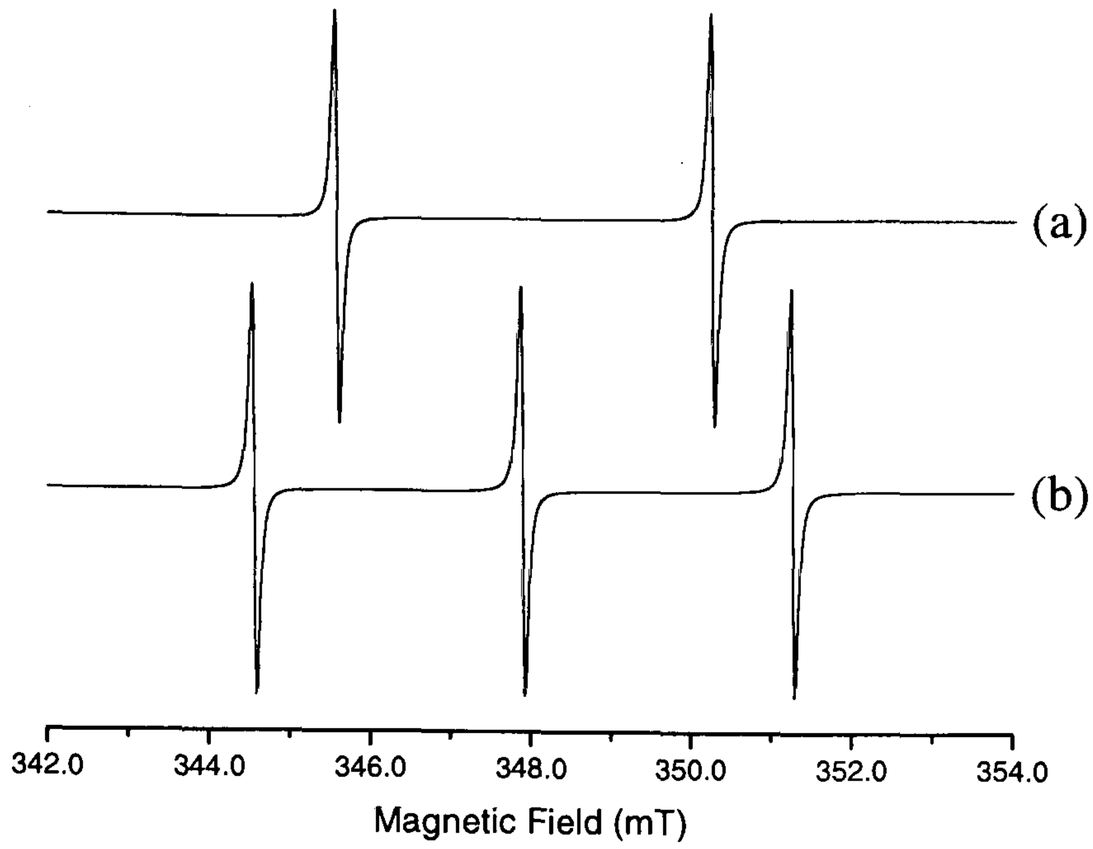

Figure 5.1(a)-(b): Difference in spectra between (a) a ^{15}N and (b) a ^{14}N doped sample. It is easy to see how the ^{15}N doped sample is clear in the central region to allow a better study of the new system of lines. Simulations were created using a microwave frequency of 9.75 GHz.

5.4 ^{14}N doped CVD diamond

As mentioned in section 5.2, Damian Hunt was the first person to report on the new system of lines observed. The main problem he had was noticed quite early on. The sample he used had been grown using natural abundance source gases, which meant it had a very large central peak arising from the $^{14}N_s^0$, figure 5.2a. Figure 5.2a clearly shows the characteristic three line pattern arising from the spin 1 ^{14}N nucleus in $^{14}N_S^0$, and figure 5.2b shows how the central line overlaps with the system of lines, therefore hiding its structure.

Figures 5.2(c)-(f) show the spectra recorded with the magnetic field orientated along the [111] and the [110] directions. It is clearly seen that the spectra become rather complicated as the sample is rotated away from [001], with many lines visible, which may or may not belong to the new defect. Each spectra shows how the central line belonging to the single substitutional nitrogen overlaps with the new system of lines. Associated with the N_S^0 spectrum are the characteristic ^{13}C hyperfine satellites that are observed due to the natural abundance of 1.1 % of the carbon atoms being ^{13}C. ^{13}C has an extra neutron and so is detected using EPR. The satellite lines are mixed up with the lines of interest will be approached in more detail in section 5.5.1.

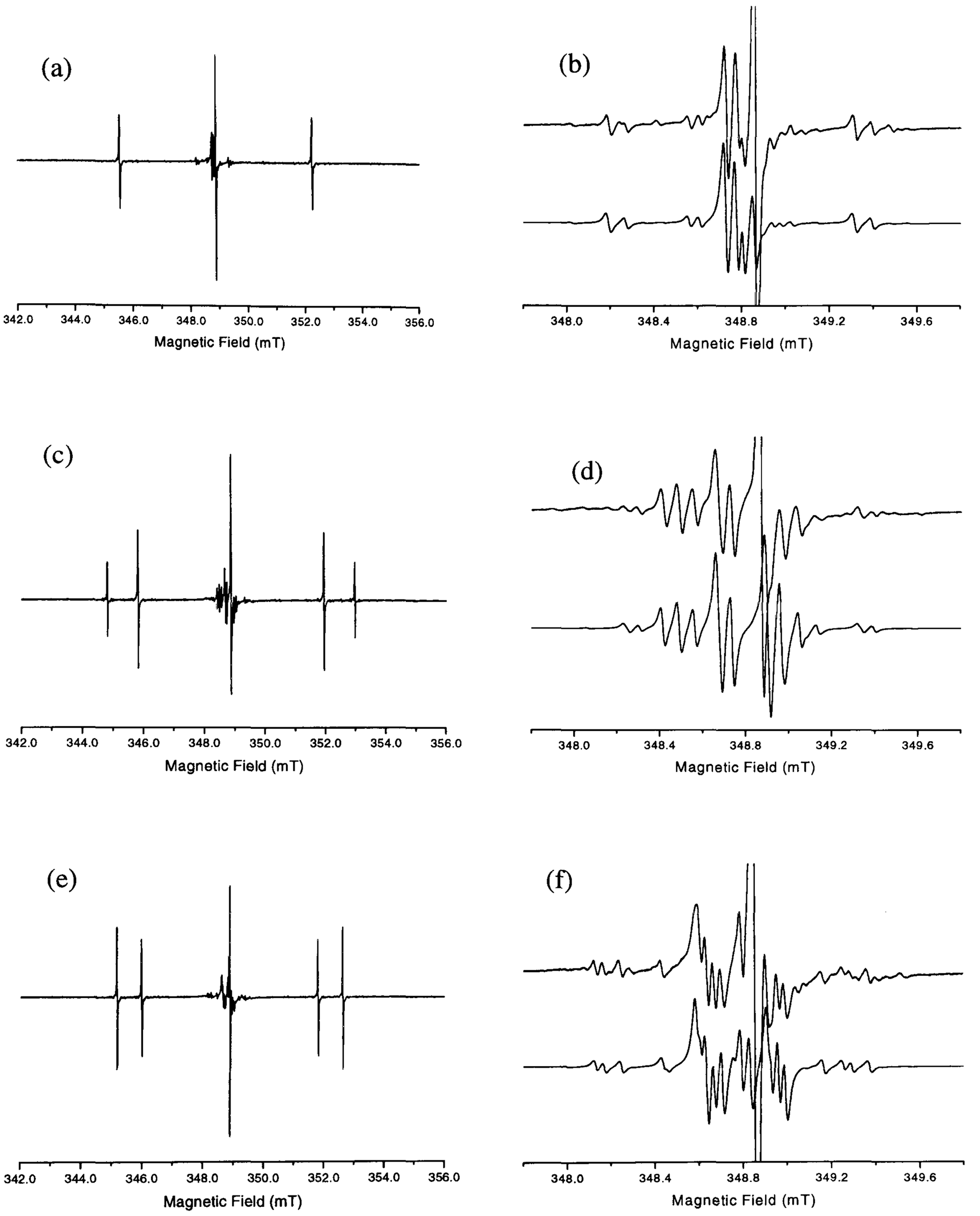

Figure 5.2(a)-(f): Room temperature EPR spectra showing the magnetic field orientated along the three principal directions. Data taken on a ^{14}N doped sample containing the new system of lines. 5.2(a), (c) and (e) show the wide scans for the [001], [111] and [110] directions respectively, and (b), (d) and (f) show zoomed in spectra of the central region in the same respective directions. In each zoomed in spectra, the top spectrum is the experimental data, and the bottom one shows a simulation of the EPR spectra for the NVH^- defect; the parameters and model for this defect are determined later in this chapter. Measurements were recorded using a microwave frequency of about 9.75 GHz.

5.5 ^{15}N doped CVD diamond

The difficulties in identifying the defect using only samples doped with ^{14}N were made apparent at the beginning of the previous section. The ^{15}N doped samples made the investigations much easier as the two-line EPR pattern produced from $^{15}N_S^0$ has no central line interfering with the new system of lines, figure 5.4(a). It is worth noting, however, that although the samples have been doped with ^{15}N, they do still contain a small amount of ^{14}N (~10%). This means that there will still be a small contribution from the ^{14}N to the lines in the centre of the spectrum. The EPR spectra obtained when the sample was positioned with the magnetic field orientated along the [111] and the [110] directions are shown in figures 5.4(c)-(f)

From the principal directions alone however, it is very difficult to fully understand what is happening with each of the lines. In order to achieve this, a full angular variation was carried out. This involved rotating the sample from [001] to [110], in a (110) plane. The shape of the roadmap produced gives a clear indication of the symmetry of the defect being studied, figure 5.3.

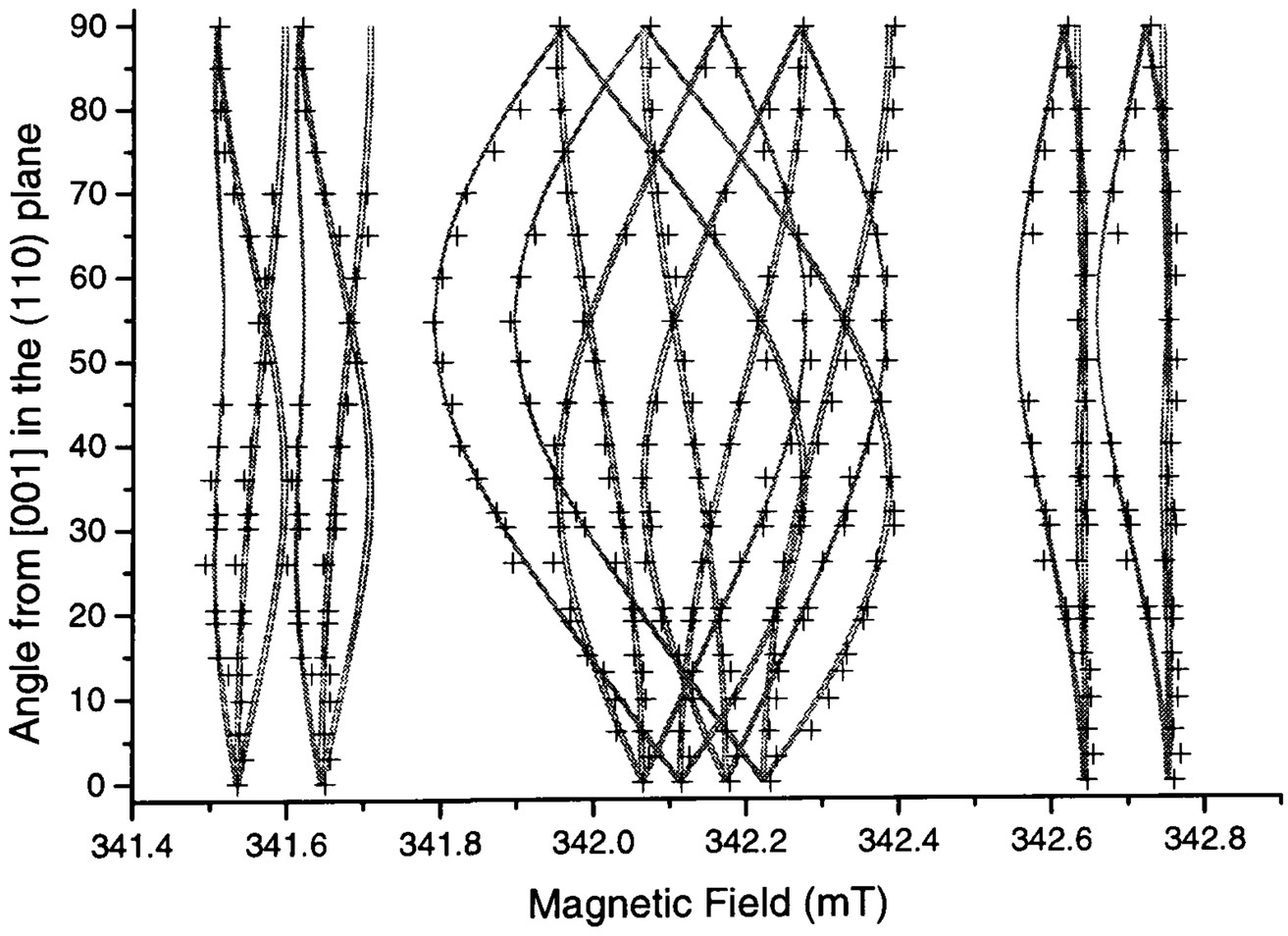

Figure 5.3: Angular dependence of the ^{15}N EPR transitions from the new system of lines for rotation about the [110] axis, starting at [001], in the (110) plane. The crosses are the experimental line positions taken at room temperature at a microwave frequency of about 9.7 GHz, and the solid grey line is the simulated angular variation determined from fitting the experimental data using EPR NMR with the calculated spin Hamiltonian parameters, see section 5.5.1.

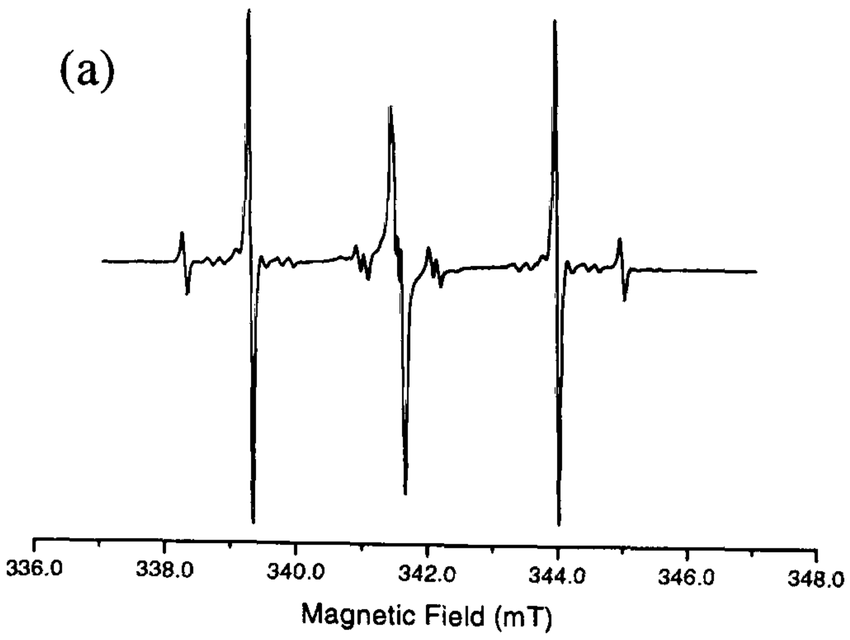

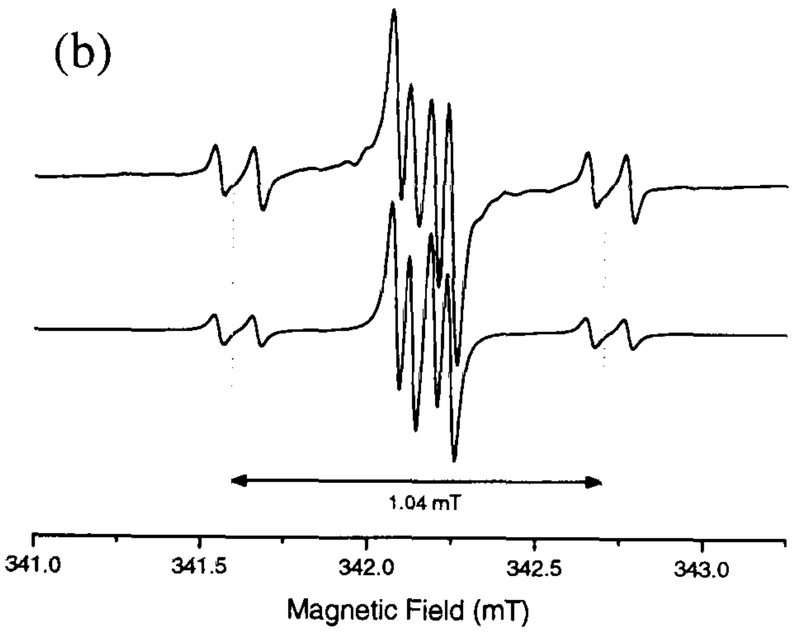

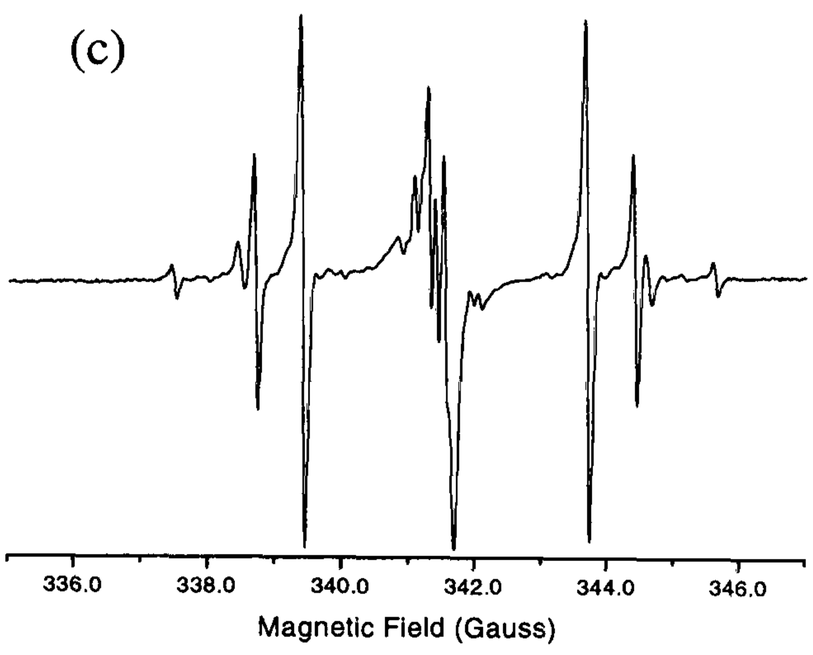

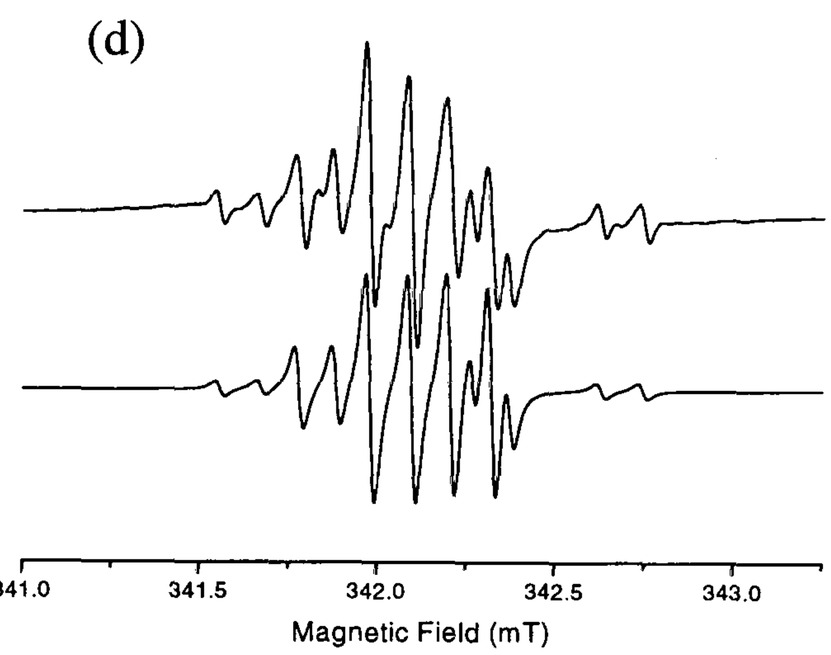

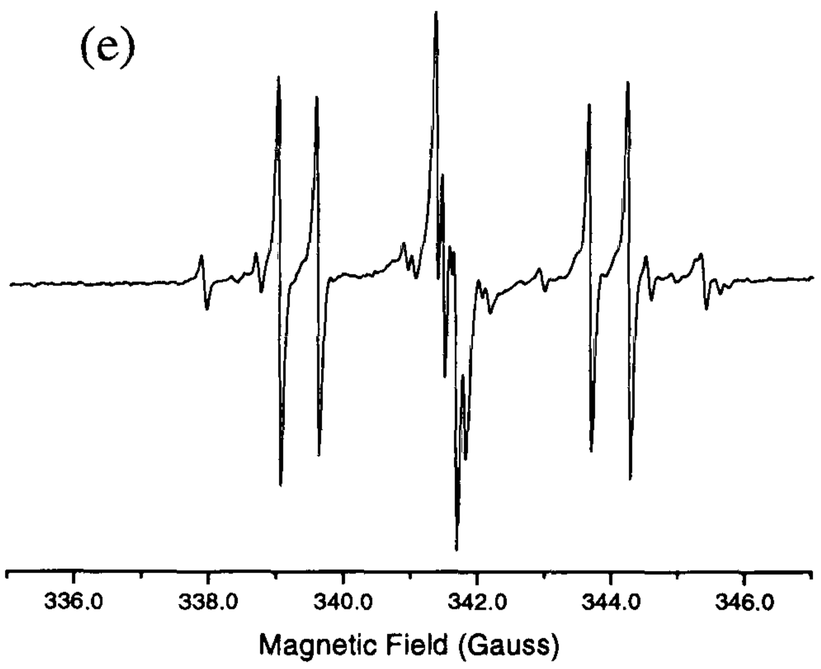

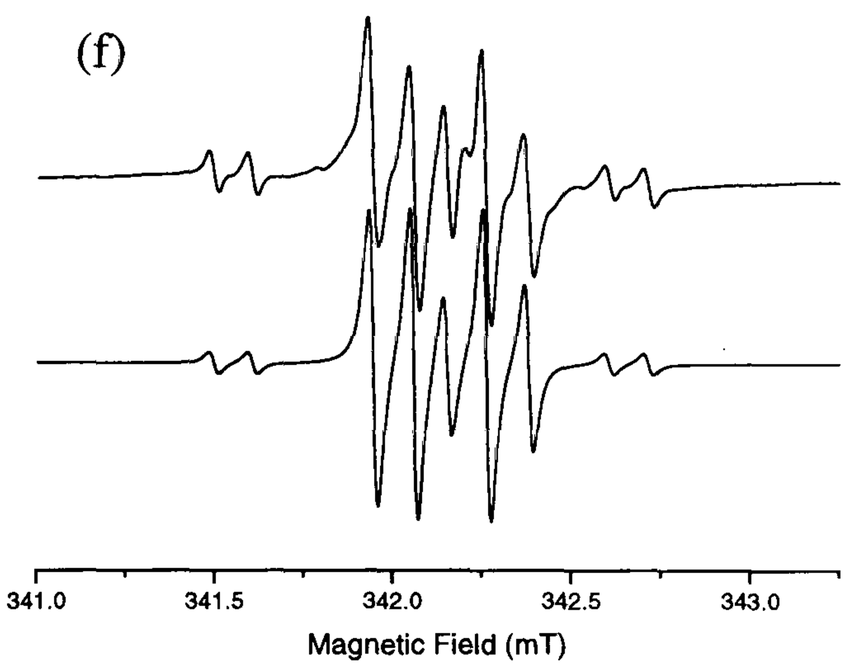

Figure 5.4(a)-(f): Room temperature EPR spectra showing the magnetic field orientated along the three principal directions. Data taken on a ^{15}N doped sample containing the new system of lines. 5.4(a), (c) and (e) show the wide scans for the [001], [111] and [110] directions respectively, and (b), (d) and (f) show zoomed in spectra of the central region in the same respective directions. In each zoomed in spectra, the top spectrum is the experimental data, and the bottom one shows a simulation of the EPR spectra for the NVH^- defect; the parameters and model for this defect are determined later in this chapter. Measurements were recorded using a microwave frequency of about 9.75 GHz.

5.6 Discussion

5.6.1 ^{15}N doped samples

The identification of the NVH^- defect was made much easier by the data obtained from the ^{15}N doped sample. For this reason, this data will be discussed in some detail before the ^{14}N data. The analysis starts with the assumption that all of the lines observed in figures 5.4(b), (d) and (f), with the exception of any overlapping features associated with N_S^0, originate from the same defect.

Referring back to figure 5.4(b) the simplest spectrum obtained for the series of lines can be seen. The magnetic field is aligned parallel to the [001] direction and the spectrum consists of a central region of four lines, with a pair of satellites either side. It is the pair of satellites at either side that draws the initial attention, because the difference in field between the two pairs of lines is 1.04(1) mT, which is twice the nuclear Zeeman frequency of a proton in the average field of the two pairs of lines [5.2]. This shows that these lines arise from the forbidden electron-proton double spin flip transitions, which proves that there is hydrogen present in the defect.

If it were only hydrogen causing the splitting of these lines however, only one pair of lines would be expected in the central region. The fact that four lines are observed, i.e. two pairs, indicates the presence of another spin ½ nucleus. The obvious candidate for this is ^{15}N as this sample has been specially doped and the ^{15}N is 90% abundant. ^{13}C can be ruled out as it is only 1.1% abundant and if it were another proton involved the pattern observed could not be obtained. Thus, the four-line pattern in the centre is explained by the presence of two in-equivalent spin ½ nuclei. These are the allowed transitions, which are split by the hyperfine interactions of both the ^1H and the ^{15}N.

The spectra showing the principal directions of the defect, figures 5.4(a)-(f), show how complicated the pattern becomes once the sample is rotated away from the 001 direction, and figure 5.3 gives the full angular variation which was carried out on the sample in the (110) plane, rotating it from [001] to [110]. As soon as the sample was rotated, the lines started to split, move and cross over each other. It quickly became very difficult to follow what was happening.

To be able to simulate the behaviour of the spectra, the experimentally determined positions of the EPR transitions had to be fitted to equation 5.1. The defect was simulated by assuming the following:

- $S = ½$. This assumption was checked by searching for half field transitions related to the same defect. Half field transitions are only present for defects with $S \geq 1$, hence this assumption is correct.
- The defect contains one hydrogen atom and one nitrogen atom.
- The defect has C_{3v} symmetry. This information was obtained from the roadmap and indicates that the ^1H and the ^{15}N lie along a $\langle 111 \rangle$ axis.

$$H = \mu_B \boldsymbol{B}.\underline{\boldsymbol{g}}.\boldsymbol{S} + \sum_i \boldsymbol{S}.\underline{\boldsymbol{A}}_i.\boldsymbol{I}_i - \sum_i g_N \mu_N \boldsymbol{B}.\boldsymbol{I}_I \qquad (5.1)$$

where each term has its usual meaning (section 3.2). From this spin Hamiltonian, the g-value, the ^{15}N hyperfine matrix and the proton hyperfine matrix could be determined, table 5.1. The Hamiltonian is not as simple for the ^{14}N samples as more terms need to be added. This will be discussed in more detail in the next section of the chapter. Simulations can be created using the parameters listed in table 5.1. These can be fitted and compared to the experimental data to check not only the line positions, but also the relative intensities. Figures 5.4(b), (d) and (f) compare the simulations with the experimental data.

$S = {}^1/_2$	
$g_{\parallel} = 2.0034(1) \parallel \langle 111 \rangle$	$g_{\perp} = 2.0030(1)$
^1H $A_{\parallel} = 13.69\ (20)$ MHz $\langle 111 \rangle$	$A_{\perp} = -9.05\ (20)$ MHz
^{15}N $A_{\parallel} = 2.94\ (10)$ MHz $\langle 111 \rangle$	$A_{\perp} = 3.30\ (10)$ MHz

Table 5.1: Room temperature spin Hamiltonian parameters calculated for NVH^- for a ^{15}N doped sample. The simulations created using these parameters are shown on figures 5.4(b), (d) and (f).

5.6.2 ^{14}N doped samples

Having successfully simulated the spectra in the ^{15}N-doped sample, the spectra in the ^{14}N samples need to be considered. It was immediately assumed that the group of lines observed in the ^{14}N doped sample originated from the same defect identified in the ^{15}N doped sample. As mentioned before, the system of transitions being studied is found within 1 mT of the central transition of the N_s^0 centre, which means that much of the structure is

obscured, and not all of the lines observed in the ^{14}N spectrum originate from the defect of interest. Figure 5.5 compares the EPR spectrum from a diamond grown by CVD containing the new defect with a spectrum from a diamond grown by HPHT methods. The HPHT diamond only contains the single substitutional nitrogen centre (N_S^0), for which ^{13}C associated hyperfine satellites are clearly visible. As figure 5.5 shows, the ^{13}C satellites overlap with the lines arising from the new defect, making identification of the defect very difficult. By holding with the assumption that the defects observed in the two samples are identical, most of the parameters can be calculated for the ^{14}N defect from the ^{15}N data. This is done by using the same g-values and proton hyperfine matrix, but using the ratio of the nuclear g-values (g^{14}_N/g^{15}_N), to calculate the expected ^{14}N hyperfine matrix from the ^{15}N parameters.

The fact that ^{14}N has a nuclear spin of 1 means that there is a quadrupole interaction associated with it. This introduces an extra term in equation (5.1), and the spin Hamiltonian required for the ^{14}N version of the defect is given in equation 5.2.

$$H = \mu_B \boldsymbol{B}.\underline{\boldsymbol{g}}.\boldsymbol{S} + \sum_i \boldsymbol{S}.\underline{\boldsymbol{A}}_i.\boldsymbol{I}_i - \sum_i g_N \mu_N \boldsymbol{B}.\boldsymbol{I}_i + \sum_i \boldsymbol{I}_i.\boldsymbol{P}_i.\boldsymbol{I}_i \qquad (5.2)$$

where each term has its usual meaning and the last term represents the quadrupole interaction, which appears only for nuclei with $I > ½$.

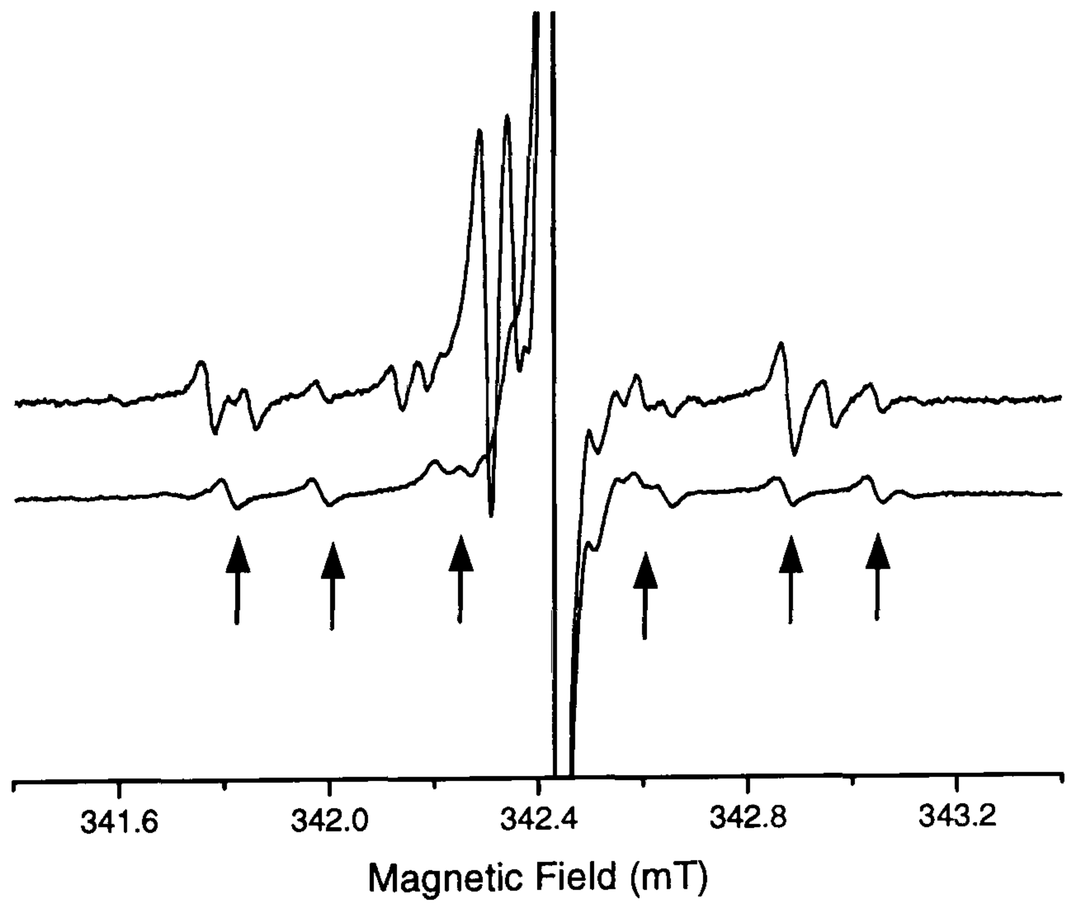

Figure 5.5: A ^{14}N-doped CVD sample containing the new system of lines (top spectrum), compared with the spectrum taken from an HPHT sample, which contains only $^{14}N_s^0$. The outer lines in the HPHT spectrum are the ^{13}C hyperfine satellites, shown in each case by the arrows. The spectra were recorded using a microwave frequency of approximately 9.5 GHz and at room temperature.

The quadrupole interaction was calculated by simulating the EPR spectra while each time just allowing the magnitude of $P_{||}$ to vary. The quadrupole interaction was assumed to be axially symmetric with its principal axis along the $\langle 111 \rangle$ C_{3v} axis, and as figure 5.6 shows, it has a significant effect on the overall shape of the spectra.

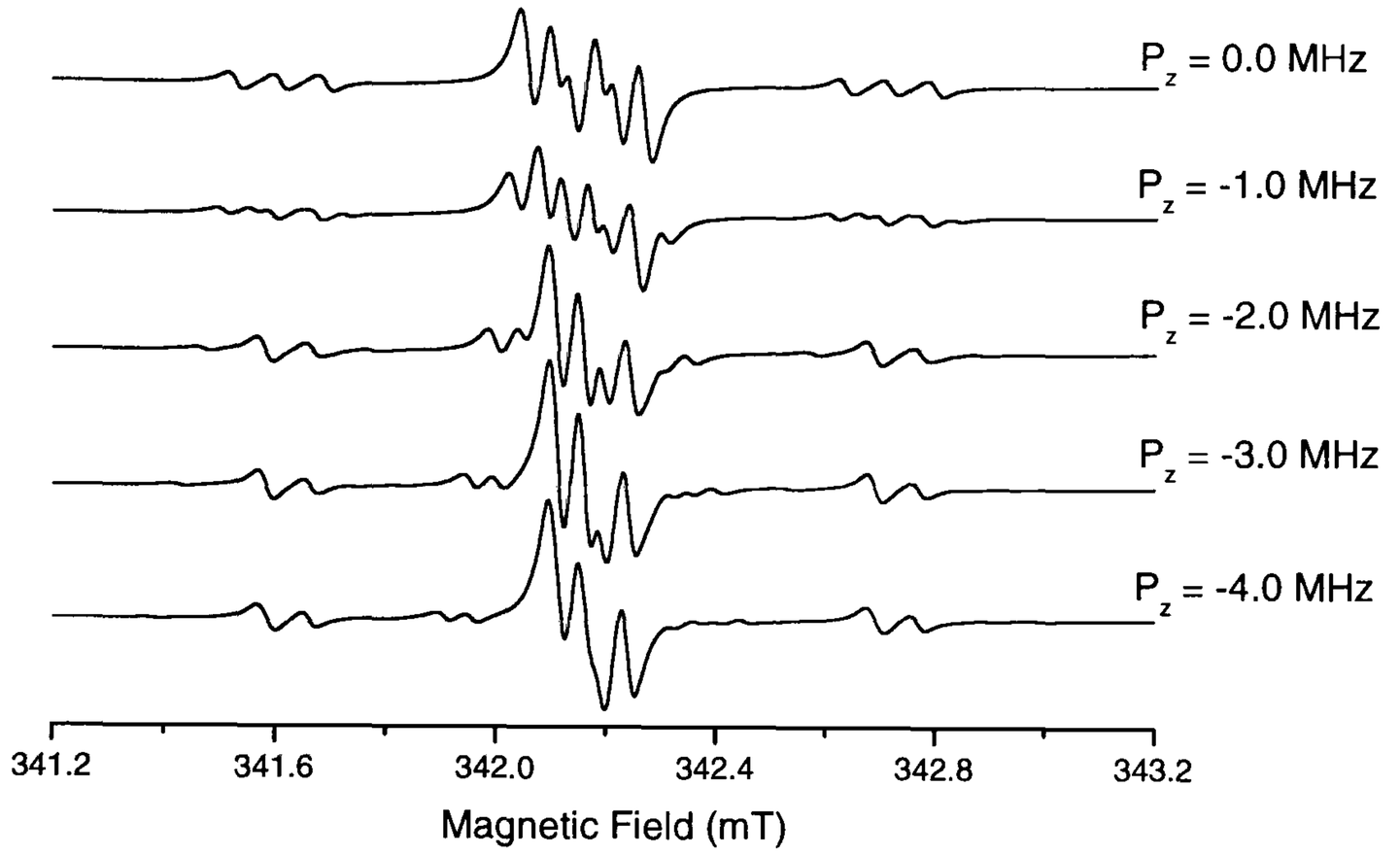

Figure 5.6: The effect of the quadrupole interaction on the shape of the spectrum. As it can be seen, it has a significant effect and changes the shape of the spectrum quite dramatically. When the term is equal to zero, the three-line pattern arising from the spin 1 nucleus can easily be seen. The simulation has been created using an overall spin of ½, and incorporating a spin ½ proton and a spin 1 ^{14}N nucleus. $P_{||} = {}^3/_2 P_Z$.

The quadrupole interaction obtained proved to be large and the experimental data could be simulated using this value with the other, already calculated, spin Hamiltonian parameters. The fact that all the parameters calculated before, used with the newly found quadrupole interaction, were able to produce an accurate simulation, proved that the defects observed in both the ^{14}N and ^{15}N doped samples were identical and could be explained by one defect. Table 5.2 gives a complete listing of all the spin Hamiltonian parameters used to describe this defect.

$g_{\parallel} = 2.0034(1)$ $\parallel \langle 111 \rangle$	$g_{\perp} = 2.0030(1)$
^{1}H $\lvert A_{\parallel} \rvert = 13.69\ (20)$ MHz $\langle 111 \rangle$	$\lvert A_{\perp} \rvert = 9.05\ (20)$ MHz
^{15}N $A_{\parallel} = 2.94\ (10)$ MHz $\langle 111 \rangle$	$A_{\perp} = 3.30\ (10)$ MHz
^{14}N $A_{\parallel} = -2.09\ (10)$ MHz $\langle 111 \rangle$ $P_{\parallel} = -4.8\ (1)$ MHz	$A_{\perp} = -2.36\ (10)$ MHz

Table 5.2: Table showing the final room temperature spin Hamiltonian parameters for the new defect.

Using the calculated parameters, simulations could be made for the experimental data. Figure 5.2 shows how the simulations fit to the data in the ^{14}N-doped sample. From this analysis it has been shown that the large ^{14}N quadrupole interaction together with the overlap from the $^{14}N_s^0$ EPR spectrum had concealed the truth about the nature of this defect in the ^{14}N-doped samples.

5.7 Model for the NVH^- centre

The spin Hamiltonian parameters given in table 5.2 provide a lot of information about the structure of the defect, all of which has been presented in [5.3]. The first piece of information obtained from the experiment is the fact that the defect has an overall electron spin of ½. This immediately indicates that there are an odd number of electrons involved in the defect. It has been found from the EPR data that this defect incorporates a single proton and a single nitrogen atom. This has been proved by the fact that simulations have been produced to accurately fit the data using parameters determined for nitrogen and hydrogen. In order to preserve the C_{3v} symmetry observed from the roadmap, these two atoms must lie on the $\langle 111 \rangle$ symmetry axis of the defect.

To be able to fully consider the model of this defect, each individual spin Hamiltonian parameter should be considered separately. The first thing to notice from all the values is that they all have axial symmetry about the $\langle 111 \rangle$ axis. Considering the numerical values of $g_{\parallel}$ and $g_{\perp}$, it is seen that it has very small anisotropy, which is consistent with the localisation of the unpaired electron in carbon dangling orbitals.

The isotropic component of the proton hyperfine matrix is small, which is consistent with negligible localisation of the unpaired electron on the hydrogen atom. The anisotropic component must therefore originate from a dipole-dipole interaction. A dipole-dipole calculation can be performed and the separation between the proton and the unpaired electron calculated, see section 3.4, equation (3.27). This will be discussed in more detail shortly.

Considering the nitrogen hyperfine splitting, it is observed that for both the ^{14}N and ^{15}N doped samples, the symmetry axis of the defect is again along the ⟨111⟩ direction, the same as both the g-tensor and the proton hyperfine splitting. The actual values of the hyperfine splittings are very small and are similar to those for the NV^- centre [5.4], which has ^{14}N hyperfine values of $A_{\|} = -2.17(3)$ MHz and $A_{\perp} = -2.81$ (3) MHz, and ^{15}N hyperfine values of $A_{\|} = 3.15$ (5) MHz and $A_{\perp} = 3.85$ (5) MHz [5.5]. This indicates negligible unpaired electron probability density on the nitrogen atom [5.6].

The last parameter to be considered is the quadrupole interaction for the ^{14}N nucleus. This is very large and again comparable to that observed for the NV^- centre, which has a value of $P_{\|} = -5.05$ (10) MHz. Baker and Newton [5.7] show that there is a linear relationship between the magnitude of the quadrupole interaction and the unpaired electron probability density on the nitrogen atom. The values obtained for this NVH^- defect fit well to this relationship.

It is known that NV^- centres are incorporated during the growth of CVD diamond, so it is possible that, if a hydrogen atom were trapped within the vacancy of a nitrogen-vacancy centre, a new defect would be formed. If the hydrogen atom were located on the three-fold axis, the defect would have C_{3v} symmetry, agreeing with what is observed. It is assumed, as is the case for the NV^- centre, that the electronic properties are determined by the unpaired electrons localised on the three carbon dangling orbitals. Thus the nitrogen atom in the NVH^- defect has its dangling bond filled with a lone pair of electrons, or is bonded to the hydrogen atom. Either way, the unpaired electrons must be accommodated in the three carbon dangling orbitals.

The charge state of the complex can now be considered. It is known that the defect has an overall spin of ½, which means it must have an odd number of electrons localised in the three carbon dangling orbitals. Considering each charge state separately, NVH^0 can immediately be ruled out. This is because an NVH centre with no overall charge would have an overall spin of either 0 or 1, neither of which fulfils the criteria of having an odd number of electrons. A defect with an overall spin of 0 would not be detected by EPR, which again rules out the option of a non-charged defect. This leaves the defect having a charge of either

+ or –. NVH^+ would have three electrons, resulting in a spin of either $^3/_2$ or ½. However, this is an unlikely charge state for the defect, because N_S^0 would have to act as a donor and there is no acceptor present to gain the extra electron. NVH^- would only be able to have a spin of ½ and is the most likely charge state of the defect. This is also consistent with infrared measurements taken on the samples, which show that $[N_s^+] \approx [NVH^-]$. This indicates the charge transfer reaction $N_s^0 + NVH^0 \rightarrow N_s^+ + NVH^-$ is taking place.

Before the actual model of the defect is considered, the electronic structure of the defect will be discussed [5.8, 5.9, 5.10]. The defect is in the negative charge state, which means there are seven electrons that need to be accommodated. Because of the C_{3v} symmetry, it is known that they will be accommodated in two a levels and an e level, figure 5.7.

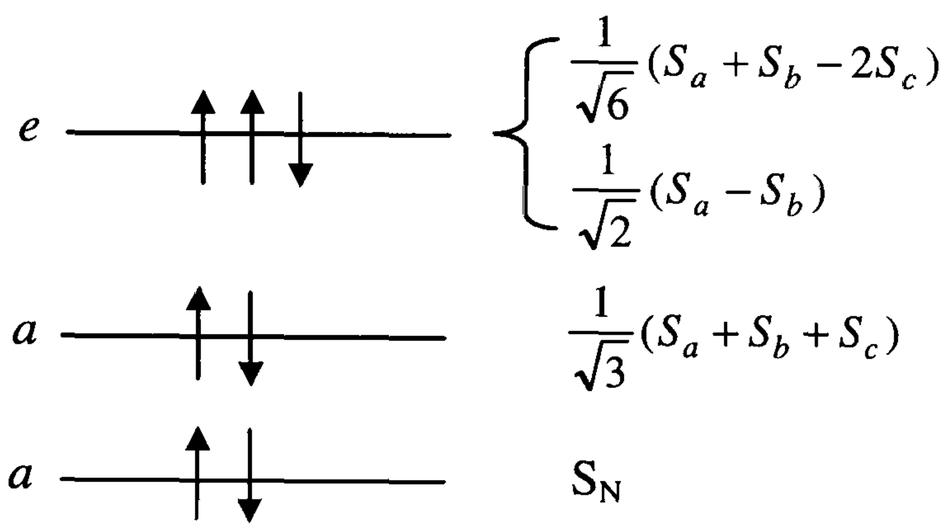

Figure 5.7: Energy level scheme for the ground state of the NVH^- defect.

Having three electrons in the *e* level is the equivalent of having a single hole in the level. Therefore the ground state of the defect can be shown to be a ^2E state. If the situation is considered where an electron is optically excited ($a \rightarrow e$), there will only be a single electron in the *a* level, but the *e* level will be full. This excited state of the defect will be a ^2A state and it is noted that the $^2E \rightarrow {}^2A$ would be an allowed optical transition.

Having discovered the constituents, symmetry, charge state and spin of the defect, an actual model is required. It is important to note that in table 5.2 there is an uncertainty in the sign of the proton hyperfine interaction. Simulations have been created for all possibilities, and have shown to be identical in each case. For this reason, at this stage, it is impossible to know what is the actual sign of each component.

In [5.3], it was shown that the hydrogen hyperfine interaction could be explained using a very simple point dipole calculation and taking $A_{\|}$ as positive and $A_{\perp}$ as negative. In order to get satisfactory agreement between this calculation and the experimentally determined values, several assumptions about delocalisation of the unpaired electron

probability distribution and relaxation of atoms were required. In this thesis, the problem is approached in a more sophisticated manner (an extended dipole calculation).

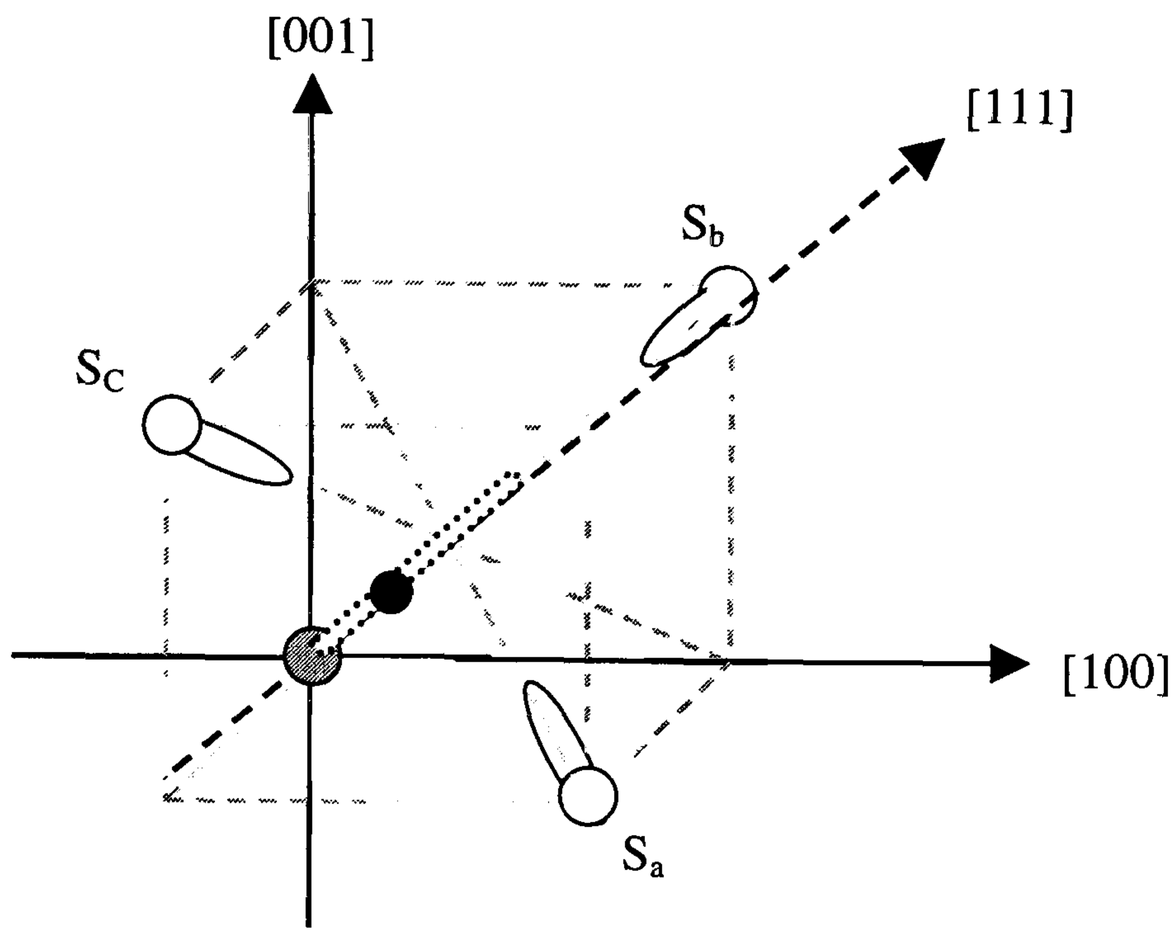

Figure 5.8: The dipolar interaction for the NVH^- defect. The grey atom is the nitrogen atom and the black one is the hydrogen atom.

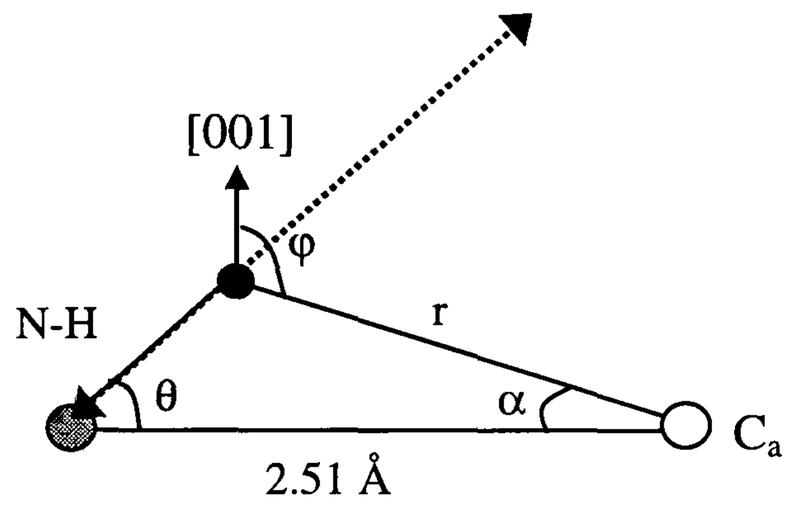

Figure 5.9: Information extracted from figure 5.8 needed to perform the necessary calculations. The hydrogen atom can be bonded anywhere along the dashed line.

This extended dipole calculation allows the hydrogen atom to be located anywhere along the [111] axis, as shown by the dotted line in figures 5.8 and 5.9. It is also assumed that one third of the unpaired electron probability density is localised on each of the three equivalent carbon neighbours. In order to calculate the contribution of the unpaired electron probability density on each carbon atom to the hydrogen hyperfine interaction, the distance r, and the angle φ, must be determined, figure 5.9. The values of r and φ for a range of different nitrogen-hydrogen separations are plotted in figure 5.10.

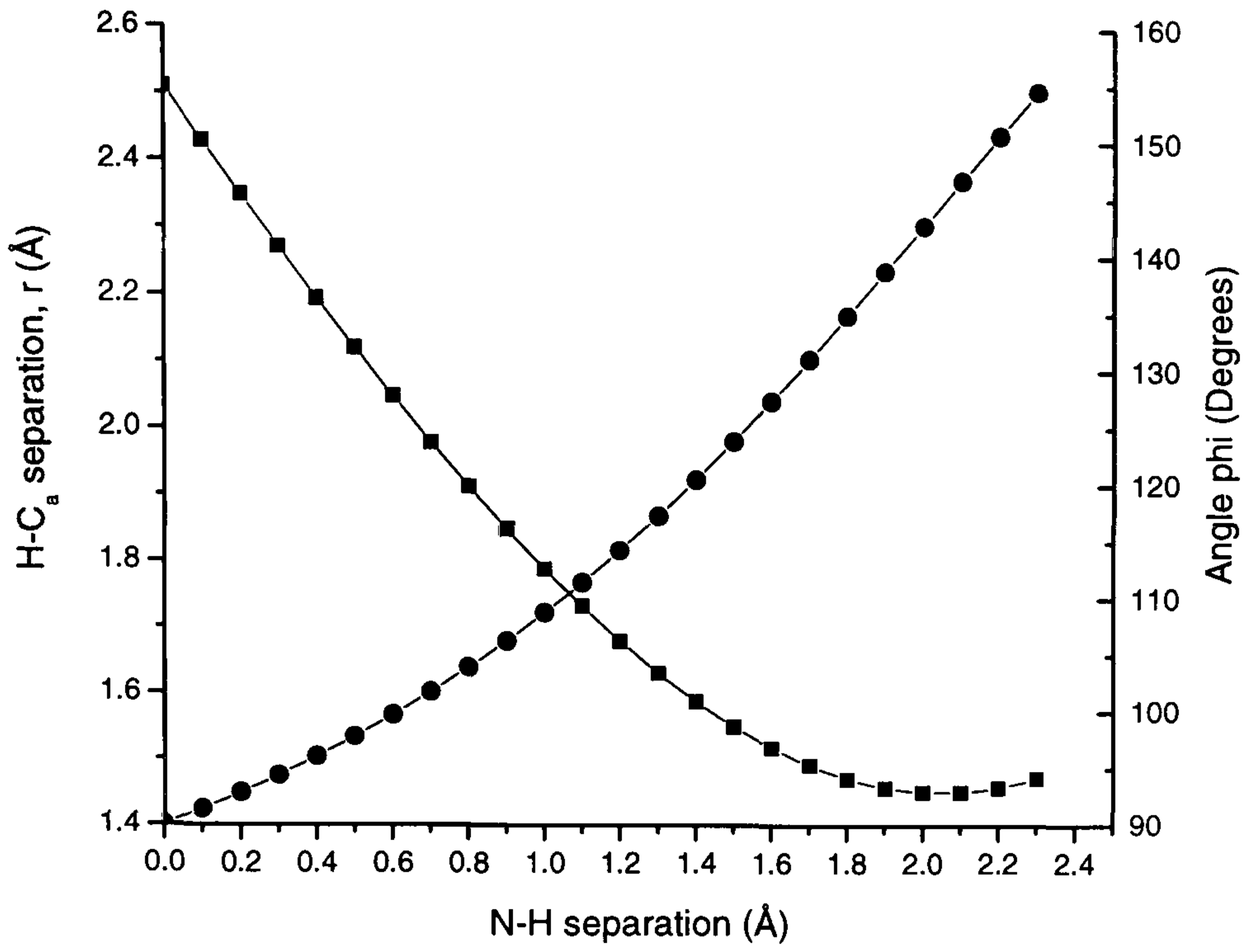

Figure 5.10: Graph showing how, as the distance between the nitrogen and the hydrogen increases, the distance between the hydrogen and one of the carbon atoms decreases and the angle the N-H bond makes with the [001] axis increases. The circles represent the angle r makes with the [001] axis, and the squares represent the H-C separation, r.

The dipolar hyperfine interaction resulting from the three contributions must be calculated by determining the individual hyperfine matrices, transforming these to a common coordinate axis system and then summing the three contributions, as shown in Appendix 4. Diagonalising this matrix produces the theoretical dipolar hyperfine matrix, of the form:

$$A_{aniso} = \begin{pmatrix} -b & 0 & 0 \\ 0 & -b & 0 \\ 0 & 0 & 2b \end{pmatrix}$$

Using this process, the variation of b with nitrogen-hydrogen separation is shown in figure 5.11. The values of r and φ corresponding to this nitrogen-hydrogen separation can be determined from figure 5.10.

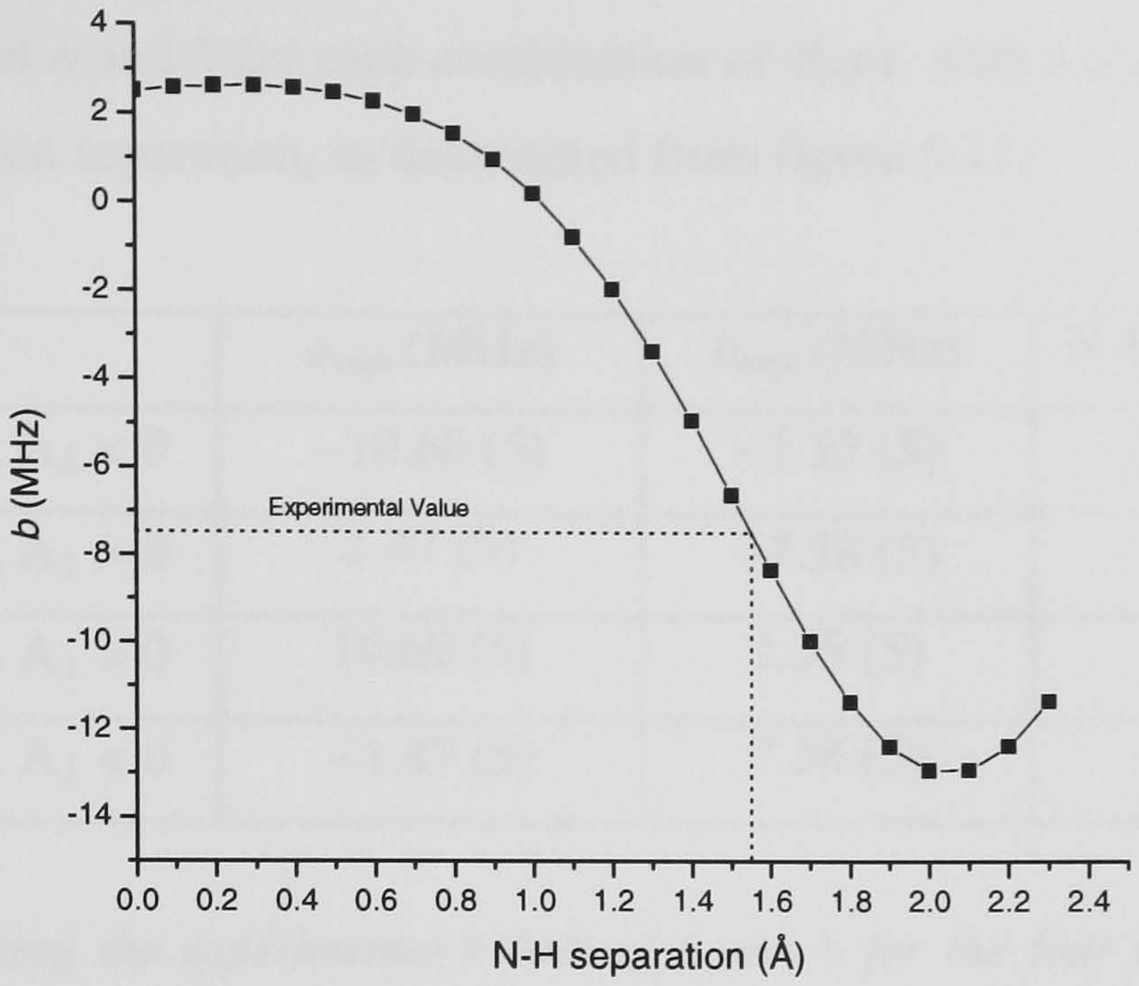

Figure 5.11: A plot showing how the value of b varies with an increase in nitrogen-hydrogen separation.

The proposed model of the defect is shown in figure 5.12.

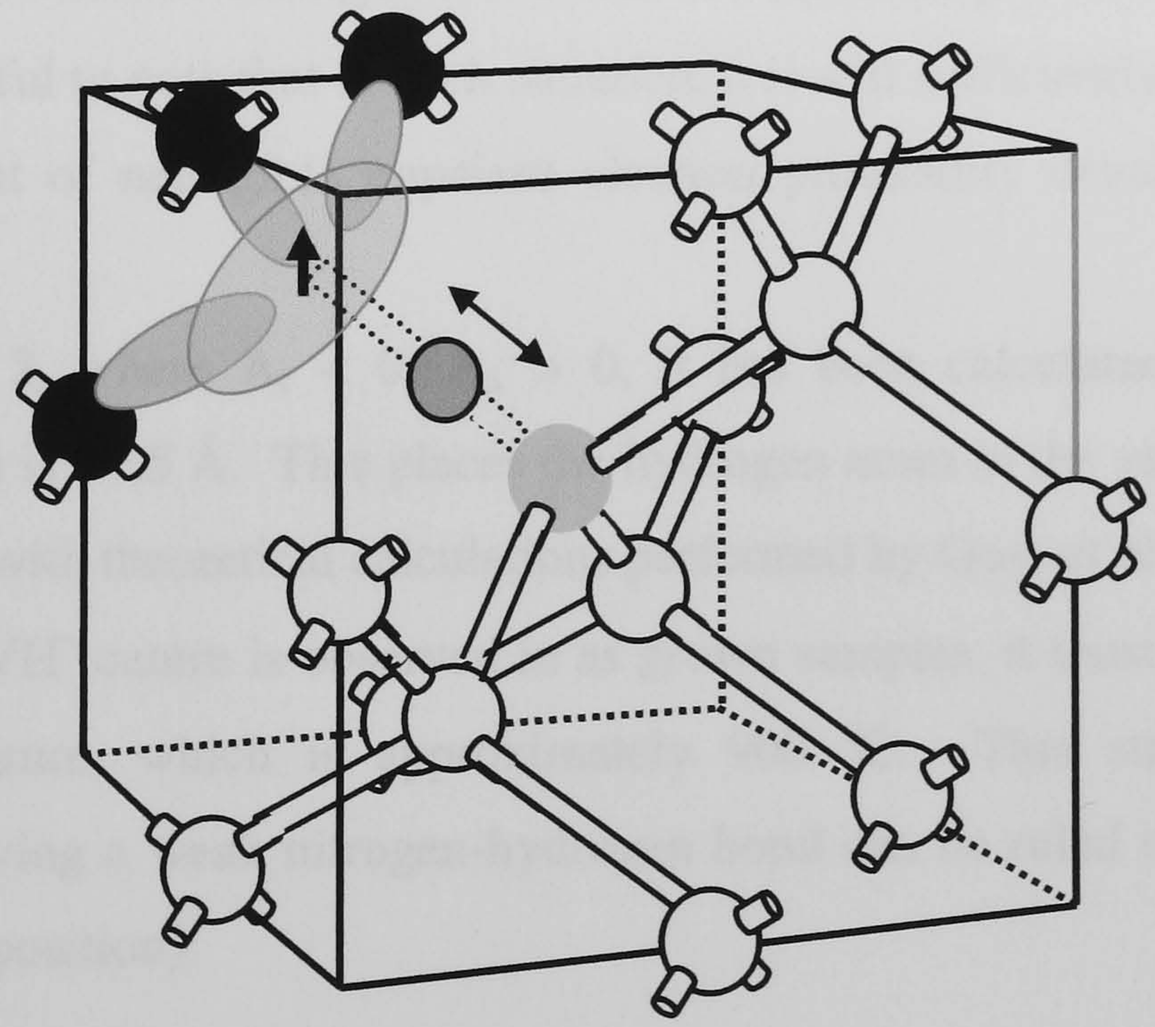

Figure 5.12: Model of the NVH^- defect. The hydrogen atom is bonded somewhere along the [111] axis, as shown by the dotted bond, in order to preserve the C_{3v} symmetry.

As mentioned before, the signs of $A_{\|}$ and $A_{\perp}$ could not be determined. Table 5.3 shows the experimental values of *a* and *b* for each combination of signs, with a corresponding value of the nitrogen – hydrogen separation, as determined from figure 5.11.

		a_{expt} (MHz)	b_{expt} (MHz)	N-H sep. (Å)
1	$A_{\|} < 0, A_{\perp} < 0$	–10.60 (5)	–1.55 (5)	1.17
2	$A_{\|} < 0, A_{\perp} > 0$	1.47 (5)	–7.58 (5)	1.55
3	$A_{\|} > 0, A_{\perp} > 0$	10.60 (5)	1.55 (5)	0.80
4	$A_{\|} > 0, A_{\perp} < 0$	–1.47 (5)	7.58 (5)	--

Table 5.3: Table showing the experimental values of a *and* b *for the four different possible sign combinations of $A_{\|}$ and $A_{\perp}$. For each value of b, a corresponding N-H separation has been determined from figure 5.11. The N-H separation assumes that there is no relaxation involved.*

There are three possibilities (1, 2 and 3) that predict an N-H separation of between 0.8 and 1.55 Å. Relaxation and further delocalisation of the unpaired electron probability density would allow a suitable solution to be determined for the remaining case. This table shows that the model cannot distinguish between the different possibilities for the signs of $A_{\|}$ and $A_{\perp}$. It is useful to note that in each situation, *a* is still sufficiently small to agree with the earlier statement of negligible unpaired electron probability density localised on the hydrogen atom.

In situation 2, where $A_{\|} < 0$, $A_{\perp} > 0$, it has been calculated that the nitrogen-hydrogen separation is ~1.5 Å. This places the hydrogen atom in the vacancy of the defect, which is consistent with theoretical calculations performed by Goss et al [5.11].

Since the NVH^- centre is observed in as grown samples, it must be stable to at least the growth temperature, which is approximately 900 °C. This stability is such that configurations involving a weak nitrogen-hydrogen bond can be ruled out, (for example, H in the back bonding position).

5.8 Polycrystalline Diamond Samples

So far, this defect has been identified and characterised using single crystal CVD diamond samples. The question is, why has it not been observed in polycrystalline diamond samples? The answer is that it could be there but it would be almost impossible to observe.

The problem with polycrystalline diamond samples is the presence of the H1 defect, as described in section 2.5. The EPR spectrum of H1 dominates the g = 2 region in any sample that contains it. Figure 5.13 below shows what NVH^- would be expected to look like in a polycrystalline sample, and how it is completely obscured by the presence of H1, and also by any single substitutional nitrogen that must be present.

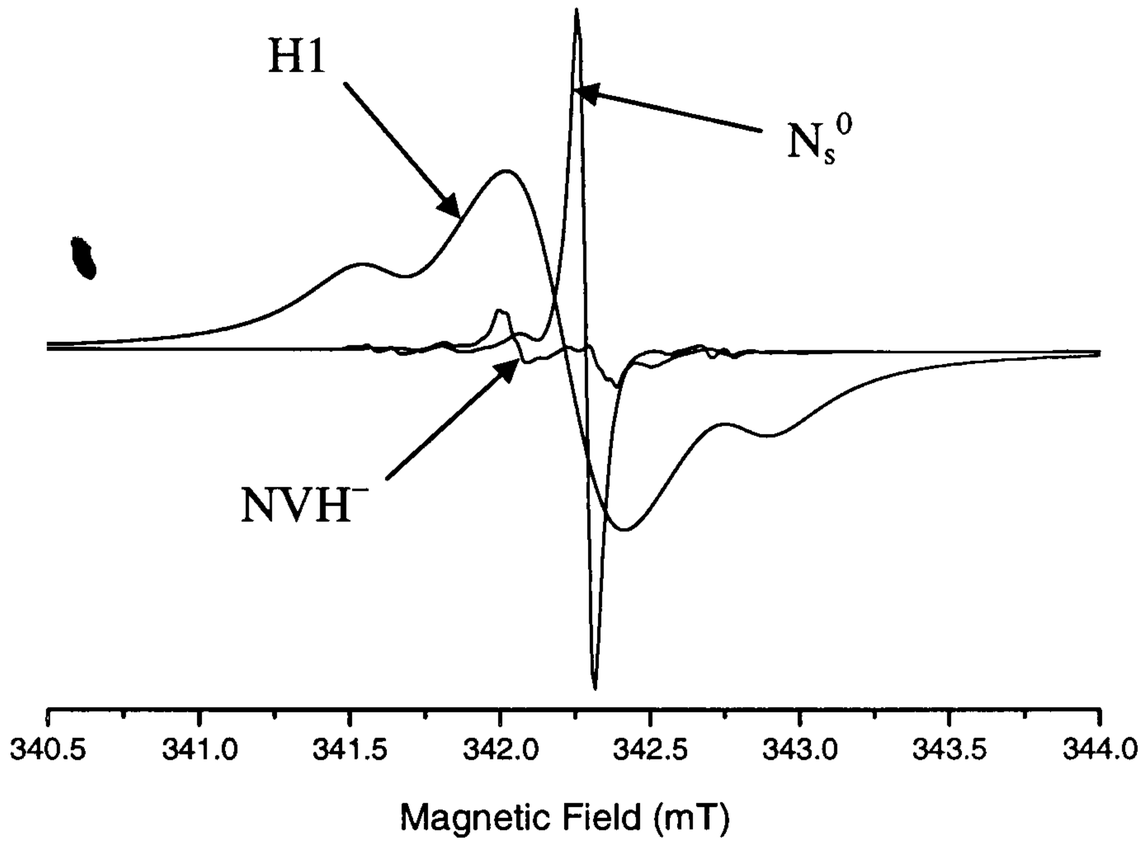

Figure 5.13: Simulated spectrum for the NVH^- defect in polycrystalline diamond samples. It is clear to see how the spectra from both the single substitutional nitrogen and the H1 defect overlap so that the pattern arising from NVH^- cannot be seen at all. The simulations were made at 9.6 GHz.

5.9 Conclusions and Further Work

The following conclusions have been drawn from the experimental results presented in this chapter. The defect has

- an overall electron spin of ½,
- an overall negative charge state,
- C_{3v} symmetry, and
- incorporates a single hydrogen atom and a single nitrogen-vacancy centre.

The hydrogen atom must lie on the [111] axis of the nitrogen-vacancy centre in order to preserve the C_{3v} symmetry, however, the exact position of the hydrogen atom, at this stage, cannot be determined.

Further work can be carried out on this defect to attempt to accurately determine the signs of the hyperfine matrix. This would allow the ambiguity in section 5.7 to be resolved.

Temperature variation experiments would help with this, as changes in the spectra at lower temperature would indicate the freezing in of motional averaging. Such observations would allow it to be determined if the hydrogen is bonded to the nitrogen, or at low temperatures, bonded to one of the three carbon atoms. In the latter case, at high temperatures the effects of motional averaging would be observed and the hydrogen would give the appearance of being shared equally between the three carbon atoms and in the vacancy.

References

[5.1] D. Hunt, D.Phil thesis, University of Oxford (1999)

[5.2] S. L. Holder, L. G. Rowan and J. J. Krebs, Appl. Phys. Lett. **64** (9) (1994)

[5.3] Claire Glover, M. E. Newton, P. Martineau, D. J. Twitchen and J. M. Baker, Phys. Rev. Lett. **90**-18, 185507 (2003)

[5.4] X. F. He, N. B. Manson and P. T. H. Fisk, Phys. Rev. B **47**, 8816 (1993)

[5.5] Modified ^{14}N hyperfine parameters to be presented in Chapter 6 of this thesis

[5.6] J. H. N. Loubser and J. A. van Wyk, Rep. Prog. Phys. 41, 1201 (1978)

[5.7] J. M. Baker and M. E. Newton, Appl. Magn. Reson. **7**, 209-235 (1994)

[5.8] C. A. Coulson and M. J. Kearsley, Proc. Roy. Soc. (Lond.) **A241**, 433 (1957)

[5.9] A. Lanef and S. C. Rand, Phys. Rev. B **53**, 13441 (1996)

[5.10] J. P. Goss, R. Jones, P. R. Briddon, G. Davies, A. T. Collins, A. Mainwood, J. A. van Wyk, J. M. Baker, M. E. Newton, A. M. Stoneham and S. C. Lawson, Phys. Rev. B **56**, 16031 (1997)

[5.11] J. P. Goss, J. Phys.: Condens. Mat. **15**, R551 (2003)

Chapter 6

The negative nitrogen-vacancy centre (NV^-)

6.1 Introduction

Since the discovery of the NV^- defect, it has been extensively studied and as a result it is one of the most well documented defects in diamond. However, new experiments have been carried out and the previously reported spin Hamiltonian parameters, which have been accepted up until this point, have been found to be incorrect. The previous parameters, although widely accepted, did not allow an accurate fit to the accepted model of the defect. Not only will this chapter present the new spin Hamiltonian parameters for NV^-, but will show that they agree with the accepted model.

The chapter will start by reviewing the work previously done on the NV^- defect. It will concentrate on how the defect was initially identified, and how theories have been proved and disproved. It will then present the results from the recent experiments and how the data was used to determine modified spin Hamiltonian parameters.

A problem encountered when carrying out the experiments involved microwave power saturation. This is a problem that has not been documented in the past and so the effects of this are described in some detail in section 6.6.

6.2 Literature Review

The nitrogen-vacancy centre has been observed in two forms, as NV^-, and as NV^0. NV^- has been observed using a variety of experimental techniques, including EPR, optical absorption and photoluminescence (PL). NV^0 has been observed using techniques such as optical absorption, cathodoluminescence (CL) and photoluminescence, but not EPR (section 2.6 lists the relevant references).

The NV^- defect is important because of its optical and EPR activity. Many other defects have been identified using both EPR and optical absorption, but NV^- is particularly important because of its properties. For example, it can be used as a building block for more complicated defects. It can also be used for quantum information processing by acting as a qubit in a quantum computer or in single photon sources [6.1, 6.2, 6.3, 6.4]. No details will be discussed in this chapter, but for further reading, the reader is referred to the references. The structure of the defect consists of a nitrogen atom adjacent to a carbon-vacancy pair, figure 6.1.

The NV^- defect has been observed in as grown CVD diamond samples, which means it can be grown into the diamond lattice as a unit or formed via a vacancy diffusing to N_S^0 during the growth process. Irradiation and subsequent annealing of type Ib diamonds can also create NV^- centres. A good review of the mechanisms surrounding this process is given by Davies et al [6.5]. To summarise this mechanism, the vacancies within the diamond lattice, which have been created by radiation damage (6.1), become mobile when the sample is annealed above about 600°C and are trapped by the single substitutional nitrogen within the lattice, forming NV^0. A subsequent charge transfer reaction takes place with the residual N_S^0 centres to give rise to the NV^- charge state (6.2), [6.6].

$$N_s^0 + V^0 \rightarrow NV^0 \qquad (6.1)$$

$$NV^0 + N_s^0 \rightarrow NV^- + N_s^+ \qquad (6.2)$$

The NV^- optical centre was first discovered in 1965 by du Preez [6.7], where it was named as the 1.945eV absorption line (637 nm). Since then, a vast amount of work has been carried out on this defect and hundreds of papers have been written. It is impossible to cover everything in this literature review, but the important information will be reported.

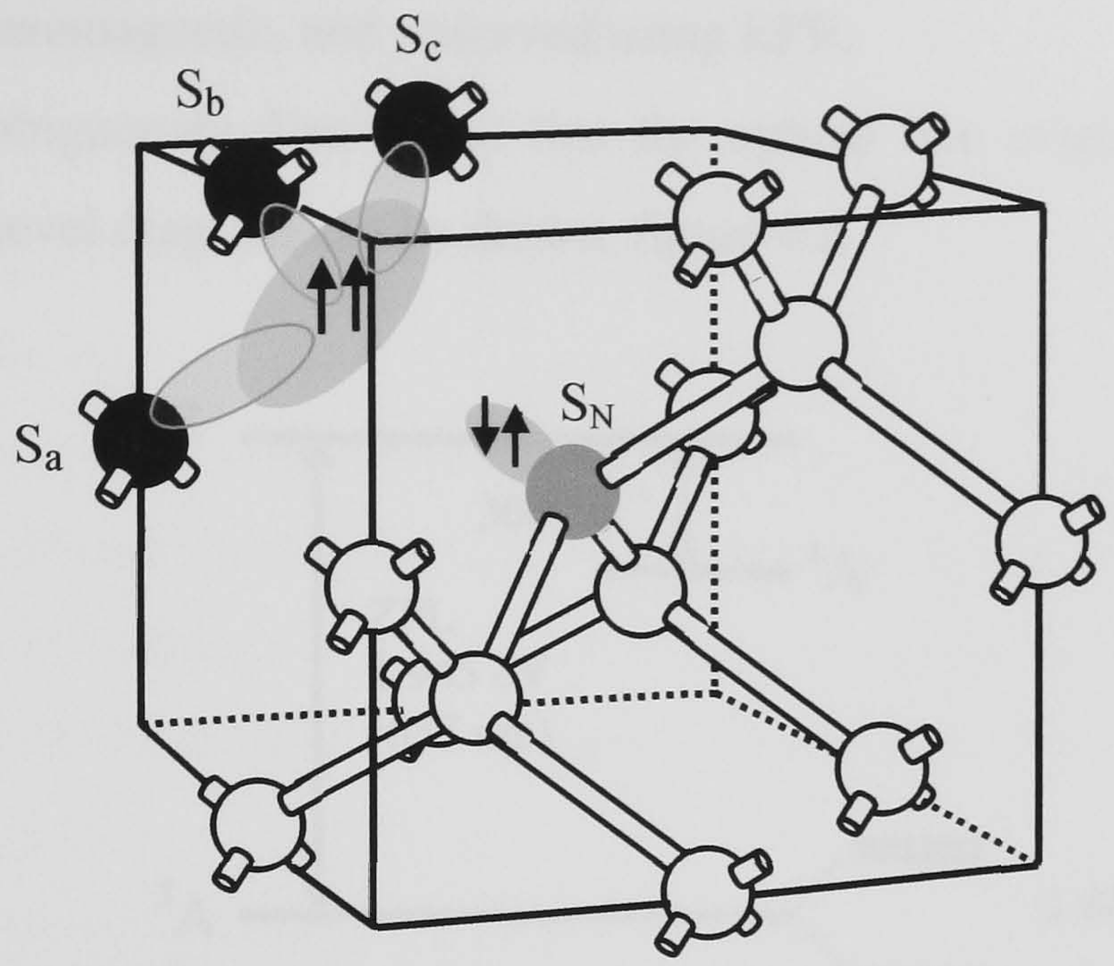

Figure 6.1: Structure of the nitrogen-vacancy centre in diamond. The black atoms are the carbon atoms on which the unpaired electrons are localised, and the grey atom is the nitrogen.

In 1976, Davies and Hamer [6.8] performed uniaxial stress measurements on the 1.945 eV absorption band and showed that it originated from a transition between an A ground state and an E excited state of a trigonal centre. Annealing experiments were carried out and the defect responsible for the 1.945 eV absorption was identified tentatively as a nitrogen-vacancy (N-V) centre.

Following the work by Davies and Hamer, in 1977 Loubser and Van Wyk went on to observe what they believed were the EPR transitions arising from the N-V centre, [6.9]. They observed a triplet state that had C_{3v} symmetry with four related sites with a zero-field splitting of 2.88 GHz, which was consistent with what Davies and Hamer had found. However, because Loubser and Van Wyk were only able to observe the EPR transitions when the sample had been optically illuminated, they believed that the signal originated from an excited, long-lived state.

Two-laser hole burning measurements were carried out by Reddy, Manson and Krausz [6.10], and from these experiments it was suggested that the N-V centre had a ^3A ground state. Various measurements using spin coherence [6.9, 6.11], cross-relaxation [6.12], Raman heterodyne [6.13, 6.14, 6.15, 6.16, 6.17], and four-wave mixing techniques [6.18] also showed this. It was, however, experiments carried out by Redman et al [6.18], which showed that the EPR transition associated with the nitrogen vacancy-centre could in fact be observed without optical illumination. Temperature dependence experiments were then performed and it was observed that the N-V centre could be seen at low temperatures.

These two pieces of information resulted in the conclusion that it is the ground state of the defect that is in fact paramagnetic, and observed using EPR.

Having unambiguously determined that the optical line originates from a $^3A \rightarrow ^3E$ transition, an energy level diagram can be drawn, figure 6.2.

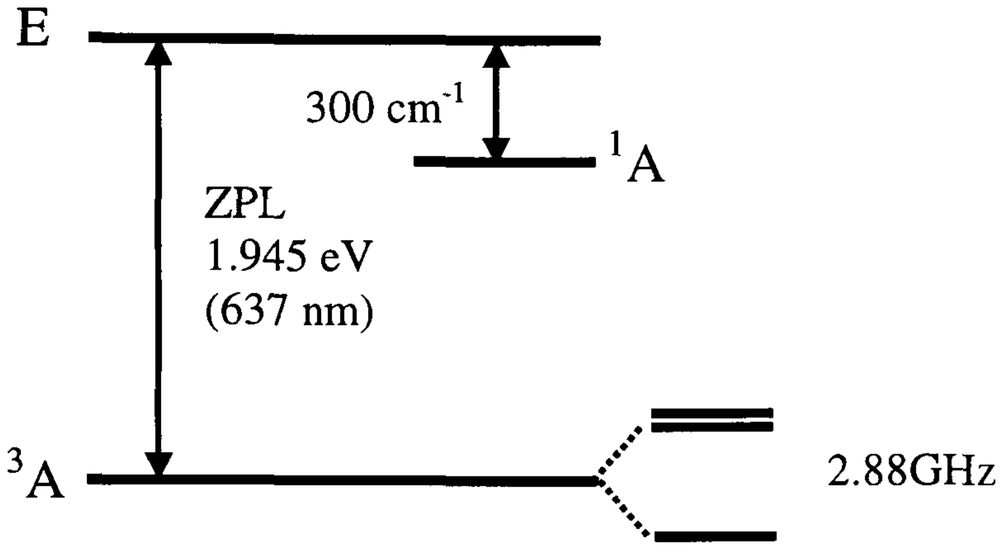

Figure 6.2: Schematic representation of the energy level scheme of the nitrogen-vacancy centre.

From this diagram, it is possible to see the ^3A ground state splitting by the zero- field splitting into a doublet and a singlet separated by |D| = 2.88 GHz at zero field, as originally shown by Loubser and Van Wyk in 1977 [6.9]. It has been determined from the nitrogen hyperfine parameters that there is negligible unpaired electron probability density on the nitrogen atom, and the unpaired electrons are instead localised on the three neighbouring carbon dangling orbitals [6.9, 6.25].

The charge state of NV^- was originally determined using heavy neutron irradiation experiments [6.19]. It was observed that a heavy dose of neutron irradiation caused the NV centre at 1945 meV to suddenly decrease in intensity at the same rate as the intensity of the NV centre found at 2156 meV was increased. This was interpreted as a change in the charge state of the defects. At a sufficiently low irradiation dose, there is an excess of N_S^0 and all of the vacancies are trapped by the nitrogen atoms, to form NV^-. However, as the dose increases past a critical level, there will be no N_S^0 left, as they would have all been converted into either N^+ or NV^-. This results in a lowering of the Fermi level and the subsequent production of the NV^0 centres. After this experiment, the absorption band at 1945 meV was labelled NV^- and the absorption band at 2156 meV was labelled NV^0: for more details on this experiment, refer to [6.19].

The electronic structure of the NV^- defect can be described by the procedure developed by Coulson and Kearsley [6.20]. The single electron molecular orbitals can be constructed from the dangling orbital on the nitrogen and the three carbon dangling orbitals,

see figure 6.1. Ignoring overlap of the orbitals, there are two levels of a_1 symmetry ($u = s_N$ and $v = [s_a + s_b + s_c] / 3$) and a doubly degenerate e level ($e = [2\ s_a - s_b - s_c] / \sqrt{6}$ and $[s_b - s_c] / \sqrt{2}$). It is assumed that the energies of the one electron orbitals follow the sequence $u < v < e$, so that for NV^- the configuration $u^2v^2e^2$ gives rise to the states $^1A_1$, ^1E and $^3A_2$. Optical measurements confirm that the 1.945 eV zero phonon transition is between a $^3A_2$ ground state and a ^3E excited state (arising from the configuration $u^2v^1e^3$). This optical transition has a very high quantum efficiency allowing room temperature single defect spectroscopy, but at low temperatures the existence of a singlet metastable state (approximately 50 meV below the state) results in "population shelving" and the saturation fluorescence intensity is dramatically reduced [6.21].

There has been some dispute regarding the electronic structure of the N-V centre, details of which will not be discussed in this review, but can be found in the following references [6.22, 6.23].

6.3 Samples and experiments

Two samples were chosen for this work, both containing a high concentration of NV^- centres. One of the samples was a ^{14}N doped high pressure, high temperature synthetic diamond (HPHT), and the other was doped with ~90 % ^{15}N and grown by MPCVD. Both of them had been electron irradiated using 2 MeV electrons to a dose of about 10^{18} cm^{-2}, and then annealed to 800 °C to produce a high concentration of NV^- centres. ^{14}N and ^{15}N doped samples were chosen so that all of the relevant spin Hamiltonian parameters could be determined. All of the previous EPR work on this defect had used samples doped with ^{14}N. Collins et al had a brief look at the isotope effects in synthetic diamonds using only optical absorption techniques, [6.24].

EPR spectra were recorded for each sample with the magnetic field aligned parallel to three principal directions. The EPR measurements were conducted at room temperature and at ~4 K using the Bruker EMX X-Band spectrometer and the Bruker ER200D X-band spectrometer. Both of the spectrometers operate at a microwave frequency of approximately 9.75 GHz.

6.4 Results and Data Analysis

As this defect has been extensively studied, this section will not go into too much detail of the previous experimental results. Instead, it will concentrate on how the new data and results were obtained, how correct spin Hamiltonian parameters were determined, and how the new parameters are consistent with the model of the NV^- defect.

In the ^{15}N doped sample, when the magnetic field is aligned parallel to the [001] direction, the NV^- spectrum consists of a pair of doublets within 2 mT (20 Gauss) of each other, figure 6.3(b). In the ^{14}N doped sample, the spectra get more complicated and it is not only a doublet that is observed, figure 6.3(a). As the sample is rotated the general movement of the lines in each sample is the same. The lines split and move apart very quickly. The behaviour of the spectrum is a result of the anisotropy of the defect, and the range over which the lines may be contained is of the order of 200 mT (2000 Gauss). This large range is due to the large zero-field splitting. In order to observe and determine the hyperfine splitting arising from the interaction of the nitrogen nucleus with the unpaired electrons, it is necessary to make high resolution scans over just a narrow region of interest.

The results from all these experiments are not going to be shown, but an idea of how quickly and how far the lines split and move away from each other is shown in the roadmap, figure 6.4. This shows a simulation of what happens to the allowed transitions of NV^- when the sample is placed in the cavity in a (110) plane and is then rotated from the [001] to the [110] direction. As it is rotated in this plane, it passes through [111], and this is the point at which the lines are the furthest apart. The roadmap was fitted using the spin Hamiltonian given in equation (6.3):

$$H = \mu_B \boldsymbol{B}.\underline{\boldsymbol{g}}.\boldsymbol{S} + \boldsymbol{S}.\underline{\boldsymbol{D}}.\boldsymbol{S} + \boldsymbol{S}.\underline{\boldsymbol{A}}.\boldsymbol{I} + \boldsymbol{I}.\underline{\boldsymbol{P}}.\boldsymbol{I} - g_N \mu_N \boldsymbol{B}.\boldsymbol{I}_I \qquad (6.3)$$

Where the first term is the electronic Zeeman interaction, the second is the zero-field splitting, the third is the hyperfine interaction, the fourth is the quadrupole interaction and the last is the nuclear Zeeman interaction, and each individual term has its usual meaning (see section 3.2). This roadmap shows the behaviour of the defect for samples doped with ^{14}N and ^{15}N. It is the same for both because the structure caused by the hyperfine splitting and quadrupole interaction, which distinguishes the two, is too small to be seen on this scale.

The difference between the spectra obtained from a ^{14}N and a ^{15}N doped sample, comes from the fact that a ^{15}N nucleus has a nuclear spin of ½, and a ^{14}N nucleus has a

nuclear spin of 1. A nucleus with a spin ≥ 1 will have a quadrupole interaction associated with it.

Figure 6.3 shows the difference between the spectra of the ^{14}N and ^{15}N doped samples. Looking closely at (b) you can see that each group shown by the arrows is made up of two lines. The ^{14}N sample however, is more complicated due to the large quadrupole splitting, and a simple three line hyperfine pattern is not apparent.

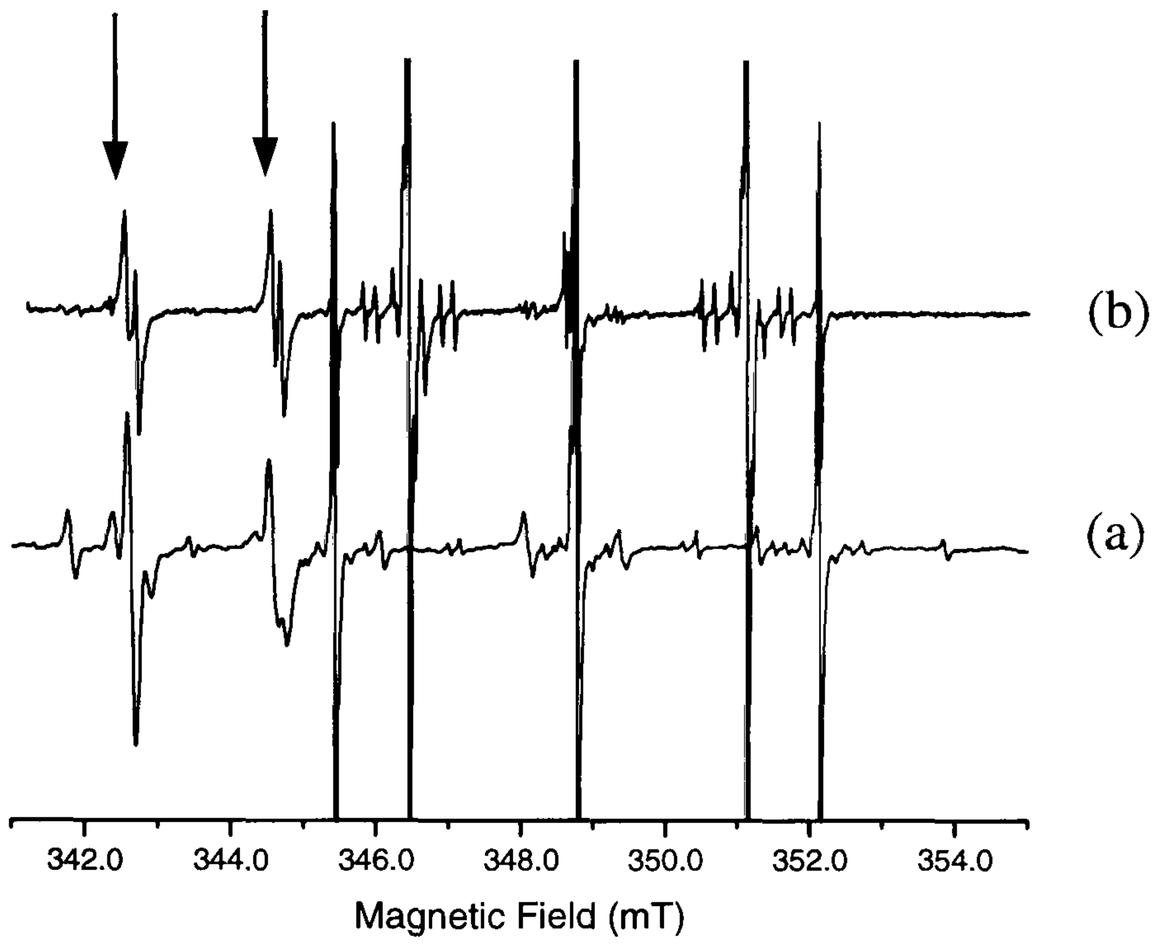

Figures 6.3: Graph showing the difference between the NV^- spectra when the sample contains (a) ^{14}N, and (b) ^{15}N. The arrows show the NV^- in each case. Each spectrum was recorded at room temperature, at a frequency of 9.75 GHz with B || [001].

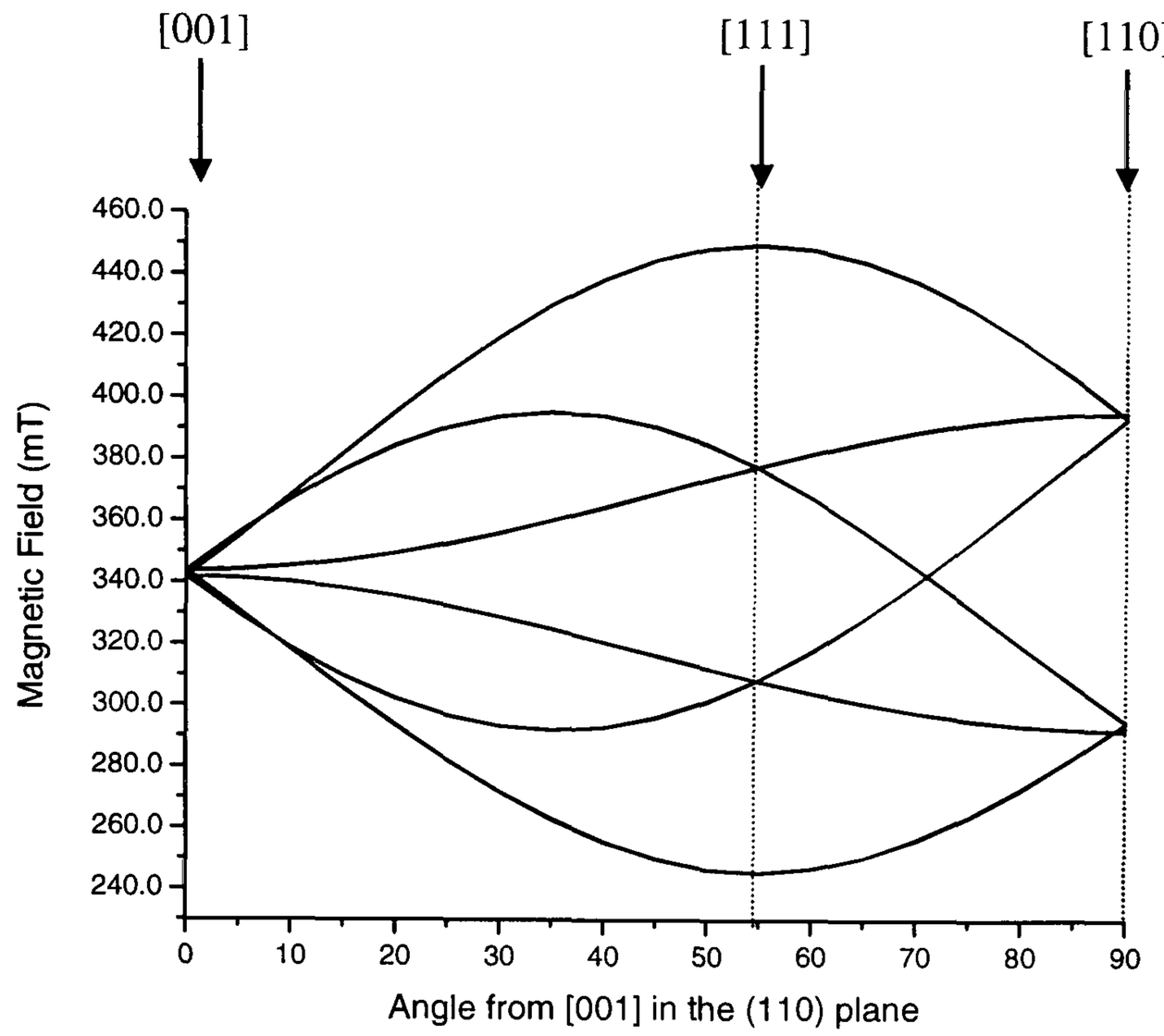

Figure 6.4: Angular dependence of the EPR transitions from the NV^- centre. This has been taken from a simulation created using the parameters in table 6.1, equation (6.3), and a microwave frequency of 9.57 GHz. Note the large spacing between the lines after just a few degrees.

EPR NMR was used to fit the EPR spectra to the spin Hamiltonian given in equation (6.3), and the relevant parameters were extracted. A procedure was followed in order to produce accurate fits and to calculate the parameters. The following steps outline the procedure used.

Step One: Starting with the ^{15}N doped sample and using the spectra obtained when the magnetic field is aligned in the three principal directions, the average position of the two lines in each transition is recorded. This enables the following spin Hamiltonian (6.4) to be solved, and $\underline{g}$ and $\underline{D}$ matrices determined.

$$H = \mu_B \boldsymbol{B}.\underline{\boldsymbol{g}}.\boldsymbol{S} + \boldsymbol{S}.\underline{\boldsymbol{D}}.\boldsymbol{S} \qquad (6.4)$$

The effect of this experimentally is shown in figure 6.5(a); two single transitions will be observed, from which $\underline{g}$ and $\underline{D}$ matrices can be determined.

Step Two: Still using the data collected from the ^{15}N doped sample, the point of interest now is the hyperfine splitting arising from the spin ½ nucleus. Because it is a spin ½ nucleus, each peak will be split into two. The Hamiltonian for this is given in 6.5:

$$H = \mu_B \boldsymbol{B}.\underline{\boldsymbol{g}}.\boldsymbol{S} + \boldsymbol{S}.\underline{\boldsymbol{D}}.\boldsymbol{S} + \boldsymbol{S}.\underline{\boldsymbol{A}}.\boldsymbol{I} - g_N\mu_N\boldsymbol{B}.\boldsymbol{I} \qquad (6.5)$$

Figure 6.5(b) shows what happens to the spectrum when there is a hyperfine interaction between a nucleus with $I = {}^1/_2$, and the unpaired electrons. In order to calculate the hyperfine splitting, the exact positions of each of the lines needed to be read off the spectra and into the fit program. Because of the hyperfine splitting, there are two lines that overlap in each case. To overcome this problem and to get the exact line position, a deconvolution program was used to determine the position of the lines. From this process, values for the ^{15}N hyperfine interaction could be independently determined.

Step Three: Now the ^{14}N nucleus needs to be considered. Because ^{14}N has a nuclear spin of 1, the quadrupole interaction needs to be included in the spin Hamiltonian, leading us to the complete Hamiltonian given in equation 6.3. Using the ratio of the nuclear g-values of $^{14}N/^{15}N$, it is possible to calculate the expected hyperfine interaction arising from the ^{14}N nucleus.

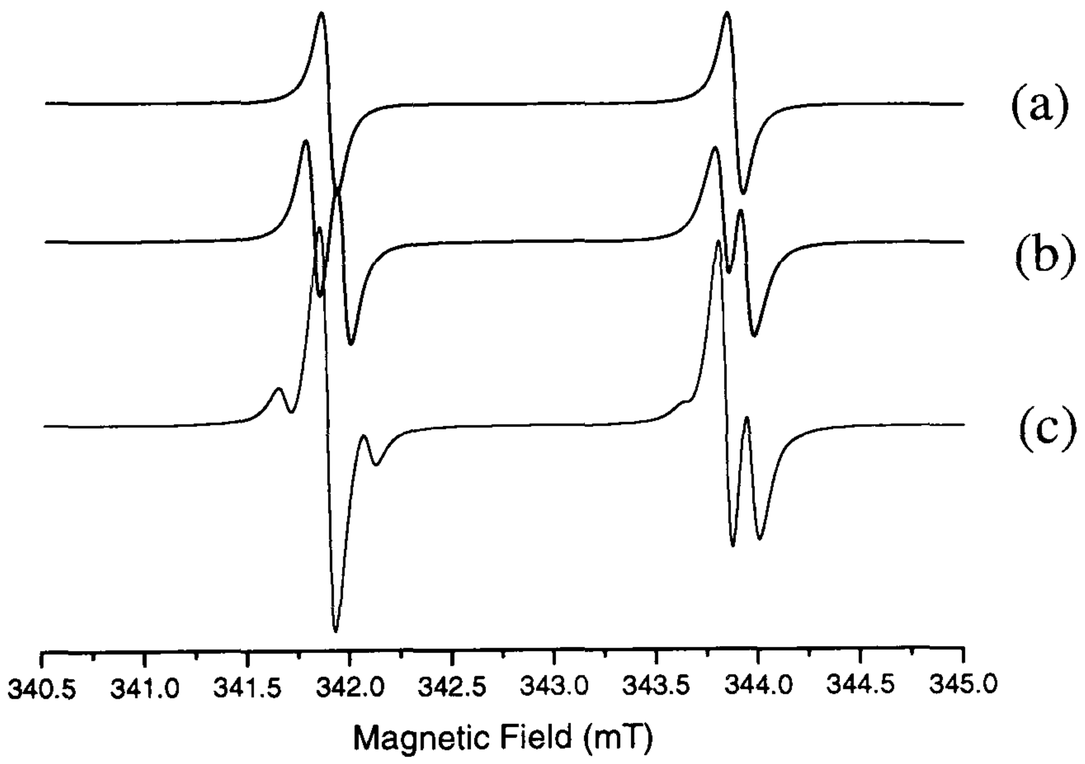

Figure 6.5: Comparing the effects of hyperfine and quadrupole interactions for a simulated NV^- EPR spectrum. (a) shows the expected spectrum if there were no nuclear spin is present, and therefore no hyperfine interaction. (b) shows the spectrum obtained when a spin ½ nucleus is involved, and (c) shows the spectrum for a spin 1 nucleus. Each simulation was created using a microwave frequency of 9.75 GHz with B || [001]

The complexity of the pattern produced from the spin 1 ^{14}N nucleus arises due to the mixing of the spin states caused by the quadrupole and hyperfine interactions and the nuclear g-value.

Having followed this procedure, modified spin Hamiltonian parameters were found and compared to the previously reported ones, table 6.1.

This work	Previous work
$g_{\parallel} = 2.0029\ (2)\ \langle 111 \rangle$ $g_{\perp} = 2.0027\ (2)$	$g = 2.0028$ [6.9]
$D_{\parallel} = 1915\ (5)$ MHz $\langle 111 \rangle$ $D_{\perp} = -957\ (3)$ MHz	$D_{\parallel} = +1916\ (5)$ MHz $\langle 111 \rangle$ $D_{\perp} = 958\ (3)$ MHz [6.9]
^{14}N $P_{\parallel} = -4.79\ (5)$ MHz $\langle 111 \rangle$ $A_{\parallel} = -2.17\ (3)$ MHz $\langle 111 \rangle$ $A_{\perp} = -2.81\ (3)$ MHz	**^{14}N** $P_{\parallel} = -5.04\ (5)$ MHz $\langle 111 \rangle$ $A_{\parallel} = 2.30\ (2)$ MHz $\langle 111 \rangle$ $A_{\perp} = 2.1\ (1)$ MHz [6.25]
^{15}N $A_{\parallel} = 3.15\ (5)$ MHz $\langle 111 \rangle$ $A_{\perp} = 3.85\ (5)$ MHz	

Table 6.1: The spin Hamiltonian parameters calculated for the NV^- defect at room temperature, compared with the previously accepted values.

A problem often encountered when finding the spin Hamiltonian parameters is determining the absolute sign of the hyperfine interaction. It is predicted that the parallel component (P_z) of the quadrupole interaction is negative [6.26], which means that by simply changing the sign of the ^{14}N hyperfine values, spectra can be simulated and the sign of the hyperfine interaction determined relative to the quadrupole interaction, figure 6.6.

Figure 6.6 shows the difference in spectra between the half field transitions when the sign of the hyperfine parameters is changed between positive and negative. The reason there is a difference observed between the spectra when considering positive or negative hyperfine parameters is that the quadrupole interaction is so large, and much larger than the value of the hyperfine interaction. This results in mixing of the energy levels, which produces a difference in spectra with a change in the hyperfine signs.

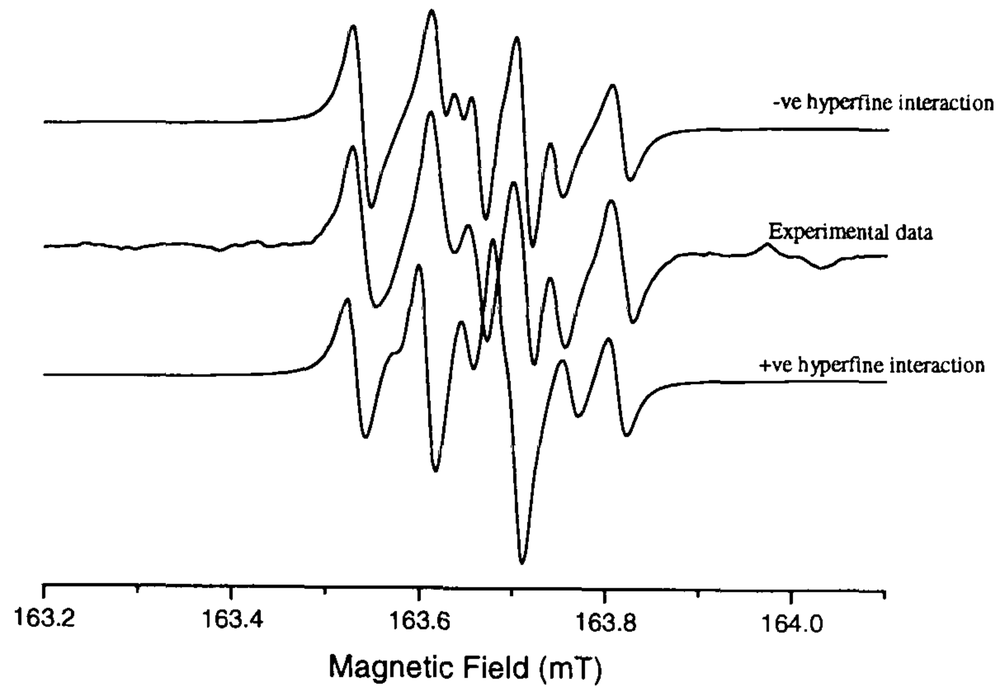

Figure 6.6: Spectra comparing the shape of the half field transitions produced when the hyperfine values are positive and negative. The experimental data fits to the negative hyperfine parameters. The magnetic field is aligned along the [001] direction in each case, with a frequency of 9.75 GHz.

The absolute sign of the ^{14}N hyperfine values enables the absolute sign of the ^{15}N hyperfine parameters to be determined. The sign of the nuclear g –value for ^{14}N is positive, whereas it is negative for ^{15}N, which means the relative signs of the hyperfine interaction will also be opposite. The signs associated with the hyperfine interactions are given in table 6.1.

As an extra check of the new calculated parameters, simulations were made to fit to the forbidden transitions at half field for both ^{14}N and ^{15}N, figure 6.7(a)-(f). The half field transitions have proved to be very useful in fitting the experimental data. Half field transitions are only observed for centres with an overall spin of at least 1. They show much less of an angular variation than the allowed transitions do, figure 6.8, because to first order, there is no contribution to the angular variation from the zero-field splitting. Instead, they are primarily determined by the hyperfine and quadrupole terms of the Hamiltonian. It is clear to see that the maximum range of the half field transitions is only about 10 mT (100 Gauss). However, taking a closer look at figure 6.9, which is a plot of the intensity of the lines with angle from [001], it can be seen that the line belonging to site two, even though appears to be moving away from the other lines, decreases in intensity as it does. The result of this is that at [111], the line belonging to site two is the furthest distance away, but has zero intensity, which means that it is not observed on the EPR spectrum.

The half field transitions have also proved very useful in fitting the new experimental data due to their relatively small angular dependence. There is also no overlap from other centres, which makes it much easier to identify the lines that belong to NV^-.

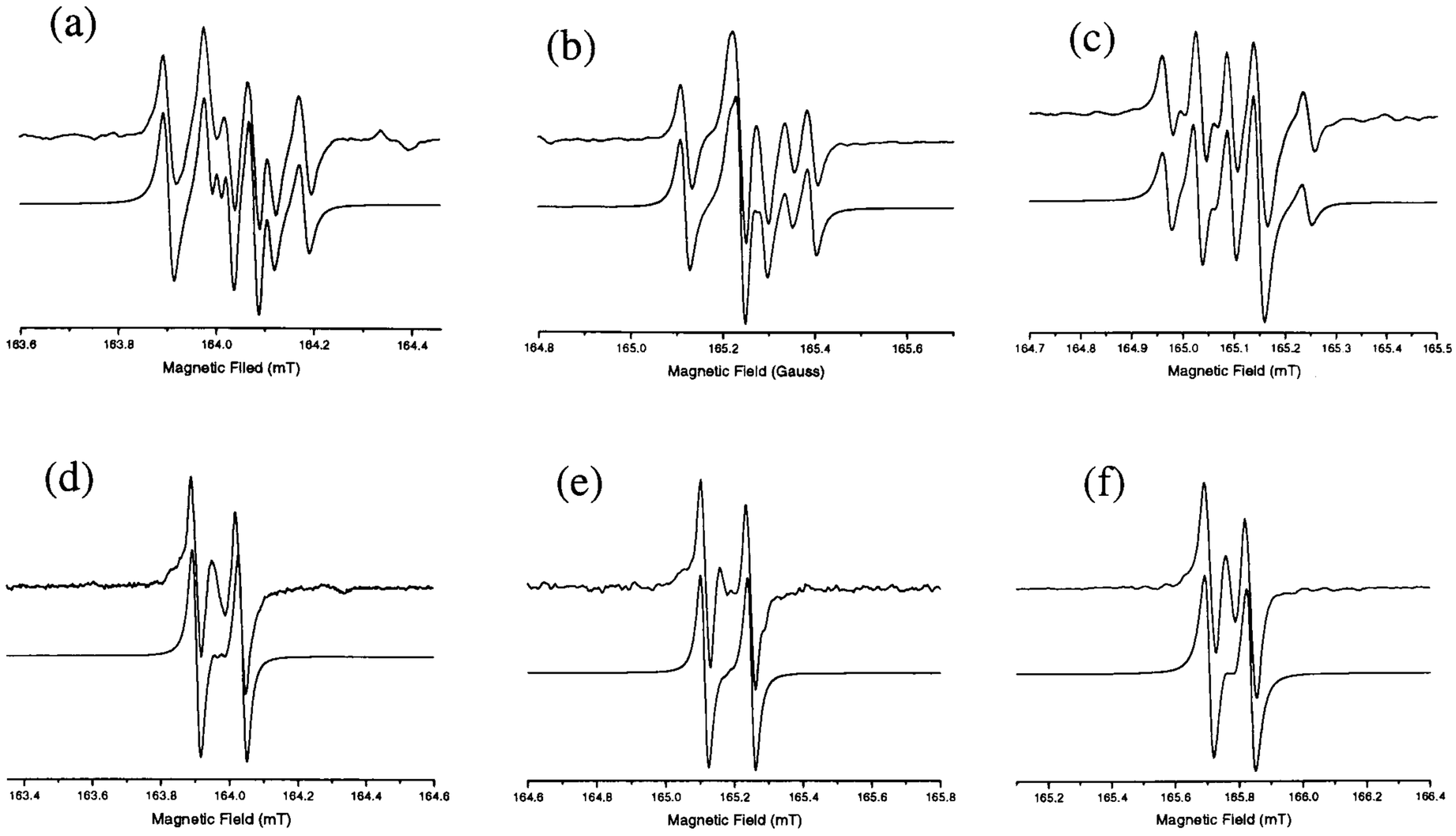

Figure 6.7(a)-(f): Figures (a), (b) and (c) give the experimental and simulated data for the half field forbidden transitions with the magnetic field aligned parallel to the [001], [111] and [110] directions respectively, in the ^{14}N doped sample. (d), (e) and (f) are the same spectra for the ^{15}N doped sample, with the directions being [001], [111] and [110] respectively. Each of the measurements was taken at room temperature, and in each case, the top line is the experimental data and the bottom one is the simulation. The measurements were recorded using a microwave frequency of about 9.75 GHz.

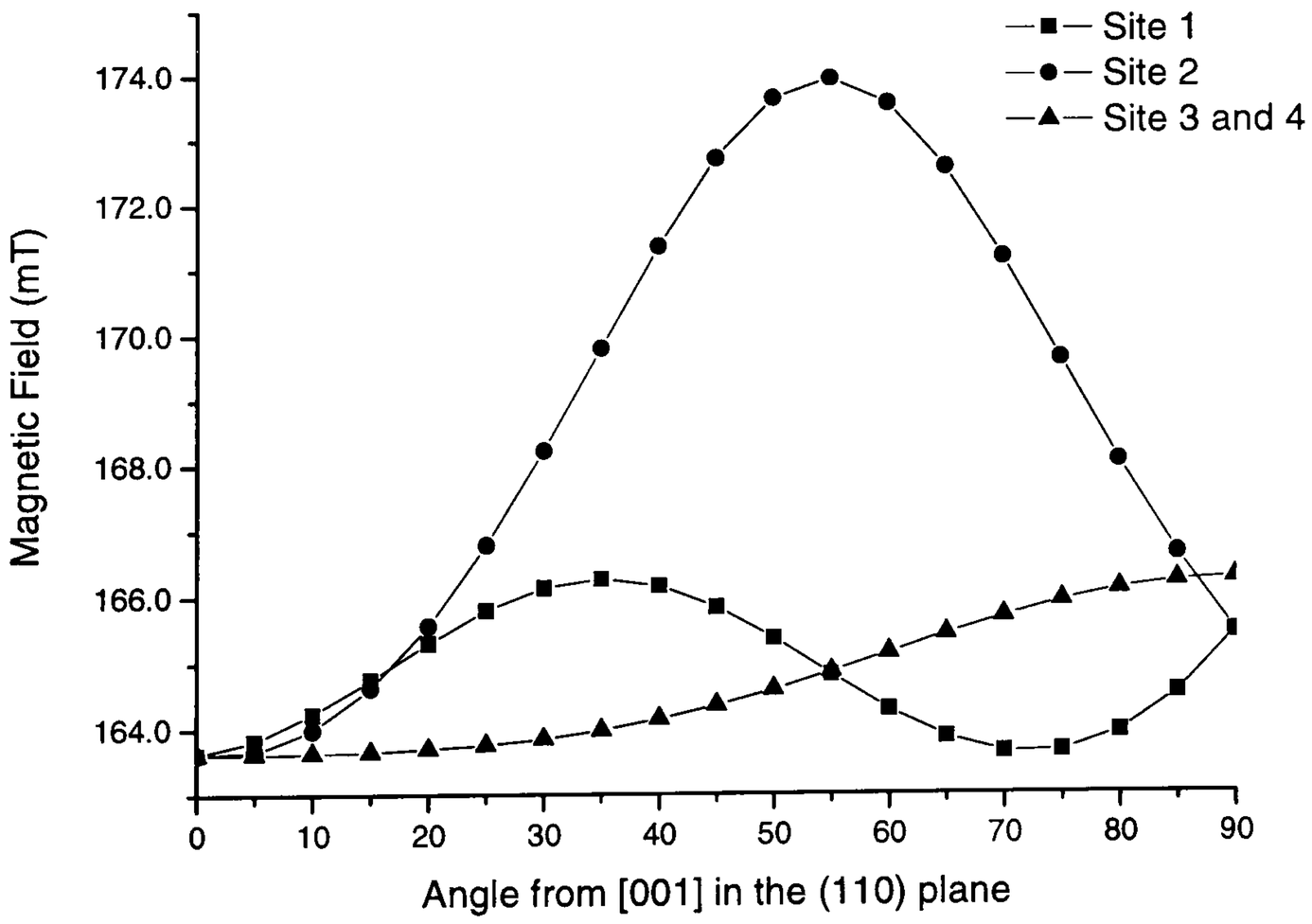

Figure 6.8: Simulated roadmap for the half field transitions belonging to the NV^- defect. The simulation was created using a microwave frequency of 9.75 GHz.

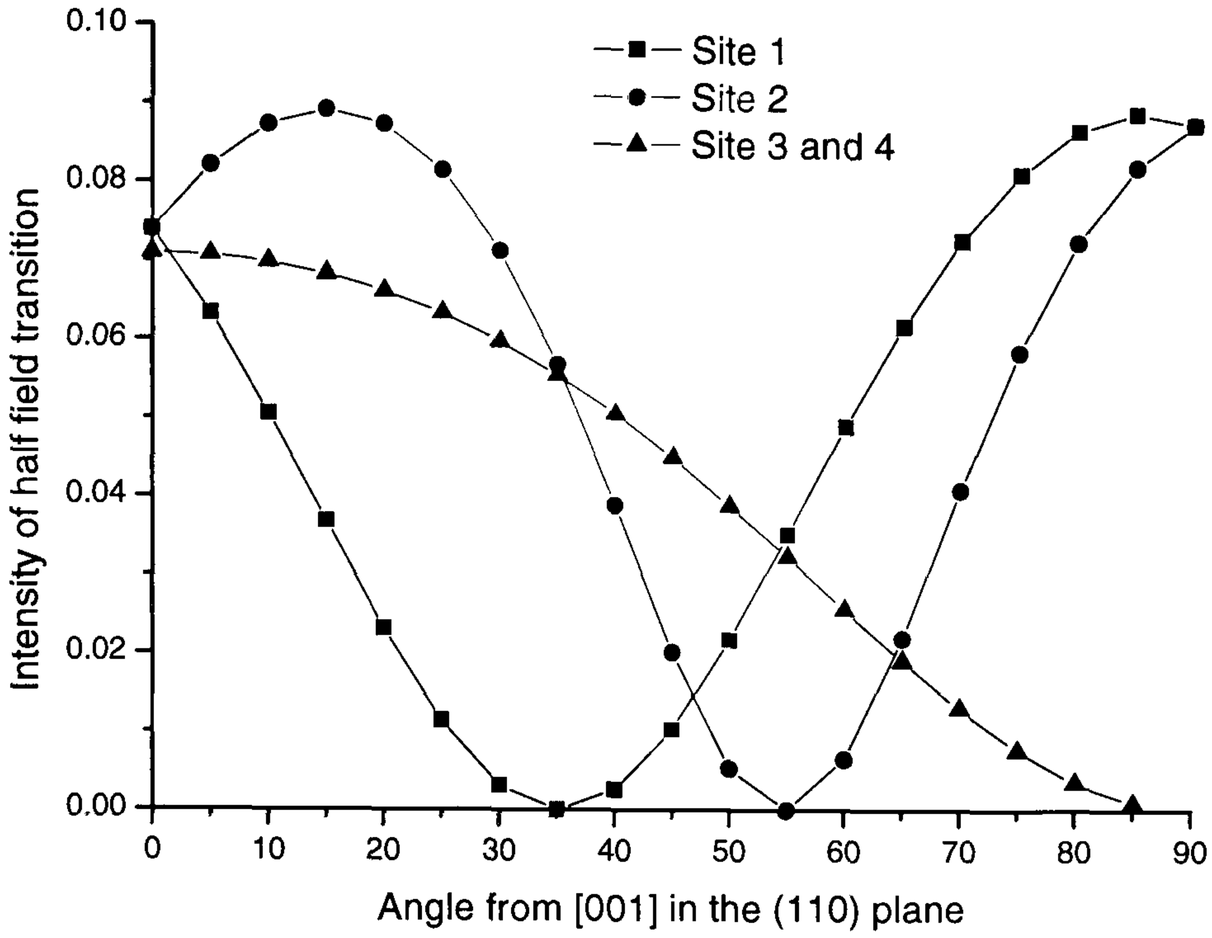

Figure 6.9: A plot showing how the intensity of the forbidden transitions varies as the sample is rotated in the (110) plane. The microwave frequency used for the simulation is 9.75 GHz. Note when comparing to figure 6.8, how the intensity of site two decreases to zero at [111].

6.5 Discussion of parameters

As table 6.1 shows, the spin Hamiltonian parameters have changed significantly from the previously accepted ones and, for the first time, the observed, small hyperfine parameters can be explained in terms of the defect model, shown in figure 6.1. From the hyperfine parameters listed in table 6.1, the isotropic and anisotropic components can be calculated using equations 3.18 and 3.19, to give:

		^{14}N	^{15}N
A_{iso}	a	– 2.60 (5) MHz	+ 3.62 (5) MHz
A_{aniso}	b	+ 0.21 (5) MHz	– 0.23 (5) MHz

Table 6.2: Table showing the isotropic and anisotropic components of the nitrogen hyperfine parameters, given back in table 1.

The small isotropic component of the hyperfine interaction indicates effectively zero unpaired electron probability density on the nitrogen atom. The fact that the sign is opposite

to that expected for localisation of the unpaired electron on the nucleus (see section 3.5) indicates that the origin of this term is likely to be spin polarisation.

The small anisotropic hyperfine interaction can be explained by the model if one assumes that one third of the unpaired electrons are localised on each of the three carbon dangling orbitals and an extended dipolar calculation is performed [6.27] between the unpaired electrons and the nitrogen atom. In each case, the fraction of unpaired electrons will be 2.51 Å (next nearest neighbour carbon separation) away from the nitrogen atom. The angle between the localisation of the electrons and the [001] direction will vary for each site, figure 6.10.

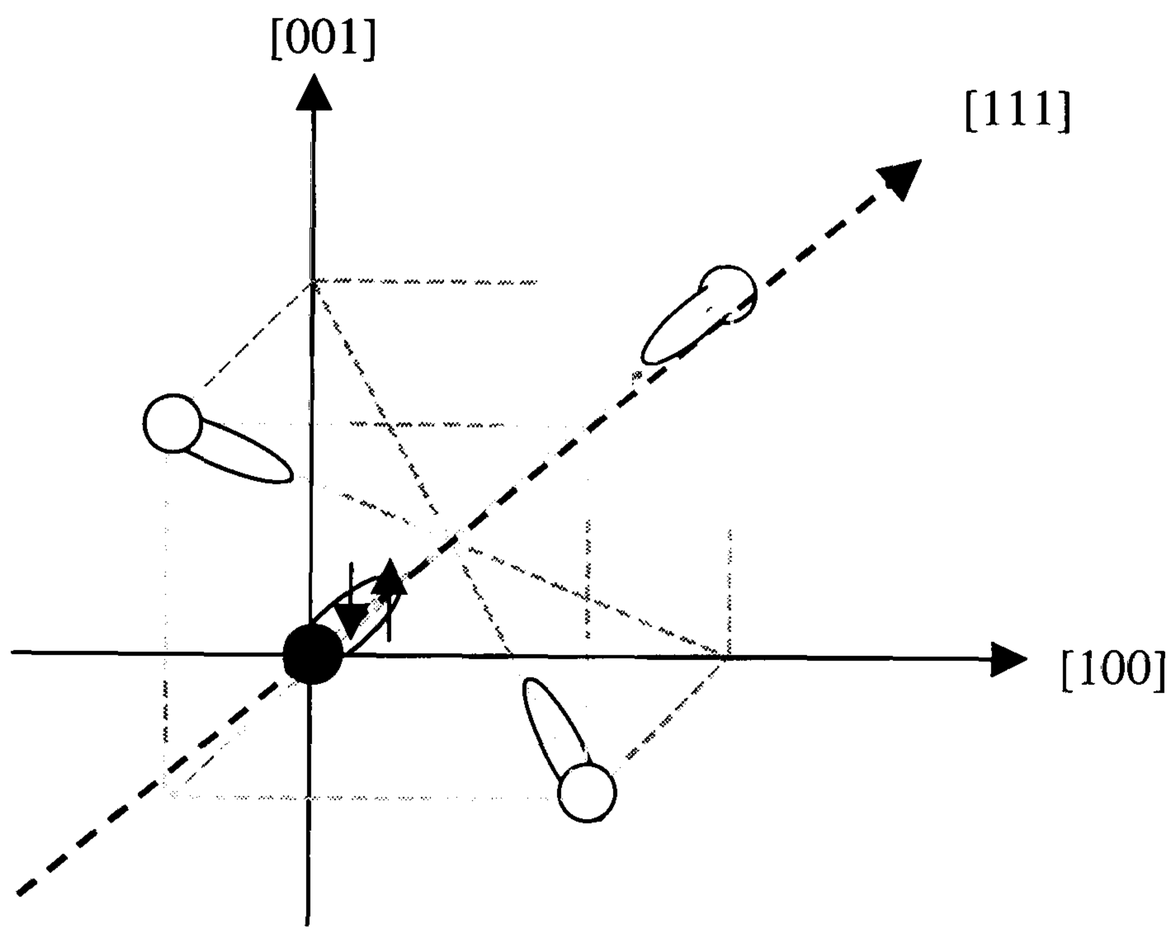

Figure 6.10: The unpaired electrons are assumed to be localised equally over the three carbon dangling orbitals, and therefore at an equal distance from the nitrogen atom (black circle).

The dipolar hyperfine interaction resulting from the three contributions is calculated, as discussed in the previous chapter, by determining the individual hyperfine matrices, transforming them to a common coordinate axis system, and summing the three together, as shown in Appendix 4. The diagonalised matrix produces the theoretical dipolar hyperfine matrix, from which b can be determined. The theoretical values calculated for ^{14}N and ^{15}N are shown in table 6.3, and compared to those determined experimentally.

	^{14}N	^{15}N
Theoretical	+0.18 (5) MHz	–0.25 (5) MHz
Experimental	+0.21 (5) MHz	–0.23 (5) MHz

Table 6.3: Comparison of the theoretical and experimental values for the anisotropic hyperfine interaction.

The theoretical calculations have been performed by assuming that 100 % of the unpaired electrons are localised on the three carbon dangling orbitals. According to Loubser and Van Wyk, only 72 % of the unpaired electrons are on the carbon dangling bonds [6.9]. When the calculation is performed by assuming that 72 % of the unpaired electrons are localised on the carbon neighbours, for ^{14}N, b = +0.13 MHz, and for ^{15}N, b = –0.18 MHz. However, the 100 % approximation is fair, given the calculation performed. Significant modifications can be made to the calculation to allow for effects such as further delocalisation of the unpaired electrons and relaxation of the neighbouring atoms.

6.6 Microwave Power Saturation

A big problem encountered when studying the NV^- defect is microwave power saturation. Saturation occurs as the microwave power is increased and the rate at which the electrons are excited to the higher energy level is faster than the rate at which they relax back down. This results in the EPR signal being much smaller than expected.

The allowed transitions of NV^- saturate very easily, as shown in figure 6.11. If a defect is not saturated, an increase in attenuation of 6 dB would halve the EPR output signal. Figure 6.11 shows this simple saturation test; starting at the highest attenuation (lowest power), the attenuation is decreased in steps of 6 dB which, if the defect is not saturated, would double the signal each time. Figure 6.11 clearly shows that this is not happening. 60 dB is the lowest power at which the Bruker EMX X-Band spectrometer can operate, and so this graph indicates that the signal will always be saturated and so will always be smaller than it should be. The result of this is that no accurate concentration measurements can be made from the allowed transitions.

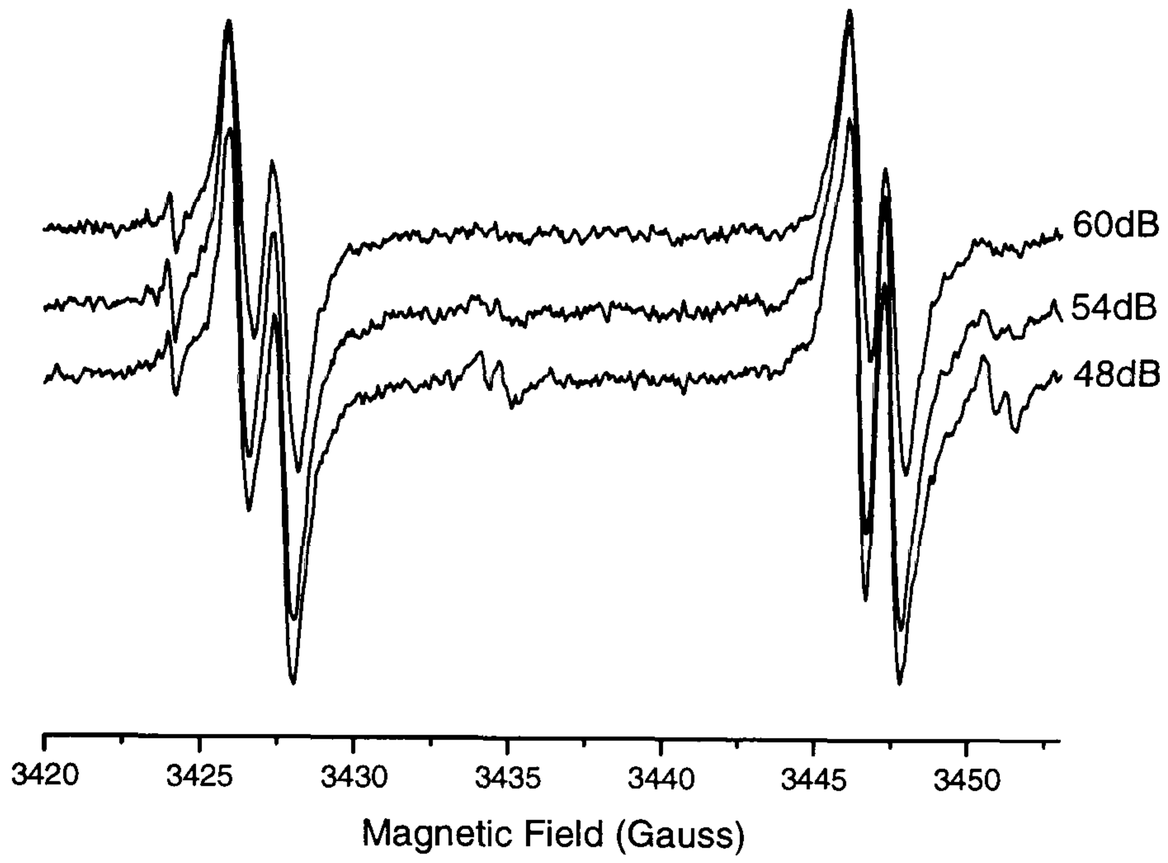

Figure 6.11: Saturation test for the allowed transitions of NV^-. If the defect were not saturated, the intensity would change by a factor of two between each spectrum. Each spectrum is recorded with the magnetic field orientated along a [001] crystallographic direction, with ν_{mw} = 9.75 GHz and at room temperature.

There needs to be another way of measuring the concentration of NV^- in the sample without having to rely on the allowed transitions. This is where, once again, the forbidden transitions are useful. The forbidden transitions saturate much less easily than the allowed transitions and so by carrying out a power variation, the optimum recording power can be determined. All of the saturation measurements discussed in this section have been carried out in the dark. It is important to mention this, because the microwave power saturation is very different in the light and dark. If the system has been illuminated, the EPR signal will not saturate as easily as it would if the measurements were taken in the dark.

Equation 6.6 is used to calculate the expected intensity of the signal, and the denominator takes into account any saturation. If there were no saturation the denominator would have an insignificant effect. The simulated saturation curve can be fitted to the experimental data to extrapolate to zero attenuation to see how the defect behaves, figure 6.12. This simulation can then be compared to the unsaturated plot, which enables accurate intensities to be determined.

$$EPR\ Integrated\ Intensity = \frac{k\sqrt{P_{\mu w}}}{\left(1+\frac{P_{\mu w}}{Q}\right)^{\frac{1}{2}}} \qquad (6.6)$$

where $P_{\mu w}$ is the microwave power and k and Q are constants, which can be found using a least squares fitting to fit the simulation to the experimental data. As the graph shows, if the defect were not saturated, a steady increase in intensity would be observed as the power was increased (attenuation decreased). The forbidden transitions can be used to calculate the concentrations because they do not saturate as easily as the allowed transitions. The ratio of forbidden transitions to the allowed transitions can be found by simulating both sets of data and then integrating each one. This ratio would carry through into the experiment and the intensity of the forbidden transition could be multiplied by this number to get the intensity of the allowed transitions. From figure 6.12, it can be calculated that at 30 dB, the measured intensity of the forbidden transitions will be a factor of 11.9 times smaller than in the absence of microwave power saturation. Ignoring the effect of microwave power saturation makes quantitative EPR measurements highly inaccurate.

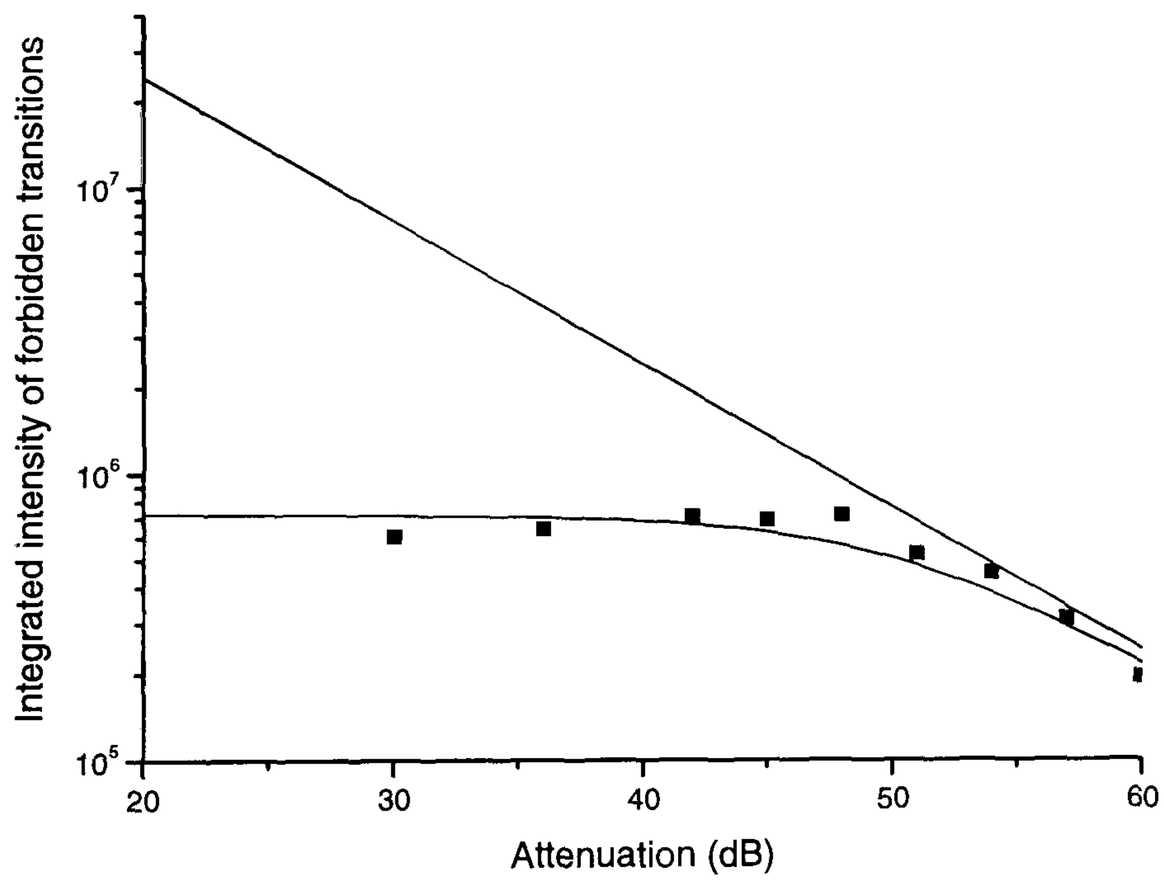

Figure 6.12: Room temperature saturation curve for NV^-. The grey line gives the simulated saturation curve, equation (6.6), fitted to the experimental data, which has been recorded with B || [001] and is shown on the plot by the squares. The straight black shows the integrated intensity predicted in absence of saturation saturation, equation (6.6) without the denominator. Using the right attenuation, a multiplication factor can be determined to convert the saturated intensity to one that would be expected if the defect were not saturated. The simulations were created using a microwave frequency of 9.75 GHz.

6.7 Conclusion

The recent experiments carried out on the NV^- centre in diamond have proved to be extremely informative. Modified spin Hamiltonian parameters have been determined for both ^{14}N and ^{15}N nuclei, with the most significant change observed with the hyperfine parameters. In the case of the ^{14}N nucleus, not only has the magnitude of the hyperfine interaction been modified, but the sign has also been changed. For ^{15}N, there were no previous hyperfine parameters.

For the first time, the observed hyperfine parameters have been explained in terms of the accepted model for the NV^- defect. They are explained by an equal distribution of the unpaired electrons over the three carbon dangling orbitals surrounding the vacancy. The value of b determined from the dipolar calculation comes about due to the partial cancellation of the three contributions to the interaction. By assuming that 100 % of the unpaired electron probability density is localised on the three carbon neighbours, the theoretical calculations are in good agreement with those determined experimentally. If the prediction of Loubser and Van Wyk is considered, the theoretical values are smaller than the theoretical ones. However, these values can be further modified by consideration of effects such as further delocalisation of the unpaired electrons, and relaxation of the neighbouring atoms.

The saturation effects of the NV^- defect have been studied in some detail. This is important because there was no previous work on the effect of saturation and the power at which saturation occurs. A direct result of the power saturation investigation is the ability to accurately calculate the concentration of NV^- within a sample.

References

[6.1] A. Beveratos, R. Brouri, T. Gacoin, A. Villing, J. P. Poizat and P. Grangier, Phys. Rev. Letts. **89**, 187901 (2002)

[6.2] A. Drabenstedt, L. Fleury, C. Tietz, F. Jelezko, S. Kilin, A. Nizovtzev and J. Wratchup, Phys. Rev. B **60**, 11503 (1999)

[6.3] S. Kuhn, C. Hettich, C. Schmitt, J-Ph. Poizat and V. Sandoghdar, Jnl. Micros. **202**, 2 (2000)

[6.4] F. T. Charnock and T. A. Kennedy, Phys. Rev. B **64**, 041201 (2001)

[6.5] G. Davies, S. C. Lawson, A. T. Collins, A. Mainwood and S. J. Sharp, Phys. Rev. B **46**, 13157 (1992)

[6.6] F. Jelezko, C. Tietz, A. Gruber, I. Popa, A. Nizovtsev, S. Kilin and J. Wrachtrup, Single Mol. 2-4, 255 (2001)

[6.7] L. du Preez, PhD Thesis, University of Witwatersrand, South Africa (1965).

[6.8] G. Davies and M. F. Hamer, Proc. R. Soc. A. **348**, 285 (1976)

[6.9] J. H. N. Loubser and J. A. van Wyk, Diam. Res., Suppl. to Int. Diamond Rev. (UK) **11**, 11 (1977)

[6.10] N. R. S. Reddy, N. B. Manson and E. R. Krausz, J Lumin. **38**, 46 (1987)

[6.11] E. Van Oort, N. B. Manson and M. Glasbeek, J. Phys. C **21**, 4385 (1988)

[6.12] E. Van Oort and M. Glasbeek, Phys. Rev. B **40**, 6509 (1989)

[6.13] K. Holliday, X. F. He, P. T. H. Fisk and N. B. Manson, Opt. Lett. **15**, 983 (1990)

[6.14] N. B. Manson, X. F. He and P. T. H. Fisk, Opt. Let. **15**, 1094 (1990)

[6.15] N. B. Manson, X. F. He and P. T. H. Fisk, J. Lumin. **53**, 49 (1992)

[6.16] X. F. He, P. T. H. Fisk and N. B. Manson, J. Appl. Phys. **72**, 211 (1992)

[6.17] X. F. He, N. B. Manson and P. T. H. Fisk, Phys. Rev. B **47**, 8809 (1993)

[6.18] D. A. Redman, S. Brown, R. H. Sands and S. C. Rand, Phys. Rev. Lett. **67**, 3420 (1991)

[6.19] Y. Mita, Phys. Rev. B **53**, 11360 (1996)

[6.20] C. A. Coulson and M. J. Kearsley, Proc. Roy. Soc. (Lond.) **A241**, 433 (1957)

[6.21] A. P. Nizovtsev, S. Ya. Kilin, C. Tietz, F. Jelezko and J. Wratchup, Physica B 308, 608 (2001)

[6.22] A. Lanef and S. C. Rand, Phys. Rev. B **53**, 13441 (1996)

[6.23] J. P. Goss, R. Jones, P. R. Briddon, G. Davies, A. T. Collins, A. Mainwood, J. A. Van Wyk, J. M. Baker, M. E. Newton, A. M. Stoneham and S. C. Lawson, Phys. Rev. B **56** 16031 (1997)

[6.24] A. T. Collins, M. Stanley and G. S. Woods, J. Phys. D **20**, 969 (1987)

[6.25] X. F. Xe, N. B. Mason and P. T. H. Fisk, Phys. Rev. B **47**, 8816 (1993)

[6.26] J. M. Baker and M. E. Newton, Appl. Mag. Res. **7**, 209 (1994)

[6.27] J. E. Wertz and J. R. Bolton, Electron Spin Resonance, Elementary theory and practical applications, Chapman and Hall, New York, p.142 (1986)

Chapter 7

The negative vacancy-hydrogen centre (VH^-)

7.1 Introduction

A previously unreported EPR defect labelled KCL1[1] has been discovered in single crystal diamond samples grown by MPCVD. This chapter reports measurements on the different samples used for the study. The defect has been identified as a hydrogen atom next to a vacancy, with an overall negative charge, VH^-. An explanation of the model is also presented. On initial observation, the EPR spectrum of KCL1 strongly resembled that of the NV^- defect. On closer inspection, however, it became apparent that the two were completely different defects. The similarities between the two defects greatly helped with the identification of the KCL1 defect. There has been no reported observation of VH^- in diamond previous to this work. However, the analogous defect in silicon is well known, so the literature review that follows will cover the vacancy-hydrogen related defects in silicon. After the review, the remainder of the chapter will cover the experiments and samples used. The results of the experiments will then the presented and discussed and the argument made for the identification of the KCL1 defect.

---

[1] Labelled KCL1 because it was the first EPR defect to be discovered at King's College, London, and at the time had not been identified.

7.2 Literature Review - The vacancy-hydrogen centre in silicon

There have been many studies on hydrogen incorporation in bulk semiconductors, but only a limited number on diamond. Silicon has been more widely studied and as a result there is much literature available [7.1, 7.2, 7.3]. Back in the late 1980's many new defects were observed using infrared absorption spectroscopy [7.4, 7.5, 7.6, 7.7], and many of these defects had been shown to contain hydrogen [7.8, 7.9, 7.10].

The first EPR identification of a vacancy-hydrogen defect in silicon was in 1997, where a neutral vacancy containing a single hydrogen atom was identified, VH^0 [7.11]. The signal observed displayed monoclinic-I symmetry below about 65 K and trigonal symmetry above about 100 K. This symmetry change together with an observed hyperfine splitting from a single proton was enough to identify the defect as VH^0. The symmetry change is observed because an extended bond is formed between two of the silicon atoms surrounding the vacancy, figure 7.1(a). At low temperatures, this extended bond is frozen between the same two silicon atoms, giving the defect monoclinic-I (C_{1h}) symmetry. As the temperature increases above 65 K, this bond can move between any two of the three equivalent silicon atoms, figure 7.1(a). This movement of the bond happens quickly enough to give the appearance of the defect having trigonal symmetry. A Si-H stretch mode originating from the VH^0 has been identified at 2038.5 cm^{-1} [7.11].

Further EPR experiments carried out on silicon went on to discover other forms of the vacancy-hydrogen centre, V_nH^0 (where n = 2-4), figure 7.1(b) [7.12], VH_m, (where m = 1-4) [7.11,7.12] and VH_2* (the excited spin triplet state of the silicon vacancy containing two hydrogen atoms) [7.13]. Unlike the behaviour of the VH^0 neither the V_2H^0 nor the V_3H^0 can reorientate into an equivalent configuration solely by the movement of the Si-Si bond. This means there is no motional averaging with temperature for these defects.

Si-H stretch modes have been observed for the numerous vacancy–hydrogen related defects. Table 7.1 lists the defects and their corresponding Si-H stretch modes.

Defect	Position of Si-H stretch mode (cm^{-1})	Reference
VH^0	2038.5	[7.11]
VH_2	2121 & 2144	[7.6]
VH_3	2166 & 2191	[7.6]
VH_4	2222	[7.6]
V_2H^0	2068.1	[7.12]
V_3H^0	2073.2	[7.12]
VH_2*	2063 & 2077	[7.13]

Table 7.1: Position of Si-H stretch modes for different vacancy-hydrogen related defects in silicon. VH_2 is the excited state of the of the silicon vacancy containing two hydrogen atoms.*

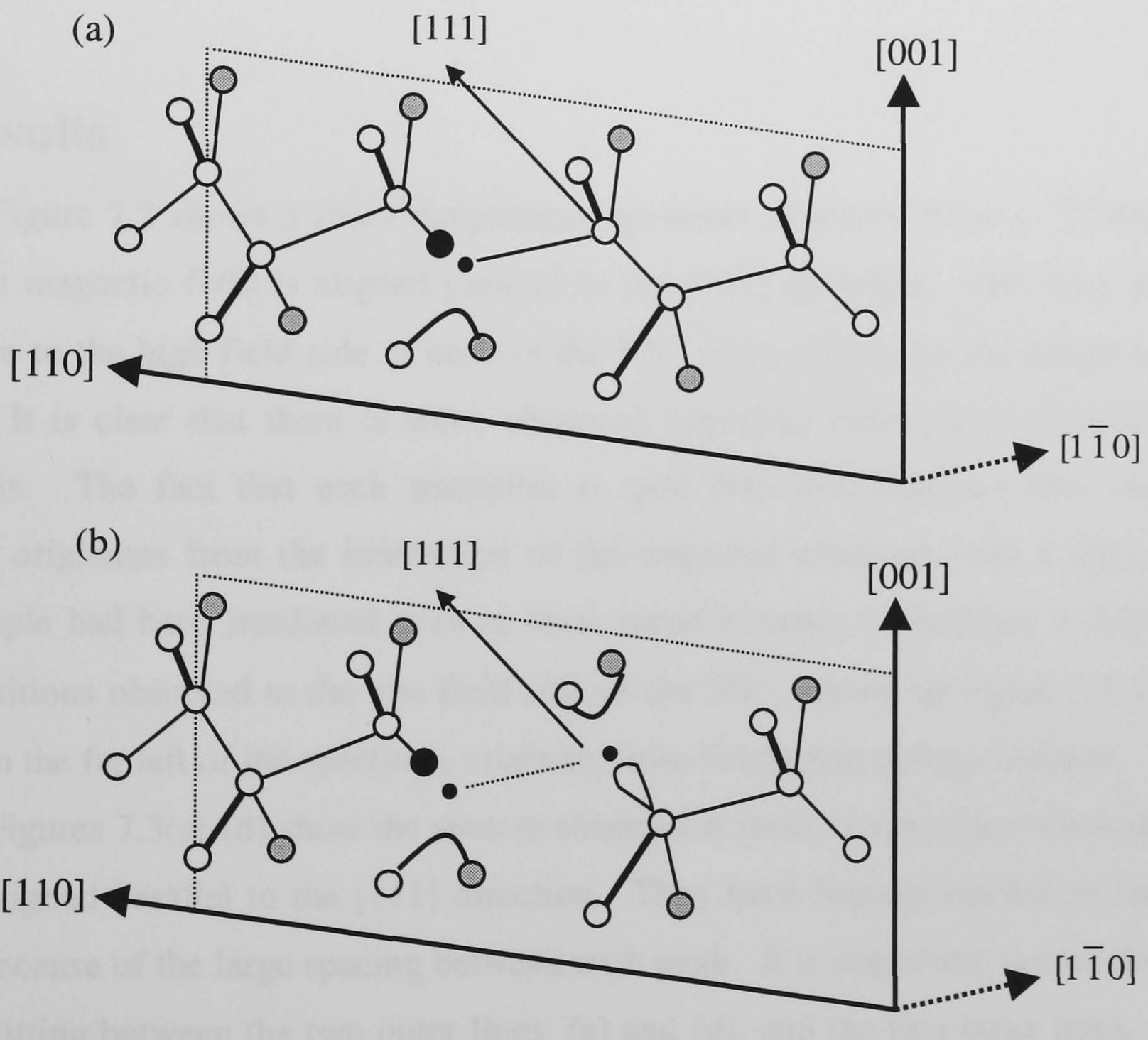

Figure 7.1: Sketch showing the (a) VH centre, and (b) V_2H centre in Silicon. It can be seen in (b) how the pattern would continue if there were more vacancies. In each diagram, the large black ball is the hydrogen atom, the small black ball is the vacancy and the white and grey balls are the silicon atoms, with the grey ones representing the atoms that extend backwards into the page.

7.3 Samples and Experiments

A selection of ^{14}N and ^{15}N doped diamond samples were used in this study. Each sample was tested but not all contained KCL1 in measurable concentrations. Eventually two samples were chosen on which to perform a more detailed study. Both the ^{14}N and ^{15}N doped samples had been grown using microwave plasma chemical vapour deposition. The ^{15}N doped sample was the same one used for the NV^- measurement reported in Chapter 6. It has been irradiated and annealed in order to create the NV^- centres. The ^{14}N doped sample had not been treated in any way.

The experiments were carried out using the Bruker EMX X-Band EPR spectrometer running at a microwave frequency of approximately 9.6 GHz. The angular variation was recorded from [001] to [110] in the (110) plane, at room temperature. A full temperature variation was also carried out on both the ^{14}N and ^{15}N doped samples, in the temperature range 5 – 300 K.

7.4 Results

Figure 7.2 shows a room temperature spectrum observed from a ^{15}N doped sample when the magnetic field is aligned parallel to the [001] direction. The lines arising from KCL1 are to the high field side of each of the NV^- lines, shown on the figure by the black arrows. It is clear that there is some observed hyperfine structure associated with these transitions. The fact that each transition is split into two indicates that the hyperfine structure originates from the interaction of the unpaired electrons with a spin ½ nucleus. This sample had been irradiated prior to these measurements to facilitate a different study. The transitions observed to the low field side of the NV^-, shown on figure 7.2 by the small arrows on the far left of the spectrum, originate from irradiation damage defects.

Figures 7.3(a)-(d) show the spectra obtained at room temperature when the magnetic field is aligned parallel to the [111] direction. They have been presented as four different spectra because of the large spacing between each peak. It is important to note the difference in the splitting between the two outer lines, (a) and (d), and the two inner lines, (b) and (c). This will be focussed on more thoroughly in the next section.

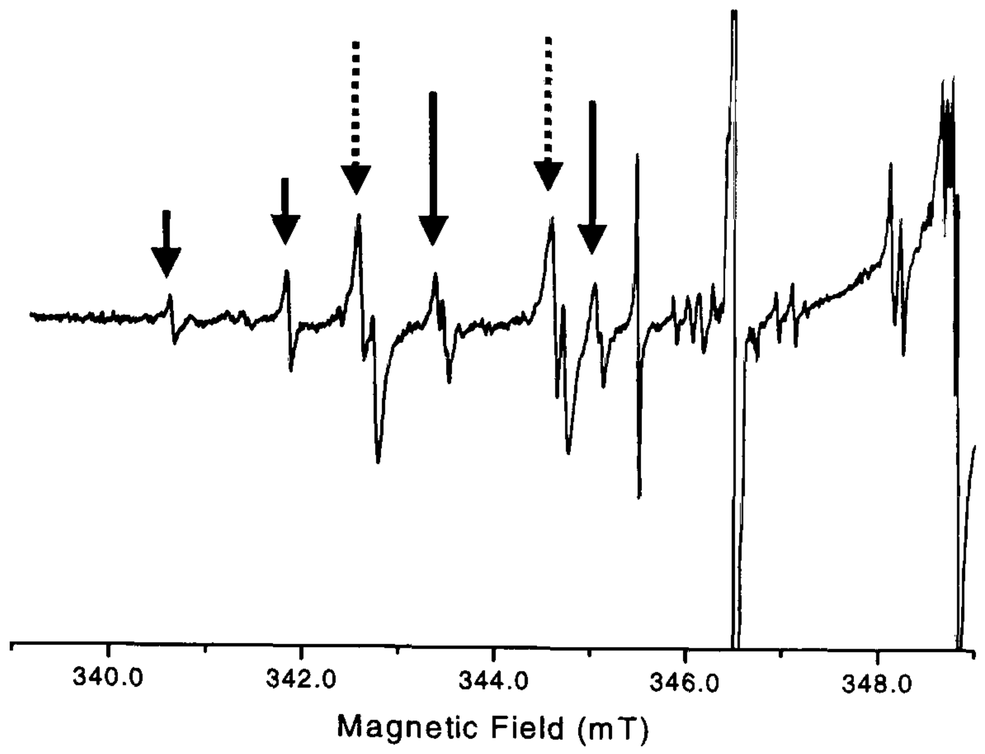

Figure 7.2: EPR spectra taken on a ^{15}N-doped sample. The KCL1 defect is shown by the large solid arrows, NV^- by the dashed arrows and the irradiation damage defects by the two small arrows on the far left. This spectrum was recorded at room temperature with B || [001].

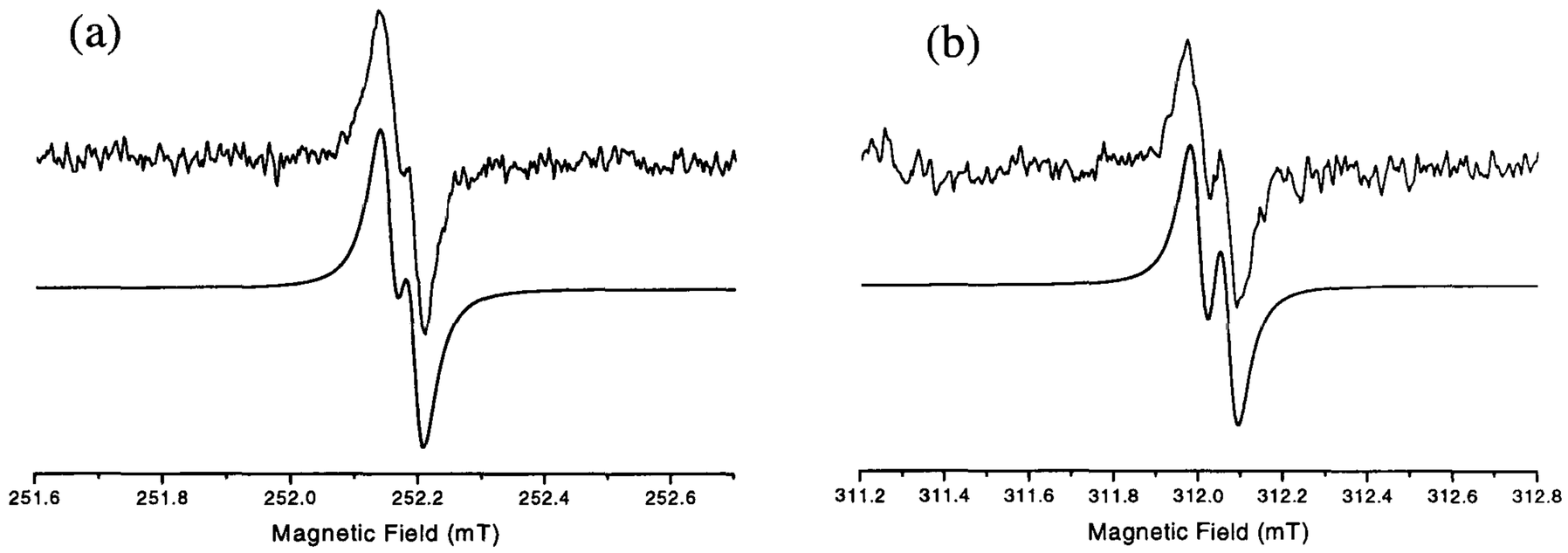

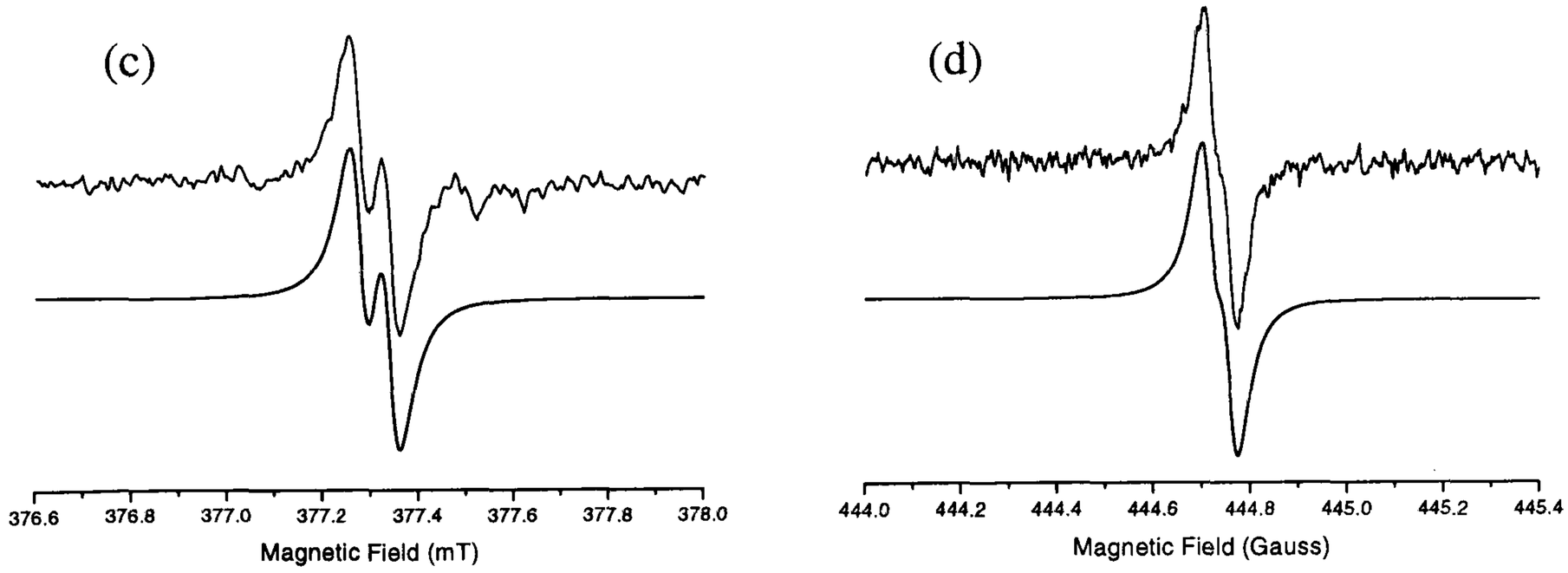

Figure 7.3(a)-(d): Room temperature spectra showing each group of lines produced from the KCL1 defect in a ^{15}N doped sample when the magnetic field is orientated along the [111] crystal axis. In each case the top plot is the experimental data, and the bottom is the simulated data.

A full angular variation was carried out in the (110) plane, rotating a sample from [001] to [110]. The roadmap produced from the angular variation is shown in figure 7.4 and shows the similarities with the NV^- defect. All measurements reported in this figure were made at approximately 10 K.

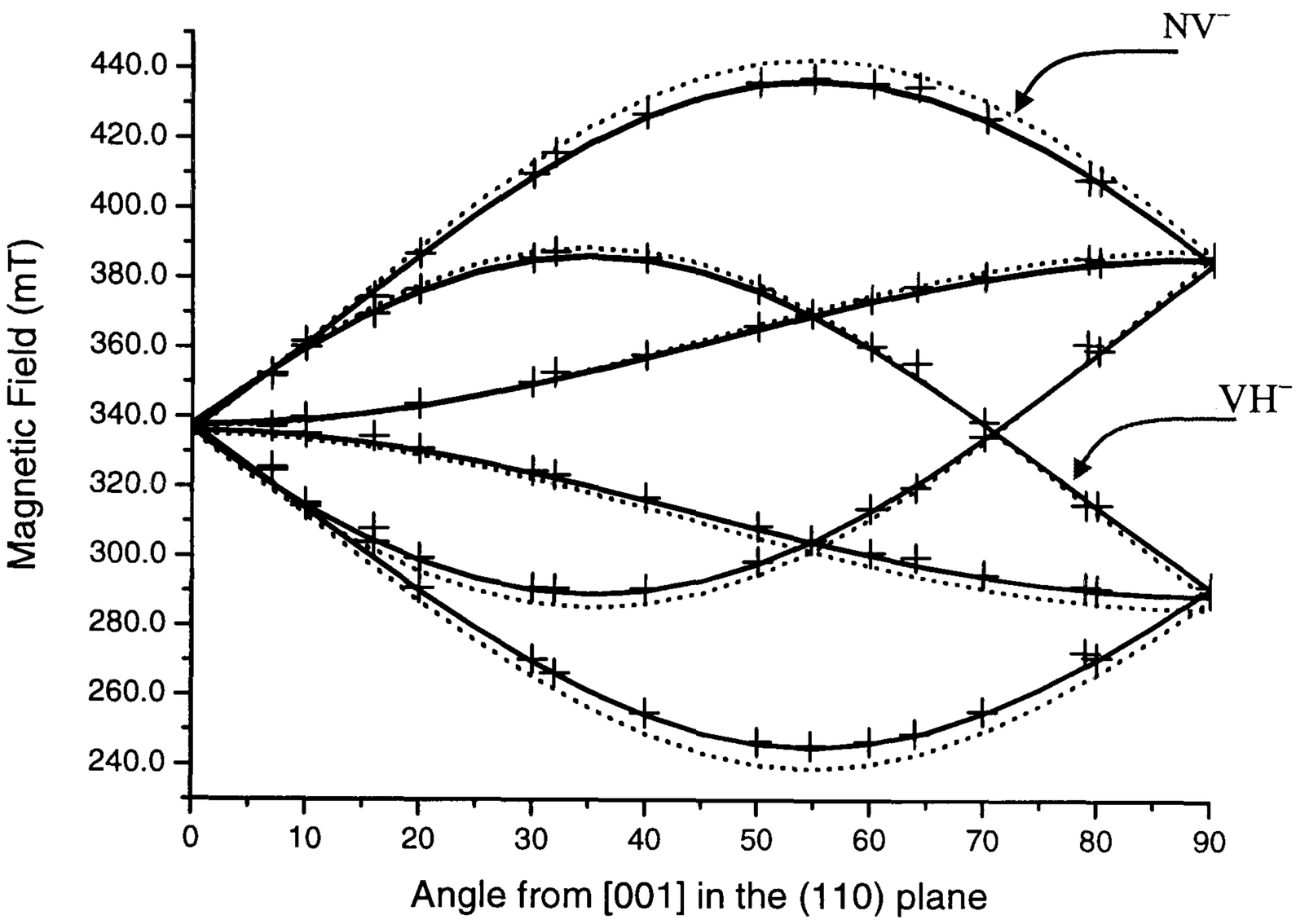

Figure 7.4: Angular dependence of the EPR transitions from the VH^- centre for rotation about the [110] axis, starting at [001] recorded at approximately 10 K. The crosses are the experimental line positions, and the solid line is the simulated fit determined from fitting the experimental data using EPR NMR with the calculated spin Hamiltonian parameters given in table 7.2. Also shown is the angular variation for the NV^- defect, dotted black line.

The roadmap is typical of a spin 1 defect with a large zero-field splitting and as a result, half field transitions were searched for, and found. Because of the speed at which the lines deviate from the principal directions, the half field transitions prove to be extremely useful. Figure 7.5 shows the half field transitions when the magnetic field is parallel to the [001] direction. As a check to see if the samples contained KCL1, the samples would often be left for up to 1000 scans to allow the forbidden transitions to average in and obtain a good signal to noise ratio. This was necessary for many of the samples because the concentration of KCL1 was often very low, ~ $^1/_{100}$ ppm. The importance of the forbidden transitions has been discussed in the previous chapter. It was made clear that they saturate much less easily than the allowed transitions and therefore can be used to calculate a more accurate value for the concentration.

The half field transitions arise from the forbidden transitions of $\Delta M_S = \pm 2$. In each case one would expect to observe the half field transitions around the same field, irrespective of the orientation of the sample with the magnetic field, as they are not very sensitive to mis-orientation. Figures 7.6 and 7.7 show the simulated roadmaps for the forbidden transitions.

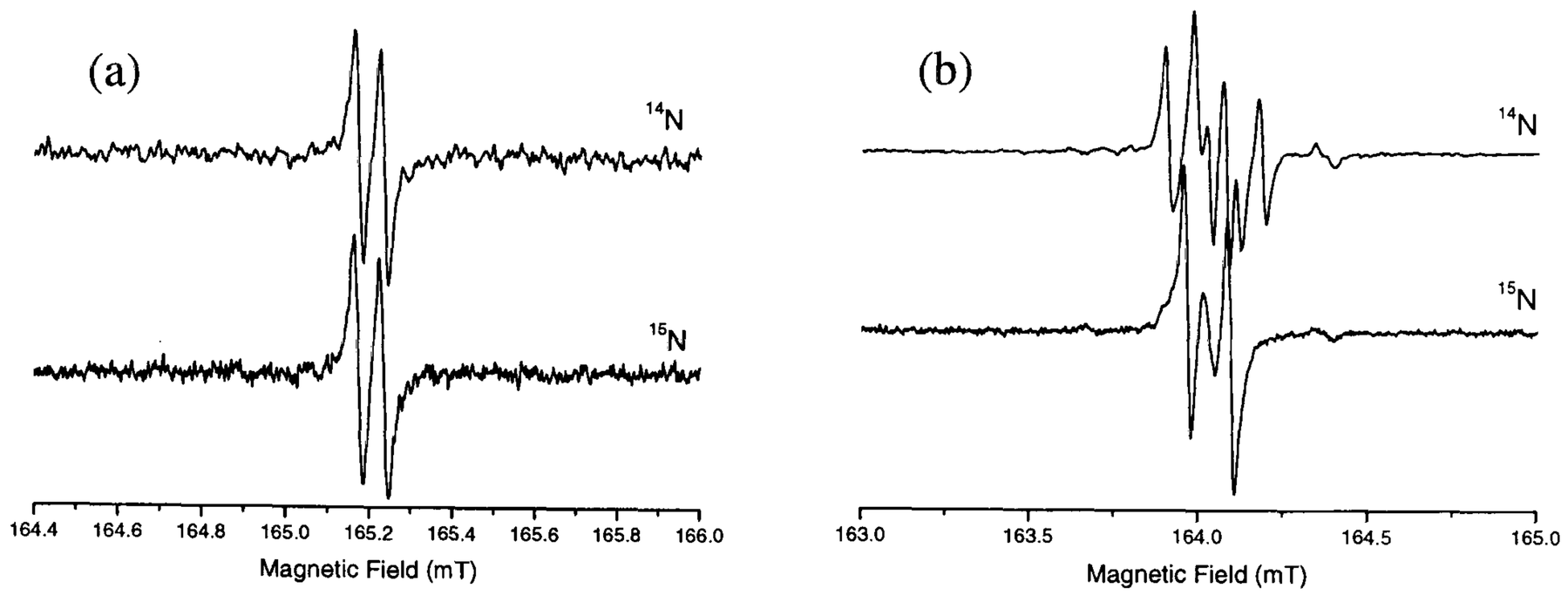

Figure 7.5: Forbidden transitions for (a) VH^- and (b) NV^- in ^{14}N and ^{15}N-doped samples. It can be seen that the two spectra are identical in the samples containing VH^-. The two spectra for NV^- however, are clearly very different. Each one was recorded at room temperature with the magnetic field parallel to the [001] direction.

A full temperature variation was performed on the samples containing VH^- and no change was observed on the EPR spectrum. Further details of this will be discussed in section 7.6.

7.5 Discussions and Data Analysis

The similarity between the KCL1 centre and the NV^- centre meant that the NV^- parameters were used as a starting point when trying to fit the KCL1 data. The presence of the half field transitions implies that the overall spin of the defect was at least 1.

A problem encountered when collecting the original data was modulation broadening. The modulation broadening hid any hyperfine structure that should have been observed in the spectrum for KCL1. The hyperfine structure was however, observed in the higher resolution experiments in the ^{15}N doped samples, as shown in figure 7.2. As figure 7.4 shows, a roadmap was still produced and used to determine some of the spin Hamiltonian parameters, table 7.2. In the same way as step one of the procedure outlined in section 6.4, the g and D parameters could be determined by fitting the roadmap, and the transitions used to create it. The Hamiltonian used to determine these parameters is given in equation 7.1.

$$H = \mu_B \boldsymbol{B}.\underline{\boldsymbol{g}}.\boldsymbol{S} + \boldsymbol{S}.\underline{\boldsymbol{D}}.\boldsymbol{S} \qquad (7.1)$$

where each term has its usual meaning, with S=1. Also shown in table 7.2 are the NV^- parameters. These are shown for a comparison.

NV^- [7.14]	VH^-
$g_{\parallel} = 2.0029(2)$ ⟨111⟩ $g_{\perp} = 2.0027(2)$	$g_{\parallel} = 2.0034(3)$ ⟨111⟩ $g_{\perp} = 2.0022(3)$
$D_{\parallel} = 1915\ (5)$ MHz ⟨111⟩ $D_{\perp} = -957\ (3)$ MHz	$D_{\parallel} = \pm 1803.8\ (20)$ MHz ⟨111⟩ $D_{\perp} = \mp 901.9(20)$ MHz

Table 7.2: Spin Hamiltonian parameters calculated for VH^- using data recorded at ~10 K. The NV^- parameters are shown for comparison.

The parameters given in table 7.2 fit the experimental data very well. Even though there was no observed hyperfine splitting in the initial spectra, when finding the values for *g* and *D*, it was initially assumed that the defect responsible for the transitions involved nitrogen. When the ^{15}N doped samples became available, this assumption continued to hold because the spectra obtained showed the presence of a spin ½ nucleus, which was assumed to be ^{15}N. The experiments were carried out and hyperfine parameters were calculated using this assumption. However, this was soon proved to be incorrect.

Figure 7.5(a) shows the forbidden transitions for KCL1 when the magnetic field is aligned parallel to the [001] direction for both ^{14}N and ^{15}N doped samples. The most important thing to notice is that the KCL1 spectra are identical for both samples. This is proof that the observed hyperfine structure arising from the KCL1 defect does not originate from nitrogen. Nitrogen is not a constituent of the defect, contrary to the original belief. In contrast, figure 7.5(b) compares the forbidden transitions for the NV^- defect. It can be seen that there is a clear difference between the samples doped with ^{14}N, and the samples doped with ^{15}N. A similar observation would be expected if the KCL1 defect contained nitrogen.

Now that the involvement of nitrogen has been ruled out, the impurity involved in the defect needs to be identified. From the fact that each line is split into two, it is known that the nucleus involved has a spin of $^1/_2$. There are no other transitions observed that could arise from a different isotope of the same nucleus, which means that whatever nucleus is involved, it must have ~100 % abundant spin $^1/_2$ isotope. The possible candidates for this are

hydrogen, fluorine and phosphorous. Fluorine and phosphorous are not involved in the growth process and so the only realistic impurity that could be involved in this defect is hydrogen.

Having found that it is hydrogen and not nitrogen involved in the defect, another fit program could be written using the high-resolution spectra obtained from the ^{15}N doped sample (e.g. figures 7.2, 7.3 and 7.5). From these spectra values for the hyperfine parameters could be determined. The new spin Hamiltonian parameters obtained for KCL1, including the interaction of the unpaired electrons with a proton, are given in table 7.3. It is important to note that the sign of the proton hyperfine interaction does not have an effect on the EPR spectrum arising from this defect.

$g_{\parallel} = 2.0034\ (1)\ \langle 111 \rangle$	$g_{\perp} = 2.0023\ (1)$
$D_{\parallel} = \mp 1803.8\ (20)$ MHz $\langle 111 \rangle$	$D_{\perp} = \pm 901.9\ (20)$ MHz
$\lvert A_{\parallel} \rvert = 1.10(5)$ MHz $\langle 111 \rangle$	$\lvert A_{\perp} \rvert = 1.95\ (5)$ MHz

Table 7.3: Table showing the spin Hamiltonian parameters for VH^-, calculated by fitting the experimental data points. All of the data used for this fitting were recorded at room temperature.

The shape of the roadmap, combined with the spin Hamiltonian parameters, shows that the defect is axially symmetric about the $\langle 111 \rangle$ axis, i.e. has C_{3v} symmetry. Using all of the information discussed, simulations were created. Figures 7.4(a) to (d) show that the simulations fit very well to the data. A simulated roadmap was also created and compared to the experimental roadmap, figure 7.5.

If the forbidden transitions are once again considered, their behaviour can be explained by comparison of figures 7.6 and 7.7 below. A roadmap has been simulated for the forbidden transitions in order to observe the angular variation in position of the transitions, figure 7.6, and also the change in intensity with orientation of the applied Zeeman field, figure 7.7. The roadmaps have been simulated without the presence of any hyperfine splitting. The result of this is that there is only one line visible. In the experimental spectrum each would be split into two. As mentioned previously, KCL1 has C_{3v} symmetry. This results in each transition having four associated sites, table 3.1. It is these individual sites that are observed as the sample is rotated.

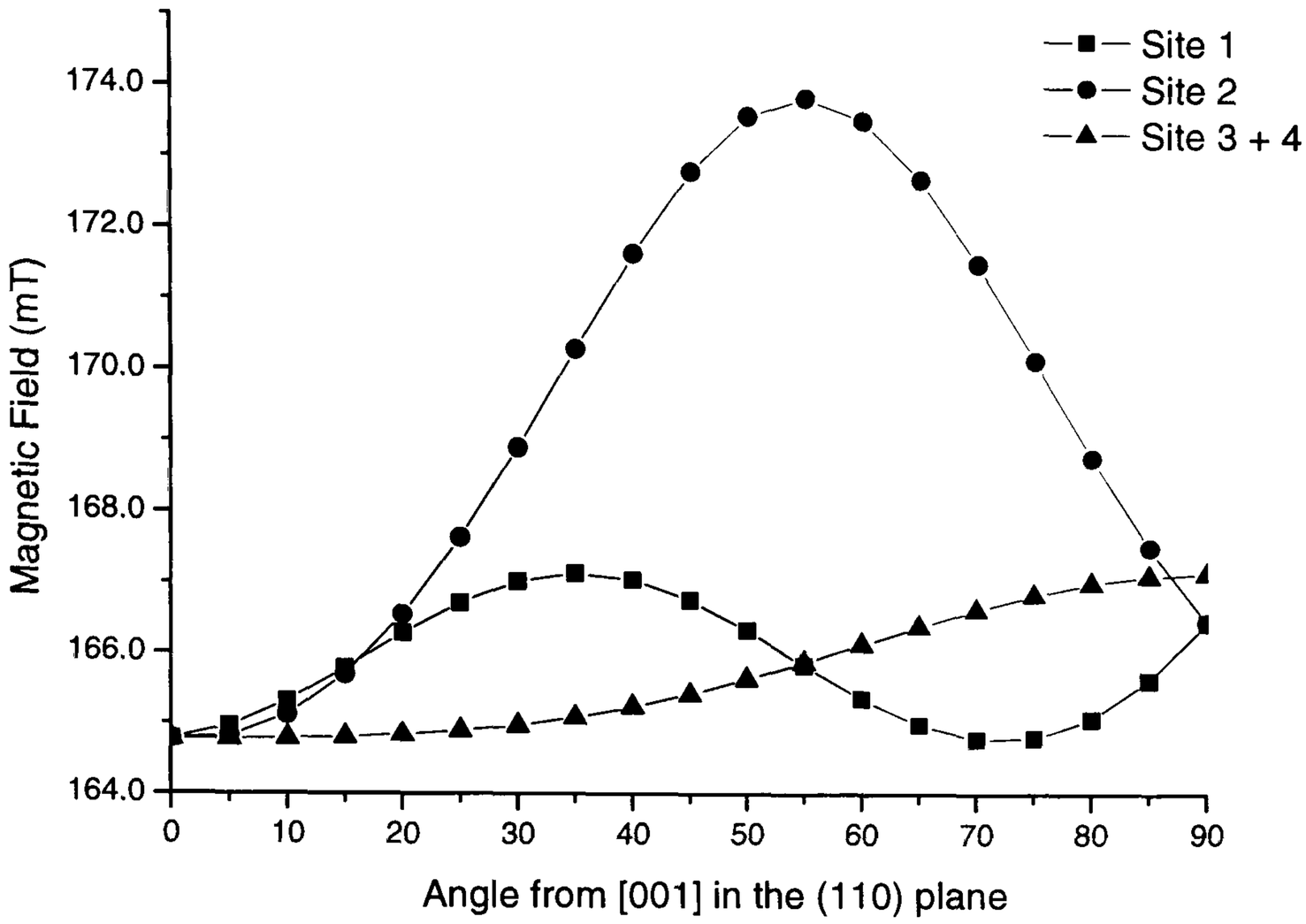

Figure 7.6: Simulated roadmap for the half field transitions arising from the spin 1 VH^- centre. The simulations were created using a microwave frequency of 9.75 GHz.

If figure 7.6 alone is considered, it appears as though there should be two lines observed in the [111] and [110] directions. This however is not the case, as comparison with figure 7.7 shows. When the magnetic field is parallel to [111], the intensity of the transition arising from site 2 is zero, thus only one line is observed on the EPR spectrum. When the magnetic field is parallel to [110], the intensity of the transitions arising from sites 3 and 4 are zero. This means, once again, there is only one line observed on the EPR spectrum. A comparison of the position and intensity plots agrees with what has been observed experimentally.

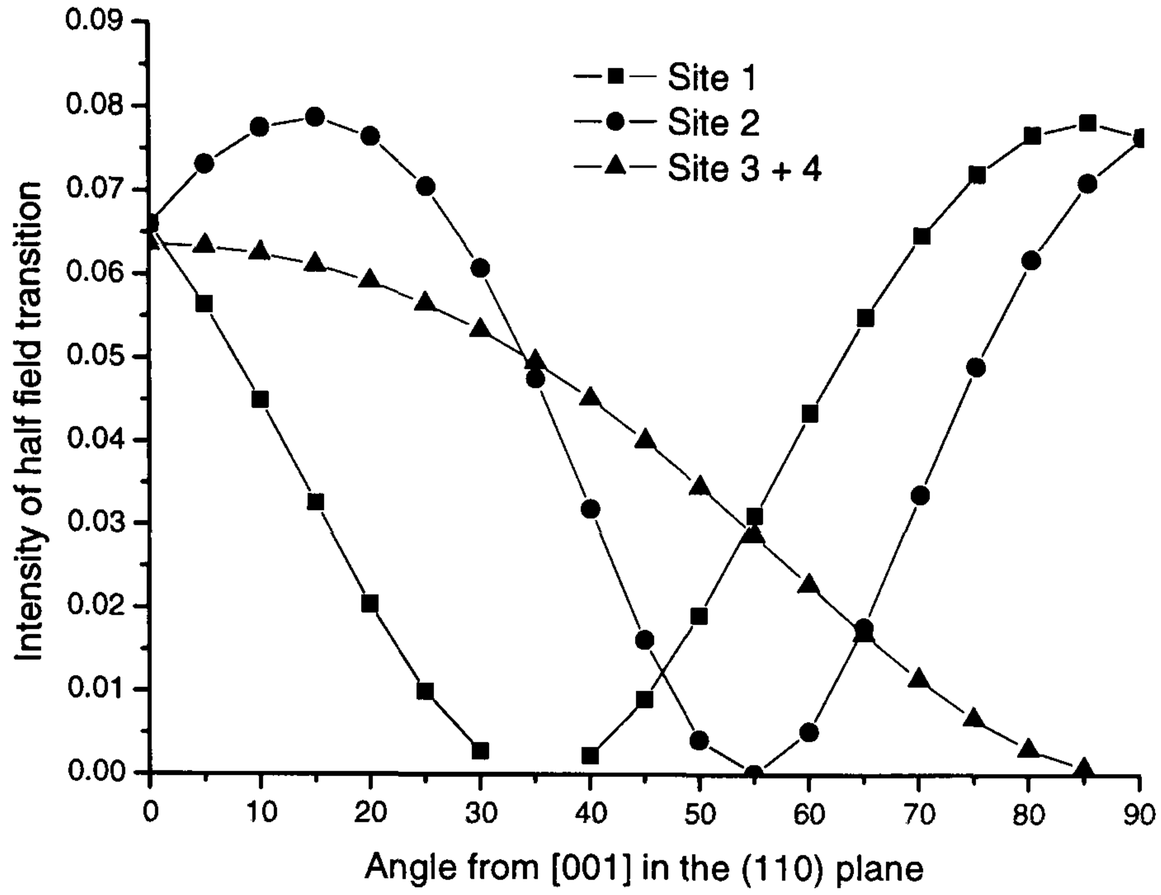

Figure 7.7: A plot showing how the intensity of the forbidden transitions varies as the sample is rotated in the (110) plane. Note when comparing to figure 7.6, how the intensity of site two decreases to zero at [111].

If the spin Hamiltonian parameters are once again considered, it is important to note the sign of the values of the zero field splitting term, D. In table 7.3 the terms are given as being either positive or negative. The reason for this is that it is impossible to determine the absolute sign of D from the angular variation of the position of the EPR line. To determine the sign of D, the population of the involved energy levels would need to be calculated at a given temperature using Boltzmann statistics. Then at low temperature, ~2 K, the ratio of the transitions being looked at could be determined. Depending on whether it was the low or high field transitions that were more intense, the sign of D could be found. This has not been possible for VH^- because the experimental facilities were not available.

The proton hyperfine parameters are so small that other than the observed splitting on the forbidden and allowed transitions, the contribution to the spectrum is negligible. The difference between $A_{\parallel}$ and $A_{\perp}$ is large enough to contribute to a significant change in splitting between transitions at different sites, as is observed in the data recorded when the magnetic field is aligned parallel to the [111] direction, given in figures 7.3(a)-(d). However, as was reported back in Chapter 5 in relation to the NVH^- defect, the involvement of hydrogen has a characteristic EPR pattern which involves a pair of lines separated by 1.04 mT. The hyperfine structure was significantly larger in NVH^-, which meant the forbidden spin flip transitions were observed. The output file for KCL1 was studied and the spin flip transitions were predicted. However, they were not seen on the actual EPR spectrum

because their intensity was about 1000 times smaller than the allowed transitions that were observed.

While fitting, it was assumed that the proton hyperfine interaction was axially symmetric with its principal axis along the [111] direction. Tests were done to check this assumption by allowing the symmetry of the hyperfine interaction to be lowered and observing the effect. C_{3v} symmetry assumes that the hydrogen hyperfine interaction is directed along a [111] bond axis. Therefore $A_1 = A_{\|}$, which is parallel to the [111] axis, and $A_2 = A_3 = A_\perp$. Lowering the symmetry removes this constraint and allows the hyperfine interaction to directed along any direction, figure 7.8, and $A_1 \neq A_2$. Calculations and fits were carried out without the constraint, and the fits did not improve. The principal axis still came out to be along the [111] axis, and it was concluded that the defect has C_{3v} symmetry.

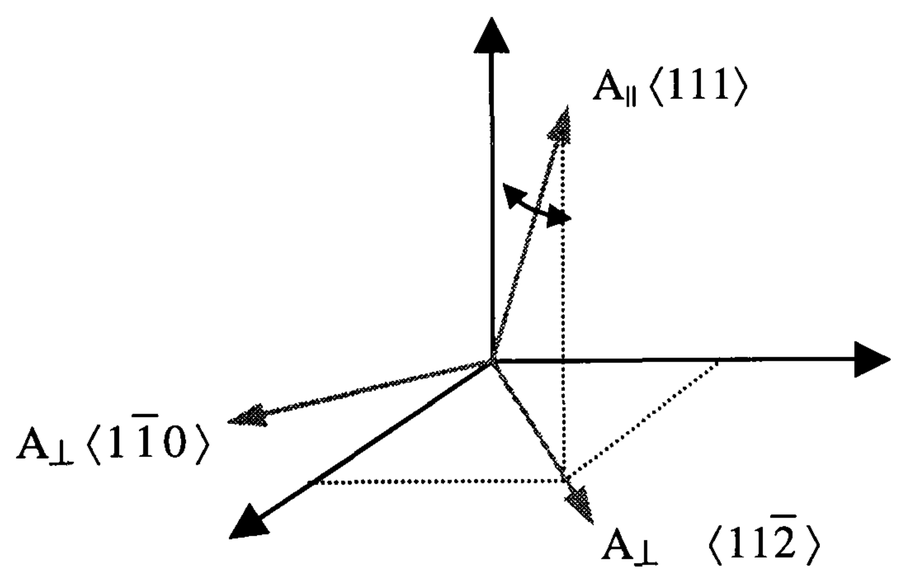

Figure 7.8: Axes showing how the components of the hyperfine interaction could be changed. When the symmetry is C_{3v}, the hydrogen is constrained to be along the $\langle 111 \rangle$ axis, and the two perpendicular components are shown. If however, the $A_{\|}$ was allowed to move slightly, the symmetry would be lowered to C_{2h} and the hydrogen atom would no longer be along the $\langle 111 \rangle$ axis. The only constraint for this would be one of the $A_\perp$ would have to be along the $\langle 1\bar{1}0 \rangle$ direction.

7.6 Model of the VH^- centre

A model for the VH^- defect can now be considered. The information gained from the experimental analysis can be summarised:

1. The symmetry of the defect is C_{3v}.
2. The overall electron spin of the defect is 1.
3. The zero field splitting term, D, is very similar to that for NV^-.

4. The defect involves a single hydrogen atom.
5. There is no change in the EPR spectrum when the temperature is lowered to ~5 K.

From the simulations, hydrogen has been identified as the only impurity atom incorporated in this defect, and it is proposed that the new defect is a VH^- complex, with the hydrogen bonded to one of the four carbon neighbours surrounding the vacancy, figure 7.9. The unpaired electrons will therefore be localised in an orbital constructed from the remaining three carbon dangling orbitals.

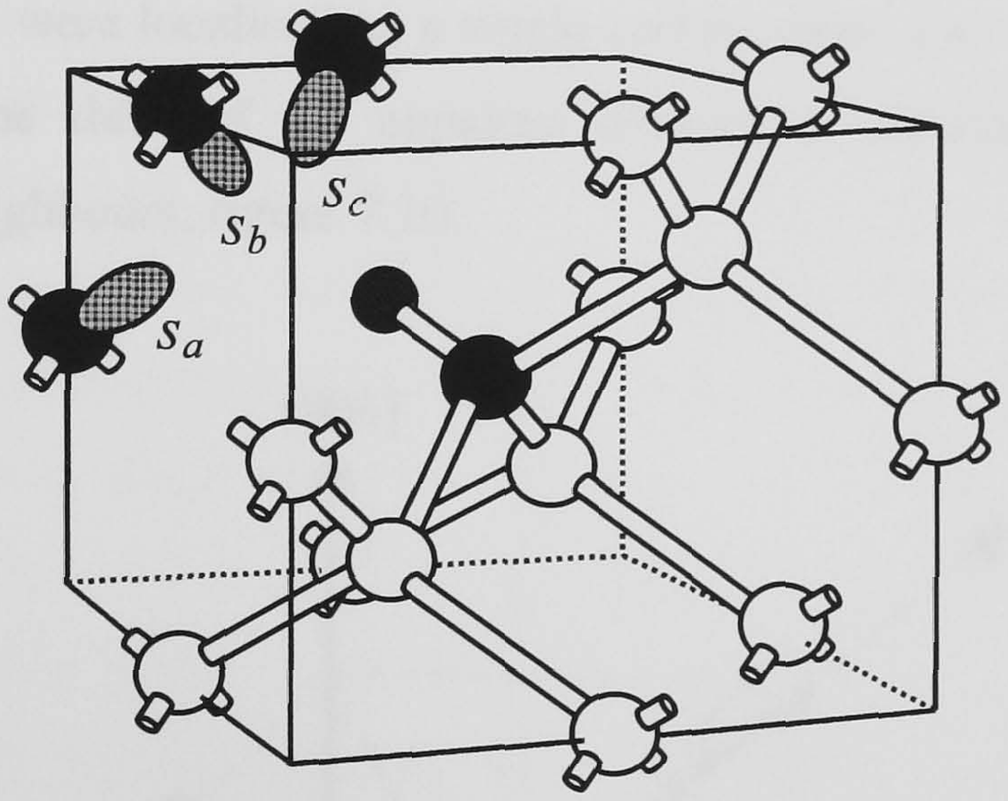

Figure 7.9: Model of the VH^- defect in diamond. The black atoms are the four carbon atoms that surround the vacancy and the small grey atom is the hydrogen atom.

Each term of the spin Hamiltonian needs to be considered separately to argue the model proposed for this defect. The g-value is similar to that for the NV^- defect and is characteristic of a vacancy-related defect. The *D*-value is also similar to the value for NV^-, which implies the unpaired electron probability wavefunction is similar for the two defects. The proton hyperfine interaction can be expressed in terms of the isotropic and anisotropic components, table 7.4.

a	$= {}^1/_3 (A_\parallel + 2A_\perp)$	1.7 (1) MHz
b	$= {}^1/_3 (A_\parallel - A_\perp)$	–0.28 (1) MHz

Table 7.4: Isotropic (a) and anisotropic (b) components of the proton hyperfine interaction.

If the proposed model is correct, this small hydrogen hyperfine interaction must be explained. The isotropic component is very small (table 7.4), which indicates that there is

negligible unpaired electron probability density on the hydrogen atom. This is consistent with the proposed model in that the unpaired electron probability density is localised on the three carbon dangling orbitals surrounding the vacancy. The small value of a most probably originates from spin polarisation. The fact that $A_{\|} < A_{\perp}$ indicates that a and the isotropic component b have opposite signs ($A_{\|} = a + 2b$, $A_{\perp} = a - b$).

The anisotropic hydrogen hyperfine interaction must arise from a dipolar interaction between the unpaired electron distributed over the three carbon dangling orbitals and the hydrogen atom. The distribution of unpaired electron makes the dipole calculation more complicated than if it were localised on a single carbon atom, and the problem is approached by assuming that one third of the unpaired electron is localised on each of the three equivalent carbon neighbours, figure 7.10.

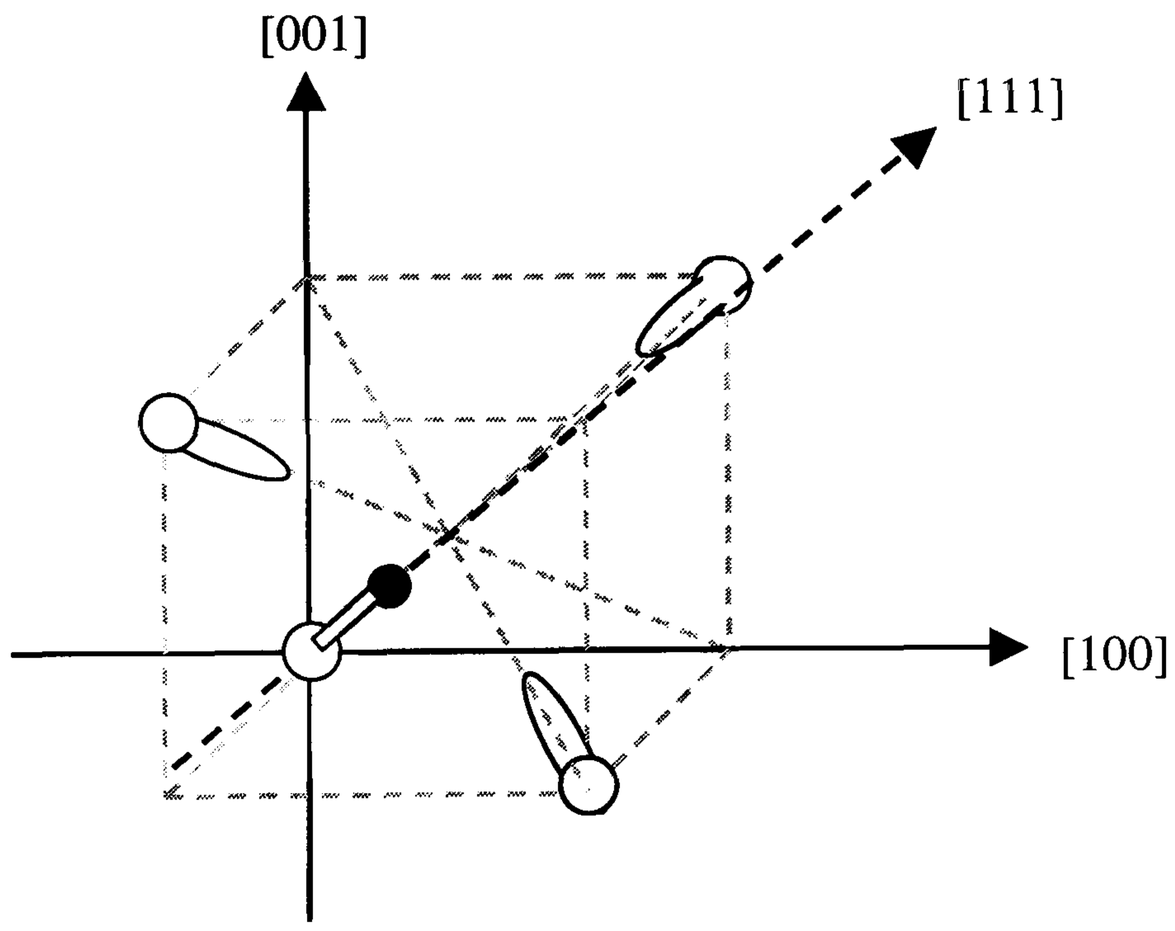

Figure 7.10: The dipolar calculation for the VH^- defect.

In order to calculate the contribution of unpaired electron from each carbon dangling bond on the hydrogen atom, the distance between the two, r, and the angle the vector makes to the [001] axis, φ, must be determined, figure 7.11. For the calculation, the C – H bond length is taken to be 1.05 Å, and the next-nearest-neighbour carbon separation as 2.51 Å. Using the cosine and sine rule respectively, the value of r is 1.76 Å, and φ is 110.15°.

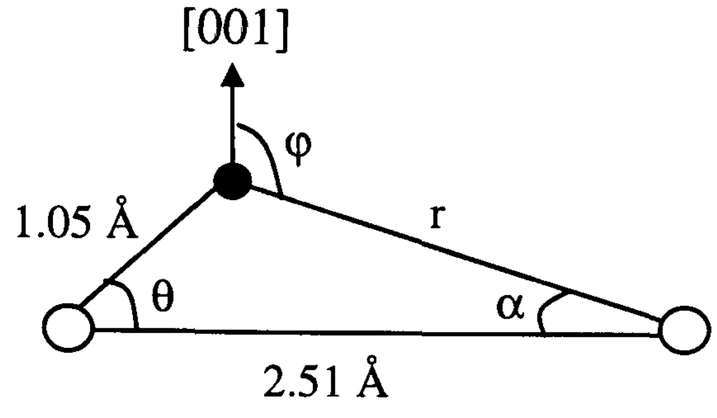

Figure 7.11: Information extracted from figure 7.10 needed to calculate the value of r and φ.

As before, the dipolar hyperfine interaction resulting from the three contributions is calculated by determining the individual hyperfine matrices, transforming them to a common coordinate axis system and then summing them together, Appendix 4. The matrix is then diagonalised to calculate the theoretical dipolar hyperfine matrix.

This calculation predicts a value for b of –0.23 MHz. Experimentally, it was determined that b = –0.28 MHz, table 7.4. Both experiment and theory show that the hyperfine principal axis is orientated along the C – H ⟨111⟩ direction. If the unpaired electron were entirely localised on just one of the three carbon atoms, the point dipole approximation gives b = 14.5 MHz. The value of b determined from the dipolar calculation comes about due to the partial cancellation of the three contributions to the interaction. b is very sensitive to the relaxation of the defect and further delocalisation of the unpaired electron. The calculation shows that the model satisfactorily explains the small experimental value of b.

A negative charge state has been assigned to the VH defect. This is because it is known that the overall electron spin is 1, which requires an even number of electrons in the carbon dangling bonds. The zero-field splitting is the same as for the NV^- defect, and so four electrons would be expected.

One would expect to observe VH^0 using EPR because it will have an overall spin of ½. The reason it has not been observed is because it would be located very close to the central region at g ≈ 2, which, in all the samples shown to contain VH^-, also contain NVH^- in significant concentrations.

It has been shown that the VH^- model is consistent with all of the observed properties of the new EPR centre. However, comparisons were made in section 7.2 with the corresponding VH^0 defect observed in silicon. It has now been shown that the electronic structure of the V–H defect in diamond is very different to that in silicon. In summary of the

V–H defect in silicon, at low temperatures the defect has C_{1h} symmetry with the hydrogen atom bonded to one of the four silicon atoms surrounding the vacancy. Two other silicon atoms form an extended Si–Si bond, leaving the unpaired electron localised on a single Si atom. As the temperature is increased above 100 K, the symmetry is averaged to C_{3v} as a result of the thermally activated hopping of the silicon dangling bond between the three equivalent configurations. This results in no proton hyperfine structure being observed above 100 K.

No symmetry change is observed with VH^- when the temperature is lowered, and it has previously been shown that the formation of long C–C bonds from dangling orbitals is not observed [7.15, 7.16]. As a result, it is not possible to accurately predict the properties of the V–H defect in diamond using the data for the equivalent defect in silicon.

7.7 Conclusions and Further Work

The following conclusions have be made from the experiments:

- The overall spin of the defect is 1.
- The defect has C_{3v} symmetry.
- A single hydrogen atom and a single vacancy are incorporated within the defect.
- There is no symmetry lowering as the temperature is lowered to ~4 K,

The model proposed for the VH^- defect is consistent with all of these experimentally determined parameters.

It has been shown that it is not possible to accurately predict the properties of the V–H defect in diamond using the data obtained for the analogous defect in silicon. However, the V–H defect in diamond is the simplest hydrogen-vacancy complex and comparisons with the V–H complex in silicon leads one to speculate that V_mH_n (where m and n are integers ≥ 1) may exist and be responsible for many of the new, unidentified systems observed in single crystal CVD diamond.

Although a large amount of work has been carried out on this defect, there is still much more that can be done. In the same way as it has not been able to determine the absolute sign of D for NV^-, the sign cannot be determined for VH^-. In order to find this absolute sign, the process described earlier in the chapter would have to be used.

The annealing behaviour of this defect would be an interesting thing to be studied. To what temperature is this defect stable? It has been observed in as grown samples, which means that it must be stable to at least 900 °C.

What are the mechanisms involved in the production of VH^-? How and why is it grown into the lattice, and what controls the amount produced?

An infrared absorption peak at 3323 cm^{-1} has been tentatively assigned to the C–H stretch mode in this defect. Studies are in progress to prove or disprove this theory.

These are all interesting questions that need to be answered in order to have a complete understanding of the defect.

References

[7.1] S. J. Pearton, J. W. Corbett and T. S. Shi, Appl. Phys. A **43**, 153 (1987)

[7.2] Yu.V. Gorelkinskii and N. N. Nevinnyi, Physica B **170**, 155-167 (1991)

[7.3] R. Jones, B. J. Coomer, J. P. Goss, B. Hourahine and A. Resende, Solid State Phen. **71**, 173 (2000)

[7.4] K. Bergman, M. Stavola, S. J. Pearton and T. Hayes, Phys. Rev. B **38**, 9643 (1988)

[7.5] J. D. Holbech, B. Bech-Neilson, R. Jones, P. Sitch and S. Oberg, Phys. Rev. Lett. **71**, 875 (1993)

[7.6] B. Bech-Nielson, L. Hoffmann and M. Budde, Mater. Sci. Eng. B **36**, 259, (1996)

[7.7] M. Budde, B. Bech-Nielson, P. Leary, J. Goss, R. Jones, P. R. Briddon, S. Oberg and S. J. Breuer, Phys. Rev. B **57**, 4397 (1998)

[7.8] B. Bech-Neilson, J. Olajos and H. G. Grimmeiss, Phys. Rev. B **39**, 3330 (1989)

[7.9] B. Bech-Neilson and H. G. Grimmeiss, Phys. Rev. B **40**, 12403 (1989)

[7.10] P. Deak, L.C. Snyder, M. Heinrich, C. R. Ortiz and J. W. Corbett, Physica B **170**, 253-258 (1991)

[7.11] B. Bech-Nielson, P. Johannesen, P. Stallinga, K. Bonde-Nielson and J. R. Byberg, Phys. Rev. Lett. **79**, 1507, (1997)

[7.12] P. Stallinga, P. Johannesen, S. Herstrom, K. Bonde-Nielson, B. Bech-Nielson and J. R. Byberg, Phys. Rev. B **58**, 3842 (1998)

[7.13] P. Johannesen, R. Jakobsen, P. Stallinga, B. Bech-Nielson and J. R. Byberg, Phys. Rev. B **66**, 235201 (2002)

[7.14] Revised parameters presented in Chapter 6 of this thesis

[7.15] J. Isoya, H. Kanda, Y. Uchida, S. C. Lawson, D. Yamasaki, H. Itoh and Y. Morita, Phys. Rev. B **45**, 1436 (1992)

[7.16] J. A. Van Wyk, O. D. Tucker, M. E. Newton, J. M. Baker, G. S. Woods and P. Spear, Phys. Rev. B **52**, 12657 (1995)

Chapter 8

Mid and Near Infrared optical measurements on single crystal CVD Diamond.

8.1 Introduction

Optical absorption in diamond has been extensively studied and a list of many optical centres and some of their properties is given by Zaitsev [8.1]. However, previous work carried out on single crystal diamond grown using CVD techniques in the near infrared is extremely limited. The purpose of this chapter is to present some recent data.

The mechanisms involved during optical absorption can be divided into two; those that occur through nuclear only motions (such as lattice vibrations or phonons), at relatively low energies in the infrared range, and electronic transitions, which generally occur at higher energies. The former is the result of the interactive coupling between the motions of thermally induced vibrations of the atoms in the crystal lattice, and the incident radiation. The latter, the electronic transitions, are the result of the interaction between the incident radiation and the motions of the electrons. In order that a mode of vibration can absorb, a mechanism must exist for coupling the vibrational motion to the infrared radiation. There are three different coupling mechanisms:

1. Reststrahl absorption, which only occurs in ionic crystals and is caused by the creation of single phonons in the lattice.

2. Multi-phonon absorption, which occurs when two or more phonons simultaneously interact and produce an electric moment with which the incident radiation may couple.
3. Defect induced one-phonon absorption. The introduction of defects or impurities into the diamond lattice destroys the periodicity of the lattice and creates a weak dipole moment, which allows electromagnetic radiation to excite single phonons and hence absorb energy.

Hunt gives a good introduction to the theory of infrared optical absorption, and for this reason, no further details will be discussed in this chapter [8.2].

Many absorption peaks are observed in the range 0.2 – 1.3 eV (1600 – 10500 cm^{-1}) and many have been identified to contain hydrogen and other impurities, however, where some of them have been extensively studied, others have had relatively small amounts of work carried out on them. Details of the previous work relevant to this chapter will be presented in the literature review in the next section. This chapter presents the results of infrared optical absorption measurements taken on a range of single crystal CVD diamond samples. The intensity of the absorption bands will be determined and any correlations between bands will be studied. Arguments will then be put forward for some of the bands originating from the same defect. Throughout this chapter, the absorption bands are referred to as their energy recorded at 77 K.

8.2 Literature Review

As mentioned before, only a limited amount of work has been carried out on CVD diamond in the near infrared region, and the work that has been done has primarily been done on polycrystalline CVD diamond samples. This is important, because although many absorption peaks are present in all samples, some may be characteristic of samples grown or processed in a specific way. Hydrogen in diamond has already been discussed in some detail in section 2.5, so only infrared optical absorption measurements will be discussed in this chapter.

Some of the transitions of primary interest in this thesis were first reported in 1995 by Fuchs *et al* [8.3, 8.4]. They reported measurements in the range 1400 – 8000 cm^{-1}, figure 8.1.

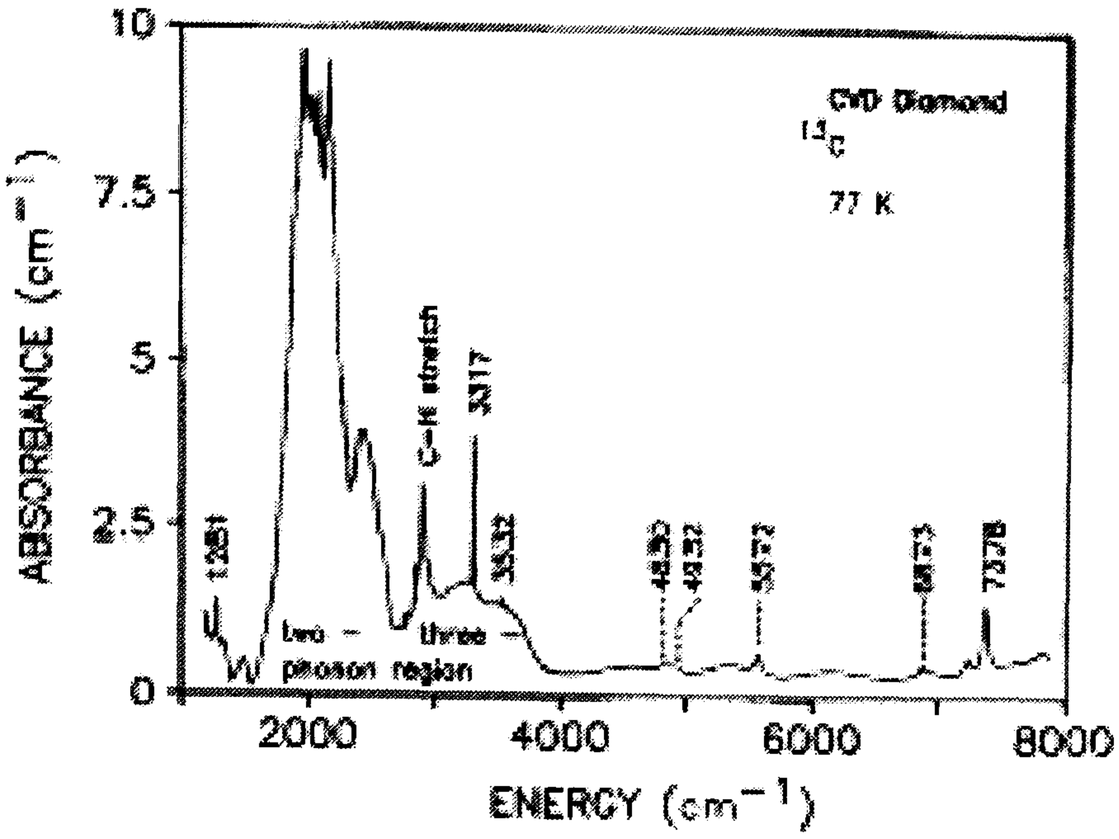

Fig. 8.1: Infrared spectrum of a homoepitaxially grown ^{13}C diamond layer deposited on a ^{12}C diamond substrate of comparable thickness. (Taken from Fuchs et al [8.4])

Isotopic replacement of carbon, hydrogen and nitrogen by ^{13}C, ^{2}H and ^{15}N helped to identify the impurities incorporated in the defects responsible for the some of the absorption bands [8.3, 8.4]. The important findings of Fuchs *et al* are summarised in table 8.1 below.

Peak (cm^{-1}) [1]	**Isotope Dependence**	**Conclusions**
3123.6	^{13}C – 3114.5 cm^{-1} Disappeared with ^{2}H, observable in mixed sample. No change with ^{14}N / ^{15}N.	C – H LVM [2], involving one carbon atom
3323	^{13}C – 3317 cm^{-1} Disappeared with ^{2}H, observable in mixed sample. No change with ^{14}N / ^{15}N.	
5572	^{13}C : H – 5572 cm^{-1} ^{12}C : D – 5449 cm^{-1} ^{13}C : (D,H) – 5483, 5514 and 5544 cm^{-1}	More complex than a single H atom, as mixed sample split into three
6870	^{13}C : H – 6872 cm^{-1} ^{12}C : D – 6833 cm^{-1} ^{13}C : (D,H) – 6833 and 6877 cm^{-1}	One H atom involved
7238	^{13}C : H – 7240 cm^{-1} ^{12}C : D – 7191 cm^{-1} ^{13}C : (D,H) – 7191 and 7238 cm^{-1}	One H atom involved
7366	^{13}C : H – 7378 cm^{-1} ^{12}C : D – 7324 cm^{-1} ^{13}C : (D,H) – 7346 cm^{-1} (broad)	One H atom involved

Table 8.1: Summary of isotope replacement experiments carried out by Fuchs et al [8.3].

[1] Peak position in samples grown using natural abundance source gases.
[2] LVM = Local Vibrational Mode

The electronic transitions of particular importance to the work presented in this chapter are the ones found between 0.65 – 1.1 eV (~5500 – 8800 cm^{-1}). Table 8.2 shows the main peaks observed in the infrared, giving energies in meV and frequencies in cm^{-1}. Fuchs used deuterated samples to study the effect on these absorption bands. The deuterated samples resulted in a pronounced red shift of the 6870, 7240 and 7380 cm^{-1} absorption bands, which implies that hydrogen must be involved in the defects responsible for the transitions. The transitions just discussed are shifted to higher energies in the ^{13}C sample, which is similar behaviour to other electronic centres observed in the visible [8.5]. This can be an indication that the transitions are electronic.

Energy (meV)	Frequency (cm^{-1})	Energy (meV)	Frequency (cm^{-1})
154	1240	691.8	5571
384	3098	797.7	6428
385	3107	851.5	6870
387	3123	892.6	7194
401	3235	896.1	7227
411	3317	897.7	7243
438	3532	913.4	7366
599	4830	915	7380
612	4932	1086	8759

Table 8.2: Table giving the conversions between eV and cm^{-1}.

8.3 Samples and Experiments

Single crystal synthetic diamonds grown by microwave plasma chemical vapour deposition were used for this study. Several were doped with nitrogen during growth. Details of the samples can be found in appendix 1. The experiments were carried out using a Bruker IFS66 Fourier Transform Infrared Spectrometer at King's College London, and a Perkin Elmer Spectrum GX Spectrometer at the University of Warwick.

These experiments extended the range initially covered by Fuchs *et al*, to include the all energies between 800 – 20000 cm^{-1}. This range extends into the visible region, but these experiments will not be discussed in any detail in this chapter. Measurements were recorded in the mid infrared region (800 – 1500 cm^{-1}, 0.1 – 0.18 eV), in order to calculate the concentration of N^+ in the samples (see appendix 3 for the Nitrogen Concentration Wizard).

The concentration of N_S^0 can also be determined using this method, and this concentration was verified using EPR calculations. However, sensitivity is an issue and N^+ can only be detected to a concentration as low as ~1 ppm, and N_S^0 ~ 5 ppm.

Because of the presence of many absorption bands, specific ones were chosen to be studied in further detail. They were; 691.8, 797.7, 851.3, 892.6, 896.1, 897.7, 913.4 and 1086 meV. Initially, a systematic study on a series of samples was carried out to identify which samples contained the relevant absorption bands. The measurements were recorded at 77 K so that a direct comparison could be made with figure 8.1 and each other. Measurements were also recorded at room temperature and it became apparent that there was a significant temperature dependence with the absorption bands. For this reason a complete temperature variation was performed between 4.8 – 300 K.

Once the data had been collected, the intensity and position of each peak was determined. To calculate the intensity of each peak, each spectrum was normalised to an absorption coefficient of 12.3 cm^{-1} at 2000 cm^{-1}. From here a Lorentzian line was fitted to each of the peaks and the area in units of $meVcm^{-1}$ determined, figure 8.2(a). A Lorentzian line was used for the fits, but only after fits using different lineshapes had been discarded. Gaussian, Voight and Lorentzian fits were all tested, and the Lorentzian produced the most accurate fit to the data in each case. Figure 8.2(b) shows the residual absorption when the experimental spectra and the Lorentzian fits are subtracted from each other.

Before the measurements were carried out, it was ensured that each sample was completely free from grease and dirt. Any dirt or grease on the sample would produce unwanted absorption. The samples were cleaned in a mixture of concentrated sulphuric acid and potassium nitrate, heated to about 250°C for about 30 minutes, and then rinsed in de-ionised water.

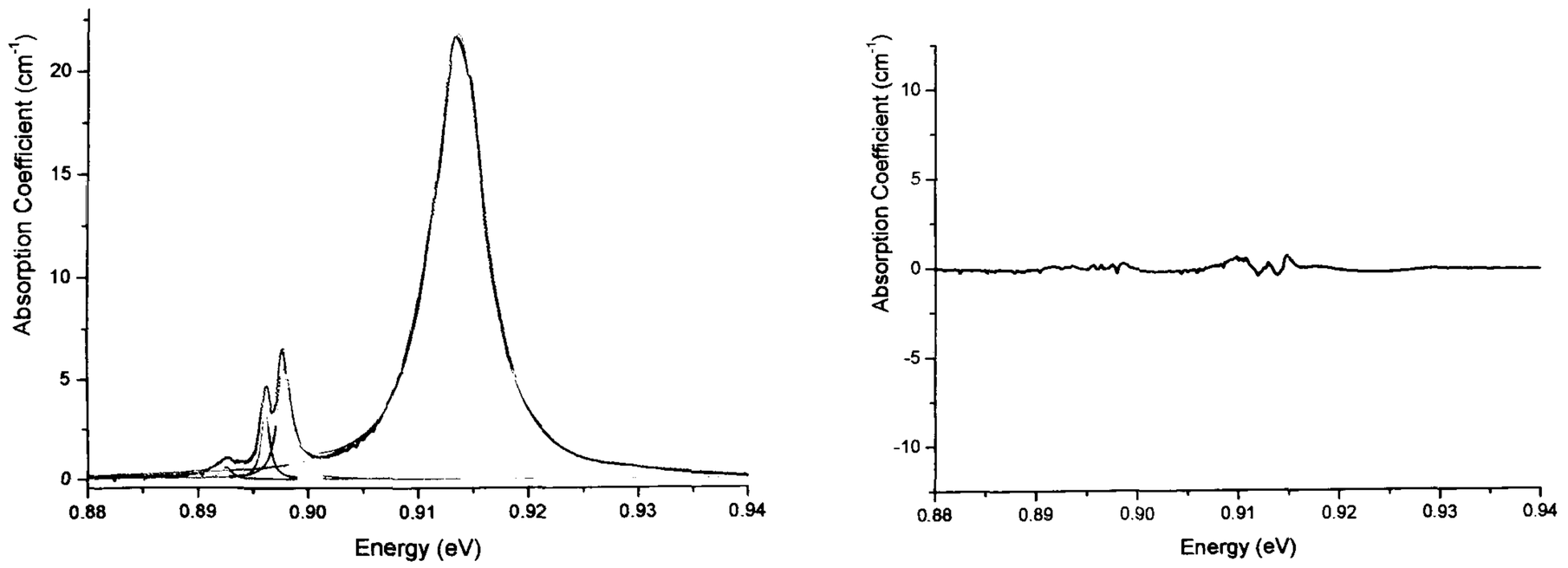

Figure 8.2: (a) 77 K spectrum showing how a series of Lorentzian lines can be fitted to a series of absorption lines and the intensity of each found. (b) The Lorentzian fit subtracted from the experimental data, shown on the same scale.

8.4 Results

8.4.1 Correlations between the lines

Figure 8.3 shows a typical spectrum taken on sample 8 at room temperature and 77 K with the peaks of interest clearly marked. As it can be seen, this sample contains many of the peaks originally observed by Fuchs in figure 8.1 [8.4].

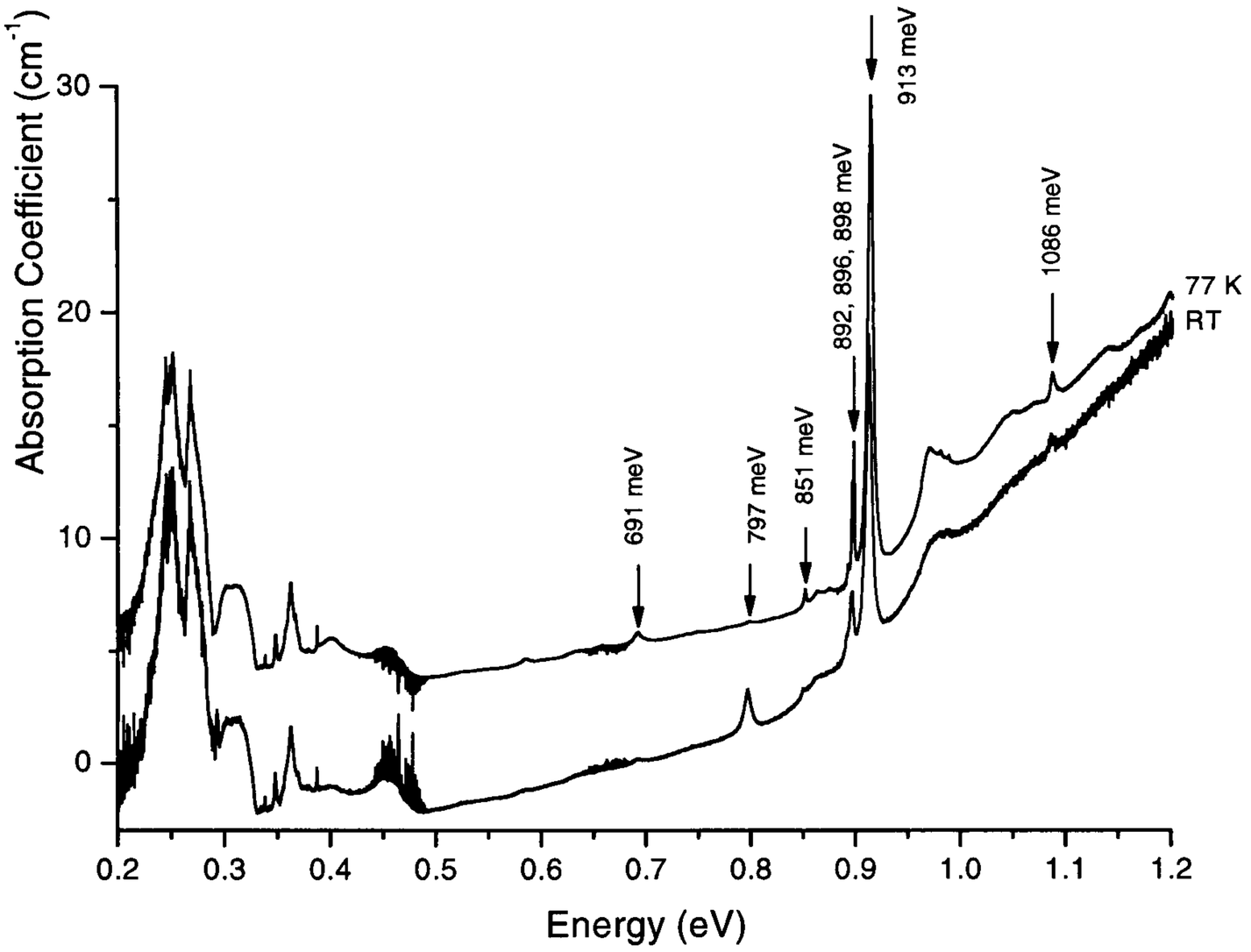

Figure 8.3: Spectrum taken from sample 8. Both room temperature and 77 K measurements are shown. The measurements were recorded using the Bruker FTIR spectrometer.

Figure 8.3 demonstrates the differences in spectra between 77 K and room temperature. All of the absorption bands observed in sample 8 are common to many of the CVD diamond samples of interest. Correlations have been observed between some of the absorption bands.

The 913.4 meV band is the most dominant peak in most of the samples, and as a result will be considered first. It is important to note that in several samples, the 913.4 meV absorption band has a shoulder at 914.8 meV, figure 8.4. Not all of the samples contain this shoulder and it has not been found to correlate with any of the other absorption bands.

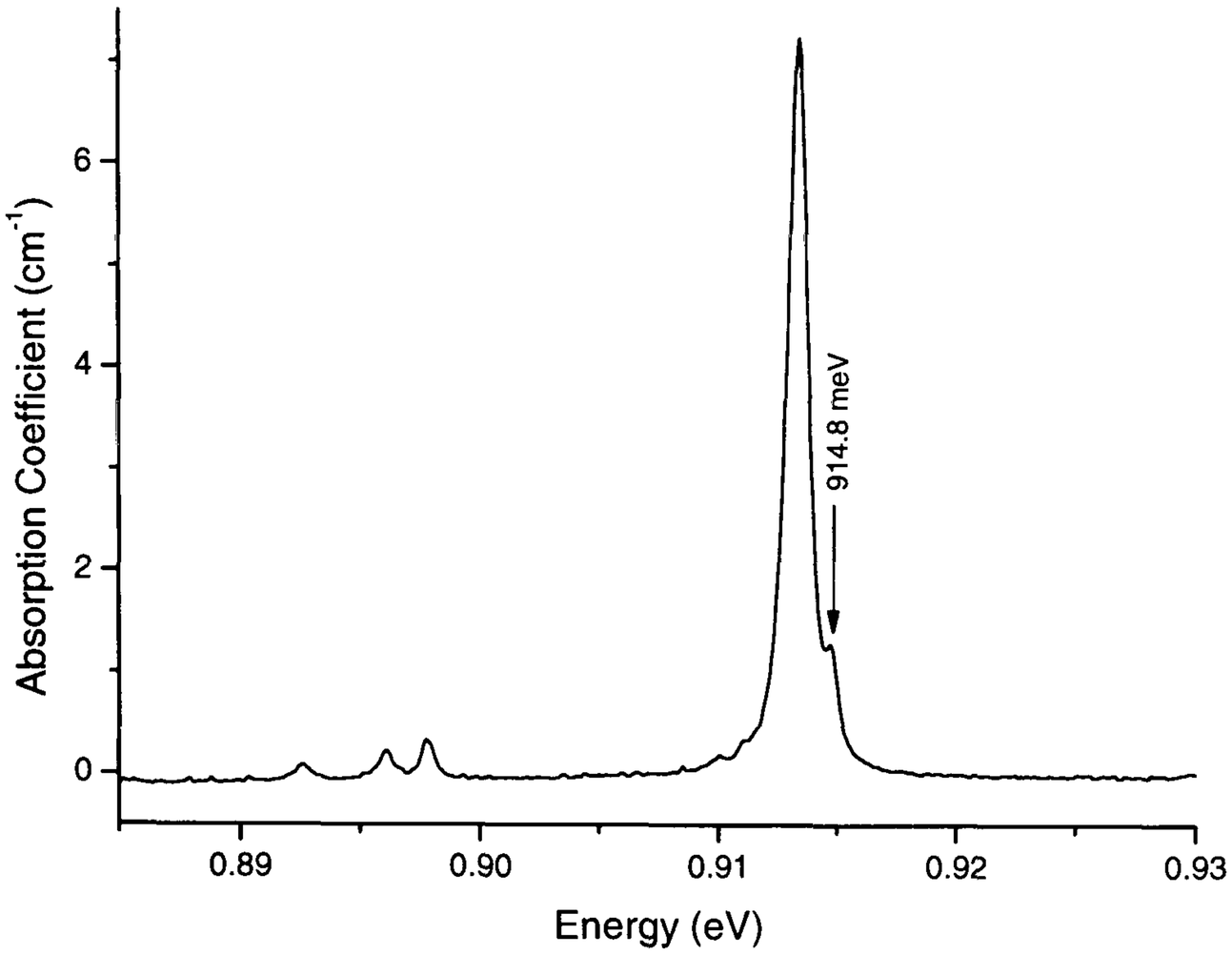

Figure 8.4: Absorption spectrum from sample 1, recorded at 77 K.

In figure 8.5, the intensity of the 797.7 meV peak is plotted against that of the 913.4 meV peak for a range of samples. Both intensities have been determined at room temperature. A clear correlation is observed between the relative intensities. The line of best fit (y = mx) has been constrained to go through the origin, and m = 0.20(5).

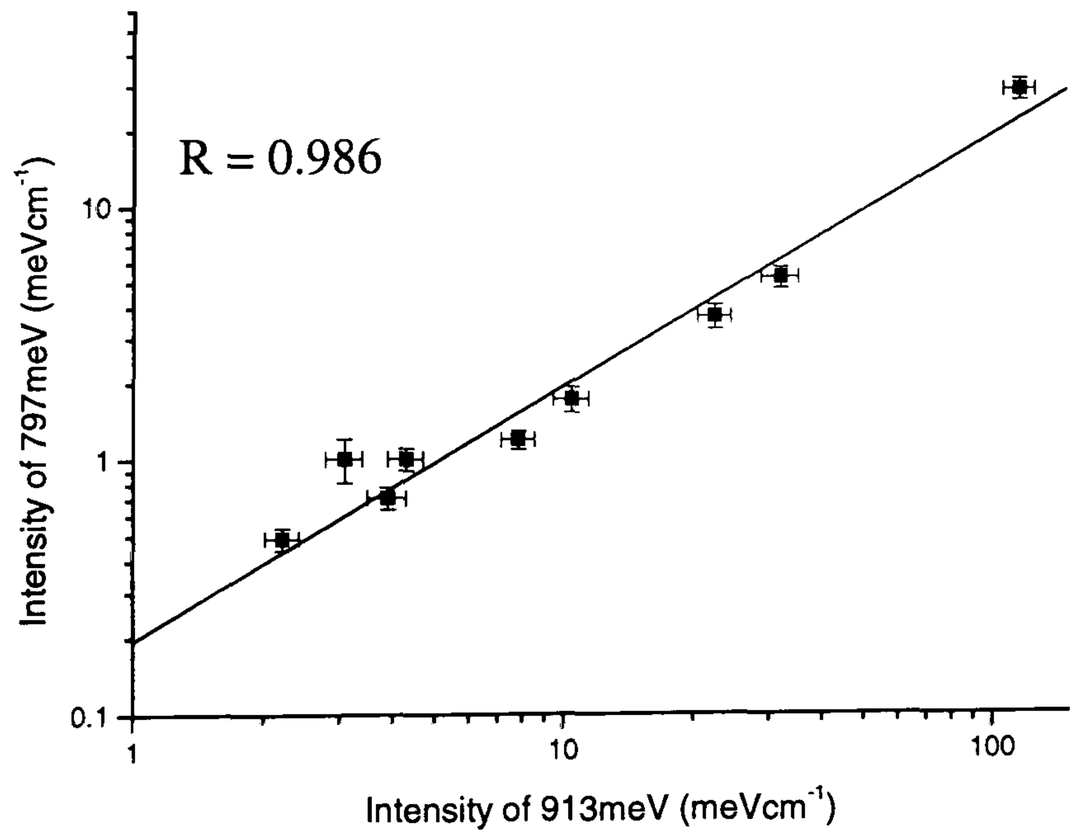

Figure 8.5: Room temperature correlation of the intensities of the 913.4 and 797.7 meV lines.

The intensity of the 1086 meV line also correlates with the intensity of the 913.4 meV line, as shown in figure 8.6. Once again, the fit has been constrained to pass through the origin, and m = 0.05(2).

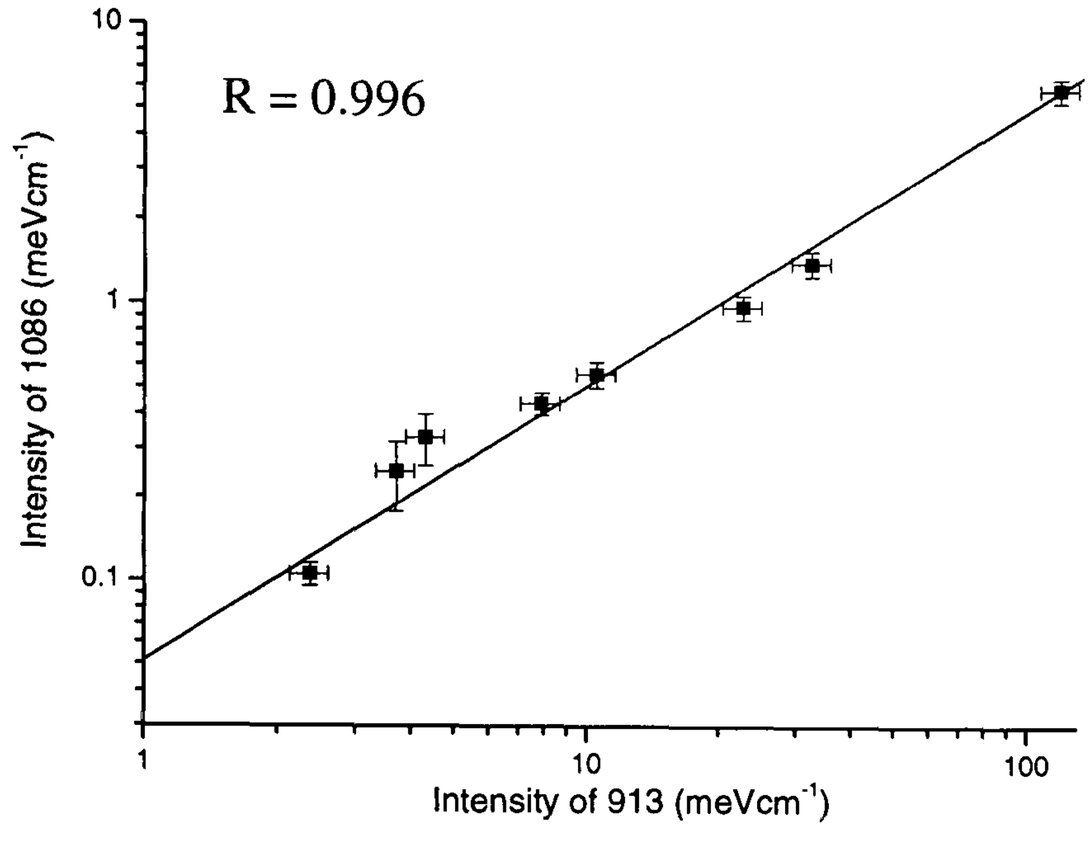

Figure 8.6: Correlation of the intensities of the 913.4 and 1086 meV absorption bands. The 1068 meV band is visible at all temperatures and decreases in intensity with the 913.4 meV line with increasing temperature. The data plotted on this graph was recorded at room temperature.

There is an R-value associated with each correlation plot, which is given on each. This is known as the Pearson's product moment correlation coefficient, which is a measure of the linear association between two variables. R only has a significant meaning when the data originates from a random sample and both variables are distributed normally. The closer R is to 1, the better the correlation between the two variables. Looking back at Figures 8.4 and 8.5, it can be seen that the absorption bands correlate with each other very well. This indicates that they may originate from the same defect.

Figure 8.7 below shows the region around the 913.4 meV absorption band in more detail. The measurement was recorded at 77 K, and clearly shows a group of three lines to the low energy side. This group of lines is present in all samples containing the 913.4 meV absorption band and on initial observation appeared to correlate.

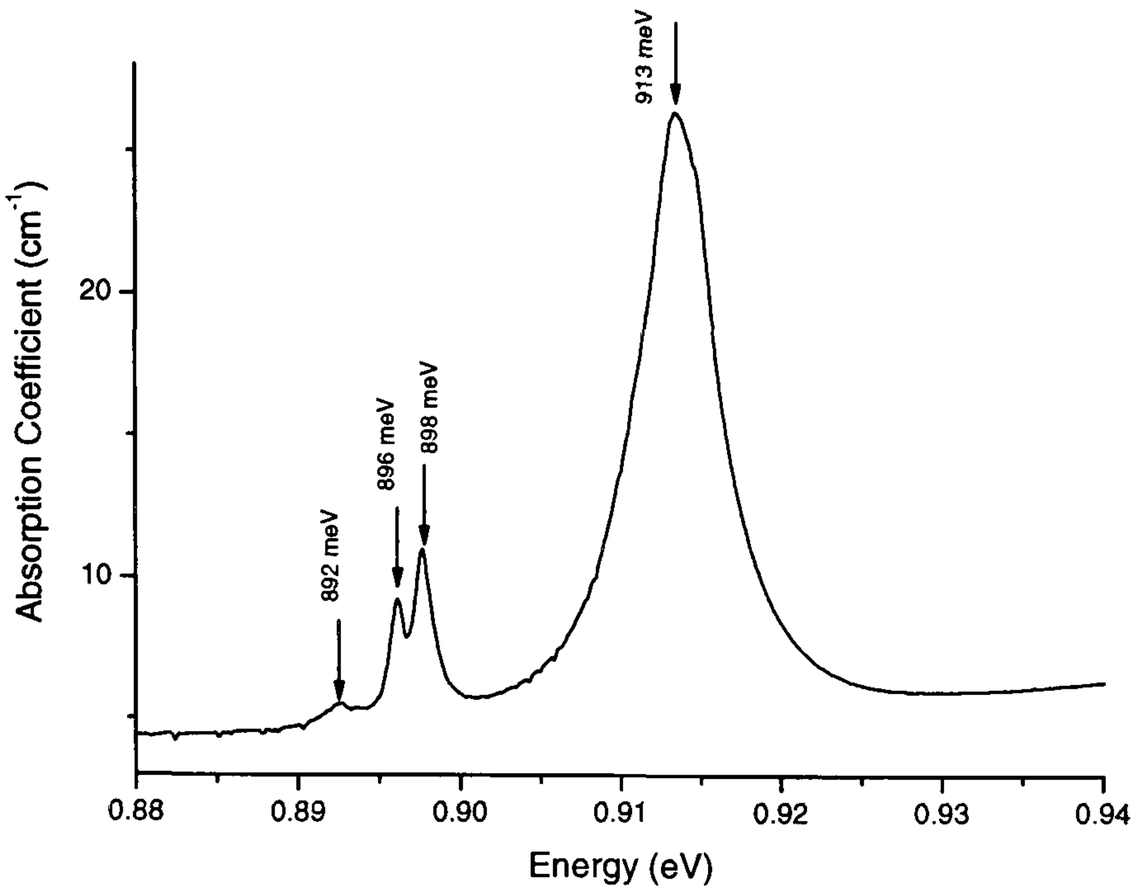

Figure 8.7: Zoomed in spectra of the absorption band at 913.4 meV and the three peaks to the low energy side.

Once again the intensities of all of the peaks were found and correlation plots were drawn. It was found that the intensities of the 897.7 and the 896.1 meV peaks correlate with each other, figure 8.8, and with the 913.4 meV peak, figure 8.9. The absorption band at 892.6 meV, however, does not correlate with anything, figure 8.10. In each case the fit has been constrained to go through the origin and m is given on each plot.

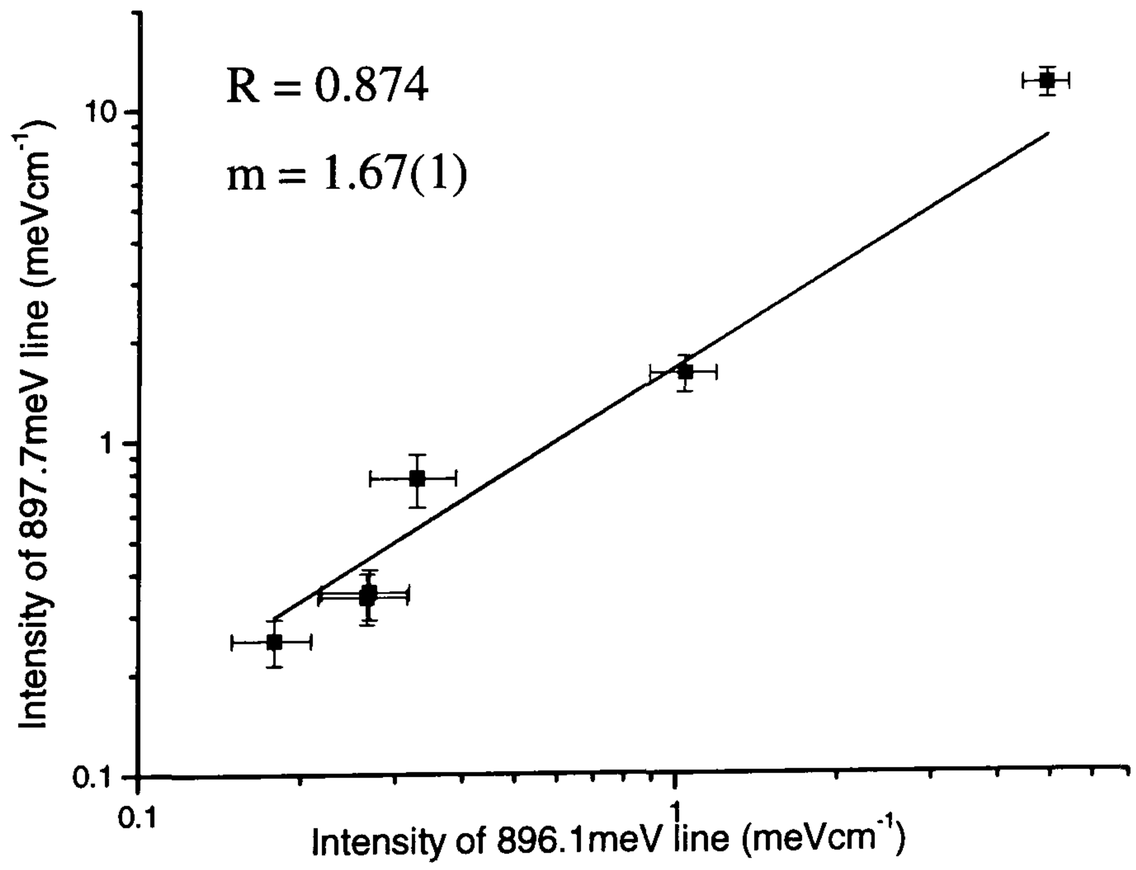

Figure 8.8: Correlation between the intensities of the 897.7 and 896.1 meV lines using data recorded at 77 K.

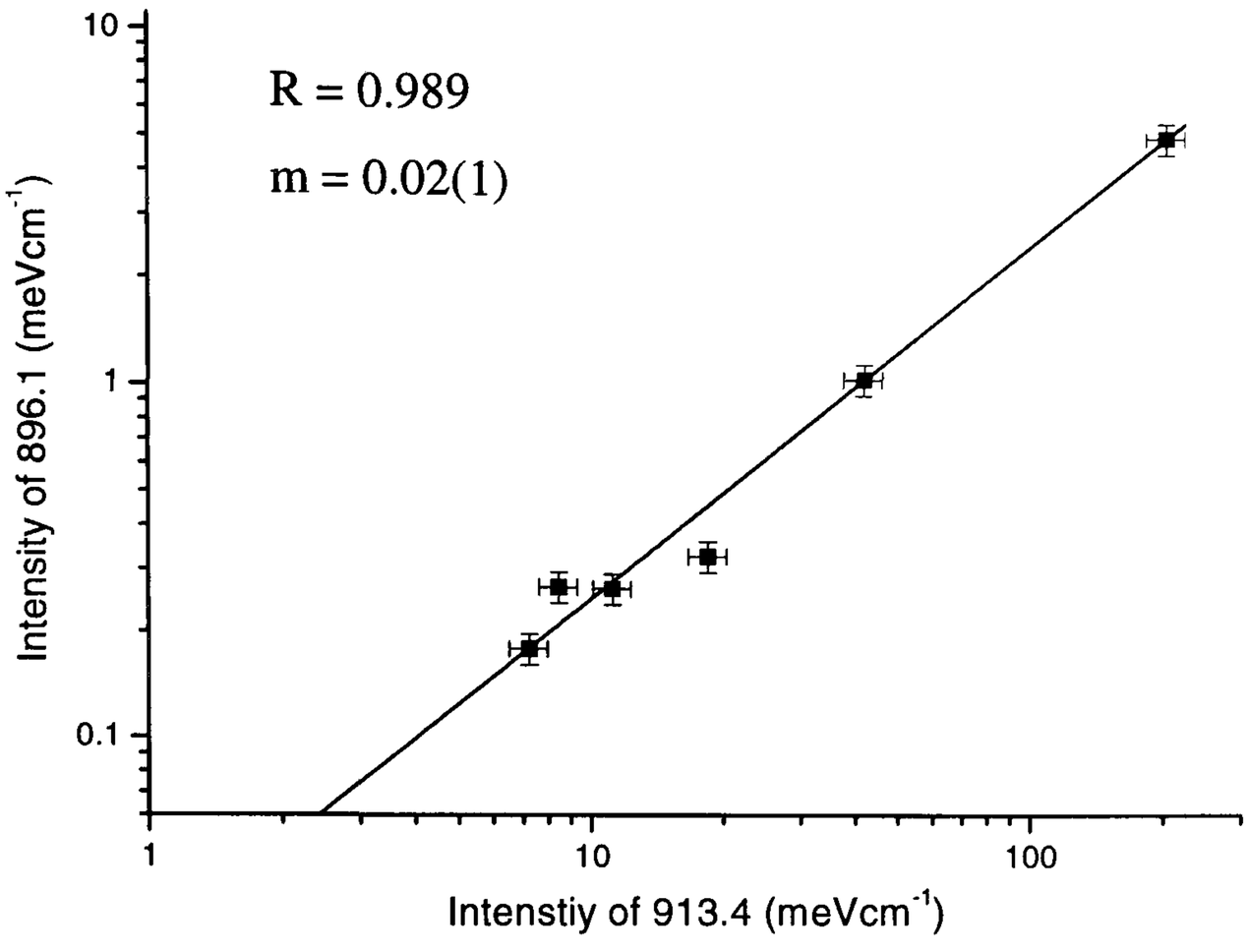

Figure 8.9: Correlation between the intensities of the 896.1 and the 913.4 meV lines. The fact that these two correlate automatically means that the 897.7 and the 913.4 meV lines correlate. Again the data used for the correlations was recorded at 77K.

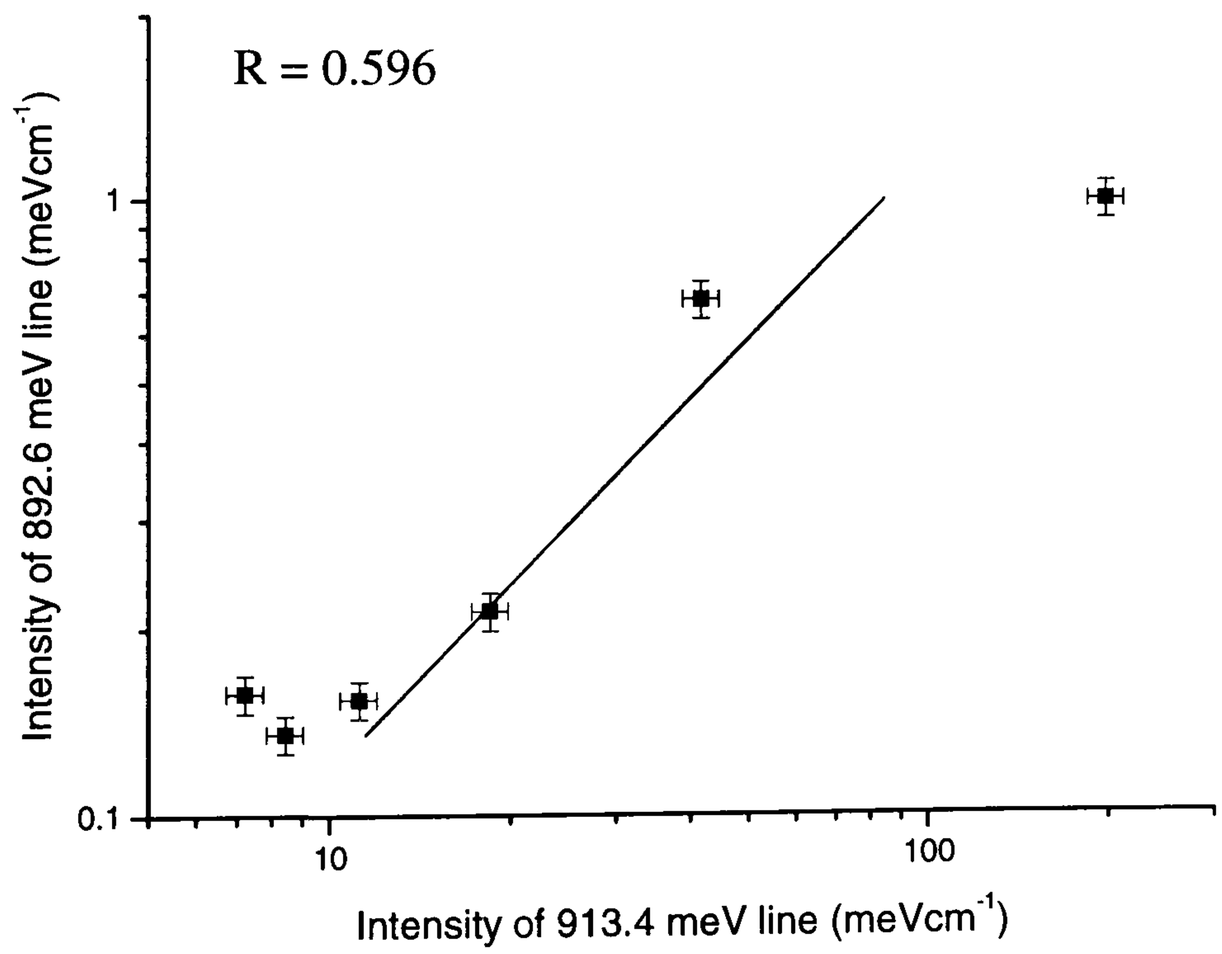

Figure 8.10: Plot of the intensity of the 892.6 against 913.4 meV lines. From the R value it can be seen that the two lines do not correlate. The data is taken from measurements recorded at 77 K.

As mentioned in section 8.3, measurements were also recorded in the visible region of the spectrum. This data will not be presented, but the absorption bands at 1945 (NV^-), 1984 and 2056 (NV^0) meV were commonly observed and no correlations were observed between any of them and the new features in the mid and near infrared.

None of the absorption bands observed in the mid infrared, as listed in table 8.2, have been found to correlate with the absorption bands in the near infrared. The broad band located at 969.8 meV correlates with the 913.4 meV band, and is believed to be a phonon sideband. This band will not be discussed any further in this chapter.

8.4.2 Temperature variation of the IR absorption lines

8.4.2a The 913.4, 892.6, 896.1 and 897.7 meV lines

Up until this point, only data recorded at 77 K and room temperature has been discussed. A full temperature variation was carried out on the samples to investigate the behaviour of each absorption band. Figure 8.11 shows the region around the 913.4 meV line as the temperature varies from 4.8 to 290 K. The data was recorded using sample 8, as in figure 8.3. Not every temperature is shown. Each of the spectra has had the absorption coefficient normalised to 12.3 cm^{-1} at 2000 cm^{-1} for a direct comparison. It is clear from figure 8.11 that not only is the intensity of each line varying as the temperature is changed, but also the position of the line.

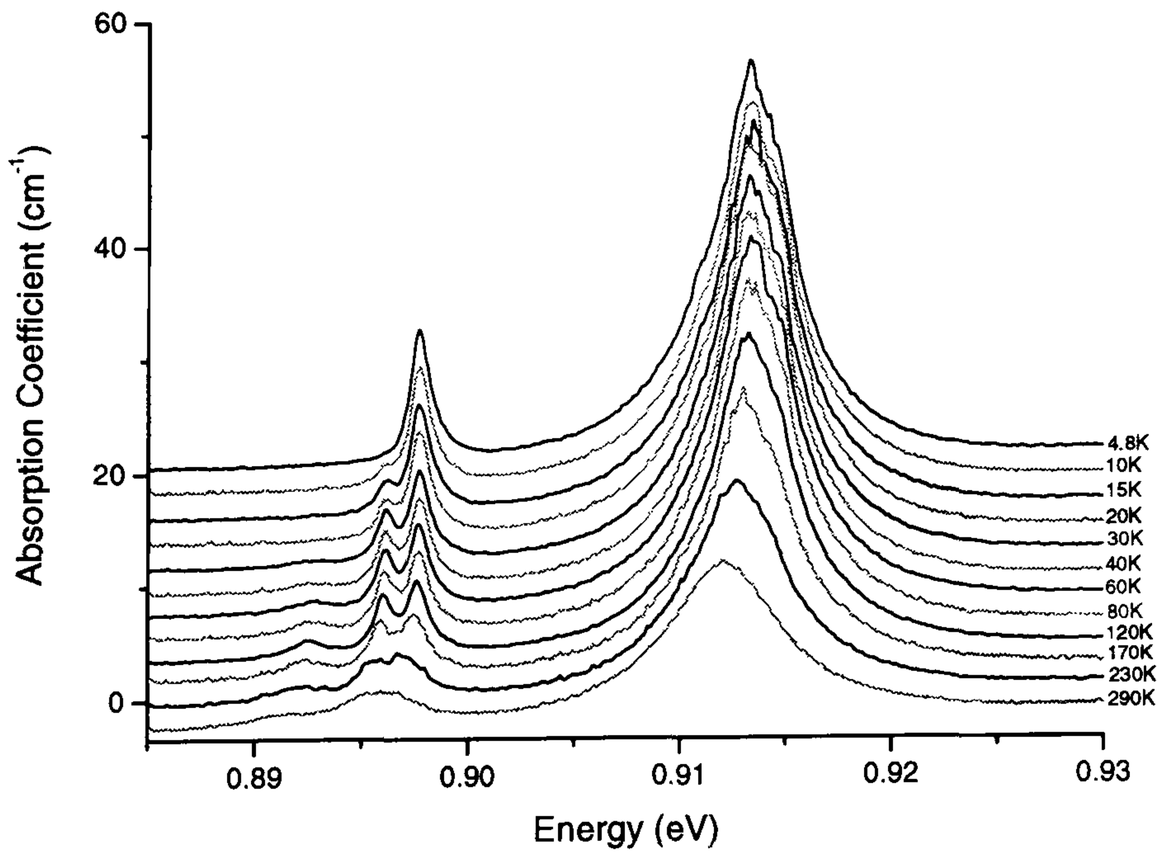

Figure 8.11: Temperature variation of the area around the 913.4 meV line

Figures 8.12(a) – (h) show how the position and intensity of each line changes with temperature. In each case the line width of the transitions have been studied and when the

transitions are very close together, for example the two at 896.1 and 897.7 meV, it is very difficult to accurately determine the change in linewidth. The linewidth of the 913.4 meV transition remains constant until approximately 100 K, when it gradually begins to increase. By room temperature, the linewidth has increased by ~23 %. The linewidth of the 892.6 meV transition is always broad and increases by ~15 % as the temperature is increased.

The errors shown on figures 8.12(a)-(h) are calculated by fitting the absorption band several times and noting the variation in intensity and position. At some of the temperatures it is very difficult to accurately determine with position and width of the bands. For this reason, some of the points plotted on the graphs can be discarded. For example, the 892.6 meV transition is not clearly visible until temperatures above 30 K, when it is very small. Because of this, the first couple of points on each graph can be considered inaccurate.

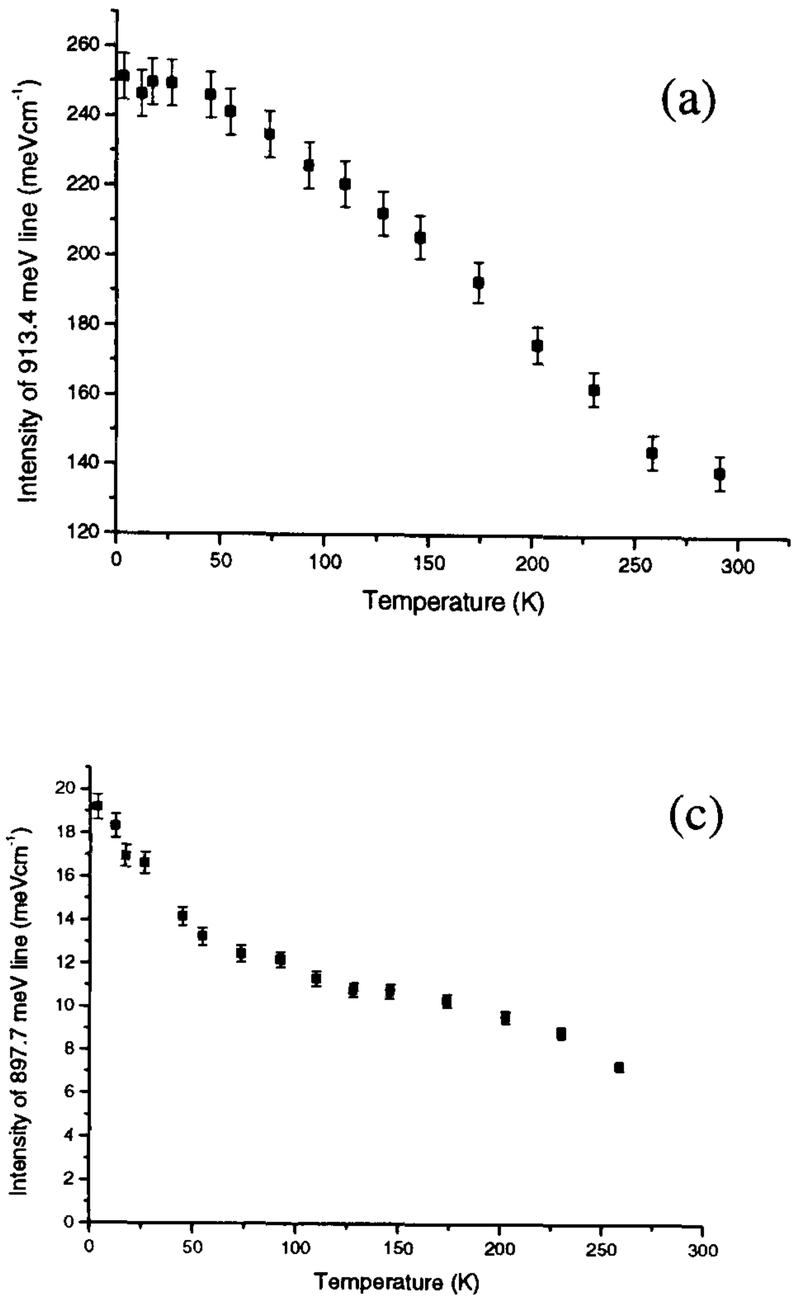

Figures 8.12(a)-(h): Plots showing how the intensity and position of each of the 913.4, 897.7, 896.1 and 892.6 meV absorption bands change with temperature.

8.4.2b The 691.8, 797.7 and 851.3 meV lines

There are three more lines that need discussing in reference to the temperature variation experiment: the 691.8, 797.7 and the 851.3 meV lines, figure 8.13. The correlation between the 797.7 and the 913.4 meV line has already been discussed in section 8.4.1.

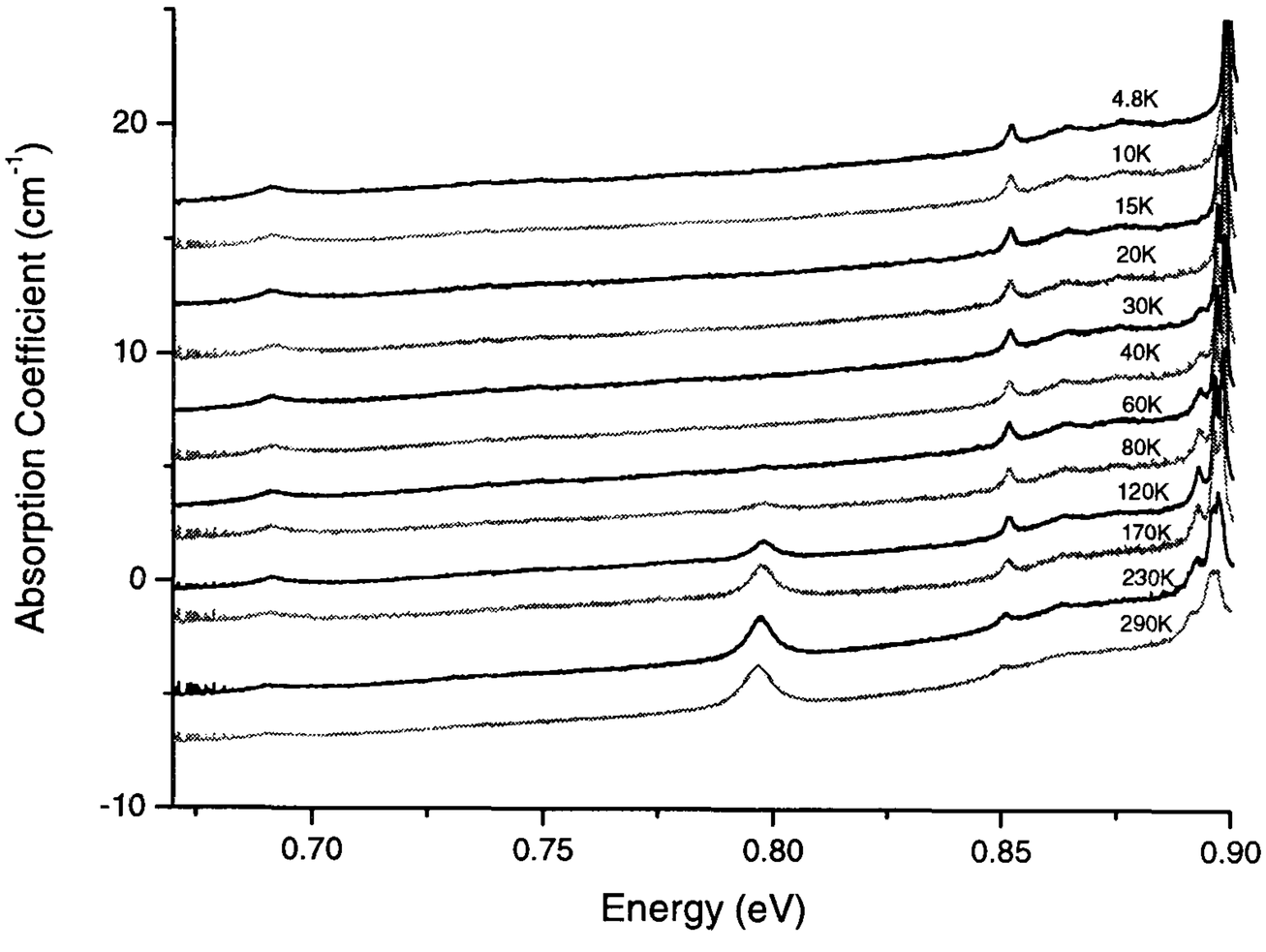

Figure 8.13: Temperature variation of the 691.8, 797.7 and the 851.3 meV lines. Again, not all temperatures are shown.

The 797.7 meV transition is not observed at low temperatures, figure 8.14(a). The linewidth increases as the temperature increases, and at room temperature is approximately 25 % wider than at 80 K.

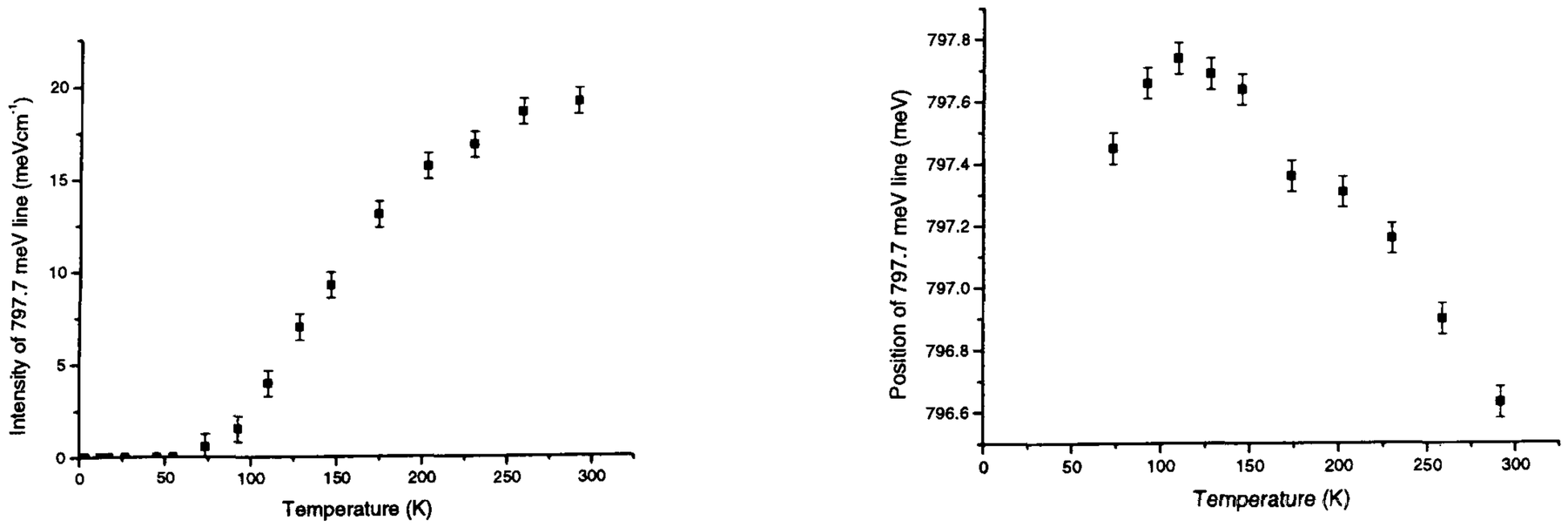

Figure 8.14(a) and (b): Plots showing how the position and intensity of the 797.7 meV line varies with temperature.

The 691.8 meV absorption band, although rather scattered, decreases in intensity as the temperature is increased, figure 8.15(a). The linewidth appears to remain constant as the temperature is decreased.

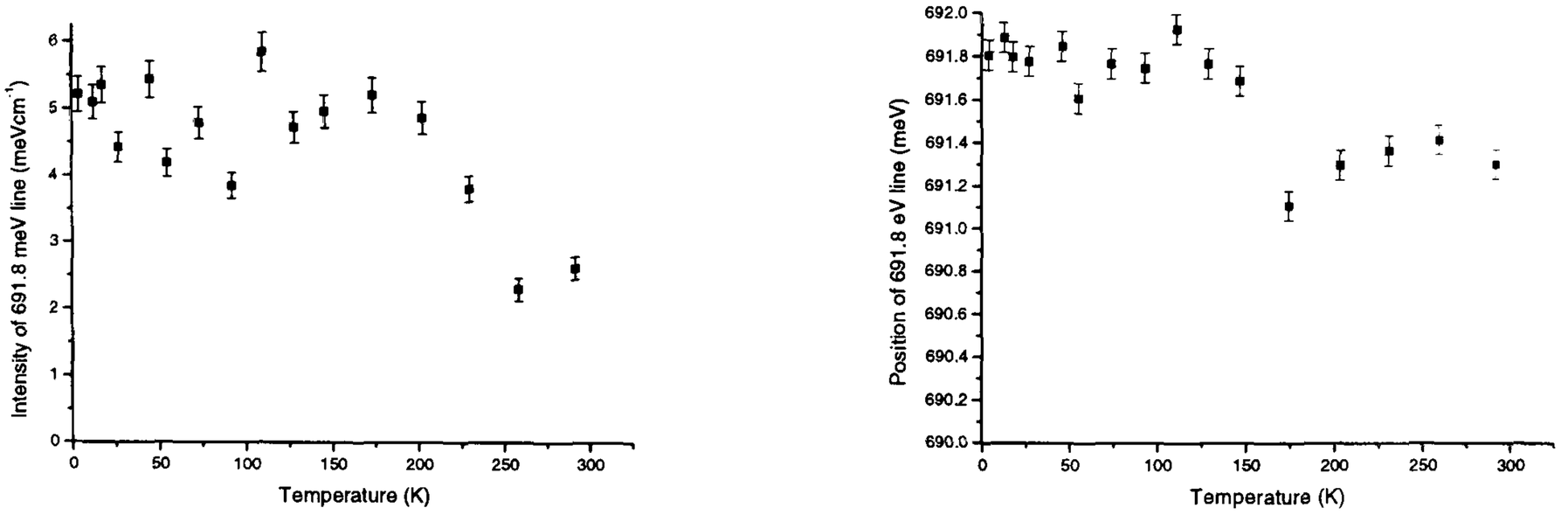

Figure 8.15 (a) and (b): Behaviour of the 691.8 meV line as the temperature is varied. The data looks very scattered so it is difficult to obtain accurate information from this.

The intensity of the 851.3 meV absorption band decreases in intensity as the temperature increases, figure 8.16(a), and the linewidth remains constant. The energy of the transition decreases from 851.3 meV at 4 K, to 850.1 meV at 290 K, figure 8.16(b).

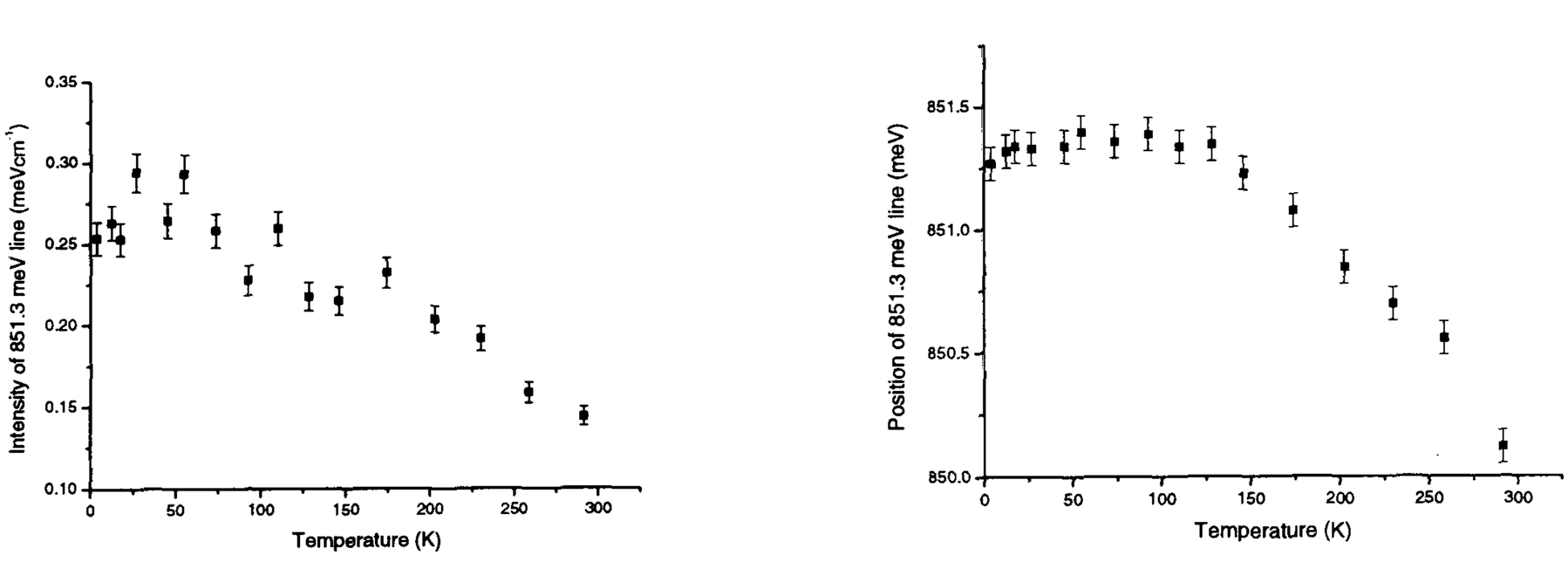

Figure 8.16 (a) and (b): Temperature variation of the 851.3 meV line. The intensity of the peak decreases as the temperature is increased, and the position of the peak shifts to a slightly lower energy as the temperature is increased.

8.5 Discussion of Results

8.5.1 The 913.4, 797.7 and 1086 meV system

From figure 8.5, it is possible to conclude that the intensities of the 913.4 and 797.7 meV absorption bands correlate with each other and possibly originate from the same centre. It has also been shown that the 1086 meV band correlates, but this will be left until the end

of this section for discussion. From this information, an energy level diagram can be constructed. The first observation from the temperature dependence of the intensities is that the 913.4 meV transition originates from the ground state of the defect, figure 8.17(a), and the 797.7 meV transition originates from an excited state, figure 8.17(b).

The intensity of each transition is calculated using equation (8.1) and using a least squares fit, the energy separation between the ground state and the first excited state ($\Delta_1 = E_2 - E_1$) can be calculated.

$$I_i = \frac{I_{0i} g_i \exp(-E_i / k_B T)}{\sum_j g_j \exp(-E_j / k_B T)} \tag{8.1}$$

where g_i and E_i are the degeneracy and energy of the ith level respectively. A fit was performed on each 797.7 and 913.4 meV transition separately and then simultaneously to allow the parameters to be calculated as though originating from a single system. The fits using equation (8.1) can be seen in figures 8.24 and 8.25. Each time the fit was performed the value of Δ_1 came out to be 34 ± 2 meV. The fact that the value of Δ_1 came out to be equal (to within experimental error) for both the 913.4 and 797.7 meV transitions is a strong indication that the two transitions originate from the same system. For this reason an energy level diagram can be drawn which incorporates both transitions, figure 8.17(c). The value of Δ_2 is determined to be 81 ± 2 meV, and has proved that the two transitions are not excited to the same energy level.

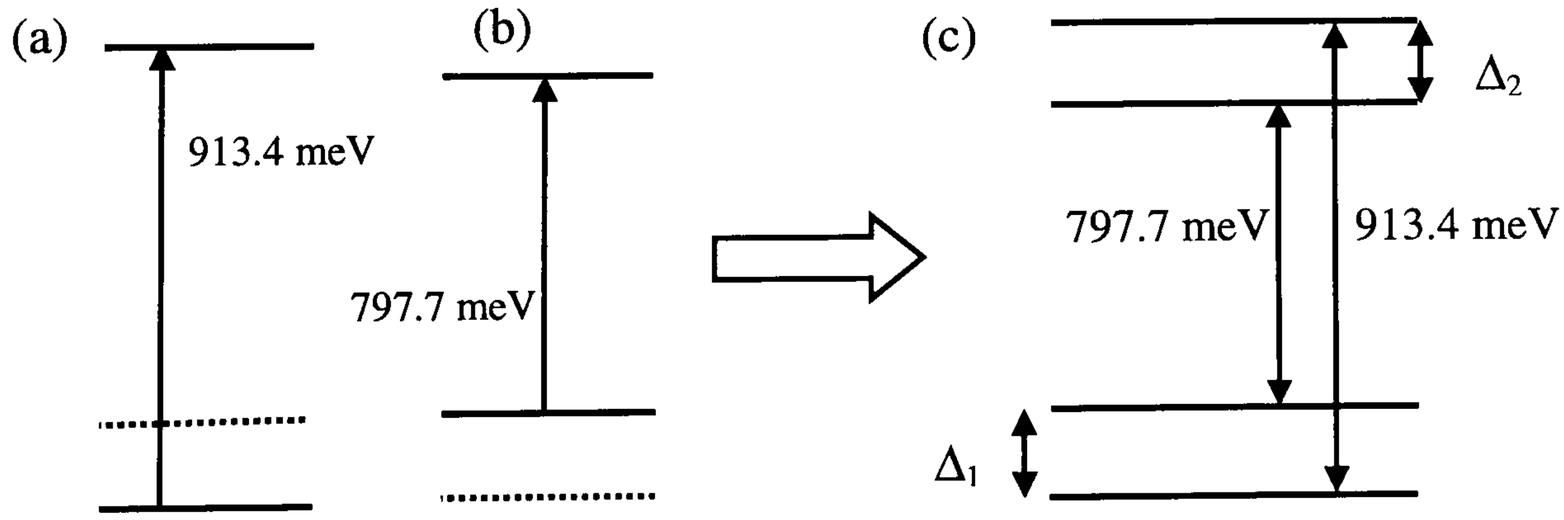

Figure 8.17: Energy level diagram for the 913.4 meV transition.

The degeneracy of the two lowest energy levels are also determined using the least squares fit and equation (8.1). The ratio of $g_2 / g_1 = 3$. Collating all of the information so far results in figure 8.18.

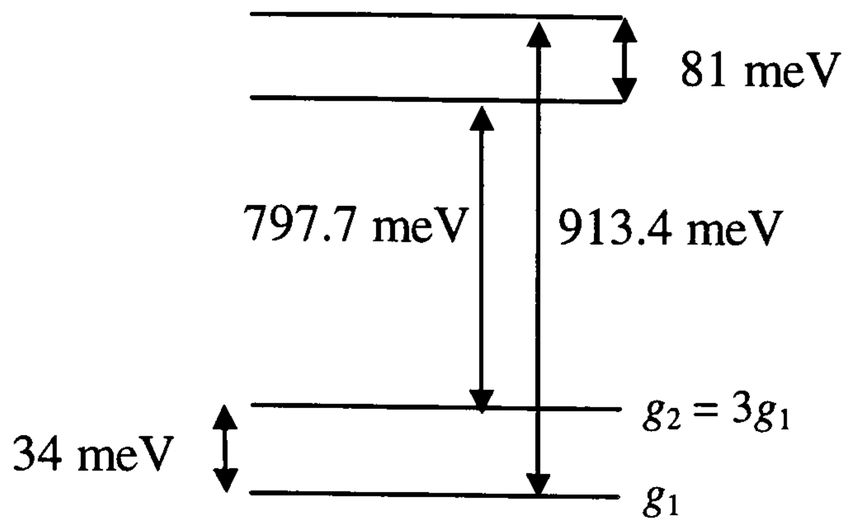

Figure 8.18: Energy level diagram for the 914.3 meV system.

However, why are there no transitions observed between the other energy levels, for example, between the ground state and the second excited state, or the first excited state and the upper level? If these possibilities are considered, one would expect to observe absorption in the infrared at 831.7 and 879.4 meV. Referring back to figure 8.3, there is no sign of any absorption at these energies. From this it is reasonable to conclude that these transitions are forbidden, and therefore not observed.

Uniaxial stress measurements were performed on the 913.4 meV absorption band and, although the results will not be presented in any detail, have been used to help with the identification of the energy levels involved. When stress is applied to the 913.4 meV absorption band, it splits into two. Figure 8.19 demonstrates the effect the temperature has on this line when stress is being applied. The black and red lines compare the data recorded at 4.2 and 100 K respectively. It is clearly seen that the lower energy band appears when the temperature increases. This indicates that the ground state of the system is a doublet and the low lying excited state becomes populated as the temperature in increased, hence an increase in intensity of the low energy line. A sketch, showing the behaviour of the transition under applied stress, in shown in figure 8.20.

Figure 8.21 shows how the spectrum changes with a horizontal and vertical polariser in place. Hughes and Runciman [8.6] show that for a centre with trigonal symmetry (E→A transition), the two observed absorption lines will be of relative intensity 1:3 for horizontal polarisation, and 4:0 for vertical polarisation. Figure 8.21 demonstrates this effect, which indicates that the 913.4 meV system being studied occurs between an E and an A state, and has trigonal (C_{3v}) symmetry. Further theory on uniaxial stress measurements can be found in [8.7].

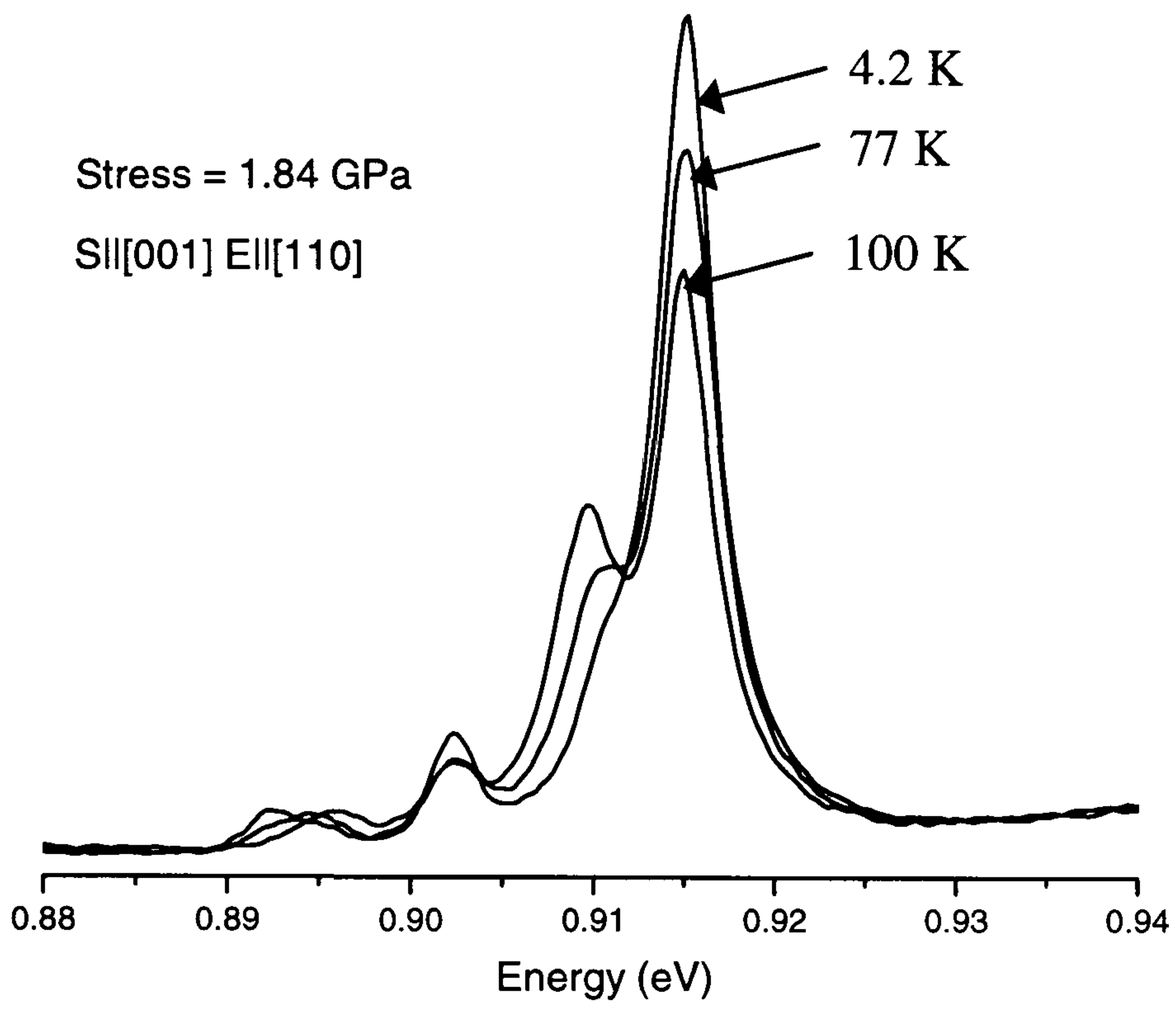

Figure 8.19: Uniaxial stress measurements taken on the 913.4 meV absorption band in the temperature range 4 – 100 K. The stress is along a [001] direction, with a horizontal polarisation.

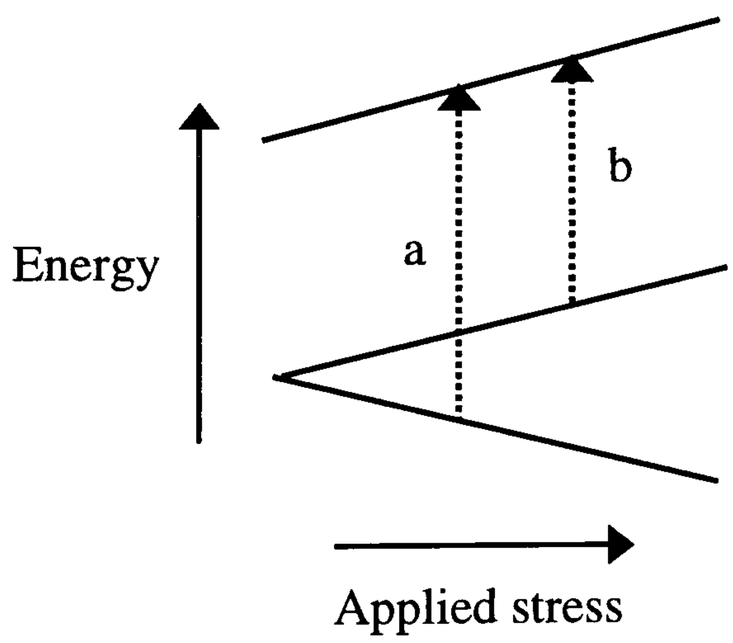

Figure 8.20: Sketch showing how the ground state of the system splits under uniaxial stress. At low temperatures, only the bottom level will be populated and so only transition a will occur. As the temperature is increased the second level becomes populated, hence the intensity of transition b will increase. Note that this figure has not been drawn to any scale.

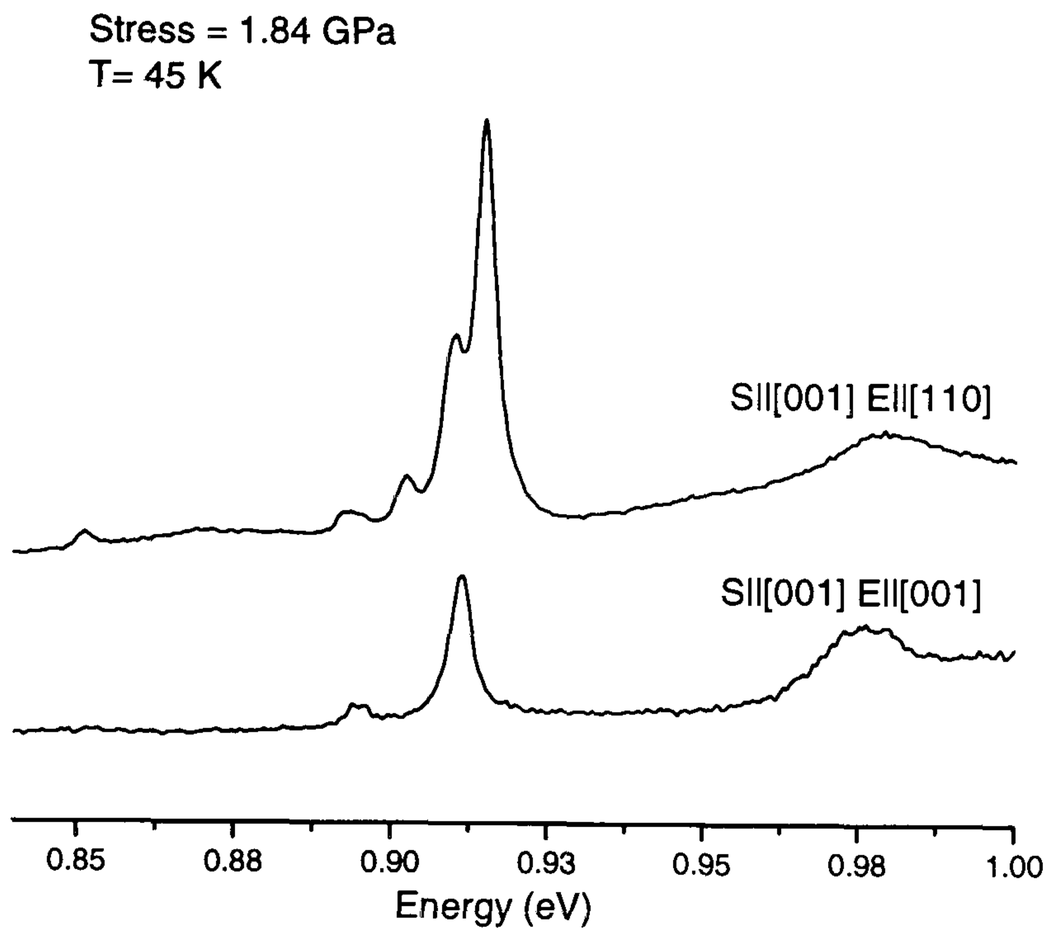

Figure 8.21: Uniaxial stress measurements taken on the 913.4 meV transition, showing the effect of a horizontal (top) and vertical (bottom) polariser.

It has already been shown from the least squares fit that the ratio $g_2 / g_1 = 3$, hence, if the lowest ground state is an E state (2-fold degenerate), the degeneracy of the excited state must be 6. The most likely possibility for a 6-fold degenerate energy level is to have a spin 1, E state, figure 8.22.

If C_{3v} symmetry is assumed, which is consistent with the results of the stress polarisation investigations, the E $\rightarrow$ A transition is allowed. This means that X and Y in figure 8.22 can be assumed to be A states. X must have a spin of 1 for the 913.4 meV transition to be allowed, as must the spin of state Y be zero.

Additional confirmation that what has been discussed is true would come from any correlation with any observed EPR transitions with the same properties. There has been no observation of a correlating EPR transition with the 913.4 meV transition. This is expected however, because it is spin 0. Defects with S = 0 cannot be observed using EPR. However, one would expect to observe an EPR transition that correlates with the spin 1, 797.7 meV transition. However, at low temperatures, the energy level from which the transition originates is not populated. As the temperature is increased the level slowly becomes populated, until room temperature when it is only 22 % full, calculated using equation (8.1). The D value (zero field splitting) is unknown for this defect, and this could significantly affect the probability of observing an EPR transition. If D is significantly larger than the energy of the microwave radiation, hν, no forbidden transitions would be observed, because the level from which they would originate, would not be populated, figure 8.22. The allowed

transitions would also not be observed because the quantum of energy would be too small to trigger the transition. This problem can be overcome by recording spectra at a much higher temperature, and/or a much higher frequency, which would result in a bigger value for hν.

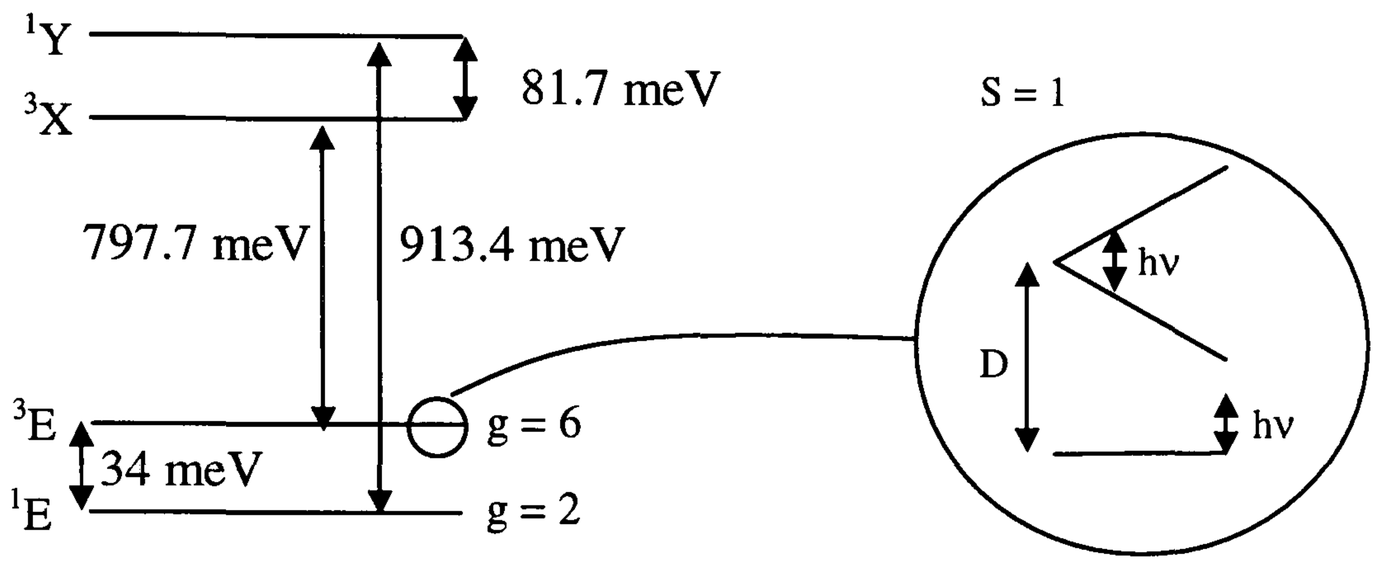

Figure 8.22: The energy level diagram for the 913.4 meV system, showing the spin 1 behaviour of the low-lying excited state.

Finally, the last point that must be discussed in this section is the transition at 1086 meV. From the temperature variation, it can be concluded that the transition originates from the ground state as it is observed at low temperatures. It can be included in the energy level diagram as follows, figure 8.23.

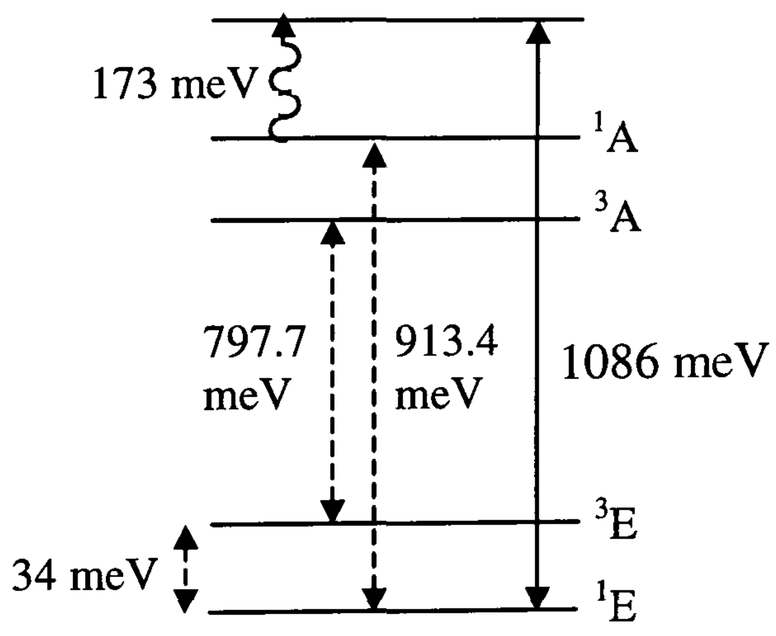

Figure 8.23: Final energy level diagram for the 913.4 meV system, with possible energy level configurations labelled.

The 1086 meV transition is located 173 meV above the 913.4 meV zero phonon line (ZPL), which is consistent with it being a local vibrational mode. The local vibrational mode can be considered in terms of the diamond lattice having a maximum allowed frequency, below which the vibrations of the atoms spread throughout the lattice. This frequency cut-off value for diamond is 1332 cm^{-1}, equivalent to 165 meV. If there is a defect within the

lattice, which is lighter than a carbon atom, the defect atom will vibrate at a frequency higher than which can be propagated along the chain. This gives rise to a localised mode of vibration with a well-defined frequency, which is outside the band of closely spaced frequencies associated with the rest of the atoms in the chain.

Having explained the intensities, the change in line position can be discussed. Figures 8.12(b) and 8.14(b) show how the position of each absorption band changes with the temperature. The same effect is observed with each of the transitions; the absorption band moves to a lower energy as the temperature is increased. This effect can be explained in terms of thermal expansion. As the temperature is lowered, the lattice contracts, which results in the energy levels shifting further apart. This results in an increase in energy of the observed transitions, which agrees with what is observed experimentally.

Finally, it was shown by Fuchs that the absorption band at 913.4 meV involves hydrogen. The samples available for this work were doped with ^{14}N and ^{15}N, but there was no isotope dependence observed in any of the spectra. Hence, there is no evidence that nitrogen is involved in this defect.

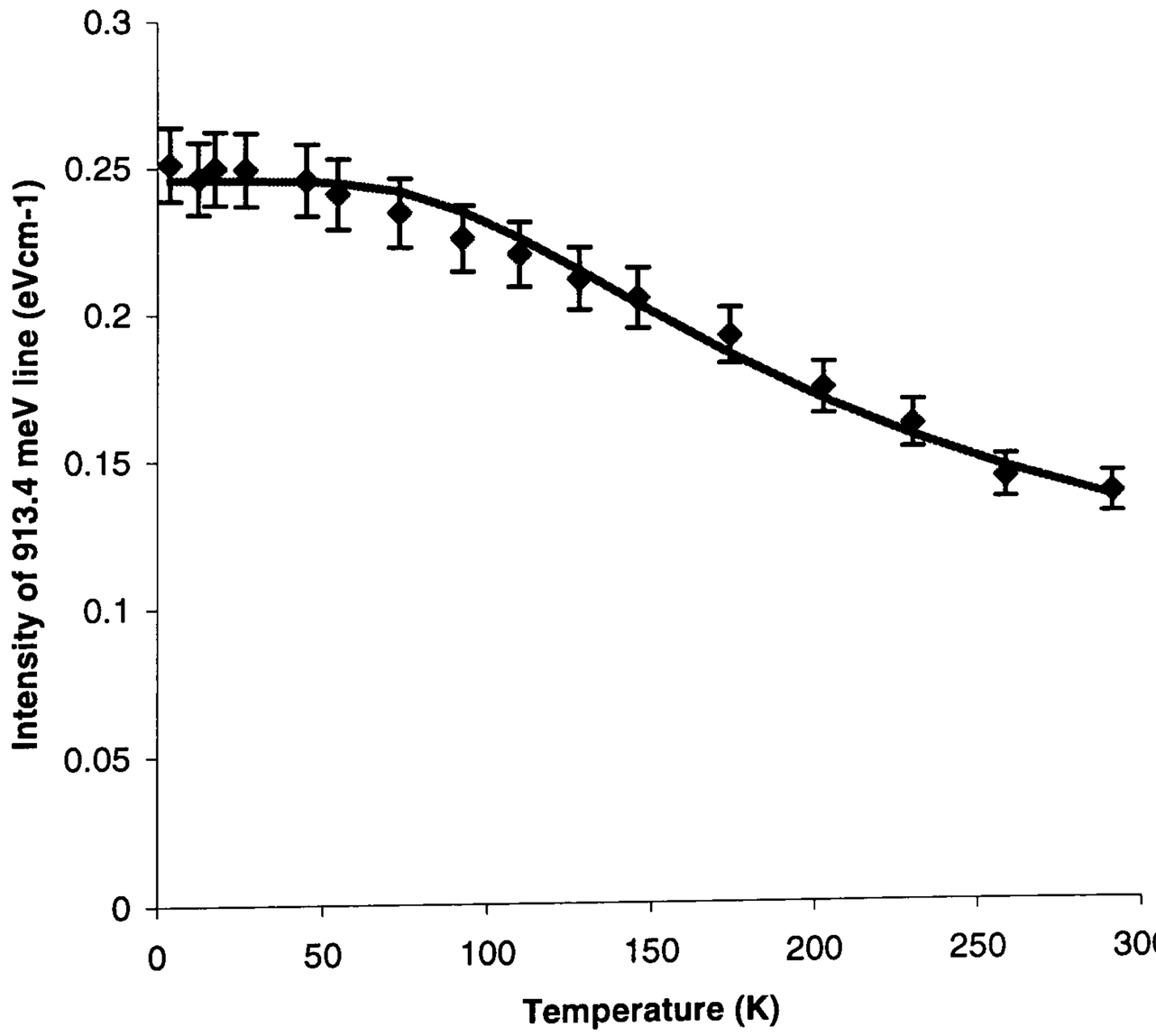

Figure 8.24: Plot showing the temperature behaviour of the 913.4 meV absorption line.

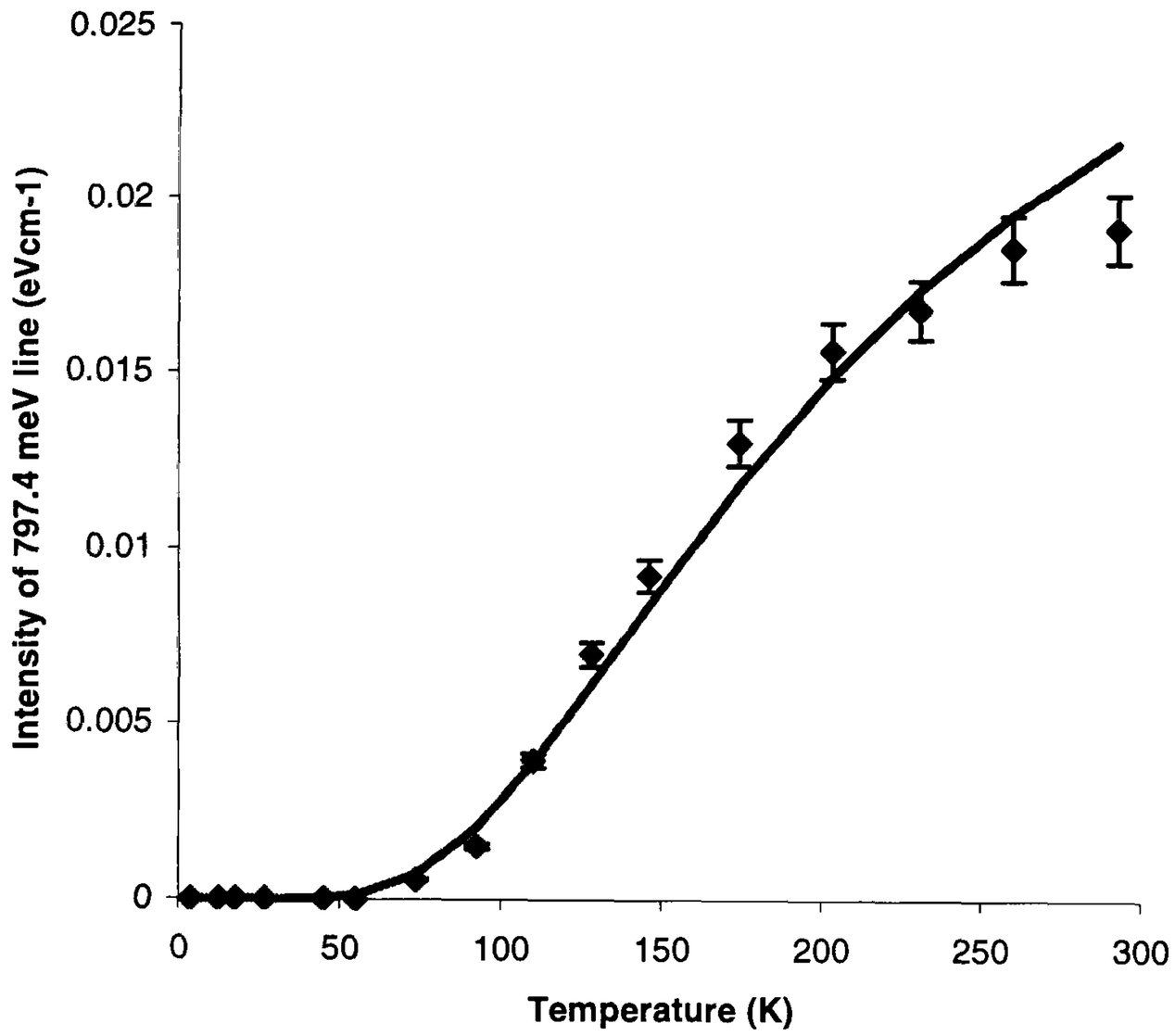

Figure 8.25: Plot showing the temperature behaviour of the 797.7 meV absorption line.

8.5.2 The 897.7 and 896.1 meV system

The same process which has been applied to the 913.4 meV system can be applied to this one. Figures 8.12(c) and 8.12(e) show the temperature variation of the 897.7 and 896.1 meV absorption bands. It is clear that the 897.7 meV band originates from the ground state of the system because it is observed at low temperatures. The 896.1 meV band only becomes visible at temperatures above approximately 15 K, which indicates that it originates from a very low lying excited state, which does not require much thermal energy to become populated. Using equation (8.1) and fitting with the least number of low lying energy levels as possible, produces the following energy level diagram, figure 8.26.

Using the least squares fit, it was found that the low-lying excited state lies just 3.4 meV above the ground state. Both of the levels have a degeneracy of 1. In order for the data to fit however, a second excited state must exist 37 meV above the ground state, which has a degeneracy of 3. From the degeneracy's it is possible to assume that the spin of the ground state and the first excited state is 0, which also implies that the spins of the upper two states are also 0. This must be true in order to obey the selection rules and observe the transitions. The fits produced using equation (8.1) and the least squares fitting are shown in figures 8.27 and 8.28. Once again, both transitions were fit simultaneously in order to simulate the data as if originating from the same defect.

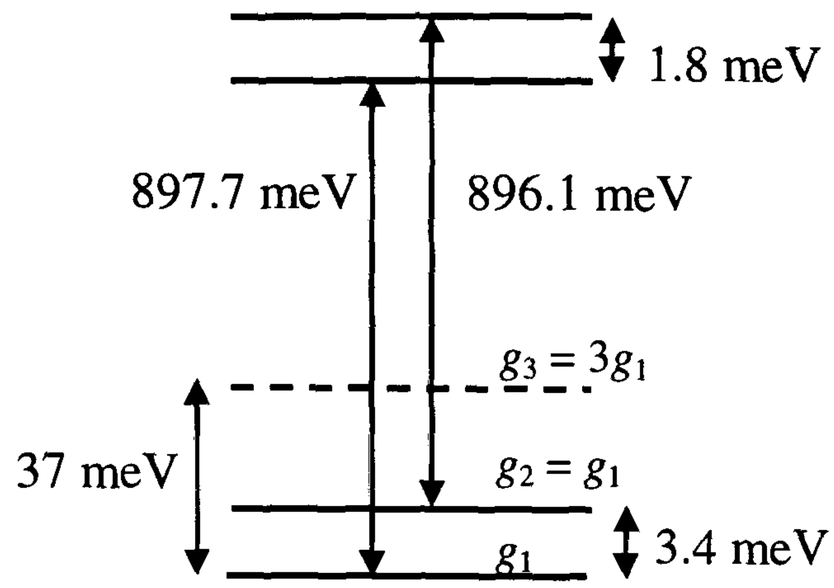

Figure 8.26: Energy level diagram for the 897.7 meV system.

If the spins of the levels are equal, it cannot be the spin selection rules that are forbidding the transitions between the other two energy levels. Instead it may well involve the symmetry selection rules.

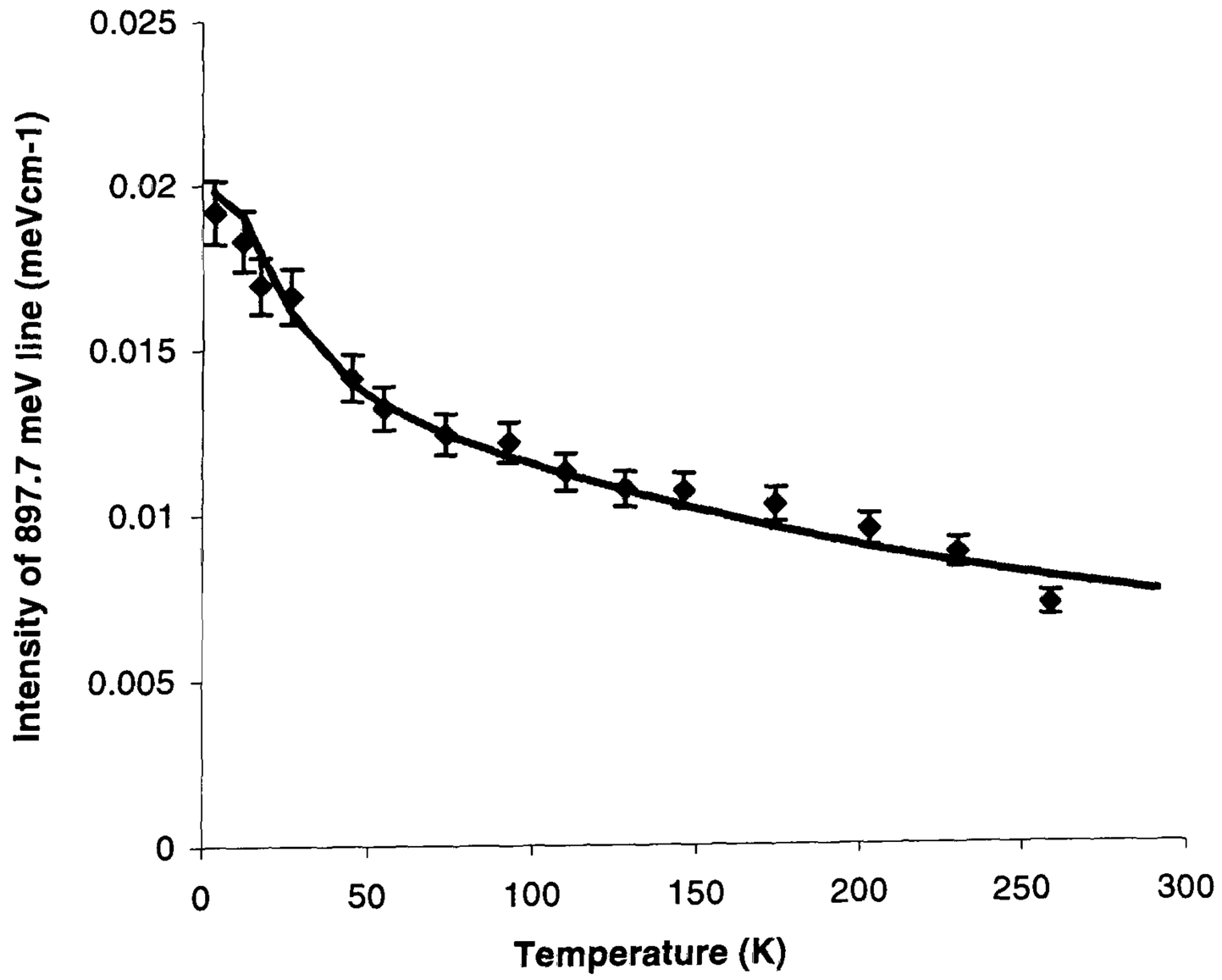

Figure 8.27: Plot showing how the intensity of the 897.7 meV absorption line varies with temperature and how, using equation 8.1, a fit has been produced.

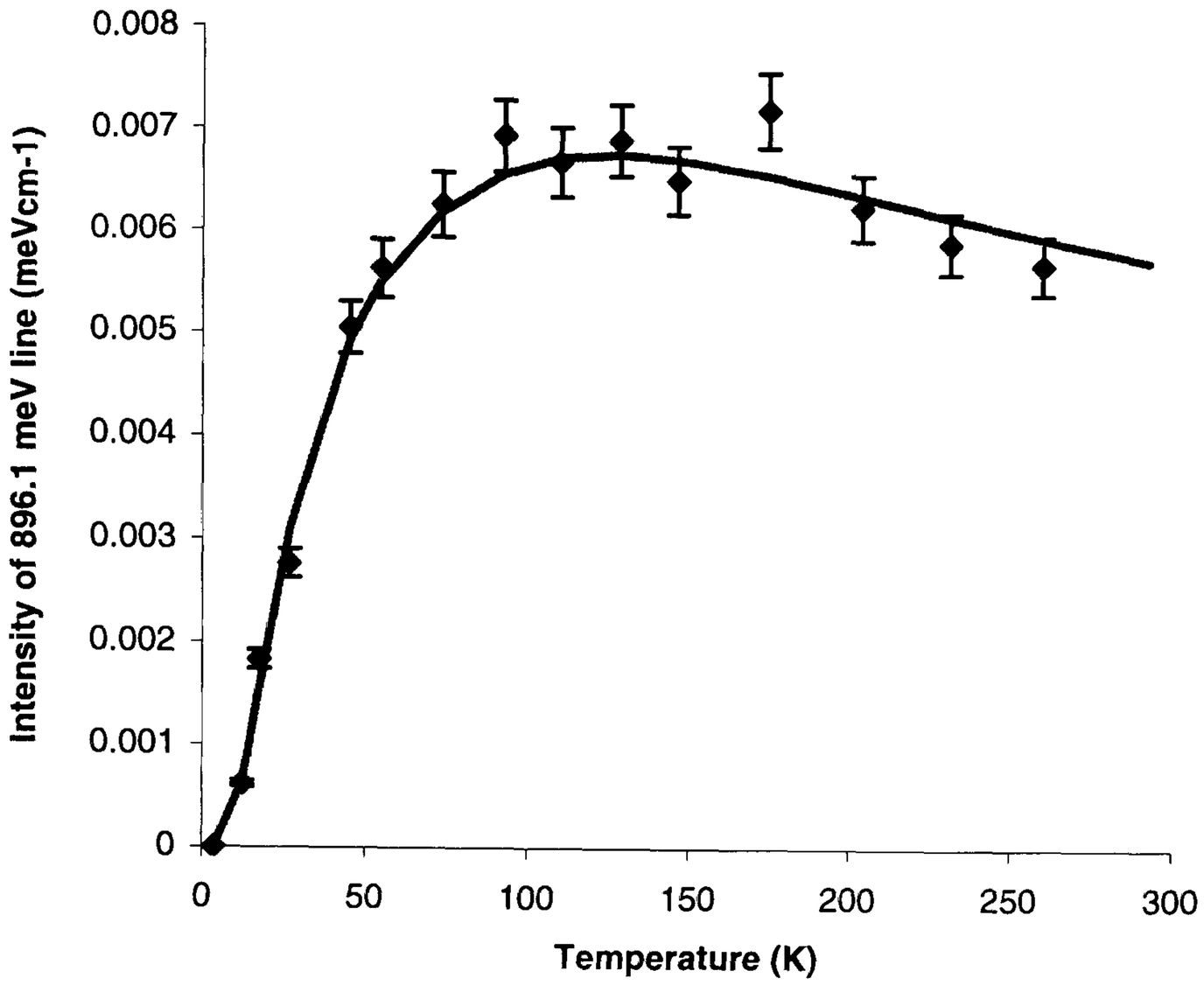

Figure 8.28: Plot showing the temperature dependence and fit for the 896.1 meV absorption line.

8.6 Conclusions and Further Work

The results of these experiments have managed to explain five of the observed transitions within the infrared region of the spectrum. It has been found that the 913.4, 797.7 and the 1086 meV absorption bands originate from the same defect. In this system the 913.4 meV transition originates from a spin 0, E ground state, which lies 34 meV below the spin 1, E excited state belonging to the 797.7 meV transition. To complete the system, the 1086 meV transition is a local mode to the zero phonon line at 913.4 meV.

It has also been shown that the 897.7 and the 896.1 meV transitions originate from the same defect. The 897.7 meV transition is from the ground state and the 896.1 meV transition is from a low-lying excited state. There is another energy level involved in the system, but there are no transitions observed from it. The electronic configurations proposed are consistent with all of the experimental data.

From figure 8.9, it was found that the 896.1 meV transition correlates with the 913.4 meV absorption line. This also means that the 897.7 meV transition correlates with the 913.4 meV transition, but a single fit, which incorporates all of the transitions, cannot be produced.

The transitions observed at 691.3 meV, 851.5 meV and 892.6 meV have not been found to correlate with any of the other lines in the infrared.

Although some work has been presented in this chapter, there is still much that can be done in order to fully understand the systems being studied.

An important thing to do would be to identify the defect responsible for the absorption lines being studied. Attempts at correlations have been made, but have so far failed to show anything. It has been shown by Fuchs [8.4] that the peaks at 691.8, 851.5, 897.7, and 913.4 meV contain hydrogen. However, none of the peaks have shown to observe any isotope shift between samples doped with ^{14}N and ^{15}N. This implies that nitrogen is not responsible for any of the defects causing the absorption. Instead, any defects shown to contain hydrogen must be considered as possible candidates for these defects. One suggestion is that the defect responsible for the 913.4 meV system is the C – H – C defect. This centre would have the observed C_{3v} symmetry, and would show isotope dependence with $^{1}H/^{2}H$ and $^{12}C/^{13}C$, but not with $^{14}N/^{15}N$. As mentioned in Chapter 2, the bond centred position of muonium is the most stable form, which would also be expected for hydrogen. The charge state of the C – H – C defect would be expected to be negative, and this is supported by theoretical calculations presented by Goss [8.8].

The absorption band at 915 meV was mentioned at the start of the chapter, but no further work was carried out. Further work should be carried out on a sample that contains this peak in a significant intensity in order to try and identify it.

Finally, further work must be carried out on the other lines in the region that have not been linked with anything else, for example the 691.3, 851.5 and 892.6 meV absorption bands.

References

[8.1] A. Zaitsev, Optical Data on Superhard Semiconductors: Diamond, ISTOK (1998)

[8.2] D. Hunt, DPhil Thesis, University of Oxford (1999)

[8.3] F. Fuchs, C. Wild, K. Schwarz, W. Muller-Sebert and P. Koidl, Appl. Phys. Lett., **66**, 2 (1995)

[8.4] F. Fuchs, C. Wild, K. Schwarz and P. Koidl, Diam. Rel. Mat. **4**, 652 (1995)

[8.5] A. T. Collins, G. Davies, H. Kanda and G. S. Woods, J. Phys. C: Solid State Phys. **21**, 1363 (1988)

[8.6] A. E. Hughes and W. A. Runciman, Proc, Phys. Soc. **90**, 827 (1967)

[8.7] K. Mohammed, G. Davies and A. T. Collins, J. Phys. C **15**, 2779 (1982)

[8.8] J. P. Goss, J. Phys. Condens. Mat. **15**, R551 (2003)

Appendix 1

Samples and Concentrations

	Type	Weight mg	$[N_s^0]$ cm^{-3}	$[NVH^-]$ cm^{-3}	[913] $meVcm^{-1}$	Treated	$[VH^-]$	$[NV^-]$ cm^{-3}	$[N_s^+]$ cm^{-3}
1	CVD	15.06	2.23×10^{17}	3.17×10^{17}	8.34	Irradiated	Yes		
2	CVD	12.0	1.06×10^{18}	N/A	N/A				
3	CVD	10.7	3.73×10^{17}	4.94×10^{16}	10.50			$< 2 \times 10^{16}$	
4	CVD	7.0	2.01×10^{17}	2.99×10^{16}	4.31	Irradiated			
5	CVD	7.7	1.09×10^{17}	6.7×10^{16}	N/A	Irradiated			
6	CVD	28.0	7.16×10^{17}	7.34×10^{16}	22.62				
7	CVD	2.0	1.35×10^{17}	1.51×10^{16}	3.69		Yes		
8	CVD	4.7	3.78×10^{17}	4.51×10^{17}	116.68			$< 2 \times 10^{16}$	2×10^{18}
9	CVD	56.7	3.98×10^{16}	5.28×10^{15}	2.36	Irradiated & annealed	Yes	$< 2 \times 10^{16}$	1×10^{17}
10	CVD	8	1.43×10^{17}	1.23×10^{17}	7.87		Yes		3×10^{17}
11	CVD	12	1.73×10^{17}	1.14×10^{17}	32.25		Yes		7×10^{17}
12	CVD	12	2.80×10^{17}	1.14×10^{17}	3.1				
13	CVD	34	7.39×10^{16}	2.29×10^{17}	7.61		Yes		5×10^{16}
14	HPHT	12.09	$< 1 \times 10^{17}$	0	0	Irradiated & annealed	Yes	$< 1 \times 10^{18}$	$\sim 8 \times 10^{17}$

Appendix 2

Concentration Calculations

The process of the concentration calculations has been described in section 4.3. The spreadsheet used for the calculations is given below:

$$[X]=\frac{[STD]I_X Mass_{STD}}{I_{STD} Mass_X}\frac{Mod_{STD}}{Mod_X}\frac{g^2_{STD}[S(S+1)]_{STD}}{g^2_X[S(S+1)]_X}\frac{AqTime_{STD}}{AqTime_X}\frac{Gain_{STD}}{Gain_X}\frac{N_{STD}[10^{(-Attn/20)}]_{STD}}{N_X[10^{(-Attn/20)}]_X} \quad \text{(A2.1)}$$

The black edged boxes below are the parameters that need to be changed each time a concentration is calculated, and the shaded boxes give the data required.

g (nitrogen) =	2.0024	[STD] =	270	ppm
g (unknown) =	2.0024	Mass (STD) =	2.54	mg
S (nitrogen) =	0.5	Mass (X) =	58	mg
S (unknown) =	1			

Integrated Intensity of reference sample:	1.17E+08	
Integrated Intensity of sample:	2658196.46	
Attenuation of sample:	60	dB
Attenuation of reference sample:	50	dB
Modulation for reference sample:	1	G
Modulation for sample:	0.2	G
Number of scans for sample:	100	
Number of scans for reference sample:	50	
Gain for sample:	5.02E+04	
Gain for reference sample:	1.00E+05	
Acquisition Time for sample:	81.92	
Acquisition Time for reference:	40.96	

Equation (A2.1) can now be applied using all of the above parameters:

[X] = 0.80 ppm

[X] = 1.40E+17 cm^{-3}

Appendix 3

Nitrogen Concentration Wizard

By fitting the experimental data to a standard simulated spectrum, the concentration of nitrogen within the sample can be calculated. The intensities of certain peaks are directly related to the concentrations. Not only can it calculate the concentration of single substitutional nitrogen, which can be checked using EPR, but also it can calculate the concentration of other forms of nitrogen, for example, N^+.

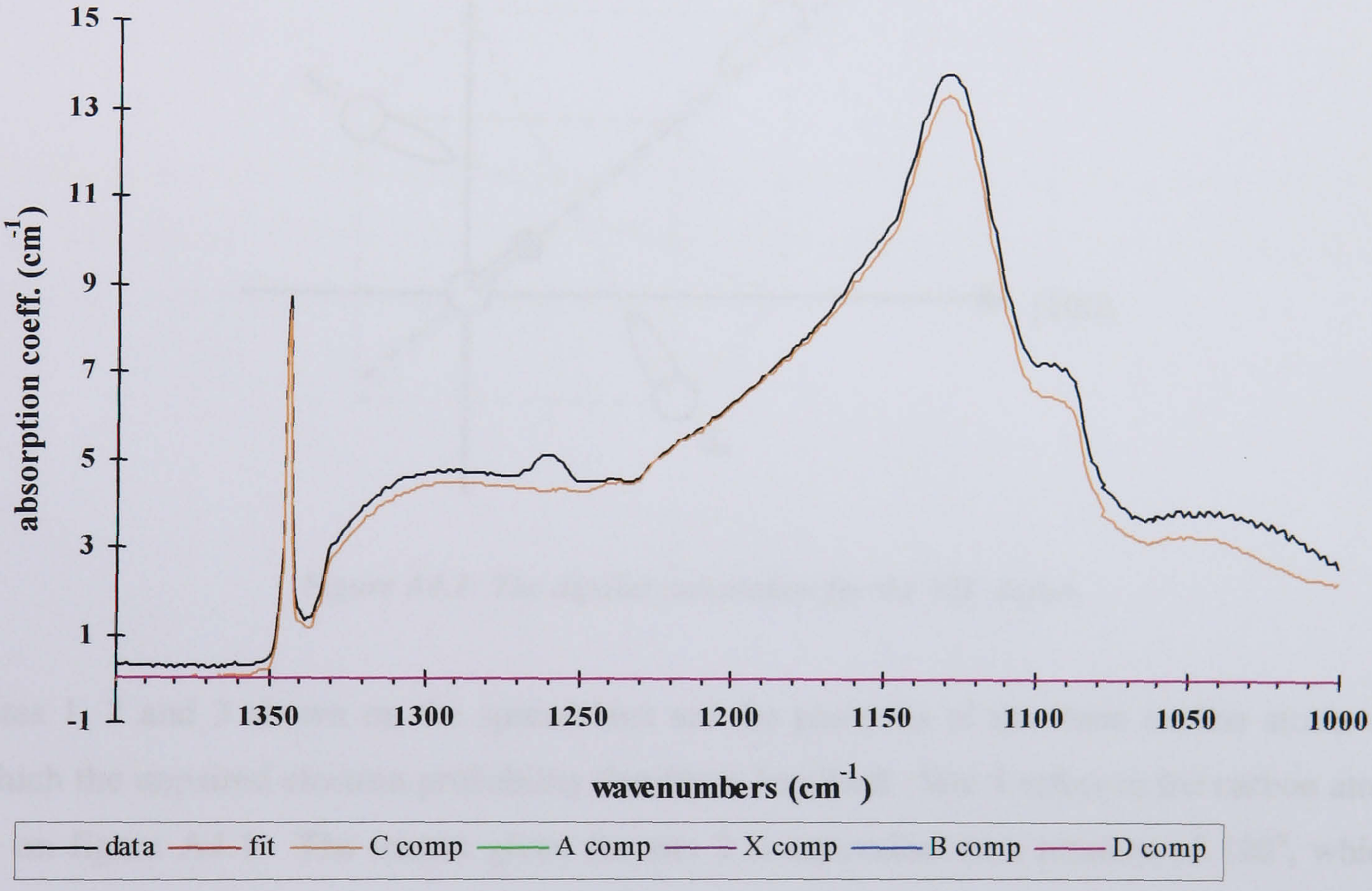

type Ib	$\mu(1130cm^{-1})$	$13.47cm^{-1}$	$[N_C]$	336.8ppm	
type IaA	$\mu(1282cm^{-1})$	$0.00cm^{-1}$	$[N_A]$	0.0ppm	
N^+	$\mu(1332cm^{-1})$	$0.00cm^{-1}$	$[N^+]$	0.0ppm	
type IaB	$\mu(1282cm^{-1})$	$0.00cm^{-1}$	$[N_B]$	0.0ppm	*fit range*
D	65536	$0.00cm^{-1}$	$[N_T]$	336.8ppm	*1399*

(Updated from the original template by D. Fischer, DTC Research Centre)

Appendix 4

Dipolar Hyperfine Calculations

The spreadsheet over the page is the one used to perform the theoretical dipolar hyperfine calculations described in Chapters 5, 6 and 7. The one shown is for the VH^- complex described in Chapter 7, but the principles are the same for all three defects: NVH^-, NV^- and VH^-. This page will explain the details of the calculation.

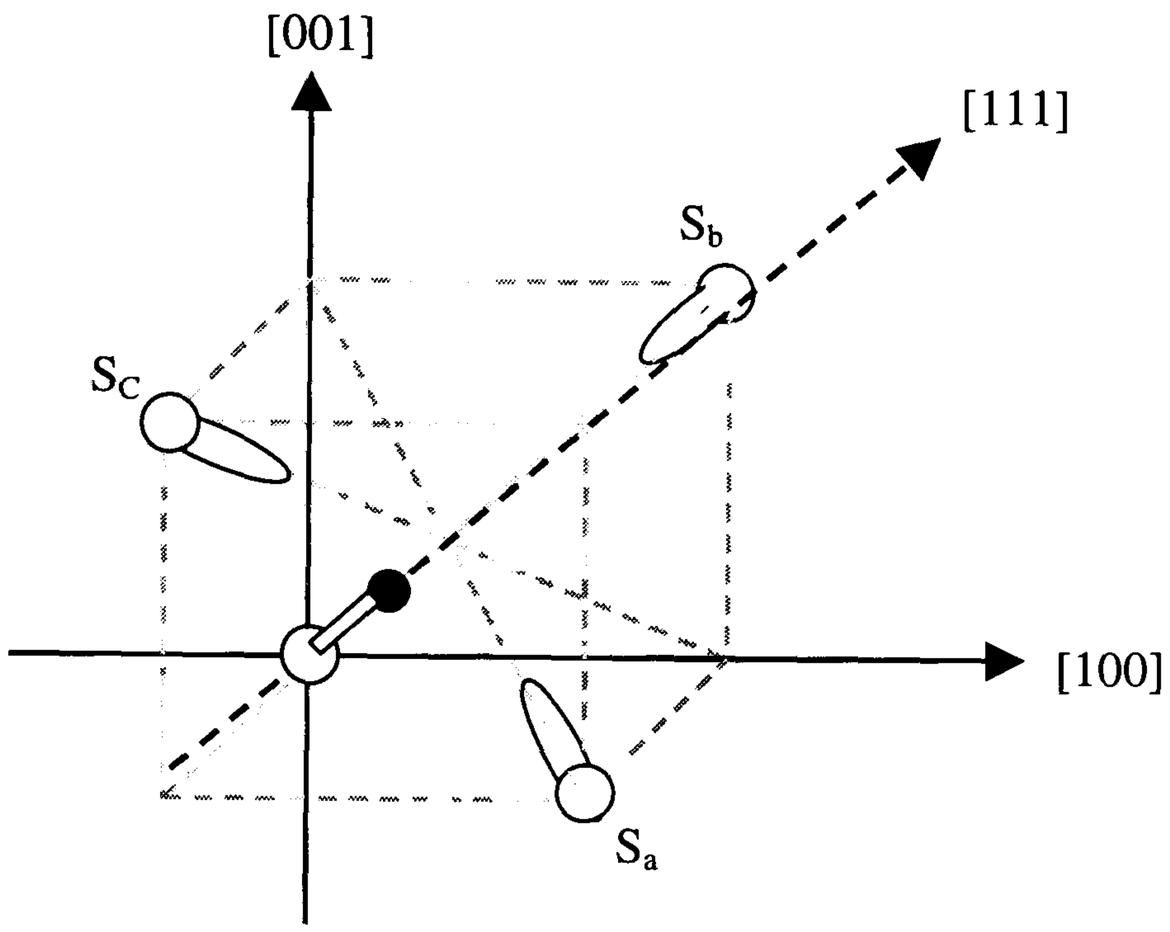

Figure A4.1: The dipolar calculation for the VH^- defect.

Sites 1, 2 and 3 shown on the spreadsheet are the positions of the three carbon atoms on which the unpaired electron probability density is localised. Site 1 refers to the carbon atom S_a on figure A4.1. The matrix given for site 2 is equivalent to a rotation of 120°, which transforms $S_a \rightarrow S_b$, $S_b \rightarrow S_c$, $S_c \rightarrow S_a$. The matrix for site 3 is the equivalent of a further rotation of 120°, or a rotation of –120°, which transforms $S_a \rightarrow S_c$, $S_c \rightarrow S_b$, $S_b \rightarrow S_a$.

The matrix R1 is the rotation matrix (where R1t is its transpose) required to transform the hyperfine matrix for site 1 from its principal axis system to the x, y and z system.

b is the theoretical dipolar hyperfine matrix in its principal axis determined by assuming that $^1/_3$ of the unpaired electron probability density is localised on each carbon neighbour (S_a, S_b and S_c), determined from equation (3.29) and figure 7.11.

$$R1\_b\_R1t = \underset{R1}{\begin{pmatrix} 1x & 2x & 3x \\ 1y & 2y & 3y \\ 1z & 2z & 3z \end{pmatrix}} \underset{b}{\begin{pmatrix} 1x & 2x & 3x \\ 1y & 2y & 3y \\ 1z & 2z & 3z \end{pmatrix}} \underset{R1t}{\begin{pmatrix} 1x & 2x & 3x \\ 1y & 2y & 3y \\ 1z & 2z & 3z \end{pmatrix}} = \begin{pmatrix} 1a & 1b & 1c \\ 2a & 2b & 2c \\ 3a & 3b & 3c \end{pmatrix}$$

, and as a check the eigenvalues and eigenvectors of the resultant are calculated (shown to the right of the matrix).

R2_*b*_R2t and R3_*b*_R3t are the equivalent matrices for sites 2 and site 3 respectively (i.e. the contribution from sites S_b and S_c), and are shown below. Again, the eigenvalues and eigenvectors of the resultant matrix have been determined and are shown to the right.

$$R2\_b\_R2t = \underset{R1}{\begin{pmatrix} 1x & 2x & 3x \\ 1y & 2y & 3y \\ 1z & 2z & 3z \end{pmatrix}} \underset{Site\ 2}{\begin{pmatrix} 0 & 0 & 1 \\ 1 & 0 & 0 \\ 0 & 1 & 0 \end{pmatrix}} \underset{b}{\begin{pmatrix} 1x & 2x & 3x \\ 1y & 2y & 3y \\ 1z & 2z & 3z \end{pmatrix}} \underset{Site\ 2}{\begin{pmatrix} 0 & 0 & 1 \\ 1 & 0 & 0 \\ 0 & 1 & 0 \end{pmatrix}} \underset{R1t}{\begin{pmatrix} 1x & 2x & 3x \\ 1y & 2y & 3y \\ 1z & 2z & 3z \end{pmatrix}} = \begin{pmatrix} 1a & 1b & 1c \\ 2a & 2b & 2c \\ 3a & 3b & 3c \end{pmatrix}$$

T is the sum of the three contributions, with its corresponding eigenvalues shown next to it. The eigenvalues of the matrix T give the theoretical value of b, and these values are then compared with those determined experimentally.

SITE 1

	Radians	**Degrees**
Phi	1.921608	110.1
rho	5.497787	**315**

R1

0.707107	-0.243	0.66404
-0.70711	-0.243	0.66404
0	-0.93909	-0.34366

b

-4.84	0	0
0	-4.84	0
0	0	9.68

R1_A_R1t + R2_A_R2t2 + R3_A_R3t

T

0	-0.22446	-0.22446
-0.22446	0	-0.22446
-0.22446	-0.22446	0

Eigenvalues

-0.44891 0.224457 0.224457

SITE 1

1	0	0
0	1	0
0	0	1

SITE 2

0	0	1
1	0	0
0	1	0

SITE 3

0	1	0
0	0	1
1	0	0

R1t

0.707107	-0.70711	0
-0.243	-0.243	-0.93909
0.66404	0.66404	-0.34366

R1_*b*_R1t

1.56258	6.40258	-3.31352
6.40258	1.56258	-3.31352
-3.31352	-3.31352	-3.12516

9.68	**-4.84**	**-4.84**
1.00	-0.38	-0.38
1.00	0.90	0.90
-0.52	1.00	1.00

R2_*b*_R2t

-3.12516	-3.31352	-3.31352
-3.31352	1.56258	6.40258
-3.31352	6.40258	1.56258

9.68	**-4.84**	**-4.84**
-0.52	0.74	1.00
1.00	-0.62	0.64
1.00	1.00	-0.12

R3_*b*_R3t

1.56258	-3.31352	6.40258
-3.31352	-3.12516	-3.31352
6.40258	-3.31352	1.56258

9.68	**-4.84**	**-4.84**
1.00	0.27	0.00
-0.52	1.00	0.00
1.00	0.25	0.00

1.9	**1.9**	**1.2**	**THEORY**
1.95	**1.95**	**1.1**	**EXPT**